

609058

U. S. A R M Y
TRANSPORTATION RESEARCH COMMAND
FORT EUSTIS, VIRGINIA

TRECOM TECHNICAL REPORT 64-49

LIFT/CRUISE FAN EXHAUST SYSTEM
RESEARCH PROGRAM

Task 1D121301A14228
Contract DA 44-177-AMC-74(T)

September 1964

DDC

DEC 2 1964

JISIA D

COPY 2 OF 3

HARD COPY \$ 6.00

MICROFICHE \$ 1.25

prepared by:

GENERAL ELECTRIC COMPANY
Flight Propulsion Division
Cincinnati, Ohio

220p



ARCHIVE COPY

DISCLAIMER NOTICE

When Government drawings, specifications, or other data are used for any purpose other than in connection with a definitely related Government procurement operation, the United States Government thereby incurs no responsibility nor any obligation whatsoever; and the fact that the Government may have formulated, furnished, or in any way supplied the said drawings, specifications, or other data is not to be regarded by implication or otherwise as in any manner licensing the holder or any other person or corporation, or conveying any rights or permission, to manufacture, use, or sell any patented invention that may in any way be related thereto.

* * *

DDC AVAILABILITY NOTICE

Qualified requesters may obtain copies of this report from

**Defense Documentation Center
Cameron Station
Alexandria, Virginia 22314**

* * *

This report has been released to the Office of Technical Services, U. S. Department of Commerce, Washington 25, D. C., for sale to the general public.

* * *

Reproduction of this document in whole or in part is prohibited except with specific written permission of the Commanding Officer, U. S. Army Transportation Research Command.

* * *


The information contained herein will not be used for advertising purposes.

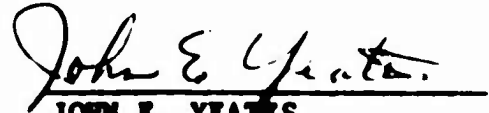
* * *

The findings and recommendation contained in this report are those of the contractor and do not necessarily reflect the views of the U. S. Army Mobility Command, the U. S. Army Materiel Command, or the Department of the Army.

HEADQUARTERS
U S ARMY TRANSPORTATION RESEARCH COMMAND
FORT EUSTIS, VIRGINIA 23604

This report has been reviewed by the U. S. Army Transportation Research Command and is considered to be technically sound. The report is published for the dissemination and exchange of technical data as well as for the stimulation of new ideas or concepts.


ROBERT D. POWELL, JR.
Project Engineer


JOHN E. YEATES
Group Leader
Aeromechanics Group

APPROVED.

FOR THE COMMANDER:


LARRY M. HEWIN
Technical Director

Task ID121301A14228
Contract DA 44-177-AMC-74(T)
TRECOM Technical Report 64-49
September 1964

**LIIT/CRUISE FAN EXHAUST SYSTEM
RESEARCH PROGRAM**

Prepared by:
General Electric Company
Flight Propulsion Division
Advanced Engine and Technology Department
Lift Fan Systems Operation
Cincinnati, Ohio 45215

for
U. S. ARMY TRANSPORTATION RESEARCH COMMAND
FORT EUSTIS, VIRGINIA

FOREWORD

The lift/cruise fan exhaust system research program was conducted for the U. S. Army Transportation Research Command. The program was designed and directed by the Contractor's Project Engineer, Mr. J. T. Kutney, previously Manager, Applications and Installations, Lift Fan Systems Operation, General Electric Company. The data analysis and the writing of the technical report were performed by Mr. W. A. Fasching, Aero-Mechanical Systems Engineer, Lift Fan Systems Operation.

The program was initiated on June 6, 1963, originally consisting of seven test configurations, then amended on January 23, 1964. Testing was begun in September 1963, and the initial test was completed on December 27, 1963. The second part of the program was started in March 1964, and it was completed on April 3, 1964.

CONTENTS

	Page
FOREWORD	111
LIST OF ILLUSTRATIONS	vii
LIST OF SYMBOLS	xix
SUMMARY	1
CONCLUSIONS	3
RECOMMENDATIONS	5
INTRODUCTION	7
ANALYSIS OF PROBLEM	9
DESCRIPTION OF TEST EQUIPMENT	11
EXPERIMENTAL PROCEDURE	17
EXPERIMENTAL RESULTS	19
EVALUATION	23
BIBLIOGRAPHY	37
APPENDIX I - Data Reduction Sample Calculation	39
APPENDIX II - Calculation Methods	43
APPENDIX III - Tables and Figures	47
DISTRIBUTION	197

BLANK PAGE

ILLUSTRATIONS

Table		Page
1	Model Geometric Properties	47
2	Model Performance Results	48
Figure		
1	Comparison of Conical and Plug Nozzle Cruise Fan Systems.....	49
2	Overall Assembly of Model in Transonic Wind Tunnel.....	50
3	Sidewall Mach Number Distribution in Transonic Wind Tunnel.....	51
4	Boundary Layer Rake Pressure Distribution at Test Mach Numbers.....	52
5	Schematic of Force Balance System.....	53
6	Balance Dead Weight Calibration.....	54
7	Effective Seal Area Calibration.....	55
8	Typical Model Installation - Models 1, 2, and 3.....	56
9	Plug Nozzle Model Installed in Transonic Wind Tunnel.....	57
10	Side View of Plug Nozzle Model.....	58
11	Close View - Plug Nozzle Model.....	59
12	Side View - Conical Nozzle Model.....	60
13	Close View - Conical Nozzle Model.....	61
14	Views of Model Details.....	62
15	Views of Model Details.....	63
16	Geometric Detail of Models 1 and 2.....	64
17	Geometric Detail of Models 3 and 4.....	65
18	Geometric Detail of Models 5 and 6.....	66

Figure		Page
19	Geometric Detail of Models 7,7A and 8.....	67
20	Geometric Detail of Models 9 and 10.....	68
21	Geometric Detail of Models 10A and 10B.....	69
22	Geometric Detail of Models 11 and 12.....	70
23	Geometric Detail of Models 13 and 14.....	71
24	Test Schedule - Pressure Ratio vs. Mach Number.....	72
25	Comparison of Performance for all Models.....	73
26	Exhaust System Performance as a Function of Mach Number and Nozzle Pressure Ratio, Model 1.....	74
27	Exhaust System Performance as a Function of Mach Number and Nozzle Pressure Ratio, Model 2.....	75
28	Exhaust System Performance as a Function of Mach Number and Nozzle Pressure Ratio, Model 3.....	76
29	Exhaust System Performance as a Function of Mach Number and Nozzle Pressure Ratio, Model 4.....	77
30	Exhaust System Performance as a Function of Mach Number and Nozzle Pressure Ratio, Model 5.....	78
31	Exhaust System Performance as a Function of Mach Number and Nozzle Pressure Ratio, Model 6.....	79
32	Exhaust System Performance as a Function of Mach Number and Nozzle Pressure Ratio, Model 7.....	80

Figure		Page
33	Exhaust System Performance as a Function of Mach Number and Nozzle Pressure Ratio, Model 7A.....	81
34	Exhaust System Performance as a Function of Mach Number and Nozzle Pressure Ratio, Model 8.....	82
35	Exhaust System Performance as a Function of Mach Number and Nozzle Pressure Ratio, Model 9.....	83
36	Exhaust System Performance as a Function of Mach Number and Nozzle Pressure Ratio, Model 10.....	84
37	Exhaust System Performance as a Function of Mach Number and Nozzle Pressure Ratio, Model 10A.....	85
38	Exhaust System Performance as a Function of Mach Number and Nozzle Pressure Ratio, Model 11.....	86
39	Exhaust System Performance as a Function of Mach Number and Nozzle Pressure Ratio, Model 12.....	87
40	Exhaust System Performance as a Function of Mach Number and Nozzle Pressure Ratio, Model 13.....	88
41	Exhaust System Performance as a Function of Mach Number and Nozzle Pressure Ratio, Model 14.....	89
42	Discharge Coefficient vs. Mach Number and Nozzle Pressure Ratio, Model 1.....	90
43	Discharge Coefficient vs. Mach Number and Nozzle Pressure Ratio, Model 2.....	91
44	Discharge Coefficient vs. Mach Number and Nozzle Pressure Ratio, Model 3.....	92

Figure		Page
45	Discharge Coefficient vs. Mach Number and Nozzle Pressure Ratio, Model 4.....	93
46	Discharge Coefficient vs. Mach Number and Nozzle Pressure Ratio, Model 5.....	94
47	Discharge Coefficient vs. Mach Number and Nozzle Pressure Ratio, Model 6.....	95
48	Discharge Coefficient vs. Mach Number and Nozzle Pressure Ratio, Model 7.....	96
49	Discharge Coefficient vs. Mach Number and Nozzle Pressure Ratio, Model 7A.....	97
50	Discharge Coefficient vs. Mach Number and Nozzle Pressure Ratio, Model 8.....	98
51	Discharge Coefficient vs. Mach Number and Nozzle Pressure Ratio, Model 9.....	99
52	Discharge Coefficient vs. Mach number and Nozzle Pressure Ratio, Model 10	100
53	Discharge Coefficient vs. Mach Number and Nozzle Pressure Ratio, Model 10A.....	101
54	Discharge Coefficient vs. Mach Number and Nozzle Pressure Ratio, Model 11.....	102
55	Discharge Coefficient vs. Mach Number and Nozzle Pressure Ratio, Model 12.....	103
56	Discharge Coefficient vs. Mach Number and Nozzle Pressure Ratio, Model 13.....	104
57	Discharge Coefficient vs. Mach Number and Nozzle Pressure Ratio, Model 14.....	105
58	External Pressure Distribution as a Function of Axial Distance and Mach Number, Model 1.....	106

Figure		Page
59	External Pressure Distribution as a Function of Axial Distance and Mach Number, Model 2.....	107
60	External Pressure Distribution as a Function of Axial Distance and Mach Number, Model 3.....	108
61	External Pressure Distribution as a Function of Axial Distance and Mach Number, Model 4.....	109
62	External Pressure Distribution as a Function of Axial Distance and Mach Number, Model 5.....	110
63	External Pressure Distribution as a Function of Axial Distance and Mach Number, Model 6.....	111
64	External Pressure Distribution as a Function of Axial Distance and Mach Number, Model 7.....	112
65	External Pressure Distribution as a Function of Axial Distance and Mach Number, Model 7A.....	113
66	External Pressure Distribution as a Function of Axial Distance and Mach Number, Model 8.....	114
67	External Pressure Distribution as a Function of Axial Distance and Mach Number, Model 9.....	115
68	External Pressure Distribution as a Function of Axial Distance and Mach Number, Model 10.....	116
69	External Pressure Distribution as a Function of Axial Distance and Mach Number, Model 10A.....	117

Figure		Page
70	External Pressure Distribution as a Function of Axial Distance and Mach Number, Model 10B.....	118
71	External Pressure Distribution as a Function of Axial Distance and Mach Number, Model 11.....	119
72	External Pressure Distribution as a Function of Axial Distance and Mach Number, Model 12.....	120
73	External Pressure Distribution as a Function of Axial Distance and Mach Number, Model 13.....	121
74	External Pressure Distribution as a Function of Axial Distance and Mach Number, Model 14.....	122
75	Plug Pressure Distribution as a Function of Axial Distance and Pressure Ratio, Mach 0, Model 4.....	123
76	Plug Pressure Distributions as a Function of Axial Distance and Pressure Ratio, Mach 0, Model 5.....	124
77	Plug Pressure Distributions as a Function of Axial Distance and Pressure Ratio, mach 0, Model 6.....	125
78	Plug Pressure Distributions as a Function of Axial Distance and Pressure Ratio, Mach 0, Model 7.....	126
79	Plug Pressure Distributions as a Function of Axial Distance and Pressure Ratio, Mach 0, Model 7A.....	127
80	Plug Pressure Distributions as a Function of Axial Distance and Pressure Ratio, Mach 0, Model 8.....	128

Figure		Page
81	Plug Pressure Distributions as a Function of Axial Distance and Pressure Ratio, Mach 0, Model 9.....	129
82	Plug Pressure Distributions as a Function of Axial Distance and Pressure Ratio, Mach 0, Model 10.....	130
83	Plug Pressure Distributions as a Function of Axial Distance and Pressure Ratio, Mach 0, Model 10A.....	131
84	Plug Pressure Distributions as a Function of Axial Distance and Pressure Ratio, Mach 0, Model 11.....	132
85	Plug Pressure Distributions as a Function of Axial Distance and Pressure Ratio, Mach 0, Model 12.....	133
86	Plug Pressure Distributions as a Function of Axial Distance and Pressure Ratio, Mach 0, Model 13.....	134
87	Plug Pressure Distributions as a Function of Axial Distance and Pressure Ratio, Mach 0, Model 14.....	135
88	Plug Pressure Distributions as a Function of Axial Distance and Pressure Ratio, Mach .4, Model 6.....	136
89	Plug Pressure Distributions as a Function of Axial Distance and Pressure Ratio, Mach .8, Model 4.....	137
90	Plug Pressure Distributions as a Function of Axial Distance and Pressure Ratio, Mach .8, Model 5.....	138
91	Plug Pressure Distributions as a Function of Axial Distance and Pressure Ratio, Mach .8, Model 7.....	139

Figure		Page
92	Plug Pressure Distributions as a Function of Axial Distance and Pressure Ratio, Mach .8, Model 7A.....	140
93	Plug Pressure Distributions as a Function of Axial Distance and Pressure Ratio, Mach .8, Model 8.....	141
94	Plug Pressure Distributions as a Function of Axial Distance and Pressure Ratio, Mach .8, Model 9.....	142
95	Plug Pressure Distributions as a Function of Axial Distance and Pressure Ratio, Mach .8, Model 10.....	143
96	Plug Pressure Distributions as a Function of Axial Distance and Pressure Ratio, Mach .8, Model 10A.....	144
97	Plug Pressure Distributions as a Function of Axial Distance and Pressure Ratio, Mach .8, Model 11.....	145
98	Plug Pressure Distributions as a Function of Axial Distance and Pressure Ratio, Mach .8, Model 12.....	146
99	Plug Pressure Distributions as a Function of Axial Distance and Pressure Ratio, Mach .8, Model 13.....	147
100	Plug Pressure Distributions as a Function of Axial Distance and Pressure Ratio, Mach .8, Model 14.....	148
101	Plug Pressure Distributions as a Function of Axial Distance and Pressure Ratio, All Mach Numbers, Model 1.....	149
102	Plug Pressure Distributions as a Function of Axial Distance and Pressure Ratio, All Mach Numbers, Model 2.....	150

Figure		Page
103	Plug Pressure Distributions as a Function of Axial Distance and Pressure Ratio, All Mach Numbers, Model 3.....	151
104	Plug Pressure Distributions as a Function of Axial Distance and Pressure Ratio, All Mach Number, Model 4.....	152
105	Plug Pressure Distributions as a Function of Axial Distance and Pressure Ratio, All Mach Numbers, Model 5.....	153
106	Plug Pressure Distributions as a Function of Axial Distance and Pressure Ratio, All Mach Numbers, Model 6.....	154
107	Plug Pressure Distributions as a Function of Axial Distance and Pressure Ratio, All Mach Numbers, Model 7.....	155
108	Plug Pressure Distributions as a Function of Axial Distance and Pressure Ratio, All Mach Numbers, Model 7A.....	156
109	Plug Pressure Distributions as a Function of Axial Distance and Pressure Ratio, All Mach Numbers, Model 8.....	157
110	Plug Pressure Distributions as a Function of Axial Distance and Pressure Ratio, All Mach Numbers, Model 9.....	158
111	Plug Pressure Distributions as a Function of Axial Distance and Pressure Ratio, All Mach Numbers, Model 10.....	159

Figure		Page
112	Plug Pressure Distributions as a Function of Axial Distance and Pressure Ratio, All Mach Numbers, Model 10A.....	160
113	Plug Pressure Distributions as a Function of Axial Distance and Pressure Ratio, All Mach Numbers, Model 11.....	161
114	Plug Pressure Distributions as a Function of Axial Distance and Pressure Ratio, All Mach Numbers, Model 12.....	162
115	Plug Pressure Distributions as a Function of Axial Distance and Pressure Ratio, All Mach Numbers, Model 13.....	163
116	Plug Pressure Distributions as a Function of Axial Distance and Pressure Ratio, All Mach Numbers, Model 14.....	164
117	Total Nacelle Drag Coefficient at Various Mach Numbers.....	165
118	Nacelle Boattail Drag Coefficient at Various Mach Numbers.....	166
119	Nozzle Plug Form Drag Coefficient at Various Mach Numbers.....	167
120	Performance Comparison of Conical Exhaust Systems.....	168
121	Comparison of Nacelle Drag Coefficients for Conical Exhaust Systems.....	169
122	Loss Breakdown of Models 1 and 3 at Mach .8.....	170
123	Loss Breakdown of Models 1 and 3 at Mach .9.....	171

Figure		Page
124	Analysis of Installed Performance.....	172
125	Performance Comparison of Conical Exhaust Systems for Test Schedule.....	173
126	Effect of Boattail Geometry on Performance for Low Boattail Plug Nozzle - Models 4 and 5.....	174
127	Comparison of Nacelle-Boattail Drag Coefficients - Models 4 and 5.....	175
128	Critical Nacelle Mach Number.....	176
129	Effect of Boattail Geometry on Performance for High Boattail Plug Nozzle - Models 12 and 14.....	177
130	Performance Comparison of Low and High Boattail Plug Nozzles.....	178
131	Effect of Plug Angle on Performance for Low Boattail Plug Nozzle - Models 5, 9 and 10.....	179
132	Comparison of Plug Forces for Models 5, 9 and 10 at Mach 0.....	180
133	Comparison of Plug Forces for Models 5, 9 and 10 at Mach .8.....	181
134	Comparison of Nacelle Boattail Drag Coefficient - Models 5, 9 and 10.....	182
135	Effect of Plug Angle on Performance for High Boattail Plug Nozzle - Models 12 and 13.....	183
136	Comparison of Plug Forces - Models 12 and 13 at Mach .8.....	184
137	Effect of Throat Area on Performance for Expandable Plug Concept - Models 6 and 9.....	185
138	Effect of Area Ratio on Performance Models 7 and 7A.....	186

Figure		Page
139	Effect of Area Ratio on Internal Peak Performance at Mach 0.....	187
140	Effect of Plug Length on Performance for Plug Nozzle - Models 5 and 10A.....	188
141	Effect of Simulated Cylindrical Flow on Boattail Pressure Coefficient - Models 8 and 10B.....	189
142	Comparison of Nacelle Boattail Drag Coefficient - Models 8 and 10B.....	190
143	Comparison of Performance for all Models with Equal Throat Area.....	191
144	Comparison of Nozzle Discharge Coefficients at Unchoked Conditions.....	192
145	Comparison of Drag Coefficients to Other Test Data at Mach .6.....	193
146	Comparison of Drag Coefficients to Other Test Data at Mach .9.....	194
147	Comparison of Nacelle Pressure Distribution to Analytical Calculations at Mach .6.....	195
148	Comparison of Nacelle Pressure Distribution to Analytical Calculations at Mach .8.....	196

LIST OF SYMBOLS

A	cross-section area, inches ²
A^*	throat area for Mach 1 conditions, inches ²
A_M	maximum model cross-section area, inches ²
A_P	projected plug area, inches ²
A_S	projected shroud area, inches ²
A_g, A_{TH}	geometric model throat area, inches ²
A_g, A_E	shroud exit area, inches ²
ΔA	effective seal area, inches ²
A_{TH}/A_M	throat area to maximum model cross-section area ratio
$A_E/A_{TH} = e$	exit area to throat area ratio
$C_{D BT}$	nacelle boattail form drag coefficient - not including friction
$C_{D P}$	plug form drag coefficient - change in plug force coefficient due to external flow - not including friction
$C_{D \pi}$	total nacelle drag coefficient - including friction, $C_{D \pi} = C_{D BT} + C_{D FB} + C_{D P} + C_{D f}$
$C_{D f}$	nacelle friction drag coefficient, $C_{D f} = C_{D \pi} - (C_{D BT} + C_{D FB} + C_{D P})$
$C_{D FB}$	forebody drag coefficient - not including friction
C_D	test nozzle discharge coefficient - ratio of actual mass flow to ideal mass flow at existing pressure ratio
C_p	pressure coefficient, $C_p = (P_1 - P_\infty)/q_\infty$
C_T	static (internal) gross thrust coefficient

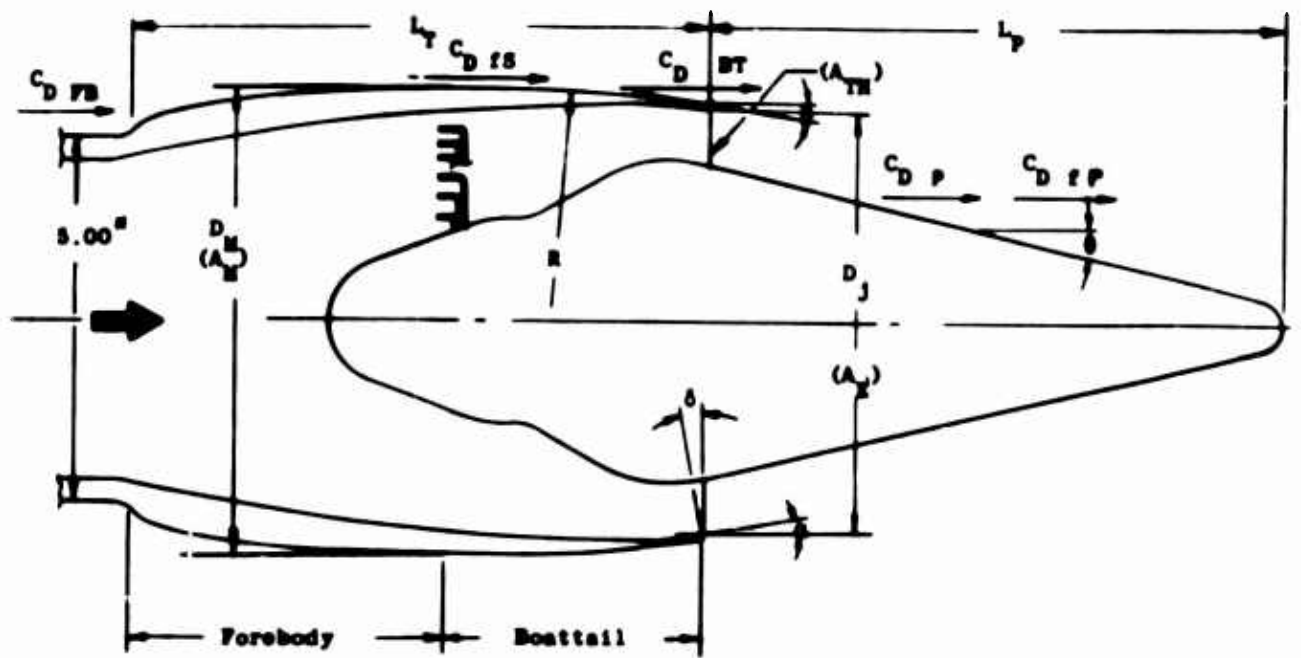
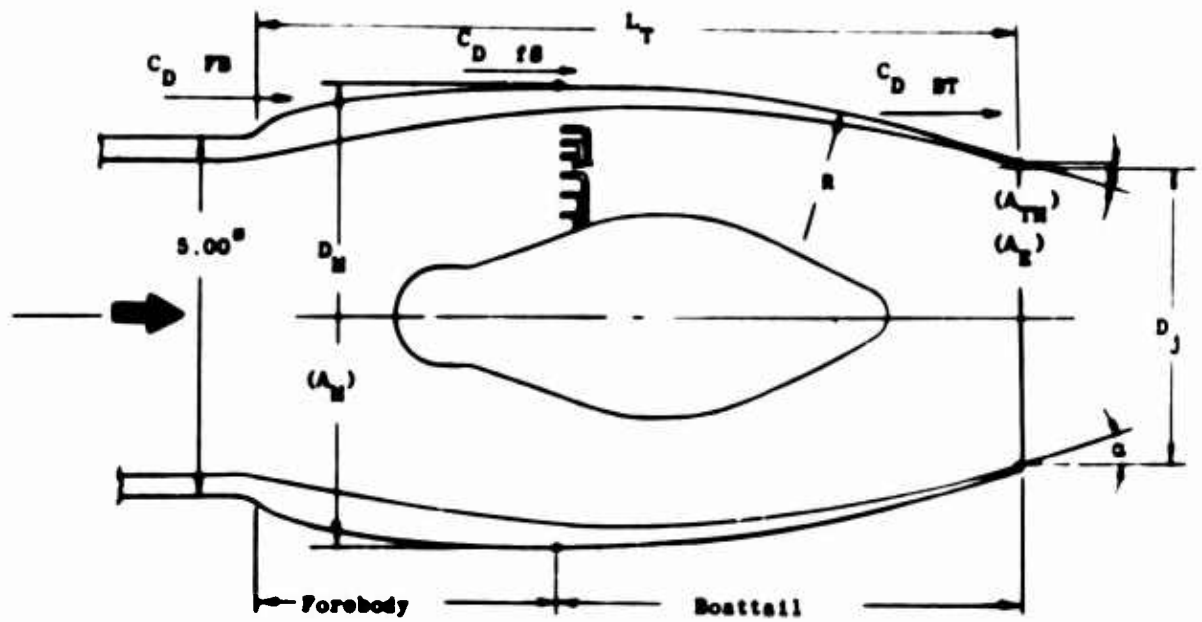
C_{T-D}	gross thrust-minus drag coefficient - including forebody drag
$C_{T \text{ Peak}}$	peak thrust coefficient
ΔC_T	thrust coefficient decrement
$\Delta C_{T \text{ BT}}$	boattail thrust coefficient decrement
$\Delta C_{T \text{ FB}}$	forebody thrust coefficient decrement
$\Delta C_{T \text{ Df}}$	friction thrust coefficient decrement
$\Delta C_{T \text{ } \pi}$	total nacelle thrust coefficient decrement
D_j	jet exit diameter, inches
D_M	maximum model diameter, inches
D_j/D_M	jet exit diameter to maximum model diameter ratio
F	stream thrust, pounds
F_p	plug force, $F_p = \int P_1 dA$, pounds
g	gravitational constant, feet/second ²
H_2	axial balance force, pounds
L	length, inches
L_C	cut-off plug length, inches
L_P	plug length, inches
L_C/L_P	cut-off plug length to full plug length ratio
L_T	nacelle length, inches
L_T/D_M	nacelle length to maximum model diameter ratio

M	Mach number
m	mass flow rate, slugs/second
P	pressure, static unless otherwise specified by subscript, pounds/inch²
P₁	local static pressure, pounds/inch²
P_{TN}	nozzle total pressure, pounds/inch²
P_{T∞}	tunnel total pressure, pounds/inch²
P_∞, P_a	free stream static (ambient) pressure, pounds/inch²
q	dynamic pressure, pounds/inch²
R	gas constant, 1716.3 feet²/second² °R, or radius, inches
R/D_M	nacelle boattail radius to maximum model diameter ratio
T	temperature, °R
V	velocity, feet/second
W	weight flow rate, pounds/second
α	internal shroud exit angle, degrees
θ	boattail angle, degrees
γ	specific heat ratio
δ	throat inclination angle, degrees
ε	nozzle area ratio, $\epsilon = A_9/A_8$ or A_E/A_{TH}
λ	nozzle pressure ratio, $\lambda = P_{T6}/P_\infty$
θ	plug angle, degrees

SUBSCRIPTS

0 or ∞	free stream
1	metering nozzle station
2	facility stagnation chamber station
3	flexible seal station
6	model entrance station
8	model throat station
9	model exit station
a	actual, or ambient
BT	boattail
C	seal cavity
CR	critical
D	drag, or discharge
D BT	boattail form drag
D FB	forebody form drag
D f	friction drag
D Σ	total nacelle form drag
E	exit (jet, station 9)
FB	forebody
f	friction
i	ideal
J	jet (exit, station 9)
l	local
M	maximum
N	nozzle (station 6)

OD	5-inch outer diameter
P	plug, or pressure
T	total conditions, or thrust
T-D	thrust minus drag
TH	throat (station 8)
X	balance exterior
∞ or 0	free-stream
λ	at nozzle pressure ratio



$$C_{D\text{ T}} = C_{D\text{ BT}} + C_{D\text{ P}} + C_{D\text{ FB}} + C_{D\text{ FB}} + C_{D\text{ RP}}$$

Model Parameters

SUMMARY

An experimental investigation has been conducted to obtain design data for low-pressure-ratio lift/cruise fan exhaust systems. The testing was accomplished in the FluidDyne Corporation wind tunnel test facility in Minneapolis, Minnesota. The test results of conical convergent and plug nozzle scale models are presented and evaluated in this report. The test data provide valuable design information for lift/cruise fan nacelle installations.

The important results of the program and conclusions drawn from the test data to date are as follows:

- . High thrust-minus-drag Mach .8 cruise performance ($C_{T-D} = .965$) was demonstrated at a low nozzle pressure ratio of 1.94 for both conical and plug nozzle lift/cruise fan nacelle installations having a throat area to maximum model area ratio (A_g/A_M) of .43.
- . For cruise Mach numbers over .85, conical nozzle installations perform better than plug nozzles for the investigated nacelle installation.
- . Friction drag plays a predominant role in the optimization of lift/cruise fan nacelle installations.

BLANK PAGE

CONCLUSIONS

From the analysis of the test results, the following conclusions can be drawn for the range of parameters investigated:

1. High thrust-minus-drag Mach .8 cruise performance ($C_{T-D} = .965$) was demonstrated at a low nozzle pressure ratio of 1.94 for both conical and plug nozzle lift/cruise fan nacelle installations having a throat area to maximum model area ratio (A_8/A_M) of .43.
2. For cruise Mach numbers over .85, conical nozzle installations perform better than plug nozzles for the investigated nacelle installation.
3. Skin friction drag played a predominant role in the lift/cruise fan models tested.
4. For Mach numbers up to .85, performance increases with a decrease in nacelle radius to maximum model diameter ratio (R/D_M) for the range investigated because of the decrease in friction drag. For Mach numbers over .85, performance decreases with a decrease in nacelle radius to maximum model diameter ratio for the range investigated because of the rise in pressure drag.
5. For Mach numbers up to .85, plug nozzle performance increases with an increase in plug angle for plug angles from 12.5 to 20 degrees. For Mach numbers over .85, plug nozzle performance decreases with an increase in plug angle because of the rise in boattail drag.

6. For higher plug angle configuration ($\theta = 20 - 25^\circ$) performance increases with plug angle only at subcritical nozzle pressure ratios $P_{TN}/P_\infty \leq 1.89$). For pressure ratios higher than critical, performance decreases with increasing plug angle.
7. Static peak performance, in general, increases with decreasing plug angle.
8. Plug nozzle performance increases with an increase in throat area (A_g) at constant nozzle exit area (A_g) and nozzle pressure ratio (P_{TN}/P_∞) because of the higher ideal thrust per nozzle exit area and its inherent decrease of the thrust decrements.
9. Truncating the plug one-third of its full length reduces the performance by about .01 to .04 in gross thrust coefficient. The loss decreases with increasing Mach number.
10. Nozzle discharge coefficients decrease with an increase in nozzle internal shroud angle.
11. Conical nozzle discharge coefficients at lower than critical pressure ratios fall off with decreasing nozzle pressure ratio.
12. Plug nozzles have higher discharge coefficients at nozzle pressure ratios below critical than conical nozzles. The discharge coefficients do not change considerably from choked nozzle levels.
13. Correlations of analytically calculated nacelle pressure distributions to measured values are fair at low subsonic Mach numbers. At high subsonic Mach numbers the analytical pressure coefficients are considerably higher than the measured ones.

RECOMMENDATIONS

Based on the results of the present investigation, the following recommendations are made with regard to the aerodynamic design of lift/cruise fan nacelles:

1. Conical nozzle nacelle installations for cruise Mach numbers below .85 should have rather high boattail angles ($\beta = 15 - 20^\circ$) and small nacelle radius to maximum installation diameter ratios ($R/D_M = 2.5 - 3.5$).

For cruise Mach numbers over .85, low boattail angles ($\beta = 10 - 15^\circ$) and high radius ratios ($R/D_M = 5 - 7$) are required for good performance.

2. Plug nozzle nacelle installations for cruise Mach numbers below .85 should have rather high boattail angles ($\beta = 12 - 20^\circ$), small nacelle radius to maximum installation diameter ratios ($R/D_M = 1.5 - 2.0$), and steep plug angles ($\theta = 15 - 18^\circ$).

For cruise Mach numbers over .85, low boattail angles ($\beta = 7 - 10^\circ$), high nacelle radius to maximum installation diameter ratios ($R/D_M = 2.5 - 3.5$) and small plug angles ($\theta = 10 - 13^\circ$) are required for good performance.

3. Lift/cruise fan nacelles should be designed with as high a ratio of throat area to maximum installation area as possible.

The present program was designed to produce general qualitative design information for lift/cruise fan exhaust systems. An extension of this program would be the optimization of a specific design, for which the following recommendations are made:

EXPERIMENTAL

1. Test model with fan driven by air turbine in wind tunnel to obtain correlation to actual nacelle thrust minus drag data in the free stream.
2. Test some of the models in a bigger tunnel to determine the effect of tunnel blockage.
3. Investigate the effect of boundary layer thickness on nacelle drag since full-scale boundary layer thicknesses are different from scale-model conditions and skin friction plays a pre-dominant role for the models tested.
4. Investigate plug contours with gradually increasing angle for improvements in plug force.
5. Investigate the effect of plug crown curvature and upstream flow path on nozzle performance.

ANALYTICAL

1. Evaluate the change in effective surface curvature with compressibility due to boundary layer influence.
2. Evaluate the influence of surface roughness on the inviscid flow field considering especially the smoothing effect of boundary layer action.
3. Develop estimation techniques for jet wake positions and their influence on inviscid flow fields.

INTRODUCTION

Exhaust system performance is a very significant parameter in the analysis of low-pressure-ratio propulsion systems, such as lift and cruise fans. The high-bypass-ratio characteristics of the lift/cruise fan result in a gross to net thrust ratio of approximately 4 to 1 at high subsonic Mach numbers. Improvements in exhaust nozzle thrust coefficient or nacelle drag coefficient of, for example, 1 percent, make the propulsion system performance better by 4 percent, or its specific fuel consumption lower by the same percentage for the high-speed cruise flight condition.

Lift/cruise fan nozzle pressure ratios lie mostly below the critical level. Very little test data is available for this range, as the many previous investigations have been conducted for turbojet or rocket engines with their inherent higher nozzle pressure ratios. Reference 2 gives a preliminary investigation of the problem and formed the basis for this program.

The objective of this program was to obtain static and installed exhaust system performance data for the ranges of interest to lift/cruise fan technology. Cruise fan nacelles with conical and plug nozzles were investigated, and the geometry of these configurations was optimized for maximum thrust-minus-drag performance.

BLANK PAGE

ANALYSIS OF PROBLEM

The thermal efficiency of a propulsion system is the product of cycle efficiency and propulsive efficiency. Cycle efficiency is defined as the ratio of energy output to energy input of the engine. The propulsive efficiency is stipulated as the ratio of the energy output to the airplane to the energy output of the engine.

The lift cruise fan propulsion concept uses a jet engine to drive a high-bypass-ratio fan which converts the high-velocity, low-mass-flow energy of the jet engine into a low-velocity, high-mass-flow energy.

Therefore, the ratio of jet velocity to airplane velocity is reduced and the propulsive efficiency is thereby increased. The more efficiently this energy conversion is accomplished, the higher is the overall system performance. Between the cruise fan components - turbine, fan, and nozzle/nacelle afterbody - the greatest gain can be made from the exhaust system installation.

The present investigation is concerned with the optimization of the thrust-minus drag of the whole cruise fan nacelle. Such an exhaust system has to be designed with the following objectives:

- 1 - High thrust coefficient,
- 2 - Low nacelle - afterbody drag coefficient,
- 3 - Low friction drag,
- 4 - Smallest length/diameter ratio,
- 5 - Low weight,
- 6 - About 50 percent throat area variation,
- 7 - Mechanical simplicity,
- 8 - High reliability,
- 9 - Adaptable for thrust reversal,
- 10 - Low noise level, and
- 11 - Low infrared radiation characteristic.

For the low nozzle-pressure ratio range of a lift-cruise fan nozzle, a convergent nozzle, without or with centerbody, gives the highest performance. The two characteristic systems are shown in Figure 1. With reference to the above objectives and depending on the specific installation and aircraft mission, either the conical convergent nozzle or the plug nozzle will produce the best overall system.

Both exhaust system configurations were, therefore, investigated in this program. The models were based on mechanical design layouts with equal throat area, nacelle diameter, and throat area variation.

DESCRIPTION OF TEST EQUIPMENT

FACILITY

The static and external flow testing was performed in the Channel 5 test facility at FluidDyne Engineering Corporation in Minneapolis, Minnesota.

Channel 5, the transonic wind tunnel shown in Figure 2, has a 22-by 22-by 72 inch long slotted-wall test section. This tunnel is an induction-type facility whereby atmospheric air is drawn through the test section using steam ejectors to reduce the downstream pressure. A large contraction ratio, 19:1, and four small-mesh screens in the inlet duct help keep the test section flow non-uniformities at a minimum. The required pressure ratio across the system (or test section Mach number) is maintained by controlling the mass flow through the ejectors. Mach number is continuously varied from 0 to 1.2. Contoured blocks on the solid walls are used to extend the upper test Mach number from 1.2 to 1.35. During days of high humidity, water condensation in the test section is prevented (for flow velocities above $M = 1.0$) by the addition of heated air upstream of the inlet contraction. Models and the balance system are supported in the test cell by a 5-inch-diameter tube (primary air supply) which is positioned by struts upstream of the inlet contraction. Primary air is piped to the model from the facility air reservoir and throttled through a gate valve.

Tunnel calibrations consisted of the determination of the tunnel wall axial Mach number distribution at the model location and the definition of the boundary layer profiles for the test Mach numbers.

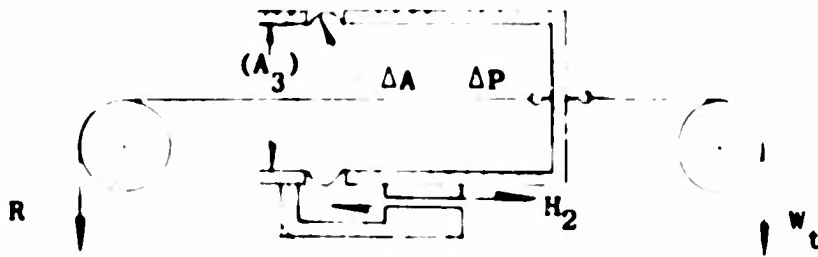
The Mach number distribution for the nominal test Mach numbers of .4, .6, .8 and .9 is shown in Figure 3 in relation to the model installation. Boundary layer profiles were measured by a boundary layer rake, which was located on the 5-inch-diameter model support just upstream (1 inch) of the nacelle leading edge. The profiles for the test Mach numbers are presented in Figure 4. If the boundary layer thickness is defined as that distance from the wall where the velocity is 99 percent of the free-stream velocity, an approximate average thickness of 1 inch is indicated.

No corrections were made to account for model blockage. If blockage corrections were necessary, the measured drag coefficients of the models would have varied with Mach number at $M < M_{CR}$. Since no such variation was found it was concluded that the effects of blockage must be negligible.

The facility is equipped with a force balance system which measures the combined effect of the nozzle internal and external flows. A schematic of the balance system is shown in Figure 5. It is located immediately upstream of the test model with only 3.5 inches of the five-inch-diameter model support being part of the metric section. Tare corrections for surface friction are, therefore, very small which minimizes the uncertainty of the data.

The force balance consists of a temperature compensated strain gage bridge. The bridge output is used to vary the frequency of an oscillator, the output of which runs into a Berkley counter and is converted to digital output which is printed out on tape at rapid intervals during the run.

A calibration of the system preceded the test program. This check-out consisted of a dead-weight calibration of the force balance, and a determination of the effective seal area, ΔA , as illustrated below.



The balance and seal characteristics were calibrated separately by the following procedure. The balance was first loaded with known weights (W_t) to obtain a curve of the balance force constant (K_b), defined as axial force divided by readout signal (H_b/C_b) versus readout signal (C_b) with no pressure difference across the seal (Figure 6). Next, the inlet duct was pressurized to test values of seal station differential pressure. A number of upstream forces (R) were then applied to the balance to reduce the net balance load in order that the seal gap would approach actual test conditions. The sum of the indicated balance load and the reverse load divided by the measured pressure differential gave the effective duct area. Subtracting the actual duct area from the effective duct area gave the effective seal area (ΔA) as a function of readout signal (balance force) and differential pressure (Figure 7). The seal tare effective area and the balance force constant were used to obtain the purely aerodynamic forces on the model. The balance calibrations were repeated after each series of runs.

Using this system, a net thrust coefficient for the simulated flight Mach number can be directly calculated. Details of this calculation are covered in Appendix I of this report. An assembly drawing of a typical model installation is shown in Figure 8, and Figures 9 through 13 present various views of test models installed in the transonic facility.

Data obtained in this facility consisted of measurements of balance force, air flow rate, model total pressure, test cell pressure, various pressures within the balance system, and nozzle contour and afterbody pressures. The pressure data were measured on multitube mercury manometer boards and precision gauges. Force balance data were recorded by an electronic digital readout system.

MODELS

A total of 14 models were tested. Three models represented lift/cruise fan nacelles with conventional conical nozzles, and eleven models had a center plug (Figure 1). The geometry of the models is described in Table 1. The models were precision-made of stainless steel with tolerances of ± 0.002 inch on all critical dimensions and ± 10 minutes on angular dimensions. All surfaces in contact with airflow were polished.

The building block construction method was used to facilitate model changes and to save fabrication costs. The hardware consisted of one adapter with choke plate and flow straightening screens, three conical nozzle shrouds, eight plug nozzle shrouds, one conical nozzle centerbody, four forward plug sections, three aft plug sections, one aft plug tip, six plugs, and a wooden cylinder for cylindrical flow simulation.

Typical model hardware is shown in Figures 14 and 15. The contours and geometric details are presented in Figures 16 through 23. The instrumentation of the models consisted of static pressure taps on the nacelle external surface, the plug surface, and plug base at various azimuth positions. A total pressure rake was installed in the adapter to measure the total pressure at the nozzle inlet section upstream of the throat (Figure 8). The boundary layer profile was measured with a rake located just upstream of the nacelle on the 5-inch diameter model support (Figures 2 and 4).

BLANK PAGE

EXPERIMENTAL PROCEDURE

A typical experiment in Channel 5 was conducted in the following manner: the external flow Mach number was set from plenum pressure measurements using the steam ejectors, and the required nozzle pressure ratio was obtained by regulating the model total pressure to the predetermined value. When these two parameters were stabilized, and all manometer readings were steady, the force balance readout recording system was started. Static pressures on the model surfaces were measured with mercury manometers and recorded photographically. The test was run according to the schedule of pressure ratio and Mach number shown in Figure 24.

The gross thrust of the system was determined from the force balance readings by correcting for the balance internal forces. Thrust coefficients (C_{T-D}) were then computed by dividing the above calculated gross thrust by the ideal thrust, defined as actual mass flow times ideal jet velocity. The ideal velocity was determined from thrust function curves as a function of nozzle pressure ratio.

Discharge coefficients were calculated as the ratio of the actual measured mass flow to the ideal mass flow at the existing nozzle pressure ratio.

From the measured static and thrust-minus drag coefficients, the total nacelle-boattail drag, including friction and external flow effects (for the plug nozzles), was computed for all test points.

The boattail drag coefficients ($C_{D_{BT}}$) and forebody drag coefficients ($C_{D_{FB}}$) were calculated by the pressure-area integration method from the static pressure measurements. Similarly, the effect of external flow on the plug nozzle (C_{D_p}) for models 4 - 14 was obtained by the

difference in plug axial force with and without external flow. The boattail drag and plug-form drag coefficients do not include friction, being only the pressure drag component. The detailed calculation procedures are described in Appendix II.

EXPERIMENTAL RESULTS

A summary of the important test results is given in Table 2 and Figure 25. The thrust coefficients represent the installed (thrust-minus-drag) performance of the cruise fan nozzle models according to the pressure ratio - Mach number schedule shown in Figure 24 for the 1.3 pressure ratio fan.

The thrust coefficients obtained as shown in Figure 5 account for the following:

- a. Internal model friction and pressure losses downstream of the total pressure rake (including plug friction),
- b. External friction and form drag over the entire length of model from the split shown in the sketch to the end of the shroud.

For these models, there was about 3.5 inches of 5-inch diameter pipe between the split and the beginning of the model contour which contributed some friction but no form drag.

The data were not corrected for this friction drag because it was considered to be small enough to be neglected. It should be observed, however, that the average friction coefficient for the models will be less than for the full-size nacelle because some boundary layer growth has already occurred on the external surface of the support pipe (Figure 4).

To determine the absolute level of thrust coefficient more accurately it would be required to reduce the boundary layer by suction in the present test set-up or to test a nacelle with an air-turbine driven fan in the free-stream without a support pipe. The presented data should be regarded, therefore, as qualitative rather than quantitative

The scatter of the test data amounts to about ± 1.2 percent from a reasonable curve drawn through the data. With noted exceptions, it appears that the general level of thrust coefficient has been defined within ± 1.25 percent based upon comparison of measured thrust and drag coefficients with pressure integrated drag coefficients and friction estimates.

The variation of the thrust coefficients (C_{T-D}) with pressure ratio and Mach number is presented in the order of model number in Figures 26 to 41.

Discharge coefficients (C_D) are presented in a similar manner for all models in Figures 42 to 57. The discharge coefficients, by definition, represent the ratio of actual mass flow to the ideal mass flow at the existing nozzle pressure ratio.

The external pressure distributions of the cruise fan nacelles are shown for each model in Figures 58 to 74 in the form of pressure coefficients, $C_p = (P_1 - P_\infty)/q_\infty$. Nozzle pressure ratio did not affect the nacelle pressure distributions for the range of test pressure ratios.

Plug pressure distributions (P_1/P_{TN}) for all models are plotted versus length for the various test pressure ratios and Mach numbers. Figures 75 to 87 show the plug pressure distributions for Mach 0; Figure 88, for Mach .4; and Figures 89 to 100, for Mach .8. Plug pressure distributions are also presented in Figures 101 to 116 for each configuration for all Mach numbers based on a Mach number - pressure ratio relationship as given in Figure 24 for a fan pressure ratio of 1.3.

The total nacelle drag coefficients ($C_{D\ n}$) were calculated from the static and installed thrust coefficients for each test point. A summary of all data is given in Figure 117 and in Table 2 as a function of Mach number. This drag coefficient includes friction.

The results of the boattail drag calculations from the model afterbody pressure data are presented as boattail drag coefficients ($C_{D\ BT}$) in Figure 118 as a function of Mach number. Surface friction is not included in these values, and the data are independent of pressure ratio.

The effect of external flow on the plug force, calculated from the plug pressure distribution at static conditions and with external flow, is presented in Figure 119. This change in plug force has been shown in the form of plug form drag coefficients ($C_{D\ p}$) versus Mach number for the pressure ratios according to the test schedule of Figure 24 for the 1.3 pressure ratio fan.

BLANK PAGE

EVALUATION

CONICAL NOZZLES (MODELS 1,2,3)

All three conical nozzle models have the same maximum nacelle diameter and throat area; they differ only in their boattail geometry (Figures 16 and 17). A comparison of the thrust coefficient results of the conical nozzles (Figure 120) indicates that, for Mach numbers up to and including .8, performance increases slightly with decreasing nacelle boattail radius to maximum diameter ratio (R/D_M) and nacelle length to maximum diameter ratio (L/D_M). For Mach .9 this trend is reversed.

Without external flow, the difference in the performance level is caused by the change in internal friction as model size and exit area are the same.

For Mach numbers up to and including .8, nacelle surface friction drag is predominant over the pressure drag on the afterbody. This can be observed in Figure 121. The total nacelle drag coefficient is almost the same for the three models. The boattail drag coefficient (not including friction), however, is decreasing with decreasing boattail angle and is about 25 percent lower for model 1 than for model 3. If models 2 and 3, with the smaller nacelle length and boattail radius show higher performance than model 1, it can only be the result of the models having less friction drag. With the calculated friction drag coefficient of Figure 121, the friction drag decrements were computed for models 1 and 3 at Mach .8 and they are shown in the loss breakdown together with boattail and forebody drag in Figure 122. The total thrust decrement is smaller for model 3 because the rise in boattail pressure drag is overcompensated for by the decrease in nacelle friction drag.

Pressure drag is more important at Mach .9, and model 1, with the greater boattail radius and inherently lower boattail angle, demonstrates the highest performance. A loss breakdown for models 1 and 3 is given in Figure 123. It can be observed that the friction drag decrement of models 3 is only slightly smaller and that the pressure drag increase is greater than the reduction in friction drag.

The breakdowns of the performance losses (Figures 122 and 123) show that installed performance increases with pressure ratio. The explanation for this is given in Figure 124, which demonstrates that, with constant nacelle drag coefficient, the thrust decrement (ΔC_T) decreases with increasing pressure ratio because of the increasing ideal thrust. Therefore, if the static performance and only one test point with external flow are known for a model, the complete performance curve can practically be calculated over a range of pressure ratios for external flow Mach numbers below the model nacelle critical Mach number (Figure 128). Naturally one external flow test point is not sufficient to establish the total nacelle drag level accurately, but this method can be used for arriving at more exact curves if only a few test points are available. A summary of the conical nozzle thrust-minus-drag performance is presented in Figure 125 for the assumed relationship of pressure ratio versus Mach number for the 1.3 pressure ratio fan (Figure 24).

From the above evaluation it is concluded that skin friction plays a predominant role for Mach numbers up to about .85. Lift/cruise fan nacelles for cruise Mach numbers in this range should, therefore, be designed with small boattail radius ratios. For higher cruise Mach numbers, lower boattail angles improve the performance because of the steep rise in pressure drag.

PLUG NOZZLES (MODELS 4-14)

1. Effect of Boattail Geometry on Performance

a. Low Boattail and Low Plug Angle Models (4,5)

Models 4 and 5 have the same plug ($\theta = 12.5^\circ$) and equal throat area as well as area ratio (Figures 17 and 18). The models differ only in their boattail geometry ($\beta = 8^\circ$ and 10°) and their throat location with respect to the plug crown. The performance comparison, shown in Figure 126, indicates that model 4 produces slightly overall higher performance except at Mach .4. This is primarily the result of the lower boattail pressure drag (lower boattail angle) as can be observed from the comparison of the boattail drag coefficients in Figure 127. The plug forces are practically identical according to the plug pressure distributions (Figures 104 and 105).

At Mach .4, the force data show a reverse of the general trend; the pressure data, however, indicate no such change in trend and the force balance measurements at this Mach number are, therefore, assumed to be in error.

Plug nozzle model 5 has about the same boattail radius ($R/D_M = 2.75$) as the conical nozzle model 3. Nevertheless, the plug nozzle performance is overall lower than the performance of the conical nozzle. This must be attributed to plug surface friction.

Based on this observation, a correlation was made of the three convergent nozzle models and the plug nozzle models 4 and 5. For each model and each test Mach number, the lowest static pressure on the shroud (highest local Mach number) was determined and plotted versus

the tunnel Mach number. A cross-plot of this graph at the critical value of pressure ratio (Mach = 1.0) versus boattail radius to maximum model diameter ratio produced the critical Mach numbers of the models (Figure 128). According to this graph, the boattail radius to maximum model diameter ratio can be reduced to about 1.75 for cruise Mach numbers of .8. Models 11 through 14 were then laid out with lower radius ratios to verify this assumption.

b. High Boattail and high Plug Angle Models (12 and 14)

A performance comparison of models 12 and 14 (Figures 22 and 23), which both have a 18.0° plug, and boattail angles of 15° and 18.0° respectively, is presented in Figure 129. Model 14, with its steeper boattail angle, lower shroud length and boattail radius, performed better at all test Mach numbers.

When the high-boattail-angle nozzle models are compared to the low boattail-angle nozzles (Figure 130), it can be concluded that, similar to the conical nozzles, plug nozzles for cruise Mach numbers up to .85 should be designed with rather steep plug and boattail angles. For higher cruise Mach numbers, lower boattail and plug angles are required for good performance.

2. Effect of Plug Angle on Performance

a. Low Boattail and Low Plug Angle Models (5, 9 and 10)

Models 5, 9 and 10 use the same shroud together with various angle plugs of 12.5, 15, and 17.5 degrees (Figures 18 and 20). The boattail angle is 10 degrees. From the performance comparison, shown in Figure 131, a general trend cannot easily be recognized. When the pressure distributions for the plugs at Mach 0 are compared in Figure 132, it can be observed that the higher plug angles cause the flow to overexpand just

downstream of the throat. After this expansion, however, the pressure rises to a higher level as for the lower plug angle which compensates for the initial overexpansion loss, and the plug forces for the models are practically equal. Friction drag on the plug decreases with an increase in plug angle because of the decrease in surface area. It is, therefore, concluded that static performance increases slightly with increasing plug angle.

Based on the plug pressure distributions (Figure 122) it is concluded that the force data of model 9 are erroneous, as there is no agreement of force and pressure data. A similar conclusion can be reached from the plot of static peak performance versus area ratio (Figure 139). Model 9 is about .4 percent low compared to the other models.

In the presence of external flow, the comparison of the plug forces yields similar results as at static conditions. Figure 133 shows the comparison of plug forces at Mach .8, and there is not much difference for the range of angles investigated. Boattail drag increases with plug angle as can be seen in Figure 134, and the model performance level depends on the sum of plug force and boattail drag as well as internal and external model friction drag. For subsonic Mach numbers below the drag rise (about $M = .85$), the steeper plug angles yield slightly higher performance. At Mach .9, pressure drag is the predominant factor and low plug angles are required to reduce the boattail drag (Figure 131).

It is therefore concluded that for Mach numbers up to .85, an increase in plug angle produces slightly higher performance for the range of angles investigated. For Mach numbers over .85, the trend is reversed.

b. High Boattail and High Plug Angle Models (12 and 13)

Figure 135 shows the comparison of the model 12 and 13 thrust coefficients. Model 12 has a 17.5-degree plug angle and model 13 has a 22.5-degree plug. The thrust coefficients show a similar trend for the low-pressure-ratio range, as observed for the low boattail plug nozzles; namely, slightly higher performance for the steeper plug angle model 13. With an increase in pressure ratio, the performance curves cross over and model 13 shows lower performance than model 12.

A comparison of the plug forces at Mach .8 in Figure 136 demonstrates that, at low nozzle pressure ratios ($P_{TN}/P_{\infty} = 1.5$), the gain from the pressure rise at the end of the plug is higher than the loss in plug force from the initial overexpansion. At the higher nozzle pressure ratio ($P_{TN}/P_{\infty} = 2.5$), the initial overexpansion loss is higher than the gain due to the pressure rise at the plug end.

From this observation, it is concluded that for steeper plug angle configurations ($\theta = 20 - 25^{\circ}$), performance increases with plug angle only at subcritical pressure ratios ($P_{TN}/P_{\infty} \leq 1.89$). At pressure ratios greater than critical, performance decreases with increasing plug angle.

Static peak performance shows a general trend of decrease with an increase in plug angle, as can be observed in Figure 139.

3. Effect of Nozzle Throat Area on Performance

a. Area Change by Expandable Plug (Models 6 and 9)

Models 6 and 9 demonstrate the expandable plug concept for changing throat area (Figures 18 and 20). The geometry of the models is exactly the same with the exception of the plug contour. The throat area of model 6 is increased by about 23 percent compared to model 9.

Performance increases with an increase in throat area because of the higher mass flow and the inherent higher ideal thrust. A performance comparison of the two models is made in Figure 137. Model 6, with a bigger throat area, is overall higher in performance. The area change by expanding the plug changes the plug angle at the throat location, and the observations for plug angle changes under paragraph 2 above also apply to this comparison.

b. Area Change by Shroud or Plug Translation (Models 7 and 7A)

A variation in throat area as demonstrated by models 7 and 7A could be accomplished by an axial translation of plug or shroud (Figure 19). The model geometry is identical except that the plug size is different. These two models, therefore, demonstrate the effect of throat area change with constant exit area - without any side effects. Figure 138 shows the performance comparison for the test Mach numbers. The performance for model 7A, having a bigger throat area, is considerably higher because throat area and flow is about twice as large in comparison to model 7.

With external flow, the total nacelle drag coefficient ($C_{D \tau}$) for the model with the bigger throat area (7A) is smaller

(Figure 117), and because of the higher ideal thrust, the thrust decrement due to external flow is relatively smaller. Throat area or the ratio of exit area to throat area (A_E/A_{TH}) is a very important parameter in plug nozzle performance as shown in Figure 139.

4. Effect of Plug Length on Performance (Models 5 and 10A)

The two models (Figures 18 and 21) are geometrically similar except that 10A has its plug length reduced to about two-thirds. Model 5, with the full-length plug, has overall higher performance (Figure 140). The performance loss for plug truncation of about .01 to .04 in thrust coefficient is due to the lower plug force for the cut-off plug model. The pressure on the plug base is about equal to the pressure just ahead of the base (Figure 112), whereas the pressure on a full-length plug rises further (Figures 105 and 112).

5. Effect of Simulated Cylindrical Flow on Boattail Drag (Models 8 and 10B)

Model 10B (Figure 21) uses the same nacelle as model 8 (Figure 19), but has a cylinder attached to the end of the shroud to simulate cylindrical flow. Measured boattail pressures were considerably higher at the end of the shroud of model 10B with the cylindrical afterbody in comparison to the 12.5-degree plug of model 8 (Figure 141). The drag coefficient is less than 40 percent for the cylindrical flow simulator model, and the drag stayed practically constant for the range of test Mach numbers; on the other hand, the plug nozzle model experienced the usual drag rise.

The reason for the low drag of the cylindrical flow simulator model is that the flow compresses at the end of the nacelle afterbody, an action which results in a pressure rise all along the boattail surface. For the case of the plug nozzle with internal flow, the external flow converges further and, therefore, experiences a much smaller rise in pressures. The plug nozzle internal flow is converging for model 8 at the test pressure ratios.

The boattail drag for the cylindrical flow simulation model is the lowest for all models tested. Only the low-boattail model 4 comes close to it (Figure 142).

PERFORMANCE COMPARISON OF ALL LIFT/CRUISE FAN NACELLE INSTALLATIONS

WITH EQUAL NOZZLE THROAT AREA

The efficiency of an installation is characterized by its value of throat area to maximum nacelle cross-sectional area (A_g/A_M). For the lift/cruise fan installation, its maximum diameter is determined by the fan diameter and the structural requirements for the nacelle. The throat area at cruise is defined by the engine exhaust gas flow and the fan flow; and, therefore, the ratio of A_g/A_M is practically fixed for a given system. The problem is then to develop an installation which offers high cruise performance with overall good off-design performance and low weight.

For the present investigation, the best installations for a given area ratio of $A_g/A_M = .43$ can be identified from the comparison shown in Figure 143. For a cruise Mach number around .8, the optimum conical-nozzle model is model 3 and the best of the plug nozzles is model 14. Both models offer practically equal high cruise performance ($C_{T-D} = .968$ and .965). However, the average performance of three conical nozzle

models in comparison to the average performance of the plug nozzle models is higher by about 1 percent over the range of Mach numbers tested. Besides performance, the selection of an installation must also include consideration of system weight, complexity, reliability and other parameters specific to the aircraft configuration.

COMPARISON OF NOZZLE DISCHARGE COEFFICIENTS

Discharge coefficients of plug nozzles at low nozzle pressure ratios show characteristics similar to those of conical nozzles. Conical nozzle discharge coefficients, for pressure ratios below critical, fall off sharply from their choked flow values with a decrease in nozzle pressure ratio (Figures 42, 43 and 44). Conical nozzle discharge coefficients are a function of internal shroud angle, and they decrease with increasing shroud angles.

A similar observation can be made for the plug nozzles, namely, that discharge coefficients decrease with an increase in internal shroud or flow angle (Figures 45 through 57). However, because of the lower flow angles, the plug nozzle model discharge coefficients at low nozzle pressure ratios are higher than the conical model discharge coefficients. This is illustrated in Figure 144, which shows a comparison of discharge coefficients for unchoked nozzle operating conditions at Mach 0.

With external flow, the discharge coefficients are influenced by the shroud base pressures. With higher-than-ambient base pressures, the flow coefficient values decrease; and with lower-than-ambient base pressures, the flow coefficients increase over their static values. The reason for this change in discharge coefficient lies in its definition as: actual mass flow over ideal mass flow based on nozzle total to ambient pressure ratio, $C_D = \dot{m}_a / (\dot{m}_1)_\lambda$. When the base pressure differs from the free-stream pressure, the discharge

coefficient changes from its static value. Because of this definition, it is also possible that C_D becomes greater than unity in the presence of external flow when the base pressure is lower than free-stream pressure.

From Figure 144, it can also be concluded that the discharge coefficient level for model 7 is high by about 3 percent. The discharge coefficient of this model should be about equal to the model 7A discharge coefficient because of the geometrical similarity of the models. It is assumed that leakage occurred between the model and the flow measuring station.

COMPARISON OF NACELLE DRAG TO OTHER TEST DATA AND ANALYTICAL CALCULATIONS

1. Comparison to Other Test Data

There is little data available for comparisons because of the special nacelle contours of the test models. The AMES full scale low speed cruise fan test is perhaps the only valid comparison to the models in this test (Reference 3). Total nacelle drag coefficients ($C_{D\pi}$) are compared in the upper part of Figure 145 on the basis of jet-to-maximum-diameter ratio and boattail angle to the the AMES test result. The AMES cruise fan drag coefficient is slightly higher than the drag values of the present test.

The comparison to NASA scale model tests of 2" diameter conical afterbodies (Reference 1) is based on the boattail form drag coefficients as obtained by pressure-area integration over the boattail. With the exception of the conical nozzle models 1, 2 and 3, the drag coefficients are in general agreement with the NASA test results at Mach .6 (Figure 145 lower parts). At Mach .9, a similar observation can be made, namely that the data agree,

in general with the NASA results with the exception of models 1, 2 and 3, which are low (Figure 146).

It should be noted that the comparison to the NASA data is perhaps only valuable for observing the general trend of drag coefficients as a function of jet-to-maximum model diameter ratio and boattail angle. The lift/cruise fan test models had all circular-arc boattails, where the NASA models had conical boattails which should give higher drag. The plug nozzles do recover a part of the boattail drag loss on the plug (C_{Dp} , Figure 119). Their afterbody drag is, therefore, to be considered as the sum of boattail drag and plug form drag. However, plug form drag is also a function of nozzle pressure ratio, thus making a general comparison of drag data on this basis impossible.

It is recommended to investigate the effect of boundary layer thickness on nacelle boattail drag coefficients since the full scale boundary layer thicknesses are different than scale model conditions.

2. Comparison to Analytical Calculations

Nacelle pressure coefficients for external flow Mach numbers of .6 and .8 were calculated for the nacelle of model 5 using the flux plot computer program. This program is being developed to provide an analytical approach for the development and optimization of axisymmetric body shapes. The program utilizes the Rayleigh-Janzen technique to correct the velocity potential for compressibility effects. The output from the program is based on the compressible potential flow solution over nacelles, which provides the pressure distribution over the surface of the body. The program does not calculate second-order effects of compressibility.

A comparison of the analytical results with the test data is shown in Figures 147 and 148. At Mach .6, the level of the pressure coefficients is in fairly good agreement with the test data whereas the Mach .8 comparison shows little agreement in level. The boattail test pressures are higher because of the effect of the jet interaction with the external flow. A cylindrical boundary has been assumed for the analytical calculation.

From this above comparison, it is concluded that the flux plot program - in its present state of development - cannot be used to predict pressure distributions at higher subsonic Mach numbers. The low Mach number correlation is fairly good.

It is recommended that the flux plot program be improved by adding subroutines for (1) estimating jet wake positions and their interactions on the inviscid flow field, (2) evaluation of change in effective surface curvature with compressibility due to boundary layer influence, and (3) evaluation of effect of surface roughness on the inviscid flow field considering especially the smoothing effect of boundary layer action.

BIBLIOGRAPHY

1. Cabbage, J.M., Jr., Jet Effects on the Drag of Conical Afterbodies for Mach Numbers of 0.6 to 1.28, NACA Research Memorandum, RM L57 B21, April 12, 1957.
2. Kutney, J.T., Cruise Fan Exhaust Nozzle Test Results, R63FPD69, General Electric Company, Cincinnati, Ohio, March 7, 1963.
3. Przedpelski, Z.J., Heikkinen, A.H., Vacek, L.L., Aerodynamic Investigation of Low Speed VTOL Transition Characteristics of X353-5B Cruise Fan, R63FPD426, General Electric Company, Cincinnati, Ohio, December 16, 1963.

APPENDIX I - DATA REDUCTION SAMPLE CALCULATION

The measurements for each test point, as defined by the specific settings of tunnel Mach number and nozzle pressure ratio, were recorded on data sheets. Pressures were converted to absolute values in inches of mercury. Model nacelle pressures were referenced to the tunnel total pressure ($P_{T\infty}$ or P_{T0}), model plug pressures were referenced to the nozzle total pressure (P_{T6} or P_{TN}). As an example, the data sheet shows run 11-14 which is a test point for model 11 at a nominal Mach number setting of .8 and a nozzle pressure ratio of 2.30.

The data were then transferred onto the data reduction forms together with the model constants (Figure 22), the balance constants (Figure 5), and the dead weight and seal calibration values (Figures 6 and 7). The measured gross thrust coefficient was calculated according to the equation presented on Figure 5. On the sample calculation form, a gross thrust coefficient of .968 was obtained for run 11-14. This thrust coefficient includes all nozzle internal losses, plug form drag, boattail drag, forebody drag and friction drag for the nacelle and plug surfaces, including 3.5 inches of the 5-inch-diameter support pipe; in short, all forces on the metric section (Figure 5). The .968 thrust coefficient was then plotted in Figure 38 and was used throughout the report without any further corrections.

The discharge coefficient was calculated on the same calculation sheet as the ratio of measured to ideal mass flow. A value of C_D .982 was obtained in the sample calculation. This coefficient was then plotted in Figure 54.

DATA SHEET

PROJECT 0362

Run Date 2-27-64

Run No. 11-14

Configuration 6E¹¹

Barometer 28.86

"Hgo 14.18

psia

Nom λ 2.30

Actual λ 2.2660

Metering Nozzle P₁

psig

psia

P₁ 43.18

psig

21.21 psia

CHANNEL (M-O)						CHANNEL #5					
P ₁					psia	Nom M	0.8	Actual M	.7915		
P ₀					psia	P ₁	(Bar 0.05")		28.81	"Hgo	
P ₁	99.65				psig	P ₀	19.06	"Hgo	9.36	psia	
	113.83				psia	P ₀			66158		
					"Hgo						
Man Tube	Model Tap	RDG	"Hgo	P/P ₁	P/P _{T0}	Man Tube	Model Tap	RDG	"Hgo	P/P ₁	P/P _{T0}
1						31	13	75.00	17.66		.6170
2						32	14	74.40	18.26	Shroud	.6338
3	P ₂	25.45	57.01			33	15	74.05	18.61		.6460
4						34	16	73.75	18.91		.6564
5						35	P ₂	73.60	19.00		
6						36		73.60			
7	P ₂	72.00	20.46			37	SW	73.40	19.26		
8						38	SW	74.00	18.66		
9						39	SW	73.55	19.11		
10	I	63.60	28.86			40	I	63.80	28.86		
11	4	74.40	18.16	Nacelle	.6303	41		53.25			
12	18	67.70	24.86			42		53.40			
13	19	71.60	20.96			43		53.40			
14	20	65.95	26.61			44	P ₂	53.30	43.18		
15	21	64.60	27.96			45		53.55			
16	22	66.35	26.21			46					
17	1	70.80	21.76		.7553	47		54.60			
18	2	70.50	22.06	Nacelle	.7657	48	29	74.50	22.26	5155	
19	3	73.50	19.06		.6616	49	I	67.90	28.86		
20	I	63.70	28.86			50	20	73.30	23.61	5468	
21	-					51	31	75.40	21.51	4982	
22	5	75.60	17.06	Nacelle	.5922	52	32	77.10	19.81	4588	
23	6	76.00	16.66		.5783	53	33	75.65	21.26	4924	
24	7	76.90	15.26		.5470	54	34	73.70	23.21	5375	Plug
25	8	77.90	14.76		.5123	55	35	75.20	21.71	5028	
26	9	77.00	15.66	Shroud	.5436	56	36	73.60	23.31	5399	
27	10	76.45	16.21		.5626	57	37	73.30	23.61	5468	
28	11	76.00	16.66		.5783	58	38	71.80	25.11	5815	
29	12	75.35	17.31		.6008	59	-				
30	I	63.80	28.86			60	I	68.05	28.86		

C 2320

Counts

M

13152

lbs

K

05669

lbs count

C

Counts

K

40

C

Counts K

CHANNEL 5 OR 2
DATA REDUCTION FORM

SHEET 1 OF 2

PROJECT 0352

MODEL GE #11

RUN DATE 2-27-64

$A_{\infty} = 19.635$ IN²

$A_0 = 3079$ IN²

$A_1 = 2.545$ IN²

$A_2 = 13801$ IN²

$A_3 = 22.129$ IN²

$K_1 = C_{D_1} A_0 = 2.525$

$K_2 = K_1 / A_1 = .1830$

$K_3 = A_{\infty} A_2 = 16.556$

$K_4 = A_3 \cdot A_2 = 0.534$

NO	NAME	OPERATION	UNITS	RUN #	RUN #	RUN #	RUN #	RUN #	RUN #
				11-14					
1	Nominal Test M			.8					
2	Barometric Pressure	Read Barometer	" Hga	28.96					
3	K_1	FROM GRAPH		3.1967					
4	$P_{1/2}$	FROM DATA SHEET	PSIA	113.83					
5	$P_{1/6}$	FROM DATA SHEET	PSIA	21.21					
6	P_B	FROM DATA SHEET	PSIA	9.36					
7	P_1	FROM DATA SHEET	PSIA	10.05					
8	P_C	FROM DATA SHEET	PSIA	28.00					
9	$F_{s, act}$	(3) x (4)	lbs	363.88					
10	H_2	BALANCE FORCE	lbs	131.52					
11	$\frac{1}{2} A_{seal}$	BALANCE CALIBRATION	in ²	.01					
12	$(P_C - P_H) \cdot \frac{1}{2} A$	(8) - (7) (11)	lbs	.18					
13	$(A_1 \cdot A_2) P_C$	$K_2 \times (8)$	lbs	24.95					
14	$A_{\infty} P_B$	$A_{\infty} \times (6)$	lbs	183.78					
15	$(A_{\infty} A_2) P_H$	$K_3 \times (7)$	lbs	166.39					
16	H	(9) - (10) - (12) - (13) - (14) - (15)	lbs	230.10					

DATA REDUCTION FORM

SHEET 2 OF 2

CODE 0352RUN DATE 2-27-64

NO	NAME	OPERATION	UNITS	RUN #	RUN #	RUN #	RUN #	RUN #	RUN #
				11-14					
17	A	FROM DATA SHEET		2.2660					
18	$\frac{M_1 V_1}{P_{10} A_0}$	FROM GRAPH OF ① vs. ②		.8270					
19	$\frac{W_0}{S} V_1$	$K_2 = ④ \times ③$	lbs.	237.70					
20	$C_{v,p}$	③/②		9680					
21	C_{D_0}	$K_2 (④/③)$.9821					
22	C_D	$\mathcal{E} = \left(\frac{A}{A_0}\right)_{A_{0.00}}$.9121					

APPENDIX II - CALCULATION METHODS

Gross Thrust Coefficients - C_T , or C_{T-D}

With reference to Figure 5 and using the terminology of this study, the gross thrust coefficients were calculated as follows:

$$C_T, \text{ or } C_{T-D} = \frac{F_3 - H_2 + (P_C - P_X) \Delta A + (A_S - A_3) P_C - A_{OD} P_\infty + (A_{OD} - A_S) P_X}{(W_a/g)V_i}$$

The entering stream thrust, F_3 , was evaluated as $(1 + \gamma) P_3 \cdot A_3 \cdot C_{T3} \cdot C_{D3}$ where C_{T3} and C_{D3} are actual thrust and discharge coefficients of the choked ASME meter inlet.

The ideal thrust, $(W_a/g)V_i$, was calculated from the actual mass flow and the thrust function based on the nozzle pressure ratio (λ) as shown below:

$$(W_a/g)V_i = C_{D3} \cdot A_3 \cdot P_{T2} \left[\frac{m_1 V_1}{P_{T6} \cdot A_8} \right]_\lambda$$

The thrust function is defined as shown below:

$$\frac{m_1 \cdot V_1}{P_T \cdot A^*} = \gamma \cdot M^2 \cdot \frac{P}{P_T} \cdot \frac{A}{A^*}$$

where Mach number (M) and area ratio ($\frac{A}{A^*}$) are functions of nozzle pressure ratio ($\frac{P_T}{P}$) based on the following relations:

$$\frac{P_T}{P} = \left[1 + \frac{\gamma-1}{2} \cdot M^2 \right]^{\frac{\gamma}{\gamma-1}}, \text{ and}$$

$$\frac{A}{A^*} = \frac{1}{M} \left[\frac{1 + \frac{\gamma-1}{2} \cdot M^2}{1 + \frac{\gamma-1}{2}} \right]^{\frac{\gamma+1}{2(\gamma-1)}}$$

with $\gamma = 1.4$.

Discharge Coefficient - C_D

The discharge coefficient was defined in this study as the ratio of the measured weight flow to the ideal flow at the measured nozzle pressure ratio as shown below:

$$C_D = \frac{C_{D3} \cdot A_3 \cdot P_{T2}}{A_8 \cdot P_{T6}} \left(\frac{A}{A^*} \right)_{\lambda < \text{critical}}$$

where A/A^* is defined as above. For higher than critical pressure ratios ($\lambda \geq \text{critical}$), the nozzle runs choked and the area ratio for the conical nozzle equals one ($A/A^* = 1.0$).

Pressure Coefficient - C_P

Pressure coefficients were calculated for the external nacelle surfaces from the static pressure measurements using the conventional definition

$$C_P = \frac{P_1 - P_\infty}{q_\infty}$$

Total Nacelle Drag Coefficient - $C_{D \pi}$

The total nacelle drag coefficient was evaluated from the static and the thrust-minus-drag coefficient in the following manner:

$$C_{D \pi} = \left[C_T - C_{T-D} \right] \frac{(W_a/g)V_1}{q_\infty \cdot A_M}$$

where $(W_a/g)V_1$ is as defined above. $C_{D \pi}$ includes all drag effects on the model, including surface friction.

Boattail Drag Coefficient - $C_{D BT}$

The boattail drag coefficients were calculated from the static pressure measurements along the nacelle afterbody by graphical integration of the pressures over the nacelle cross-sectional projected area using the relation:

$$C_{D BT} = \frac{\int (P_\infty - P_1) dA}{q_\infty \cdot A_M}$$

The friction drag of the nacelle boattail is not included in the boattail drag coefficient.

Plug Form Drag Coefficient - $C_{D p}$

This coefficient is a measure of the effect of external flow on the plug force at static conditions or, in other words, on the internal nozzle performance. It was determined by calculating plug forces from the measured pressure distributions for the test pressure ratios at Mach 0 and the respective external flow Mach number. The plug force was computed by graphical integration of the plug pressure

distribution versus projected plug area. The definition of the plug form drag coefficient is then:

$$C_{D P} = \frac{\int P_1 (M=0) dA - \int P_1 (M>0) dA}{q_\infty \cdot A_M} .$$

Forebody Drag Coefficient - $C_{D FB}$

The forebody drag coefficients were calculated from the static pressure measurements along the nacelle forebody by graphical integration of the pressures over the nacelle cross-sectional projected area with the relation:

$$C_{D FB} = \frac{\int (P_\infty - P_1) dA}{q_\infty \cdot A_M} .$$

Forebody friction drag is not included in this coefficient.

Model Friction Drag Coefficient - $C_{D f}$

The friction coefficient was determined from the above defined drag coefficient in the following manner:

$$C_{D f} = C_{D \pi} - (C_{D BT} + C_{D FB} + C_{D P}) .$$

This friction coefficient consists of the friction on the model nacelle surface (including 3.5 inches of the 5-inch diameter support pipe) and the plug surface.

TABLE 1
CRUISE FAN NACELLE
MODEL GEOMETRIC PROPERTIES

MODEL	DESCRIPTION	A_E/A_{TH} ϵ	PLUG ANGLE θ	BOATTAIL ANGLE β	INTERNAL SHROUD EXIT ANGLE α	A_{TH}/A_M	D_J/D_M	L_T/D_M	R/D_M	A_{TH}
1	Conical	1.0	-	14°	12.3°	.428	.654	2.16	5.70	13.63
2	Conical	1.0	-	17°	14.0°	.428	.654	1.93	3.90	13.63
3	Conical	1.0	-	20°	15.5°	.428	.654	1.74	2.80	13.63
4	Plug	2.13	12.5°	8°	7°	.404	.929	1.32	3.35	12.87
5	Plug	2.08	12.5°	10°	8°	.400	.910	1.36	2.75	12.73
6	Plug Collapsed	1.65	15.0°	10°	8°	.502	.910	1.36	2.75	15.98
7	Plug	3.36	12.5°	10°	7°	.227	.875	1.65	3.15	7.22
7A	Plug	1.78	12.5°	10°	7°	.428	.875	1.65	3.15	13.64
8	Plug	2.66	12.5°	12.5°	9°	.221	.770	1.86	5.85	7.06
9	Plug	2.01	15°	10°	8°	.406	.910	1.36	2.75	12.92
10	Plug	2.01	17.5°	10°	8°	.406	.910	1.36	2.75	12.92
10A	Cut-Off Plug	2.01	12.5°	10°	8°	.410	.910	1.36	2.75	13.05
10B	Cylindrical Flow Sim.	-	-	12.5°	-	-	.770	1.86	5.85	-
11	Plug	1.62	19.5°	20°	15°	.433	.836	1.27	1.41	13.80
12	Plug	1.62	17.5°	15°	12.5°	.427	.836	1.41	2.35	13.60
13	Plug	1.62	22.5°	15°	12.5°	.424	.836	1.41	2.35	13.52
14	Plug	1.62	17.5°	18°	13.5°	.429	.836	1.32	1.73	13.67

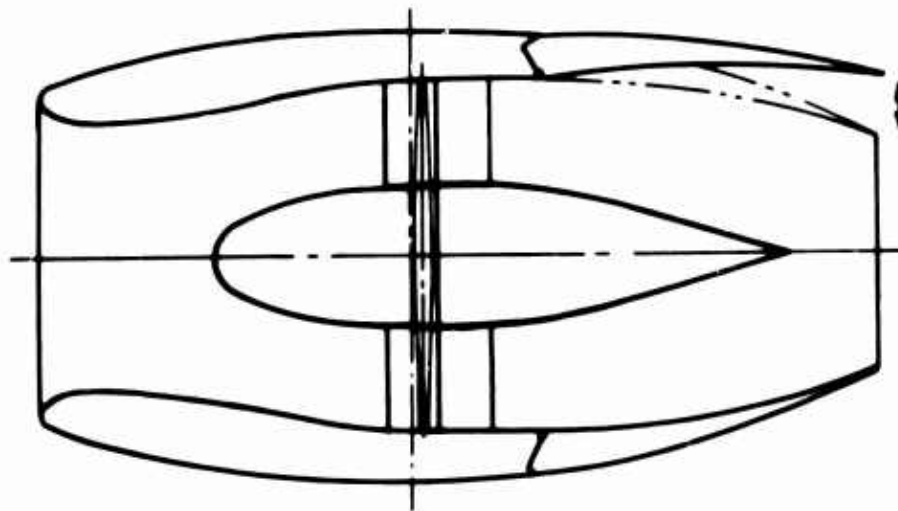
Notes: 1 - $D_M = 6.37''$

2 - $A_M = 31.869 \text{ in.}^2$

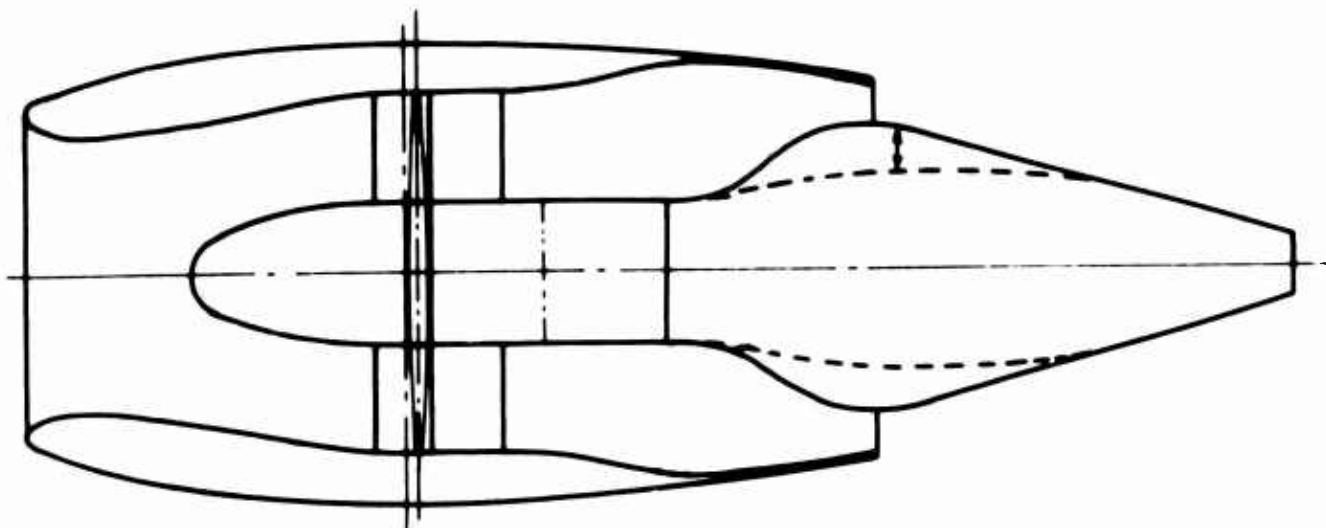
TABLE 2
CRUISE FAN NACELLE
MODEL PERFORMANCE RESULTS

MODEL	DESCRIPTION	Installed Gross Thrust Coefficient - C_T-D^*										Total Nacelle Boattail Drag Coefficient - CD_T			
		Mach = 0 $\lambda = 1.27$	Mach = .4 $\lambda = 1.42$	Mach = .6 $\lambda = 1.63$	Mach = .8 $\lambda = 1.94$	Mach = .9 $\lambda = 2.15$	Mach = .4	Mach = .6	Mach = .8	Mach = .9	All Pressure Ratios				
1	Conical	.993	.982	.975	.965	.956	.036	.037	.041	.050					
2	Conical	.994	.984	.978	.966	.953	.038	.036	.044	.056					
3	Conical	.997	.984	.978	.968	.953	.040	.037	.044	.055					
4	Plug	.989	.971	.966	.962	.953	.050	.041	.042	.047					
5	Plug	.988	.974	.966	.960	.953	.042	.035	.039	.044					
6	Plug Collapsed	.984	.974	-	.967	.963	.027	.026	.029	.035					
7	Plug	.984	.946	.929	.915	.897	.063	.056	.056	.064					
7A	Plug	.987	.972	.967	.962	.956	.054	.039	.036	.039					
8	Plug	.979	.948	.938	.922	.907	.047	.047	.046	.057					
9	Plug	.984	.970	.968	.959	.951	.039	.031	.033	.040					
10	Plug	.987	.975	.969	.962	.949	.040	.036	.038	.046					
10A	Cut-Off Plug	.982	.969	.965	.960	.953	.035	.031	.033	.038					
11	Plug	.987	-	.965	.962	.934	.042	.043	.041	.075					
12	Plug	.985	-	.964	.958	.939	.037	.037	.038	.061					
13	Plug	.985	-	.963	.957	.936	.037	.037	.037	.058					
14	Plug	.987	-	.972	.965	.940	.034	.033	.034	.066					

NOTES *According to Test Schedule of Fan Pressure Ratio 1.3 (Figure 24)



Conical Nozzle System



Plug Nozzle System

Figure 1. Comparison of Conical and Plug Nozzle Cruise Fan Systems.

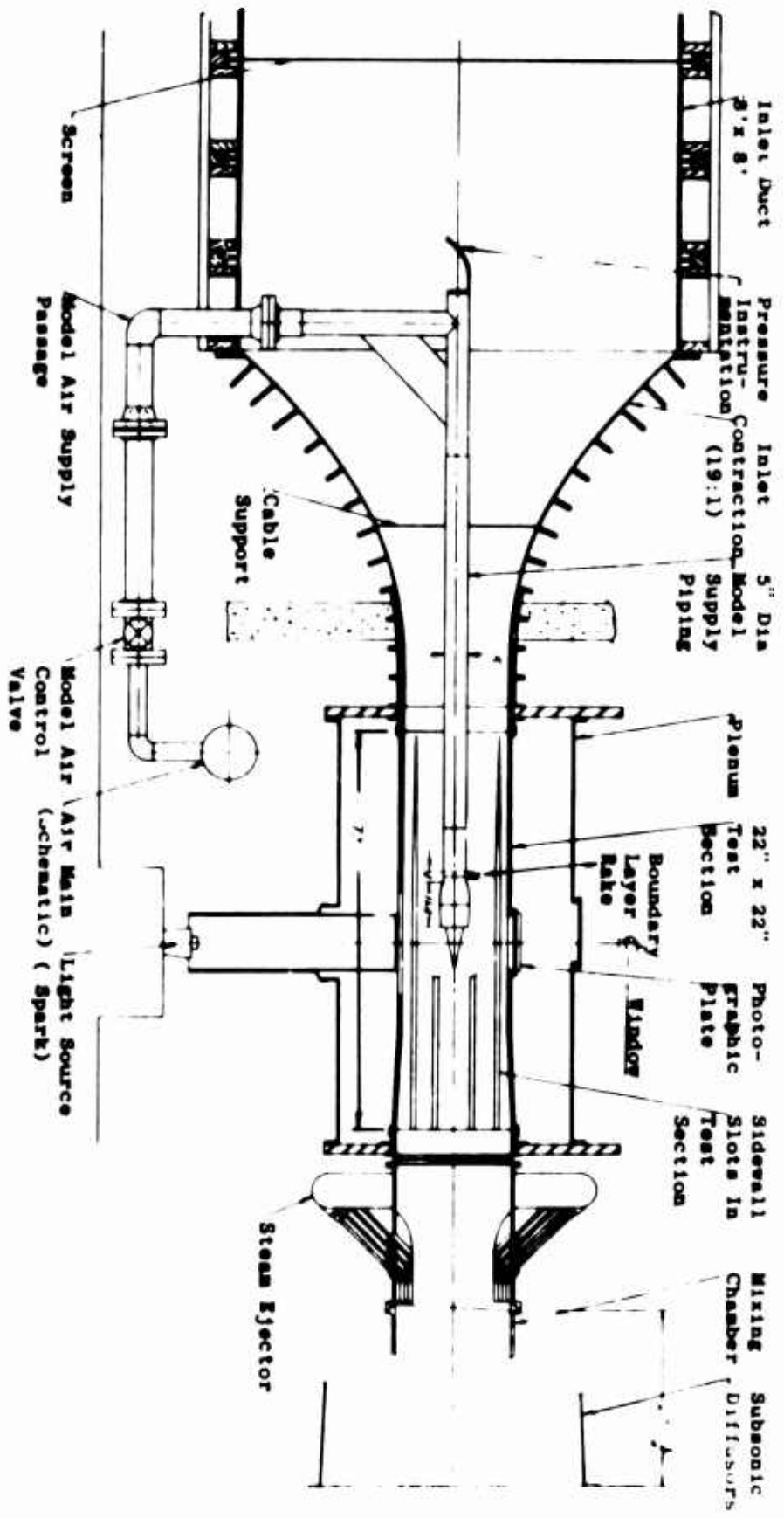


FIGURE 2. Overall Assembly of Model in Transonic Wind Tunnel

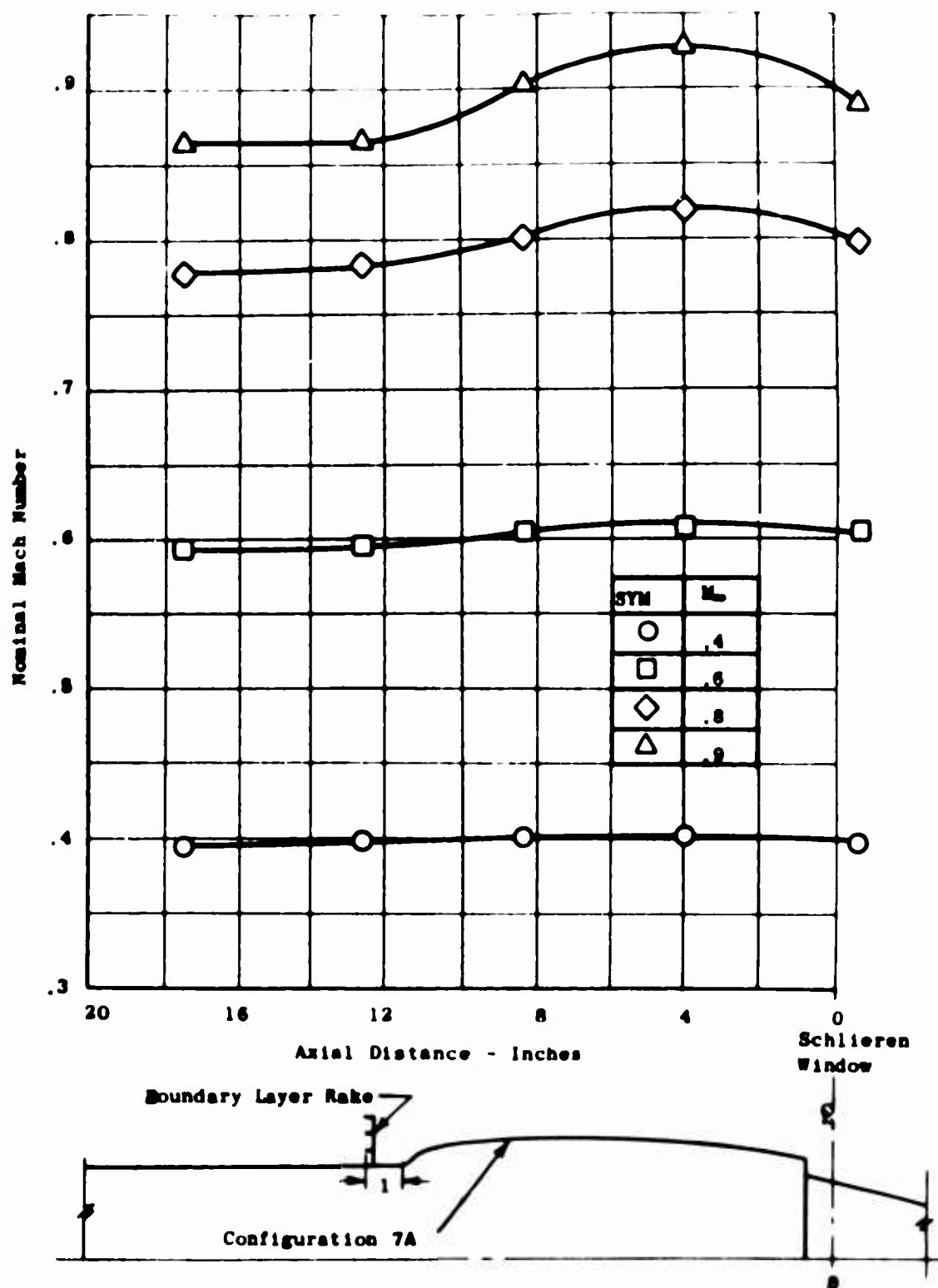


Figure 3. Sidewall Mach Number Distribution in Transonic Wind Tunnel

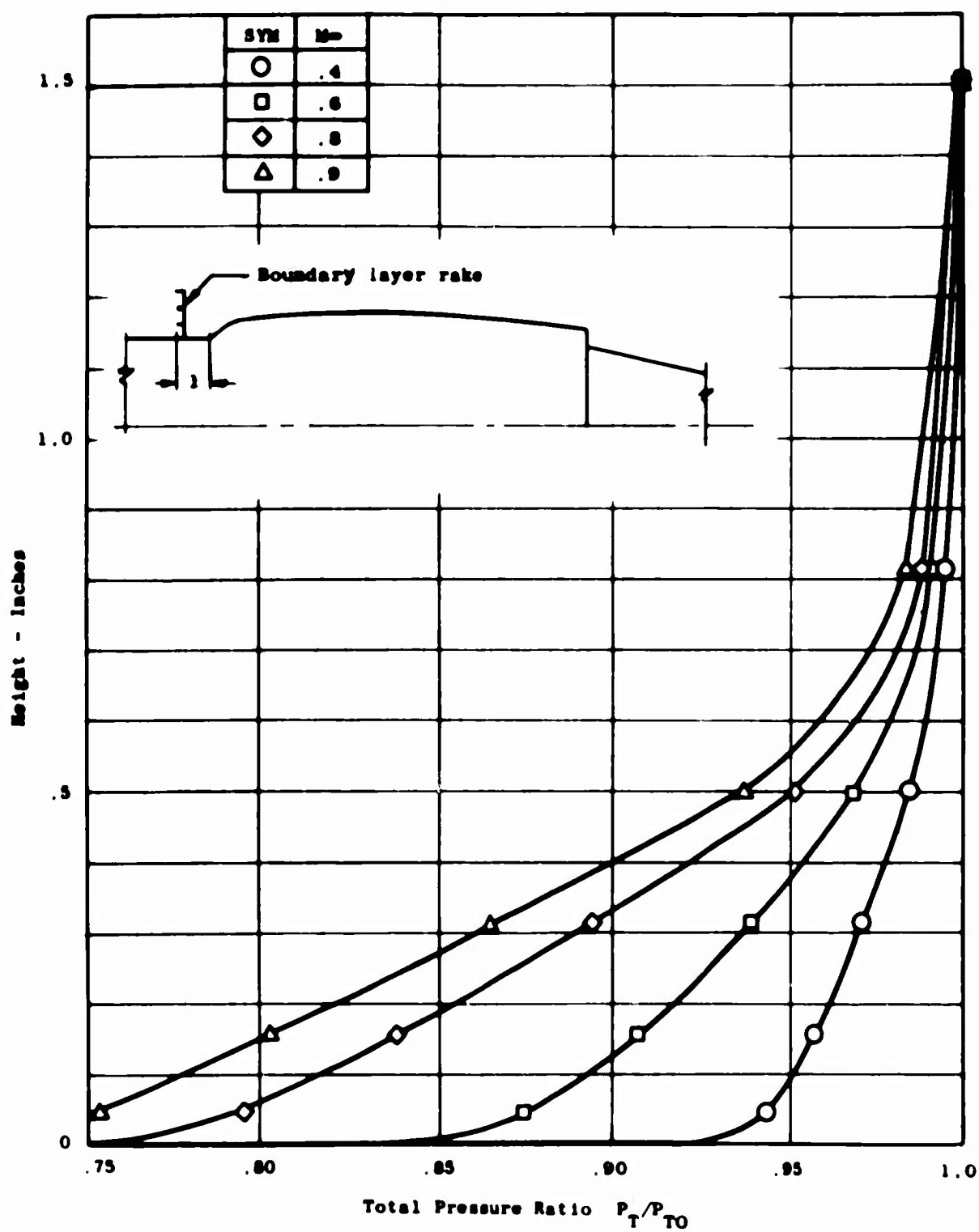


Figure 4. Boundary Layer Rake
Pressure Distribution
at Test Mach Numbers.

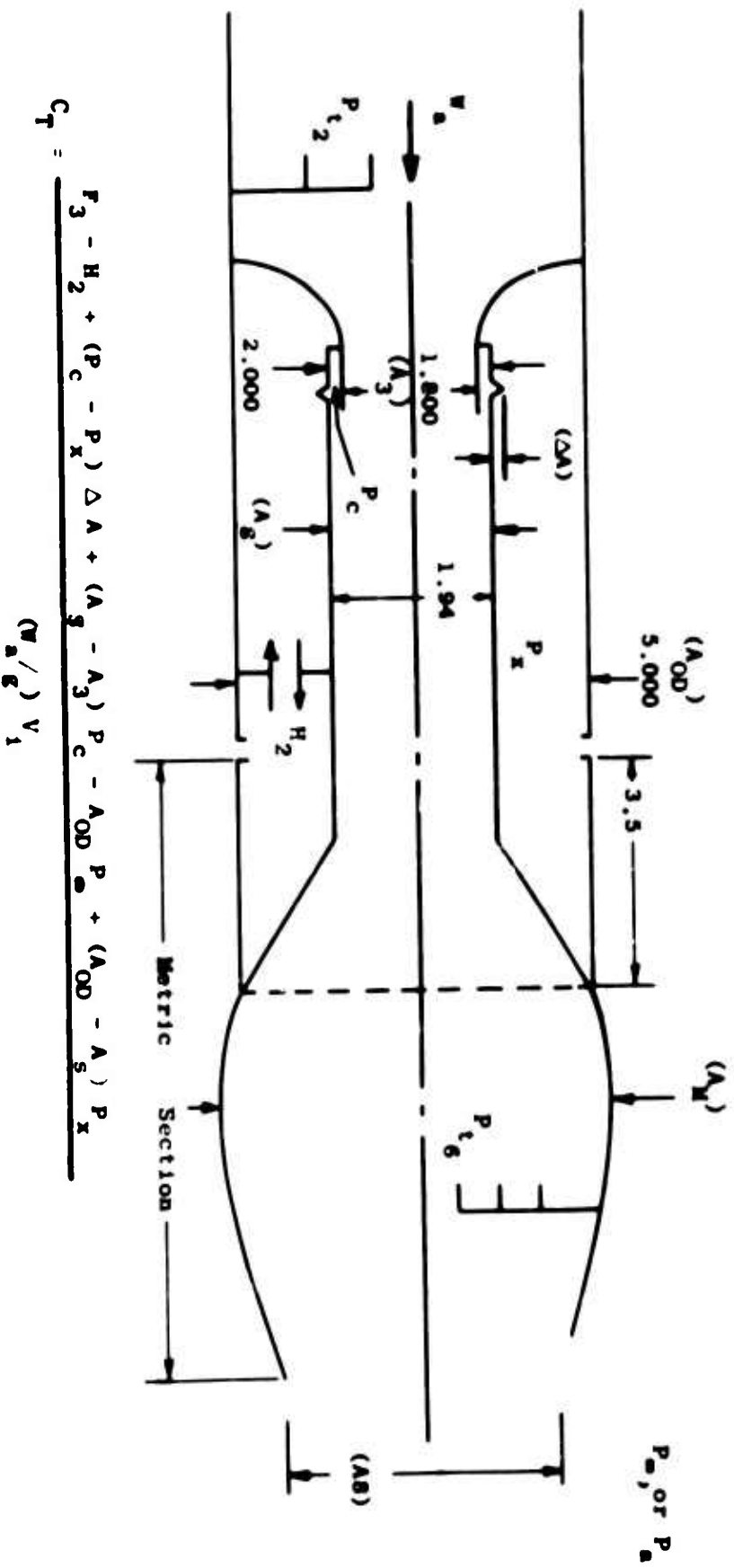


Figure 5. Schematic of Force Balance System.

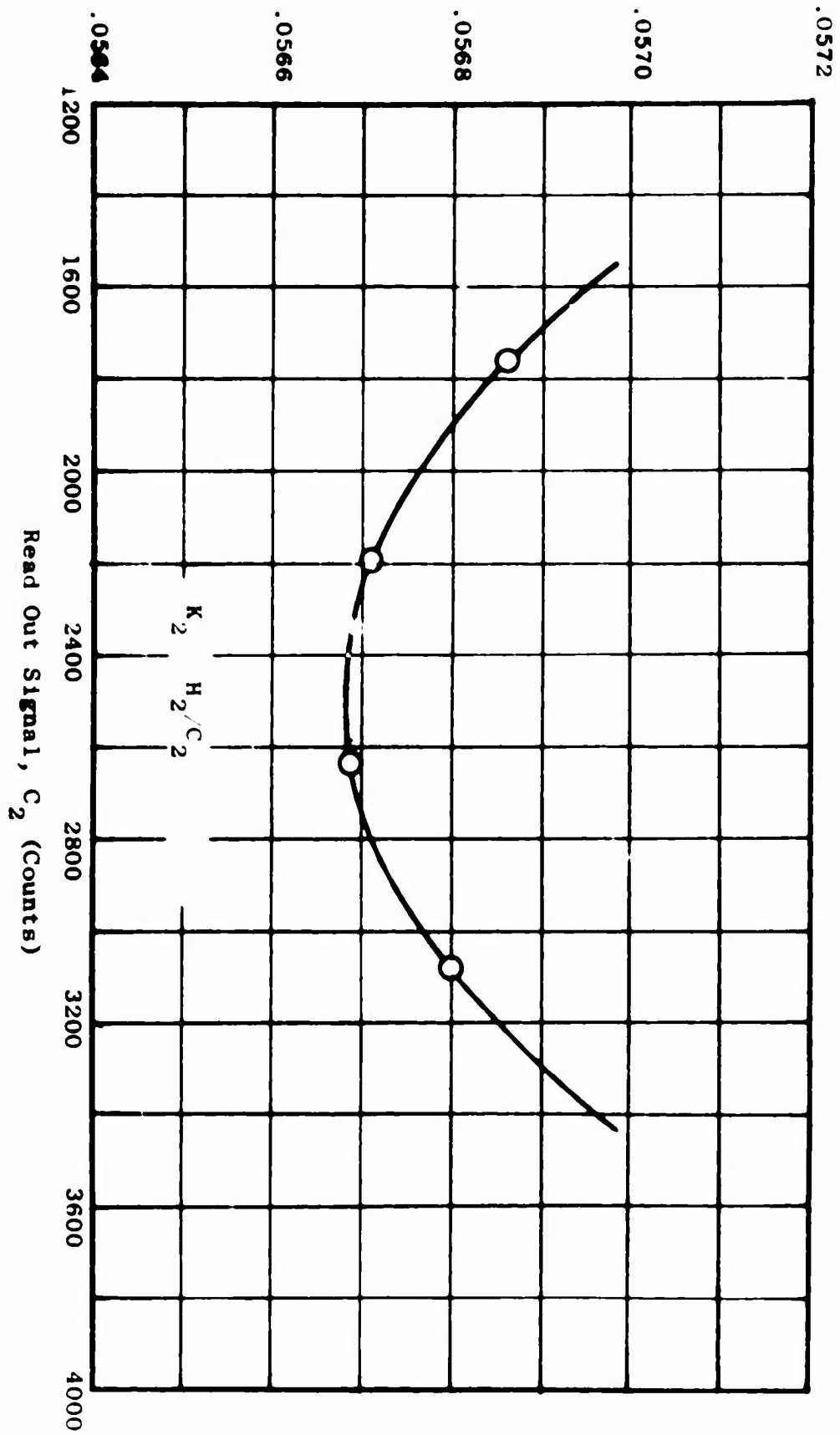
Balance Force Constant, K_2 (lb/Counts)

Figure 6. Balance Dead Weight
Calibration - Channel
5, 2-27-64.

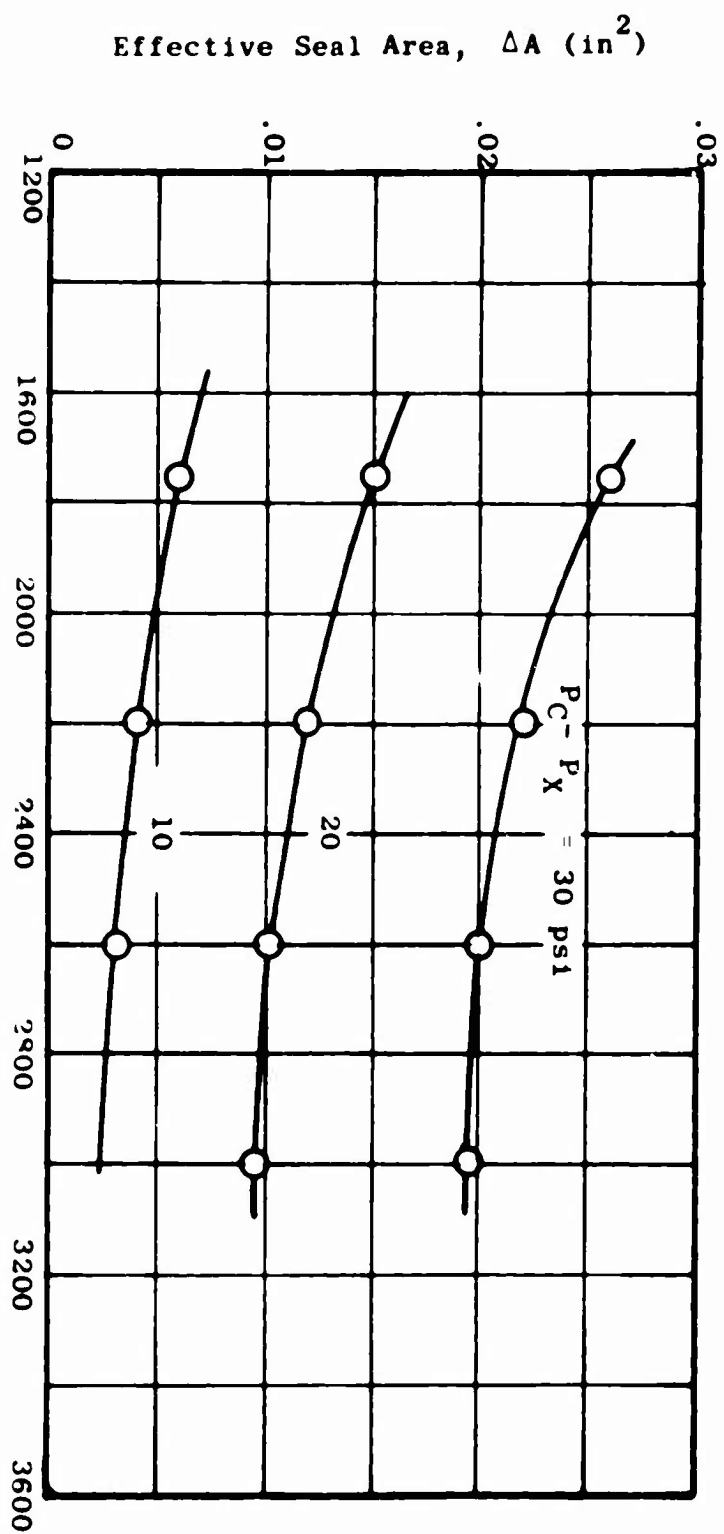


Figure 7. Effective Seal Area
Calibration - Channel 5,
2-27-64.

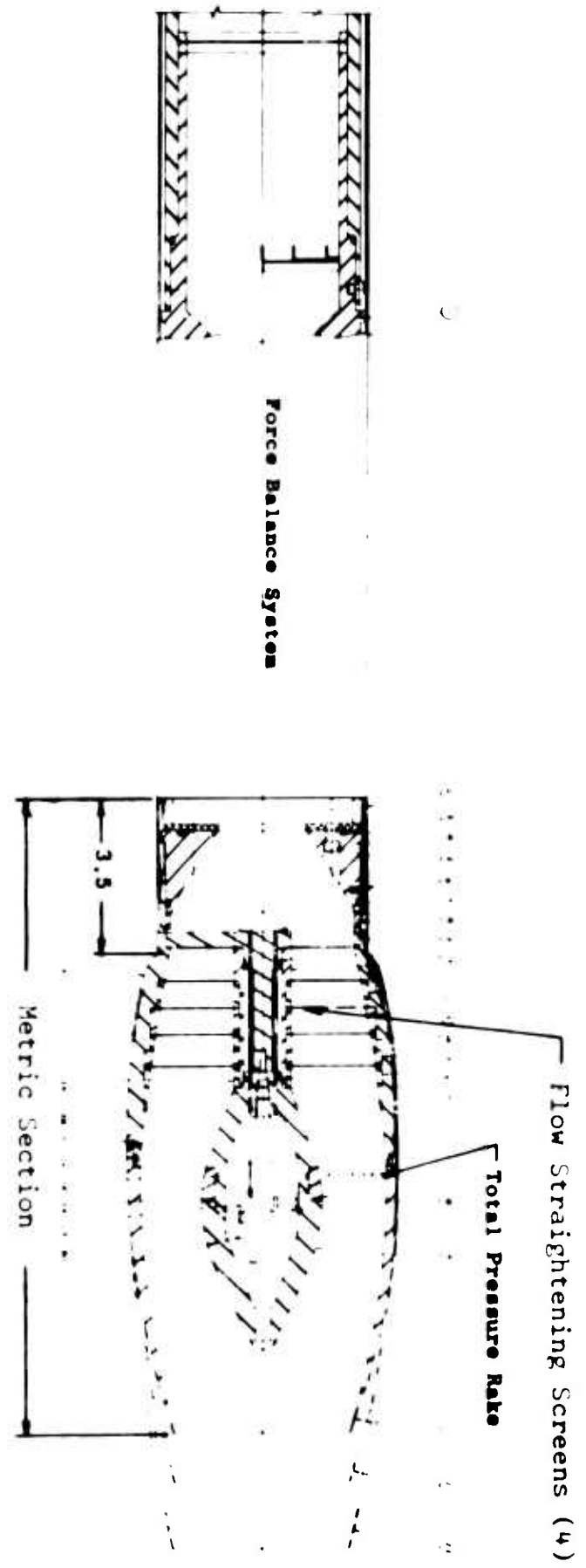


Figure 8. Typical Model Installation - Models 1, 2 and 3.



Figure 9. Plug Nozzle Model Installed in Transonic Wind Tunnel



Figure 10. Side View of Plug Nozzle Model.



Figure 11. Close View Plug Nozzle Model



Figure 12. Side View Conical Nozzle Model

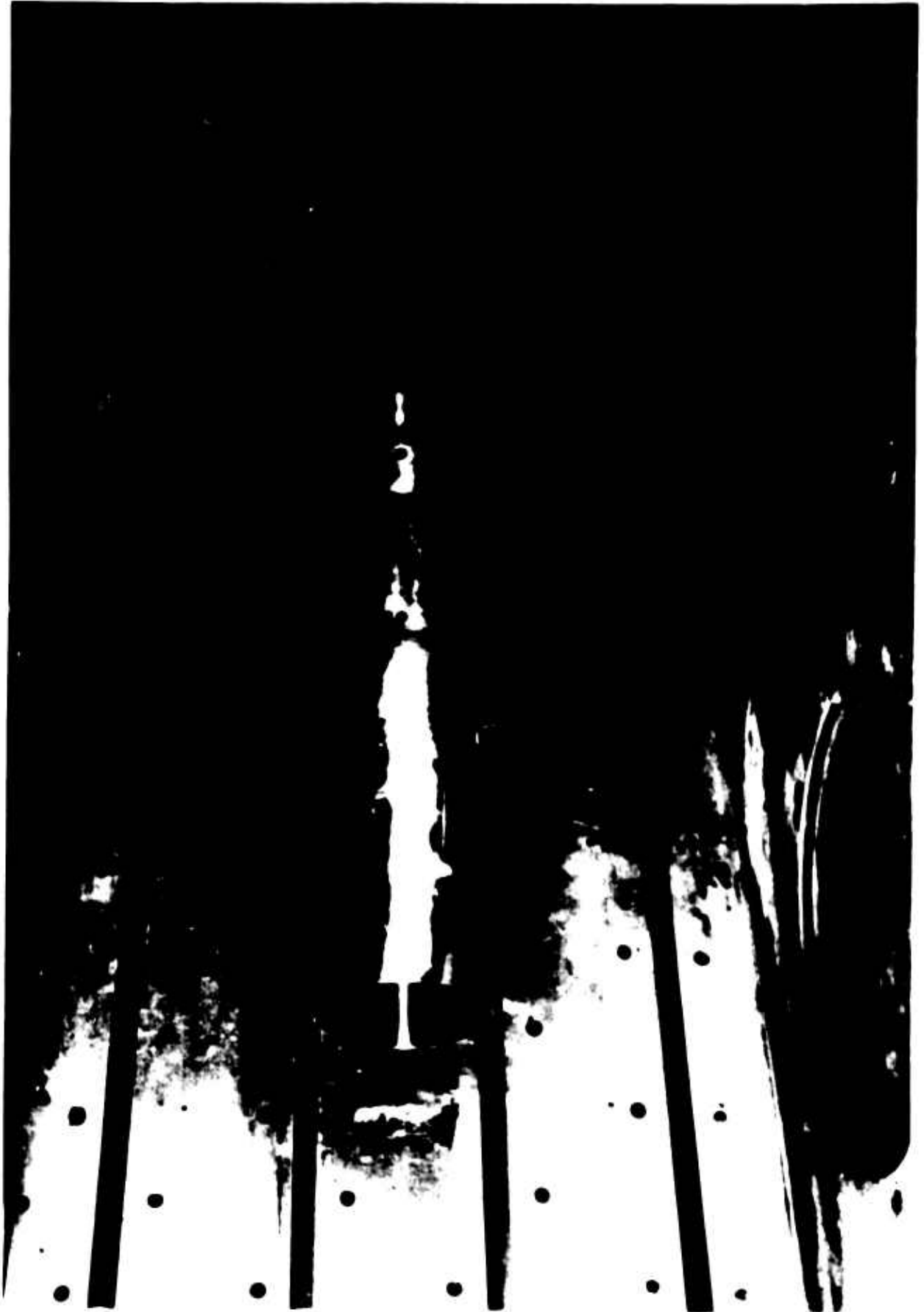


Figure 13. Close View Conical Nozzle Model

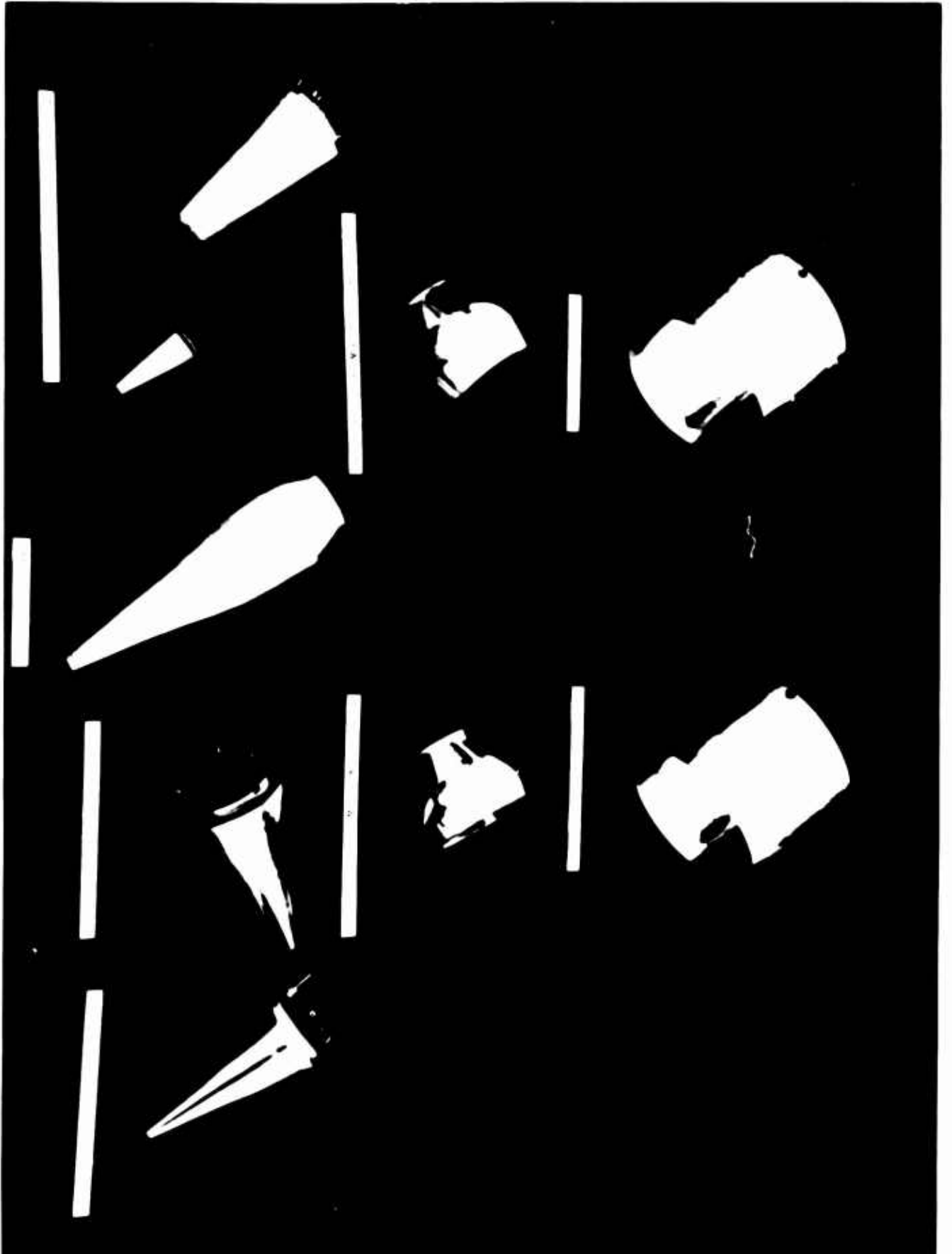
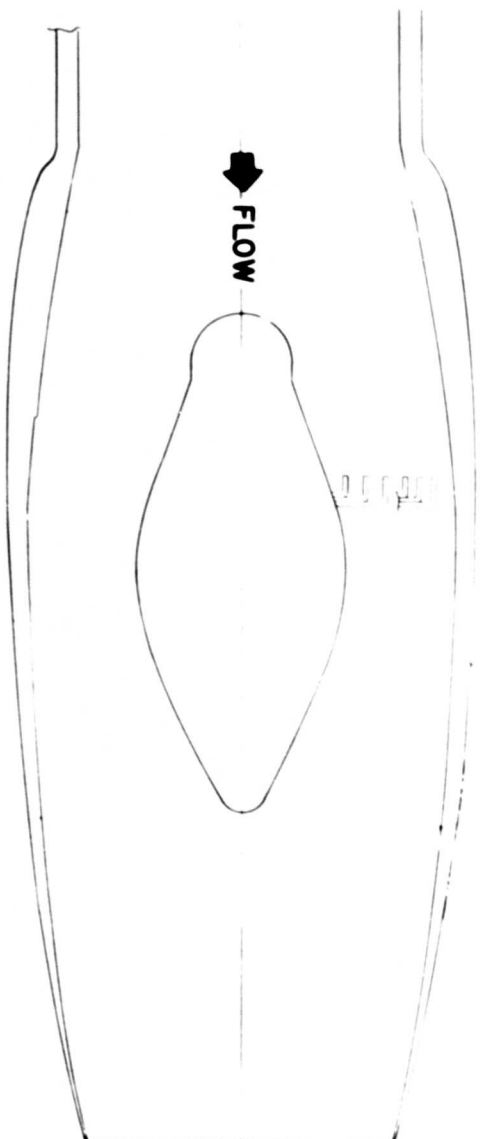


Figure 14. Views of Model Details

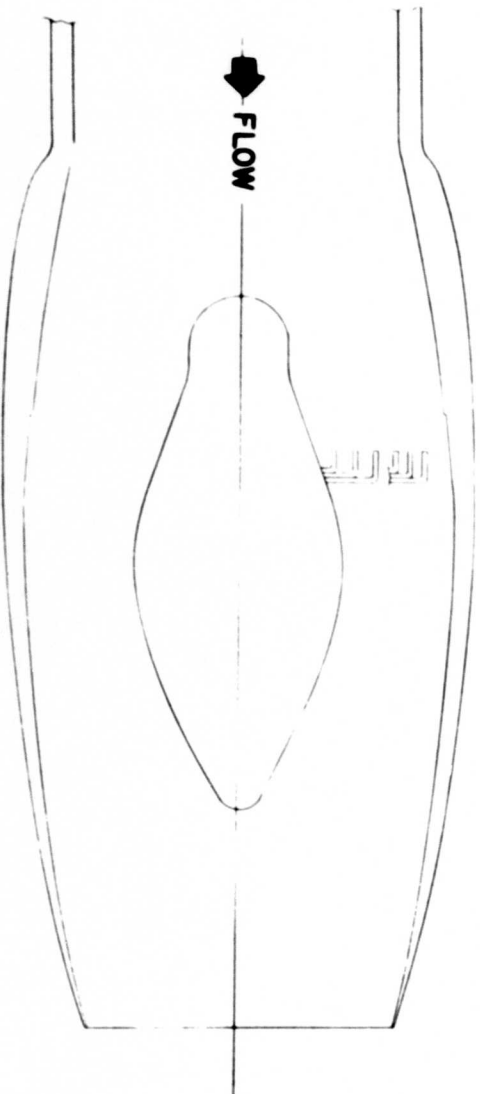


Figure 15. Views of Model Details



MODEL 1

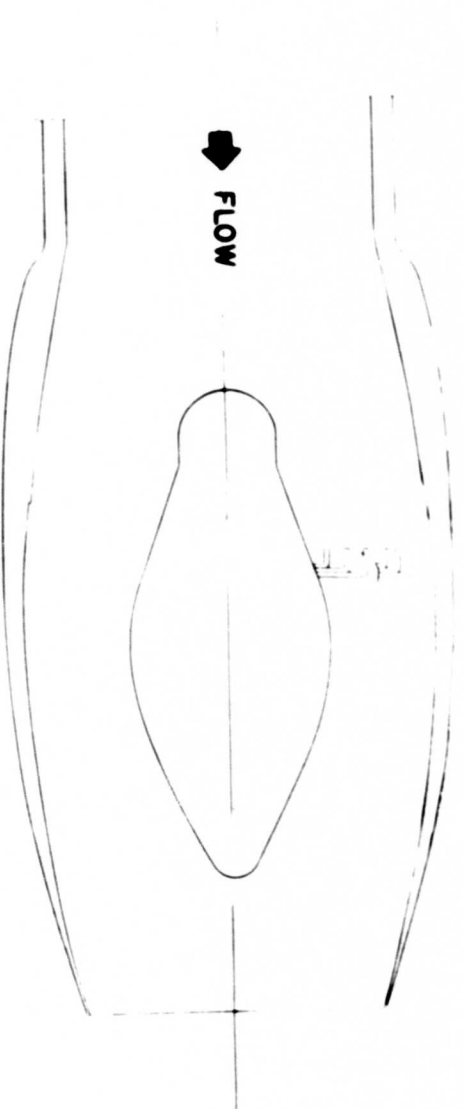
L_T / D_M	2.16
R / D_M	5.7
β	14°
D_J / D_M	.654



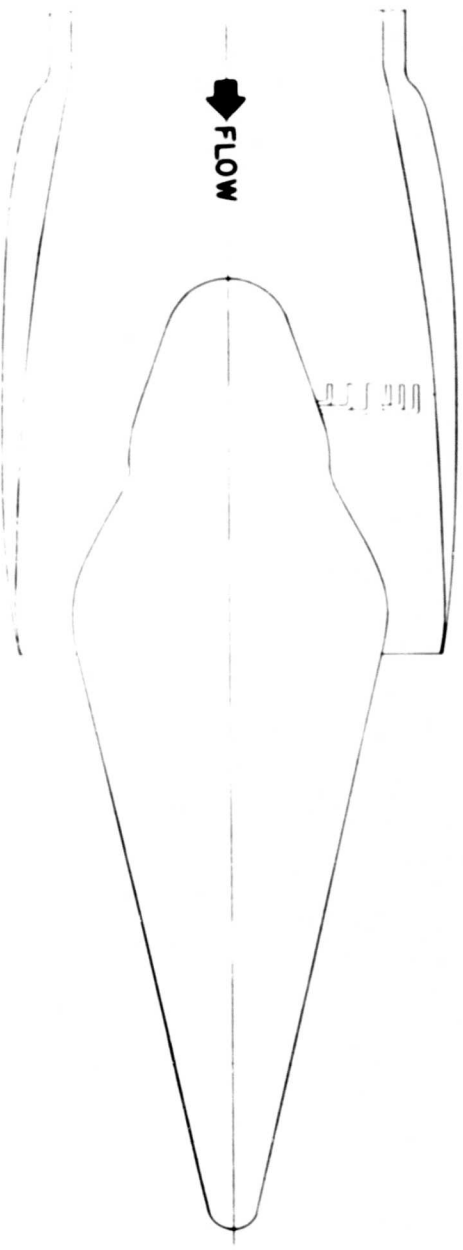
MODEL 2

L_T / D_M	1.93
R / D_M	3.90
β	17°
D_J / D_M	.654

Figure 16. Geometric Details of Models 1 and 2

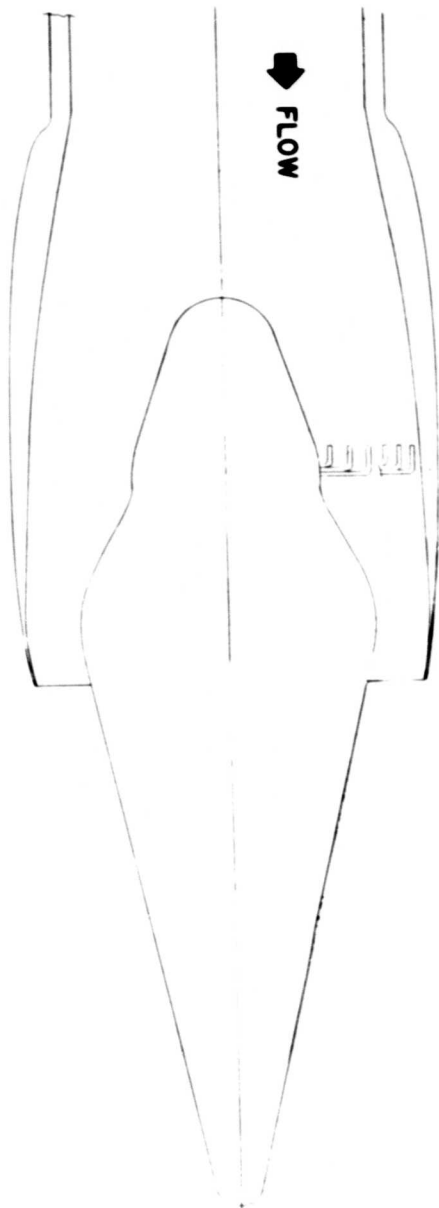


Model 3		
Lt / Dm	1.74	
R / Dm	2.80	
β	20°	
Dj / Dm	.654	

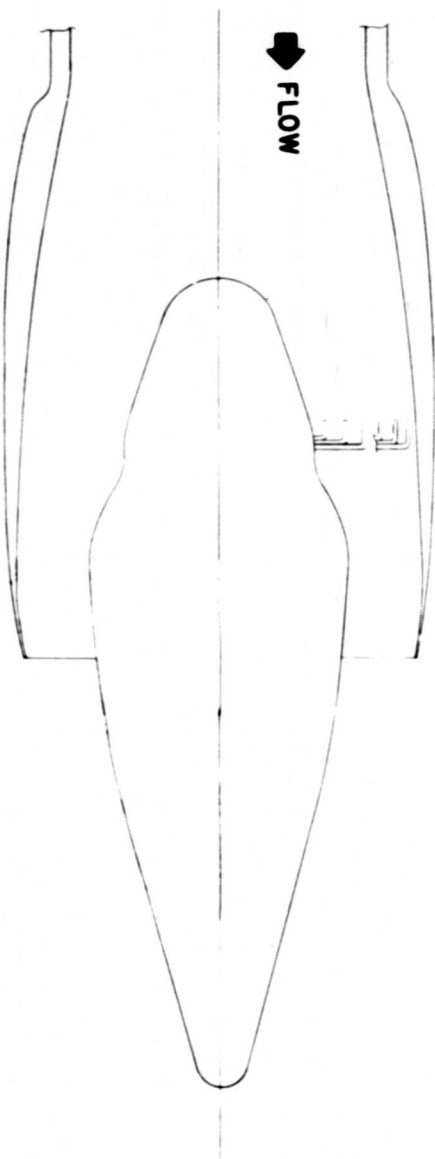


Model 4		
Lt / Dm	1.32	
R / Dm	3.35	
β	8°	
ϕ	12.5°	
Dj / Dm	.929	
Ae / Ath	2.13	

Figure 17. Geometric details of Models 3 and 4.

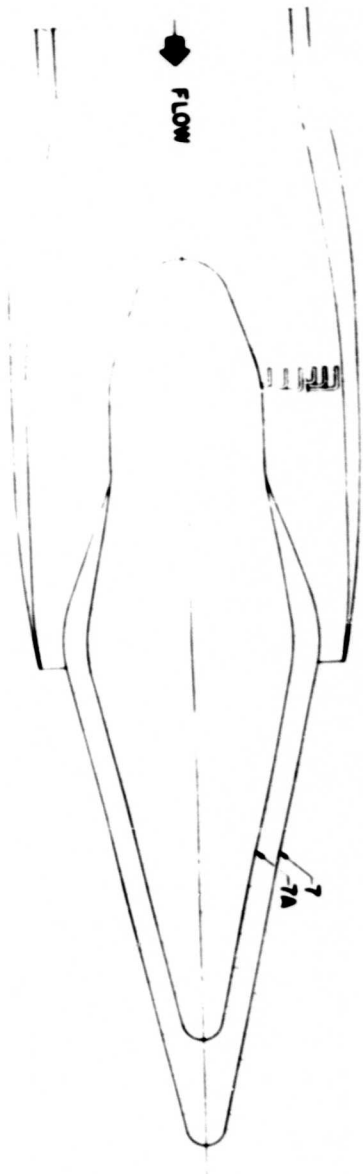


Model 5			
Lt / Dm	1.36		
R / Dm	2.75		
β	10°		
ϕ	12.5°		
Dj / Dm	.910		
Ae / Ath	2.08		



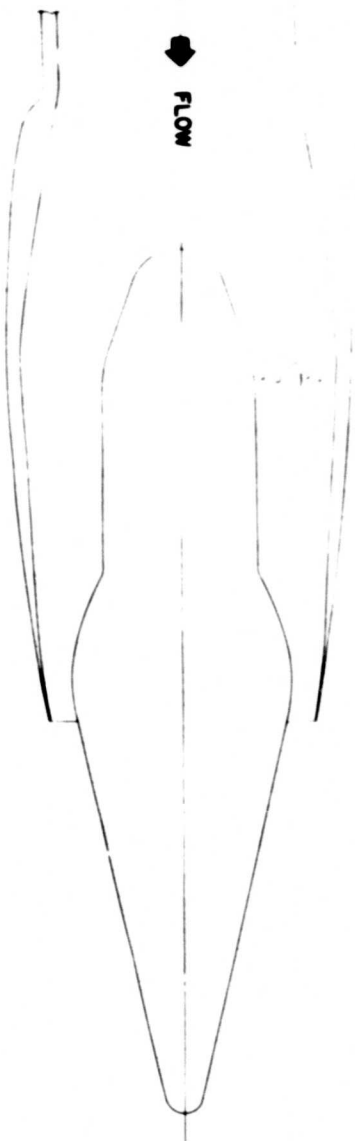
Model 6			
Lt / Dm	1.36		
R / Dm	1.94		
β	10°		
ϕ	15°		
Dj / Dm	.910		
Ae / Ath	1.65		

Figure 18. Geometric Details of Models 5 and 6.



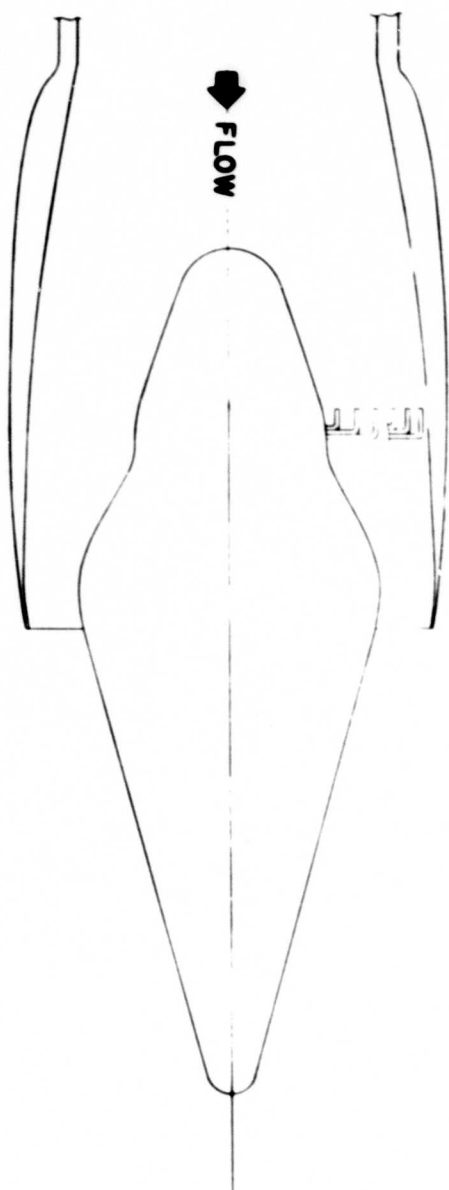
Models 7 and 7A

7	Lt/Dm	1.65
7	R/Dm	3.15
7	β	10°
7	ϕ	12.5°
7	Dj/Dm	.875
7	Ae/Atm	3.36
7A	Ae/Atm	1.78

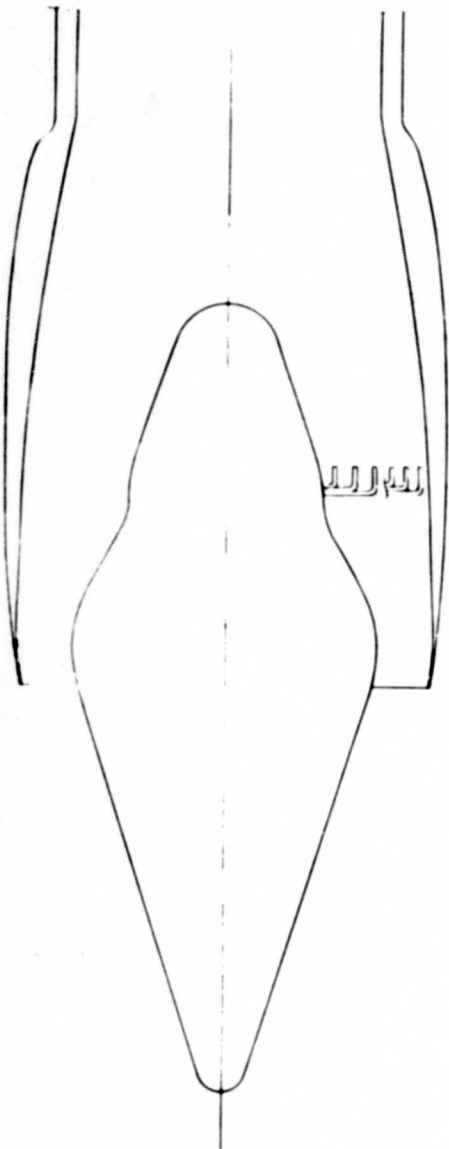


Model 8

	Lt/Dm	1.86
	R/Dm	5.85
	β	12.5°
	ϕ	12.5°
	Dj/Dm	.770
	Ae/Atm	2.66



Model 9	
Lt / D _M	1.32
R / D _M	2.75
β	10°
ϕ	15°
D _J / D _M	.910
AE / A _{TH}	2.01



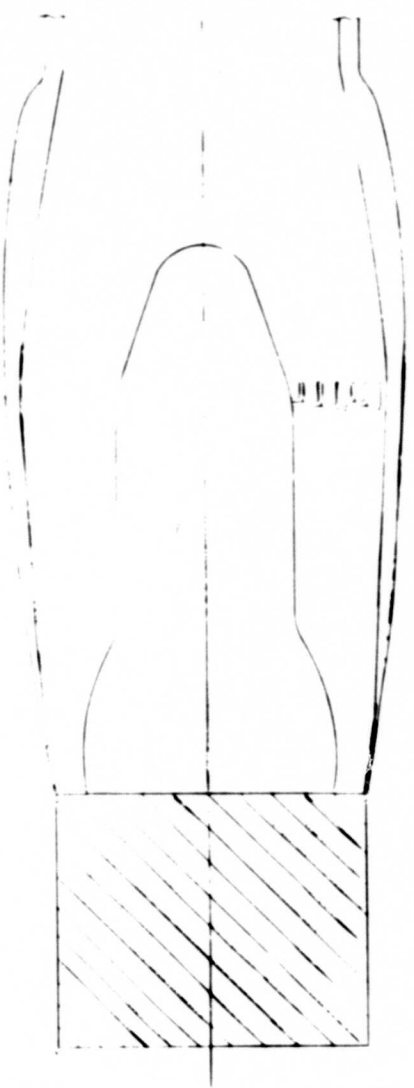
Model 10	
Lt / D _M	1.32
R / D _M	2.75
β	10°
ϕ	17.5°
D _J / D _M	.910
AE / A _{TH}	2.01

Figure 20. Geometric Details of Models 9 and 10.



Model 10A

Lt / Dm	1.32
R / Dm	2.75
β	10°
ϕ	12.5°
Dj / Dm	.910
AE / ATH	2.01



Model 10B

Lt / Dm	1.86
R / Dm	5.85
β	12.5
ϕ	-
Dj / Dm	.770
AE / ATH	-

Figure 21. Geometric Details of Models 10A and 10B.

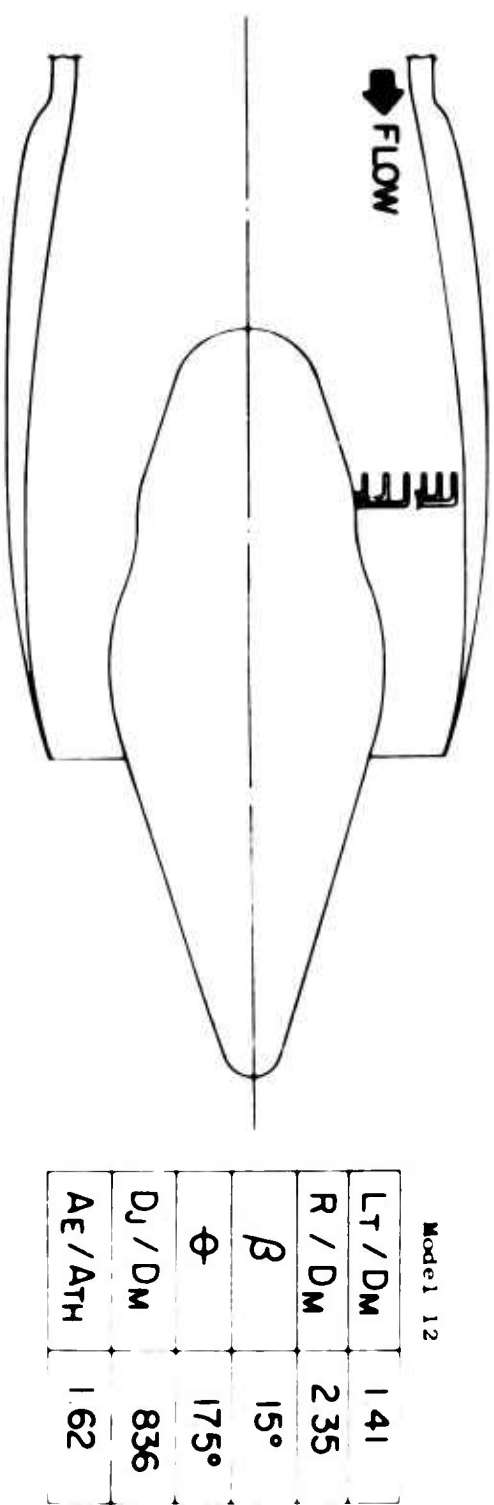
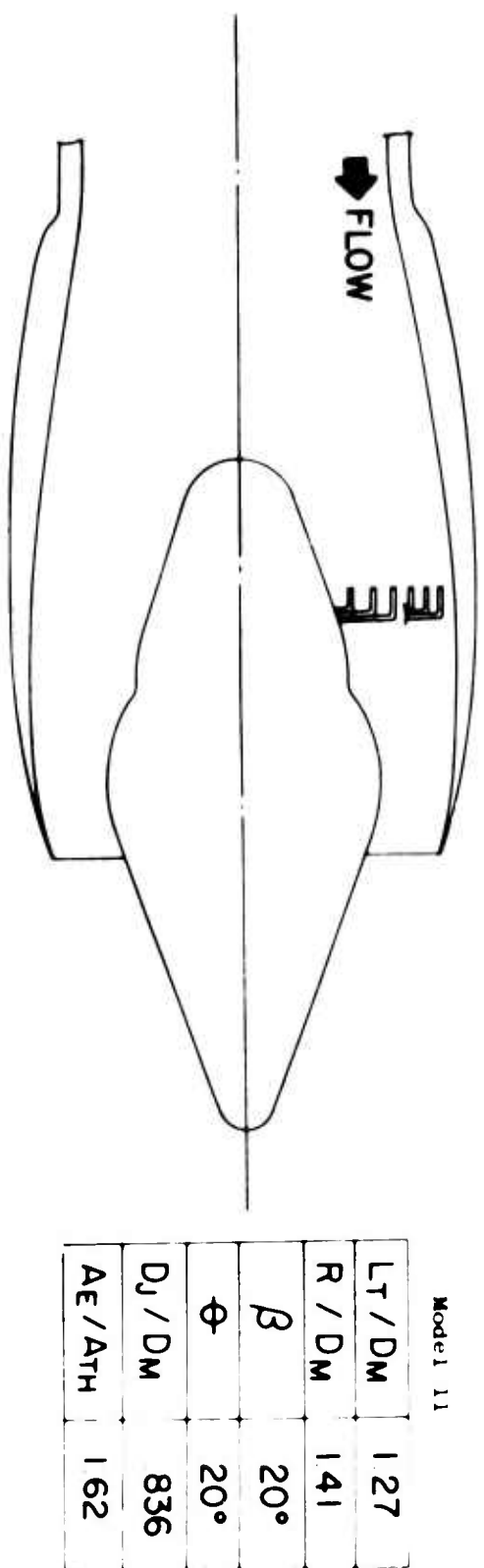
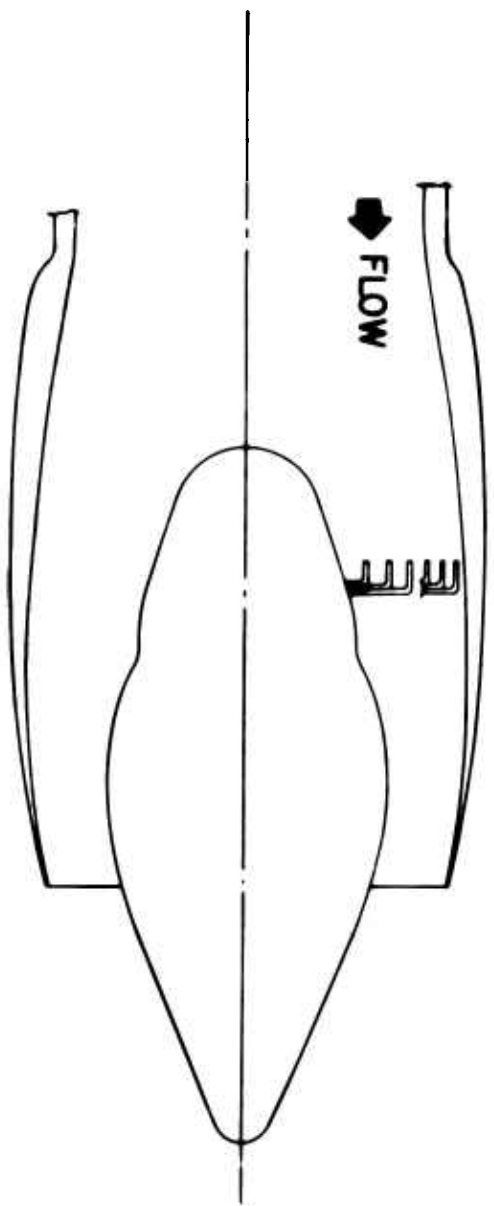
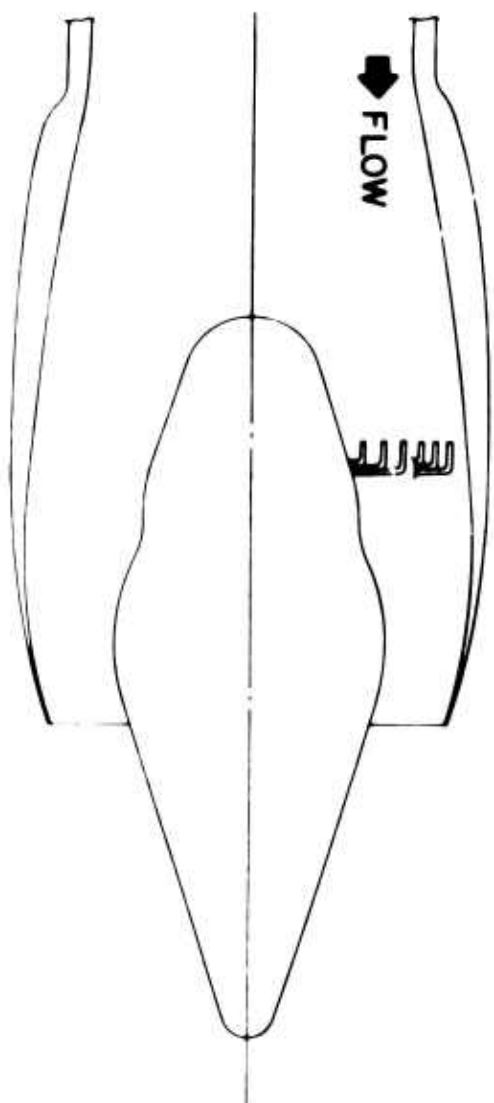


Figure 22. Geometric Details of Models 11 and 12.



Model 13	
Lt / DM	1.41
R / DM	2.35
β	15°
ϕ	22.5°
Dj / DM	836
AE / ATH	1.62



Model 14	
Lt / DM	1.32
R / DM	1.73
β	18°
ϕ	17.5°
Dj / DM	836
AE / ATH	1.62

Figure 23. Geometric Details of Model 13 and 14.

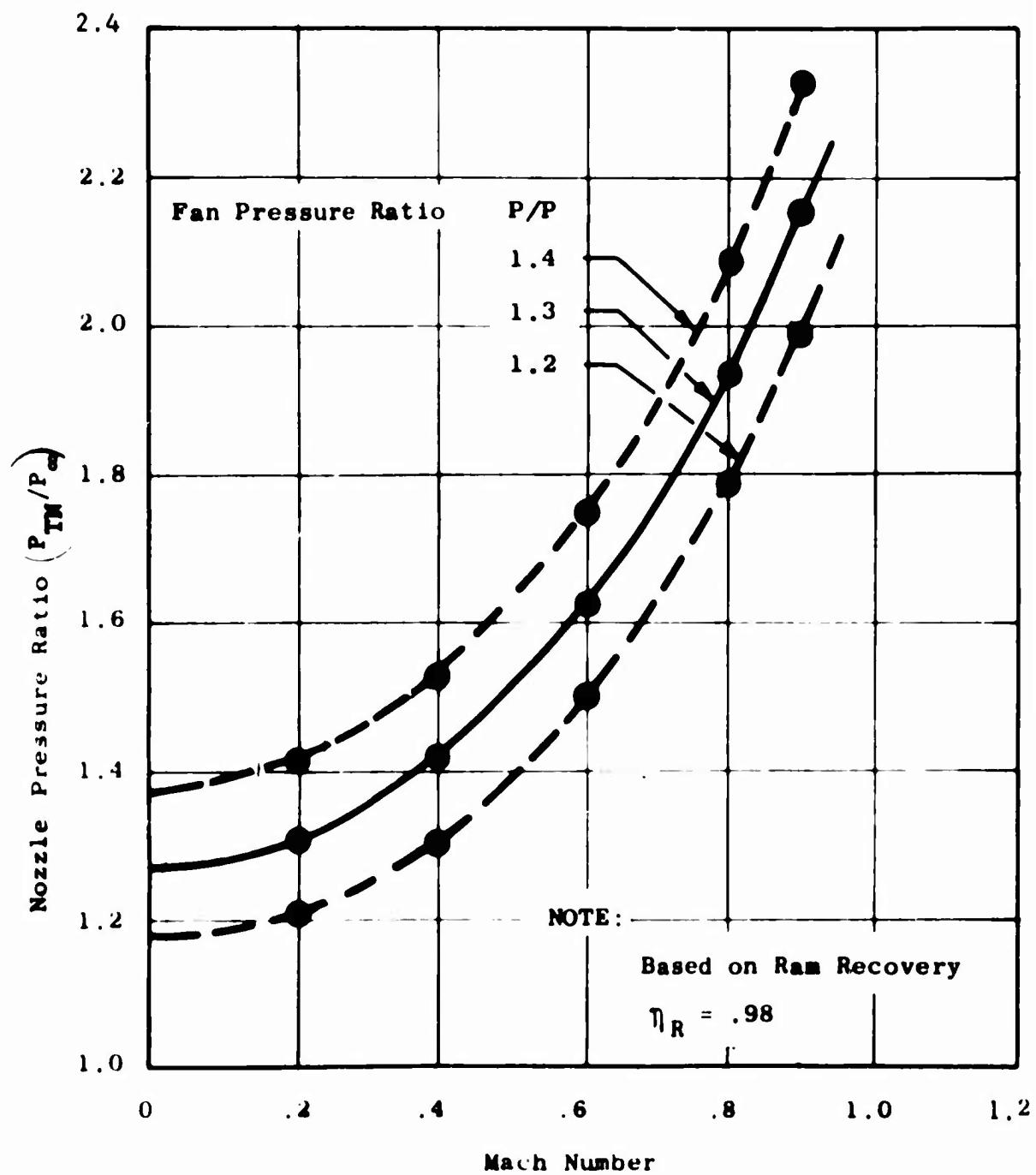


Figure 24. Test Schedule Pressure Ratio Versus Mach Number.

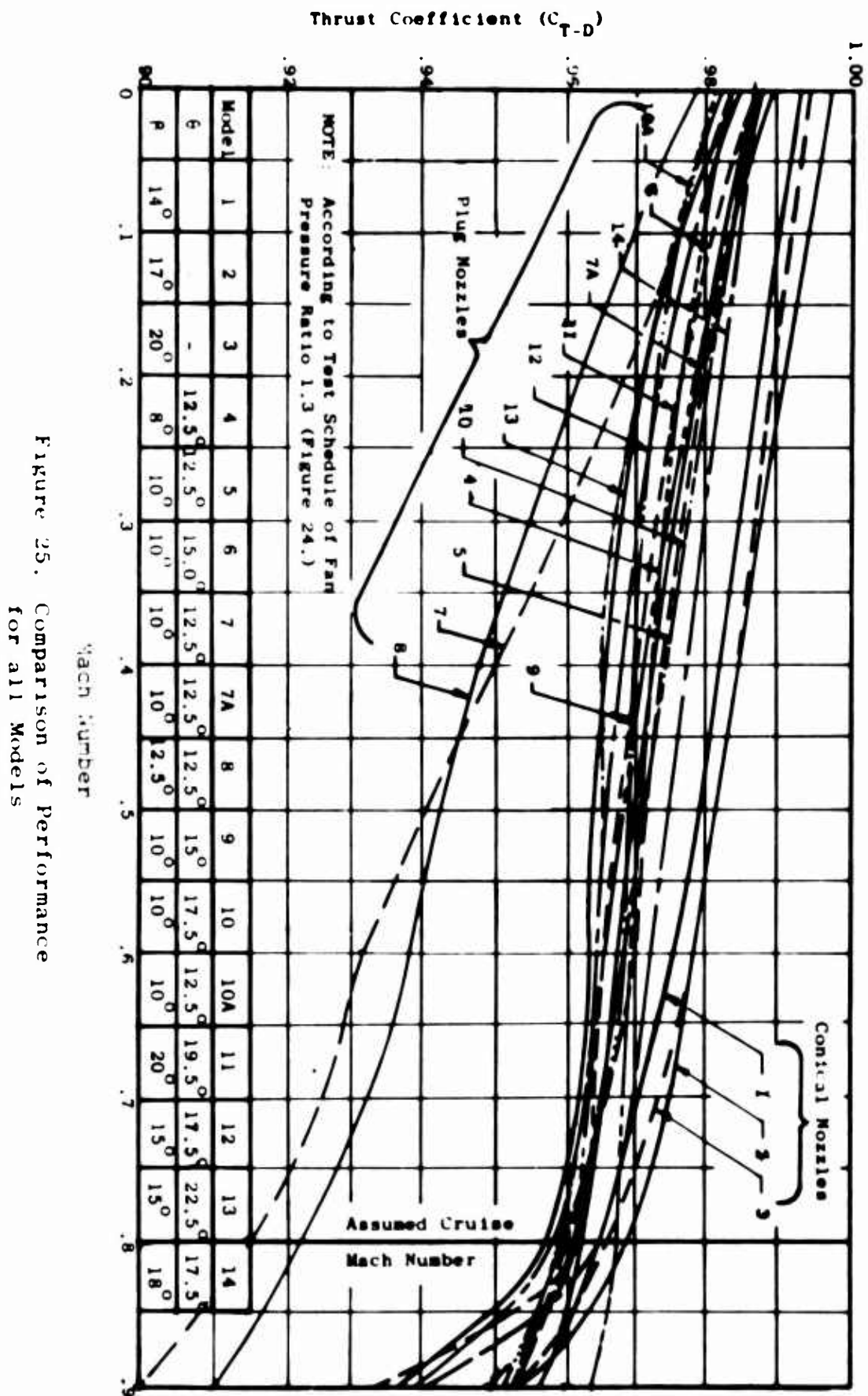


Figure 25. Comparison of Performance for all Models

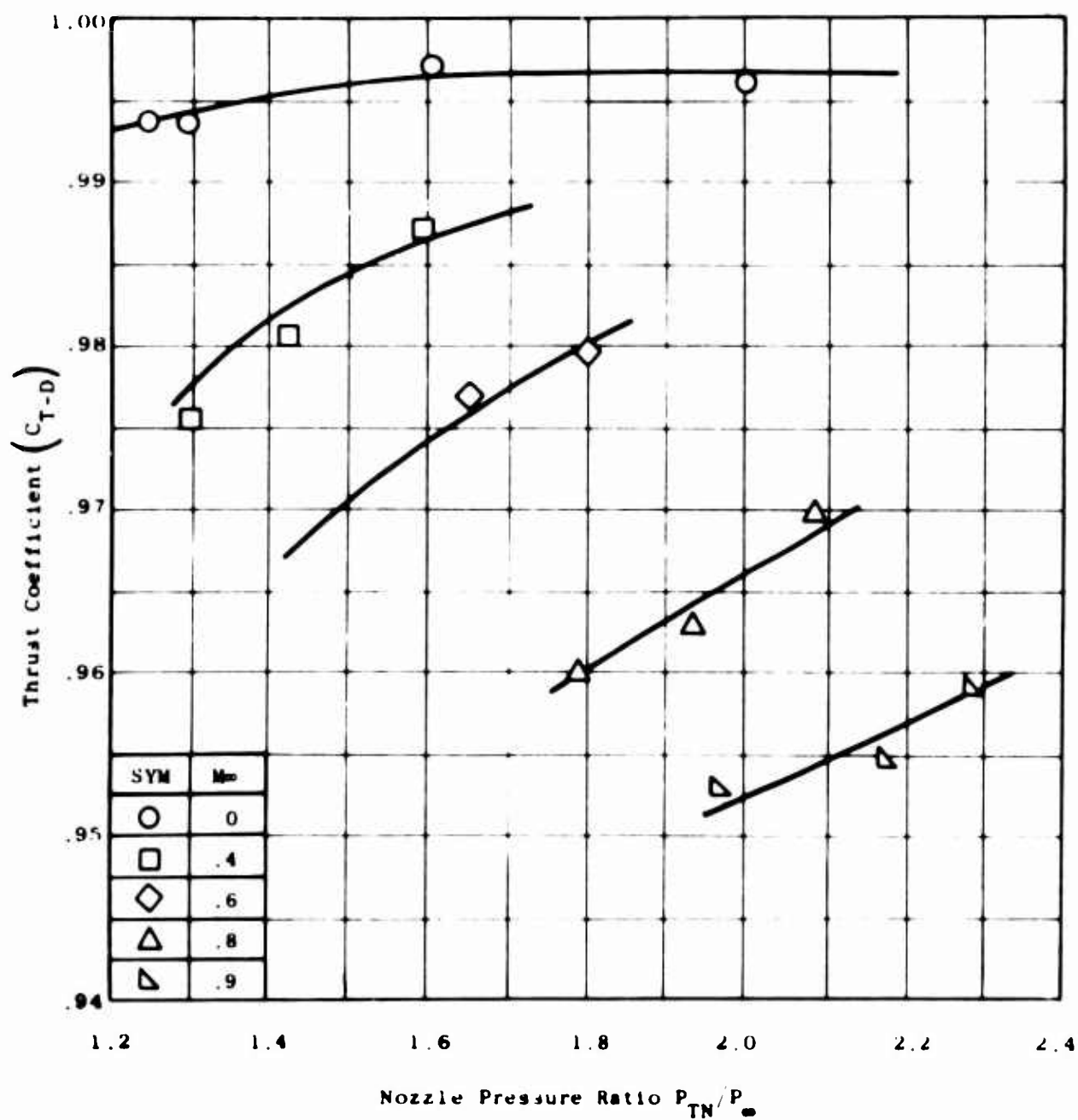


Figure 26. Exhaust System Performance as a Function of Mach No. and Pressure Ratio - Model 1.

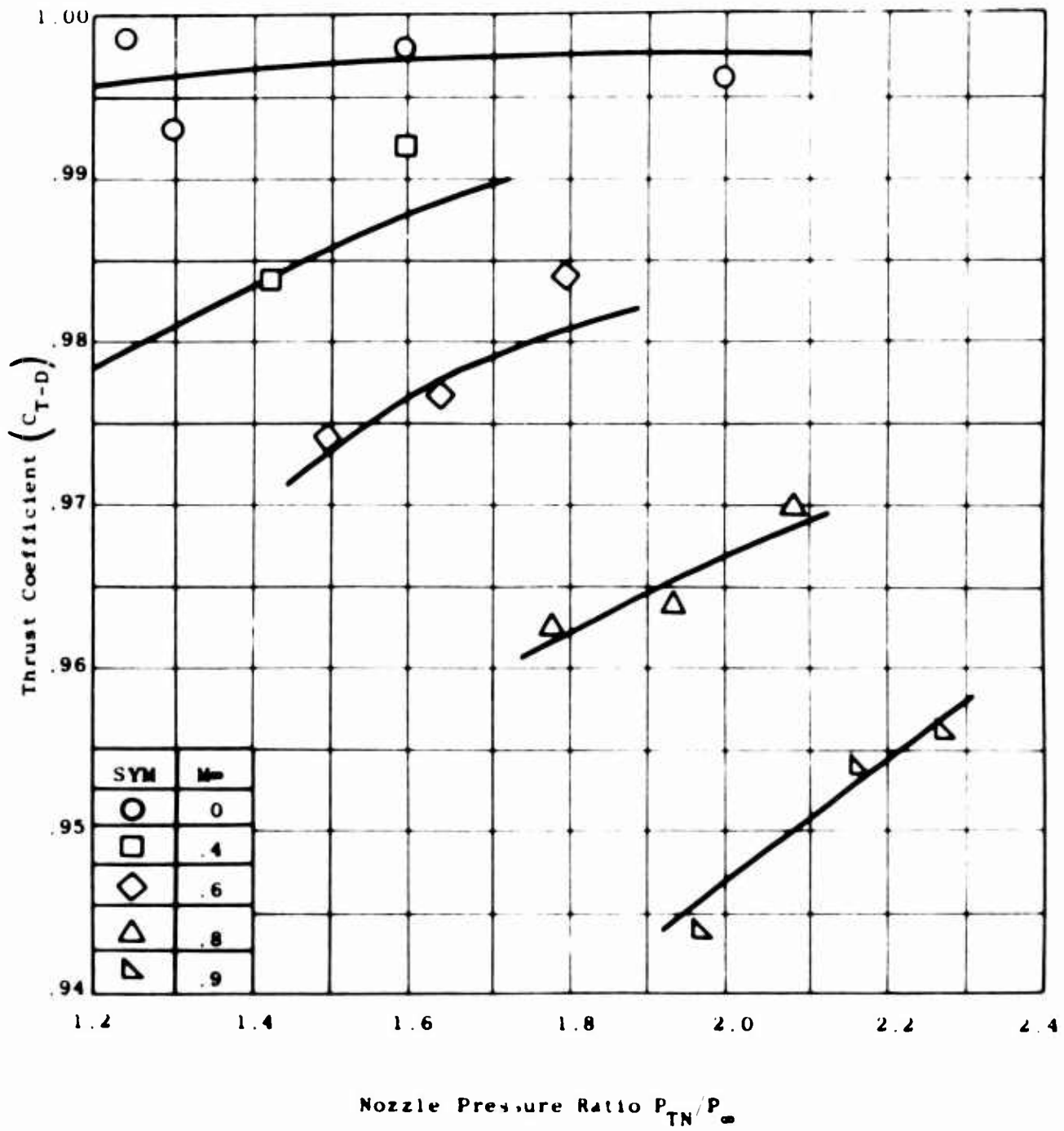


Figure 27. Exhaust System Performance as a Function of Mach No. and Pressure Ratio - Model 2.

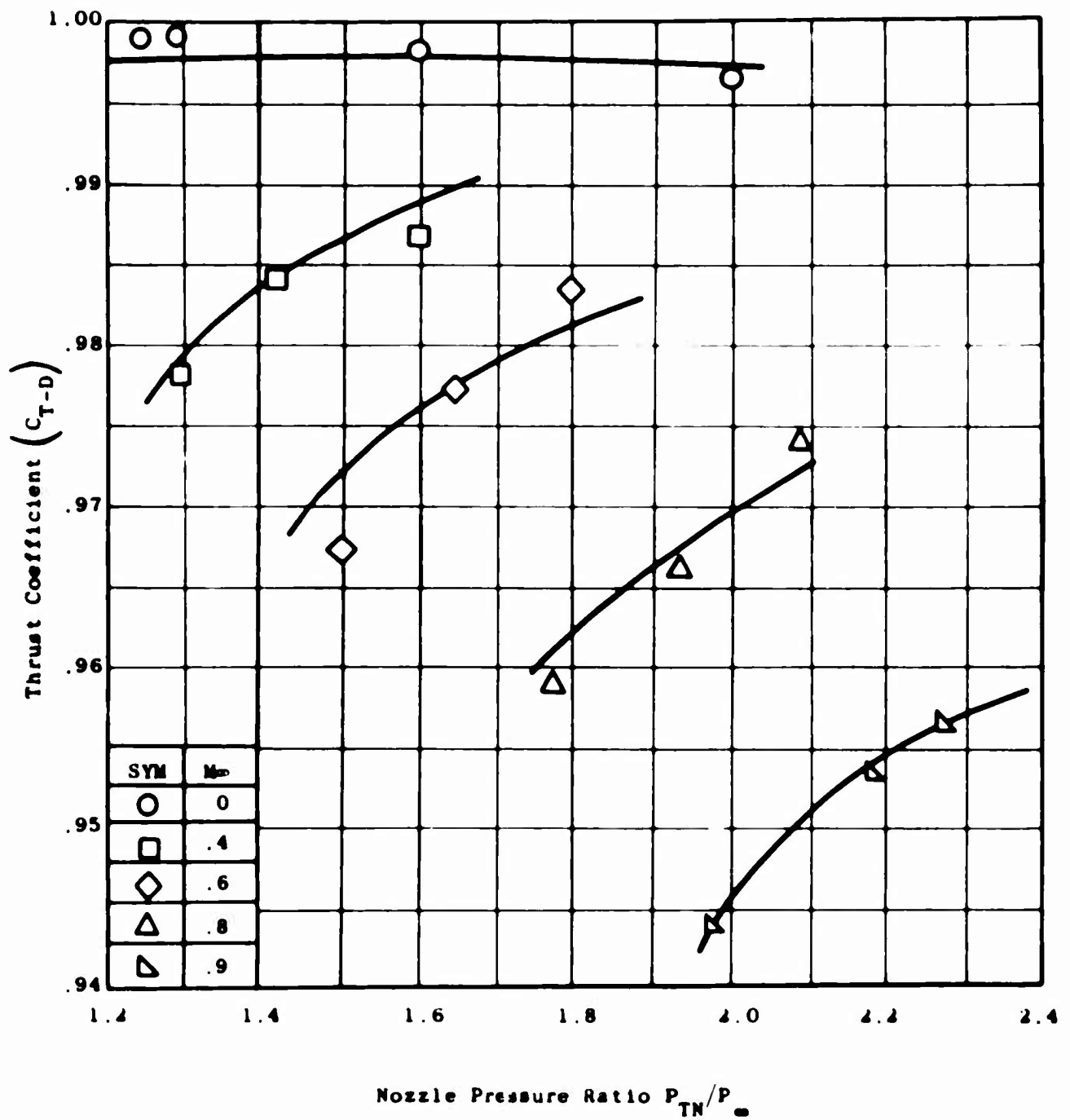


Figure 28. Exhaust System Performance as a Function of Mach No. and Pressure Ratio - Model 3.

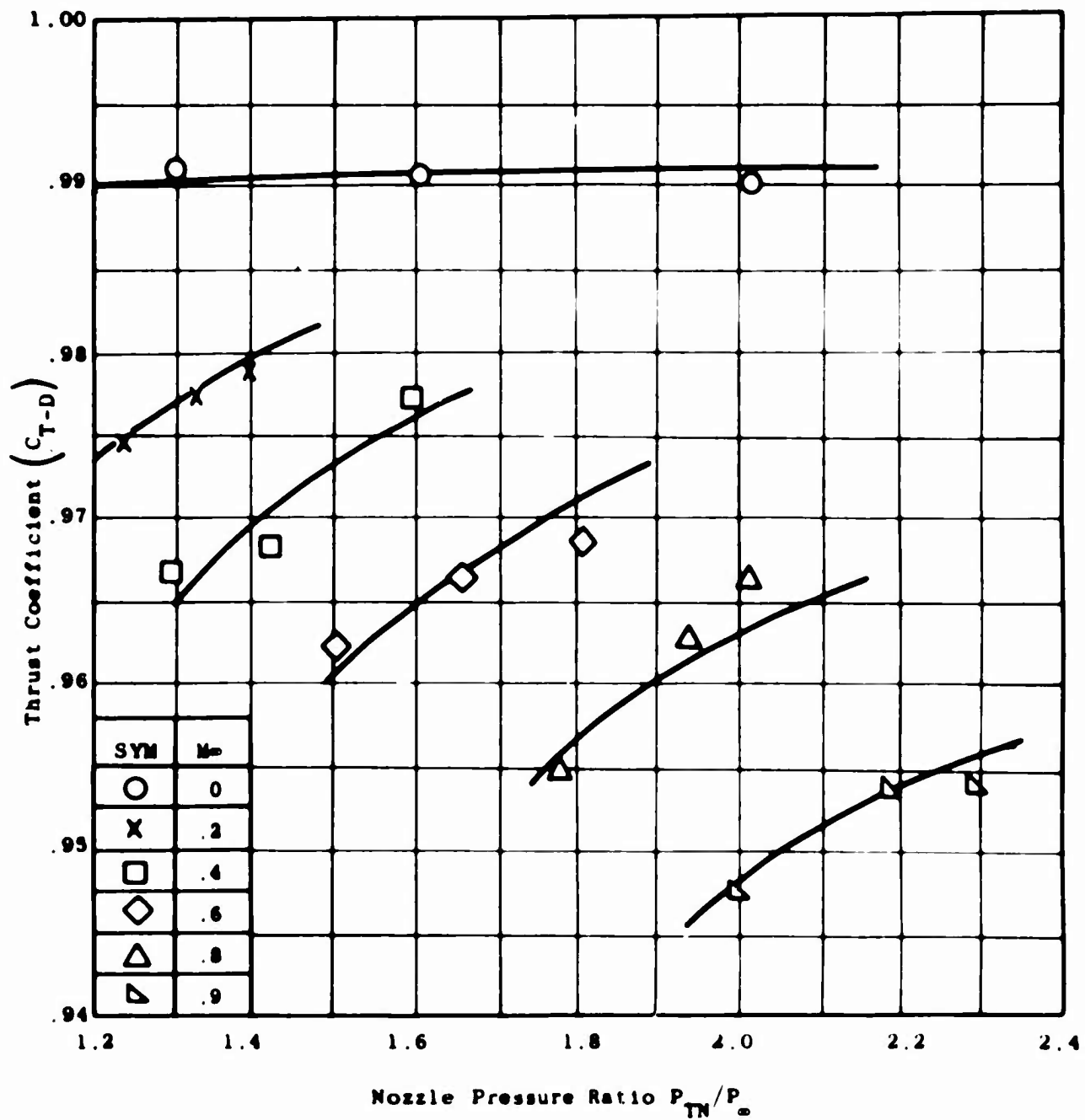


Figure 29. Exhaust System Performance
as a Function of Mach No.
and Pressure Ratio -
Model 4.

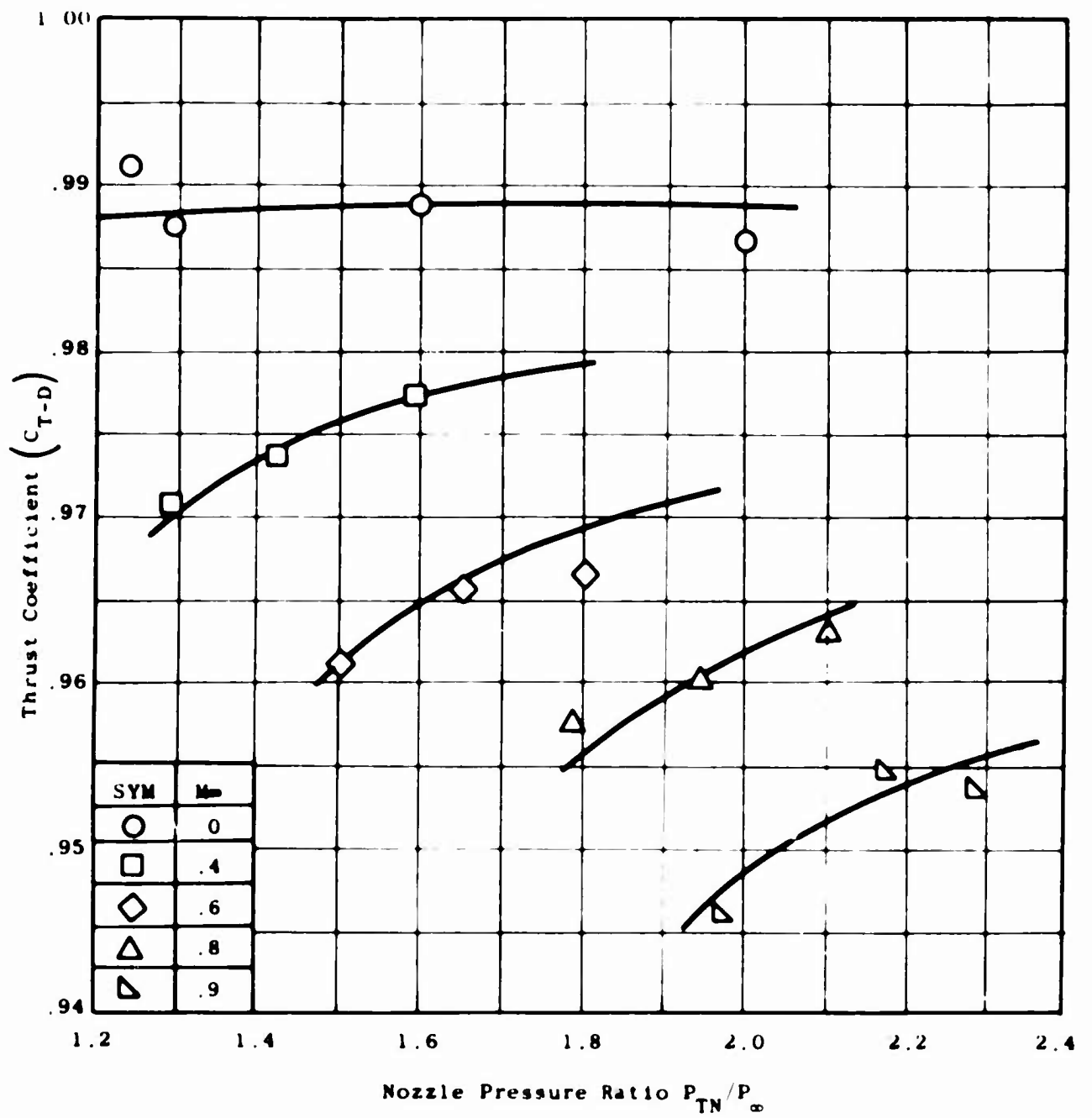


Figure 30. Exhaust System Performance as a Function of Mach No. and Pressure Ratio - Model 5.

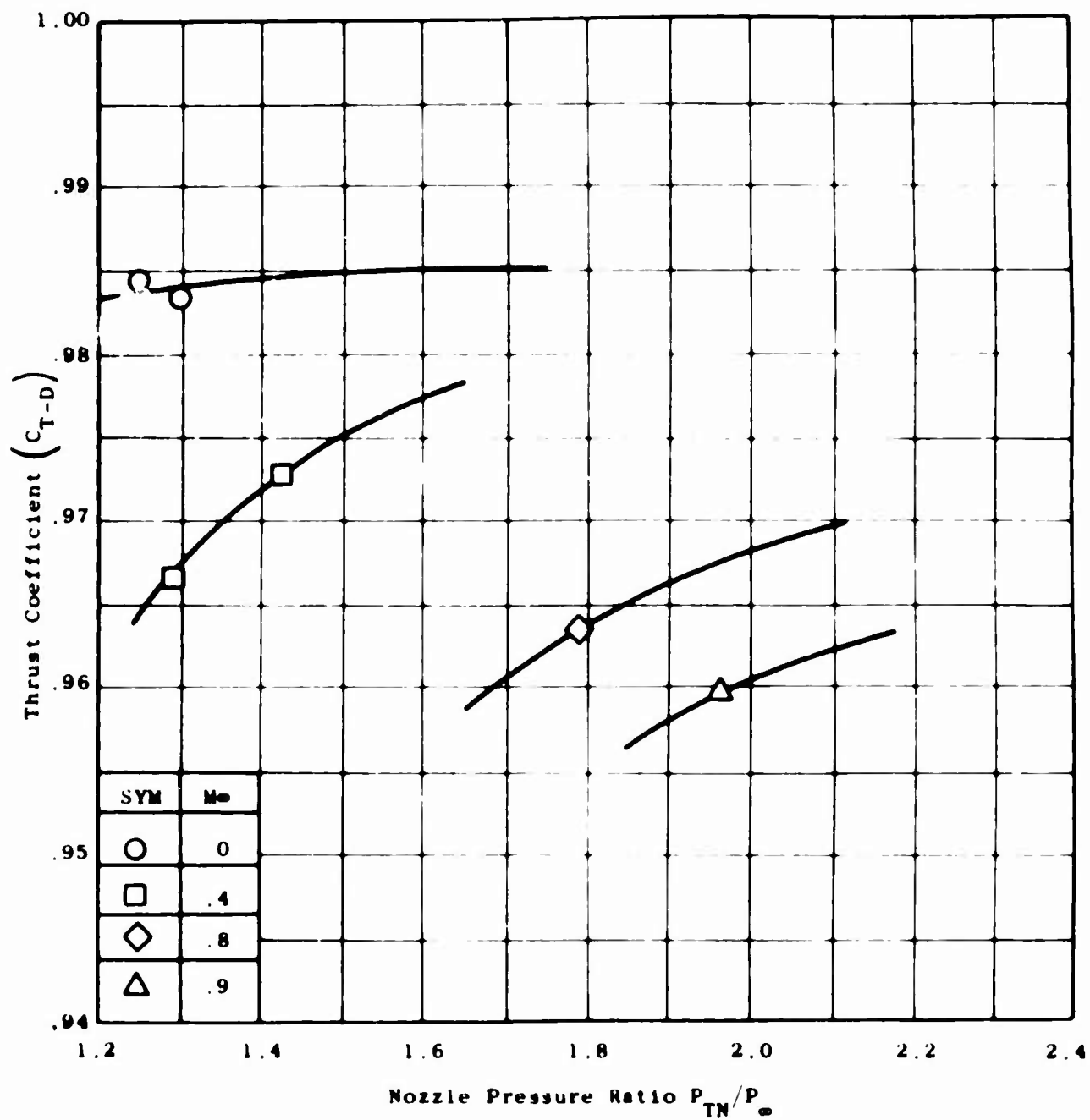


Figure 31. Exhaust System Performance as a Function of Mach No. and Pressure Ratio-Model 6.

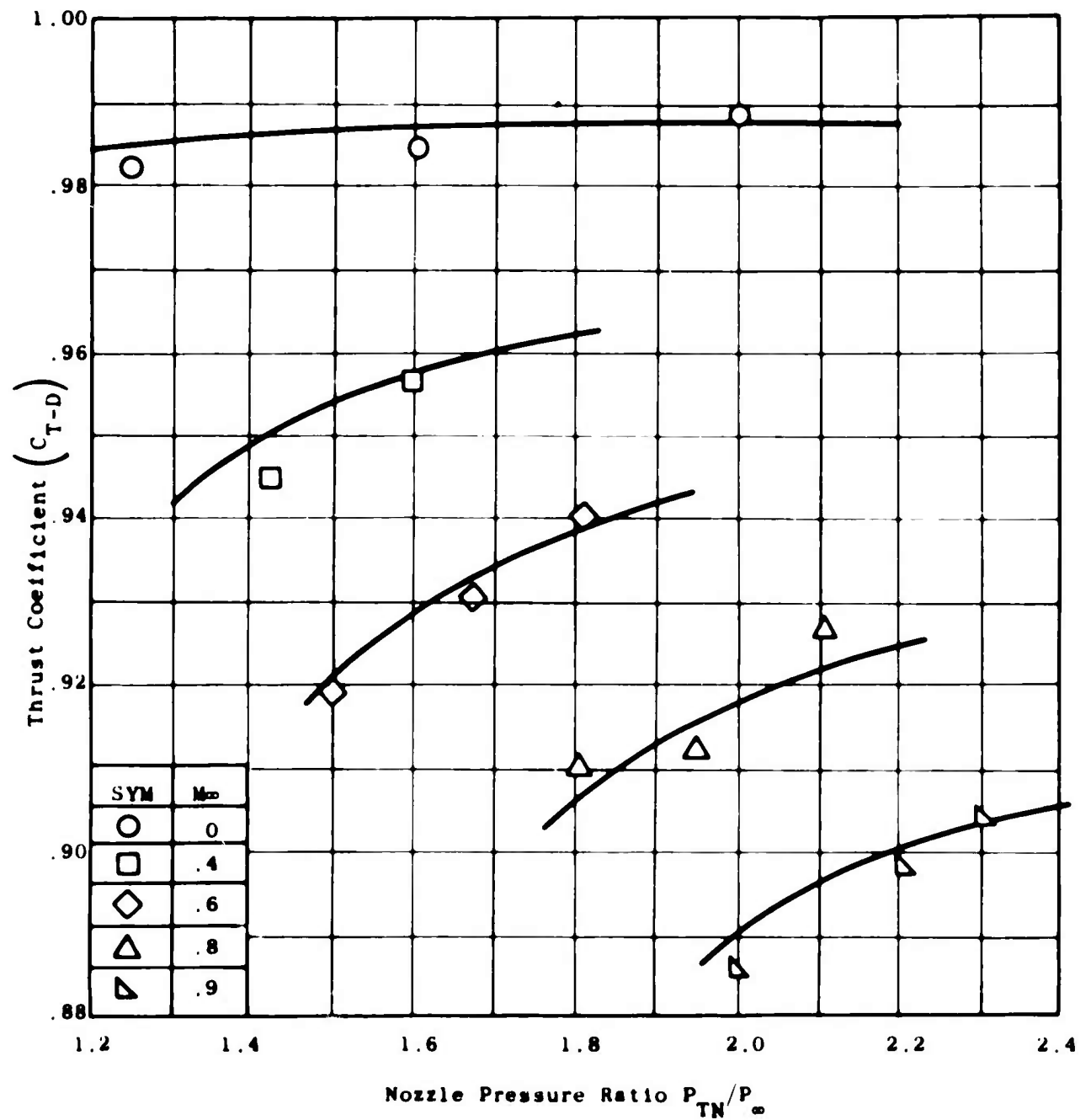


Figure 32. Exhaust System Performance as a Function of Mach No. and Pressure Ratio - Model 7.

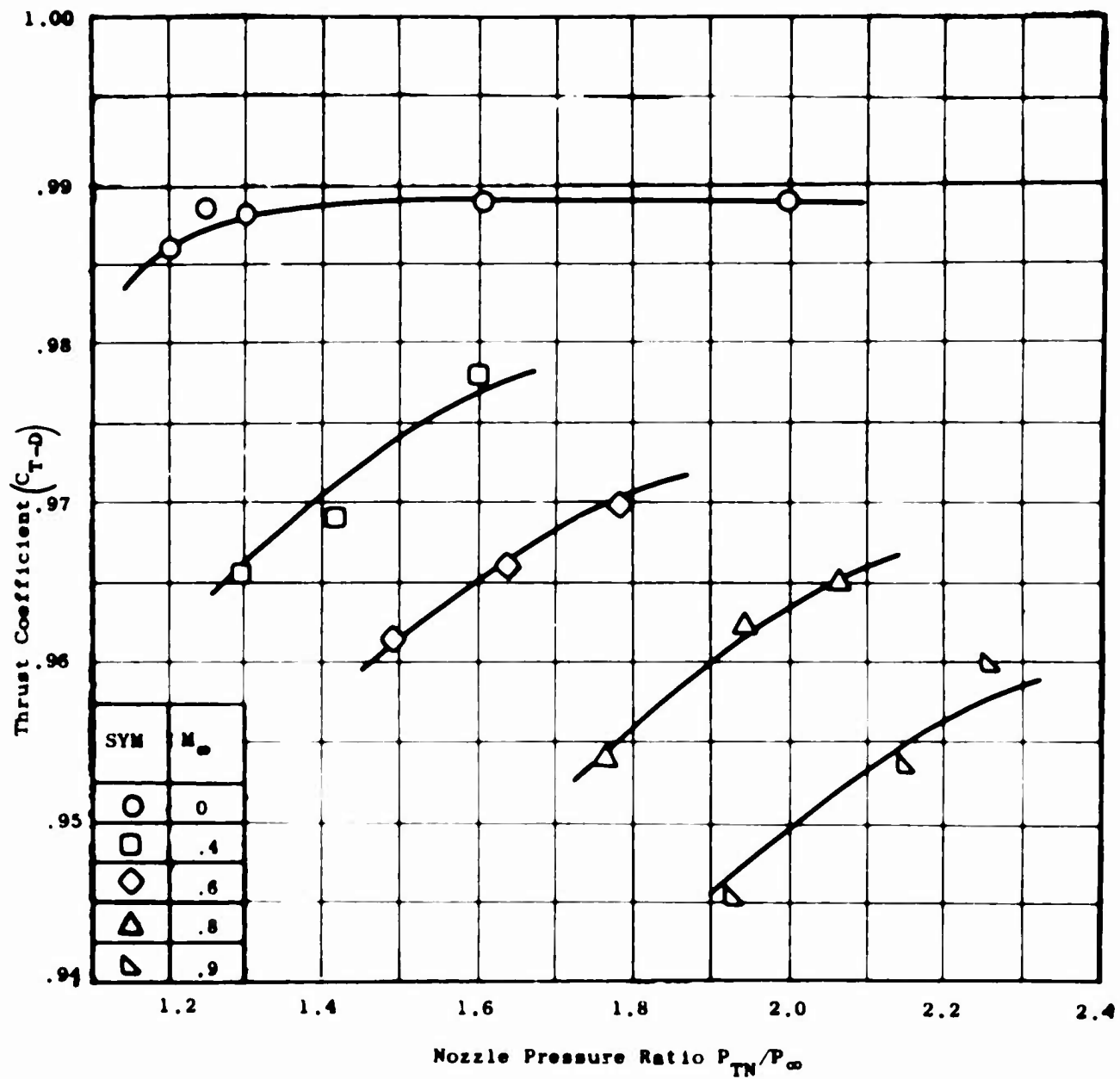


Figure 33. Exhaust System Performance as a Function of Mach No. and Pressure Ratio - Model 7A.

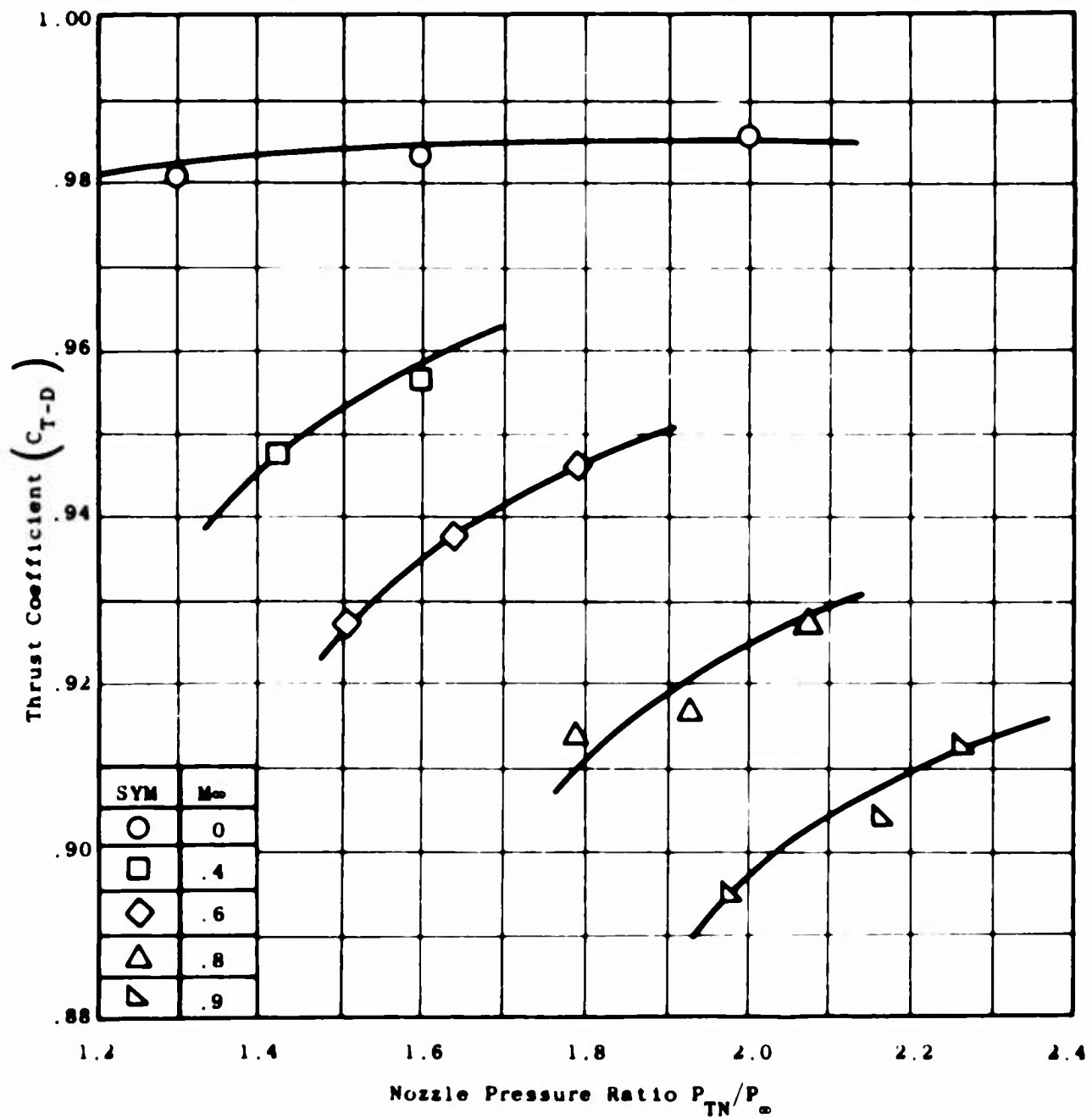


Figure 34. Exhaust System Performance as a Function of Mach No. and Pressure Ratio - Model 8.

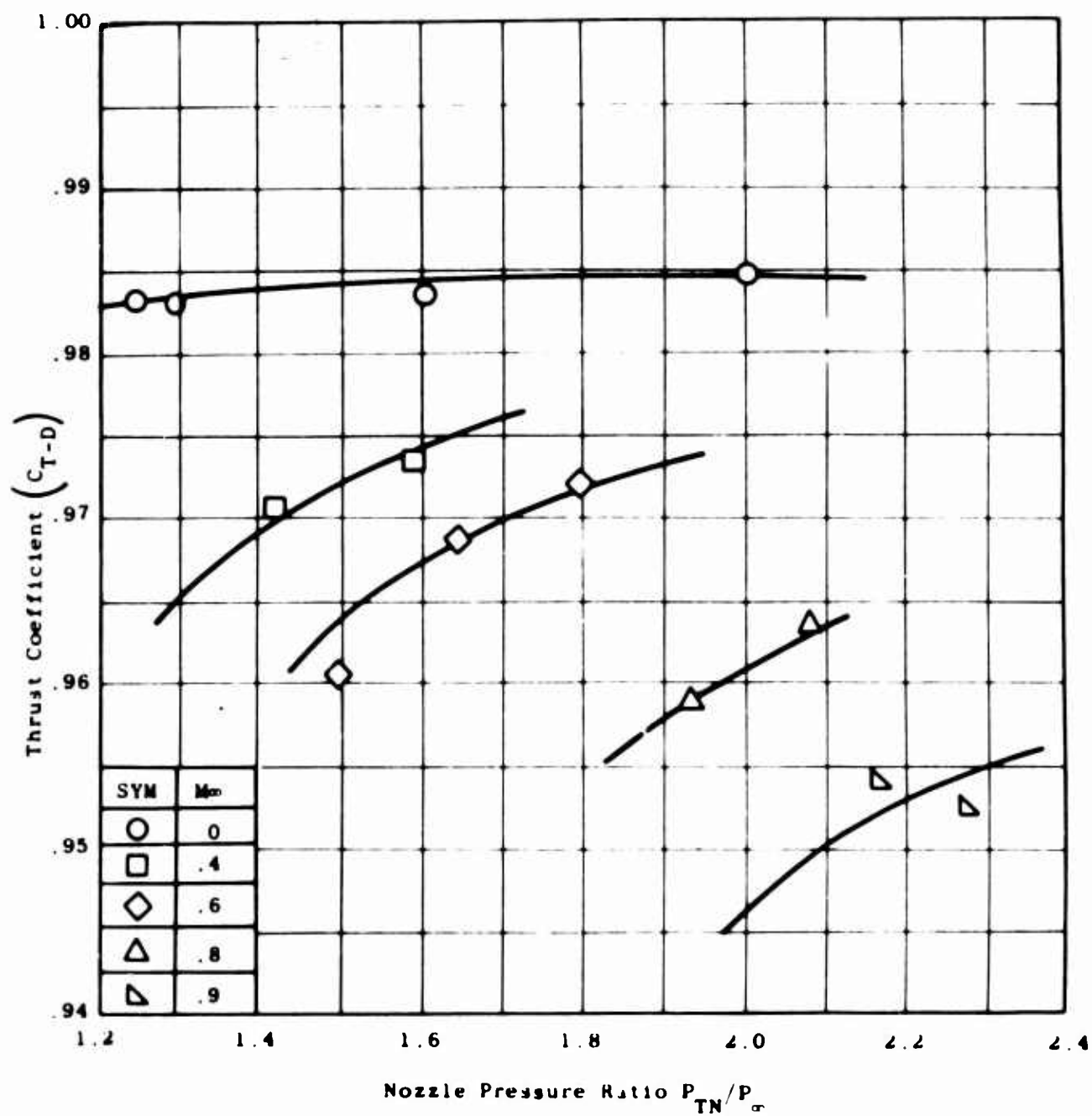


Figure 35. Exhaust System Performance
as a Function of Mach No.
and Pressure Ratio -
Model 9.

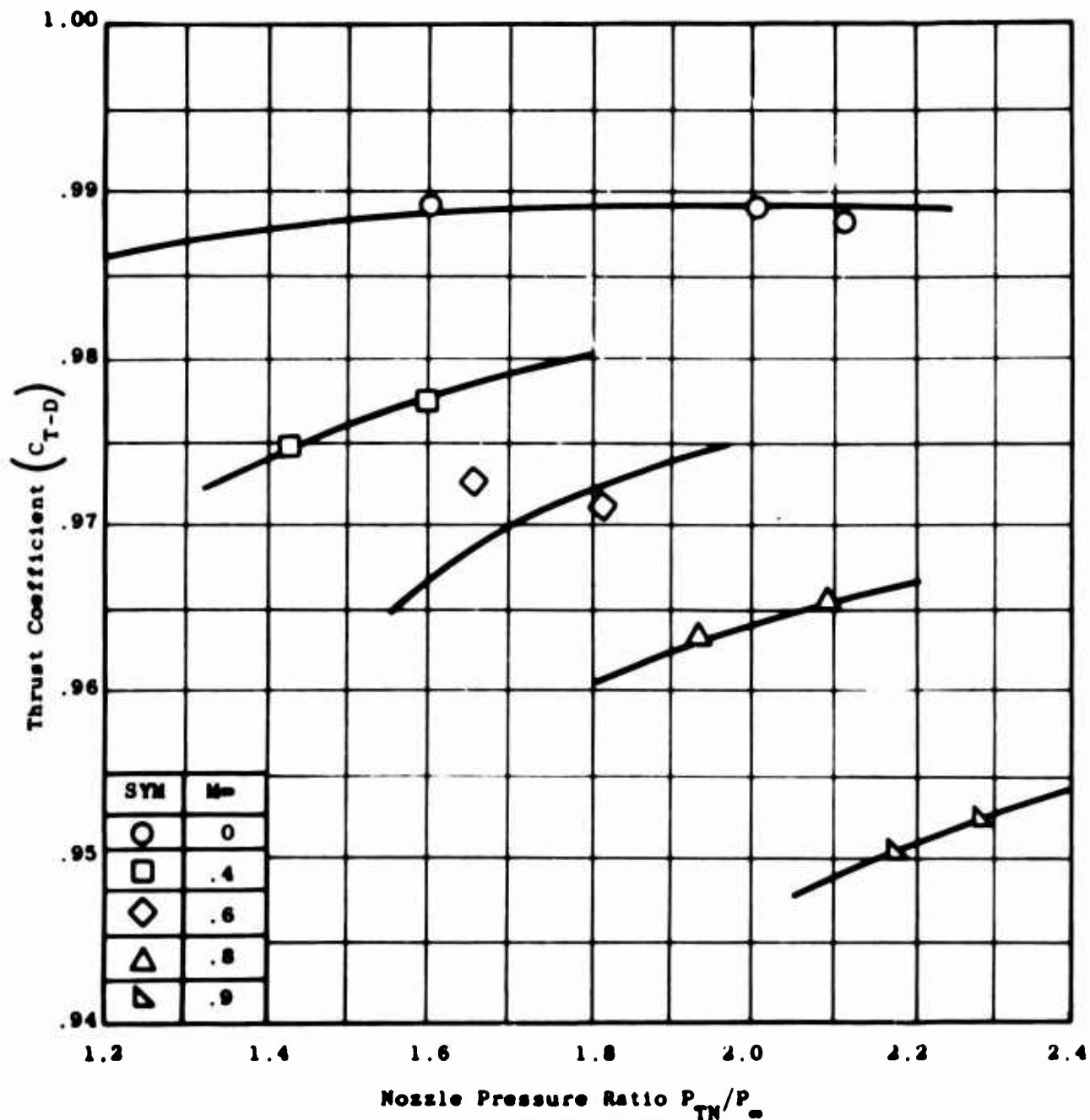


Figure 36. Exhaust System Performance as a Function of Mach No. and Pressure Ratio - Model 10.

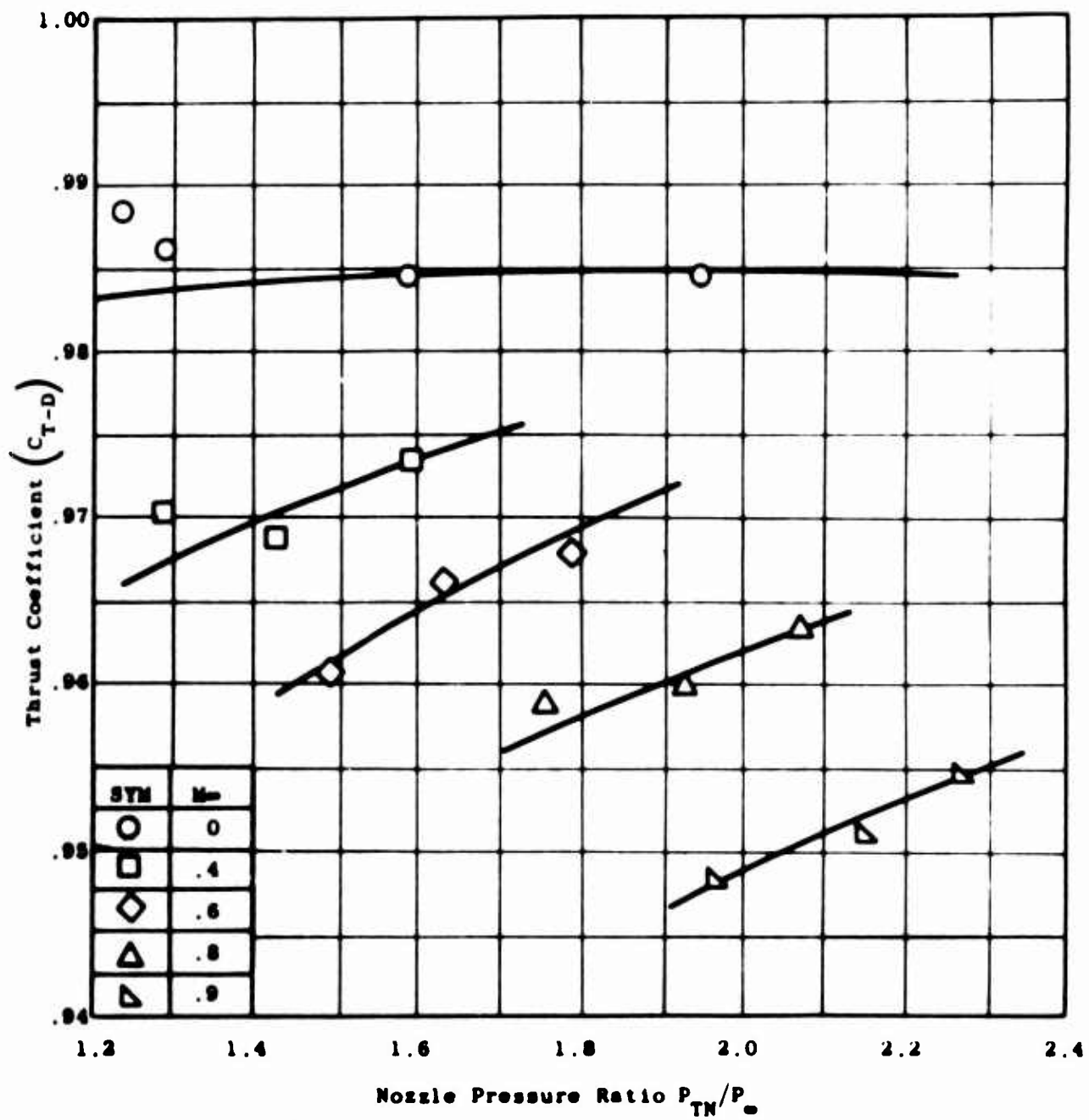


Figure 37. Exhaust System Performance as a Function of Mach No. and Pressure Ratio - Model 10A.

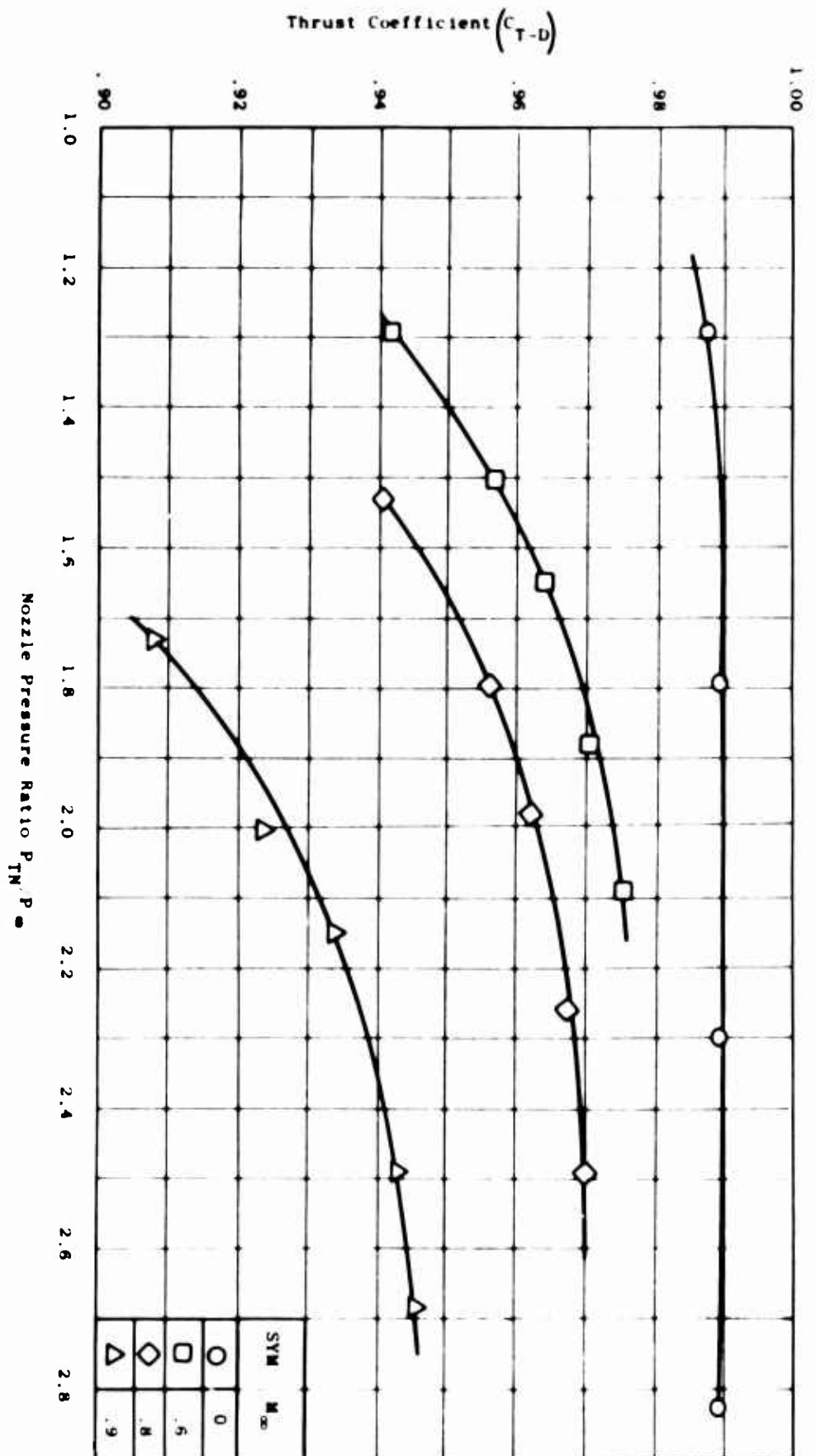


Figure 38. Exhaust System Performance as a Function of Mach No. and Pressure Ratio - Model 11.

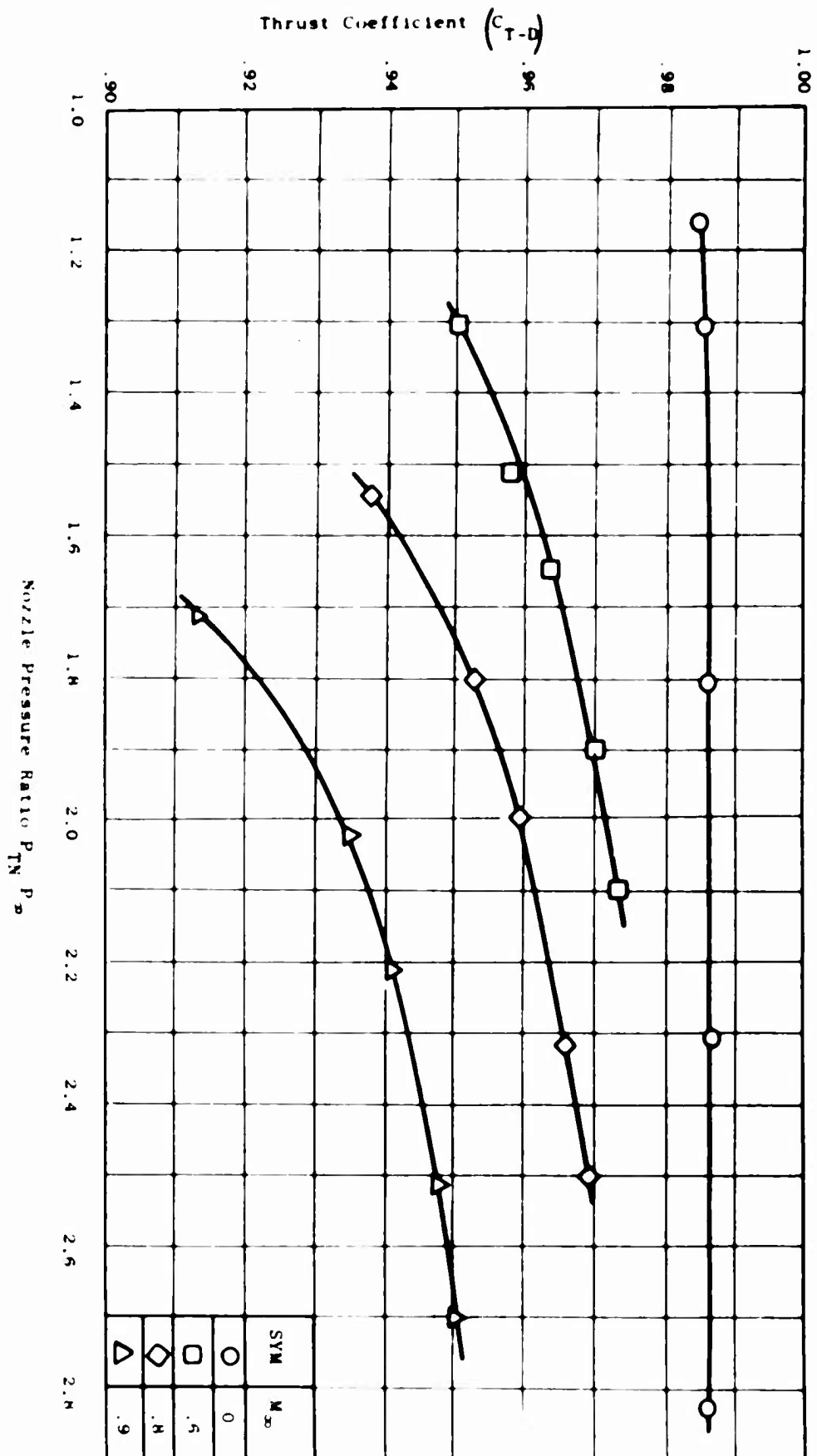


Figure 39. Exhaust System Performance as a Function of Mach No. and Pressure Ratio - Model 12.

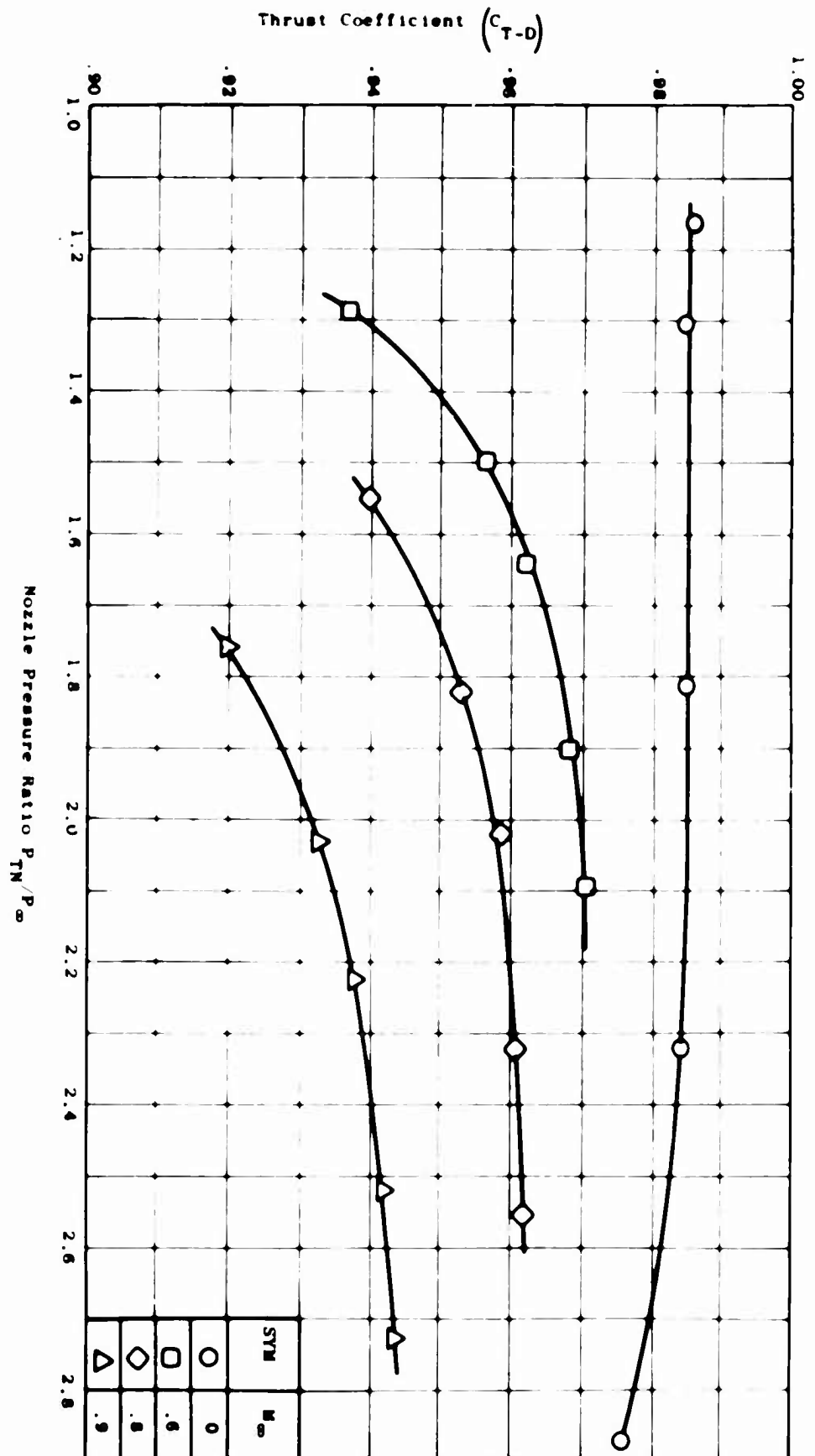


Figure 40. Exhaust System Performance
as a Function of Mach No.
and Pressure Ratio -
Model 13.

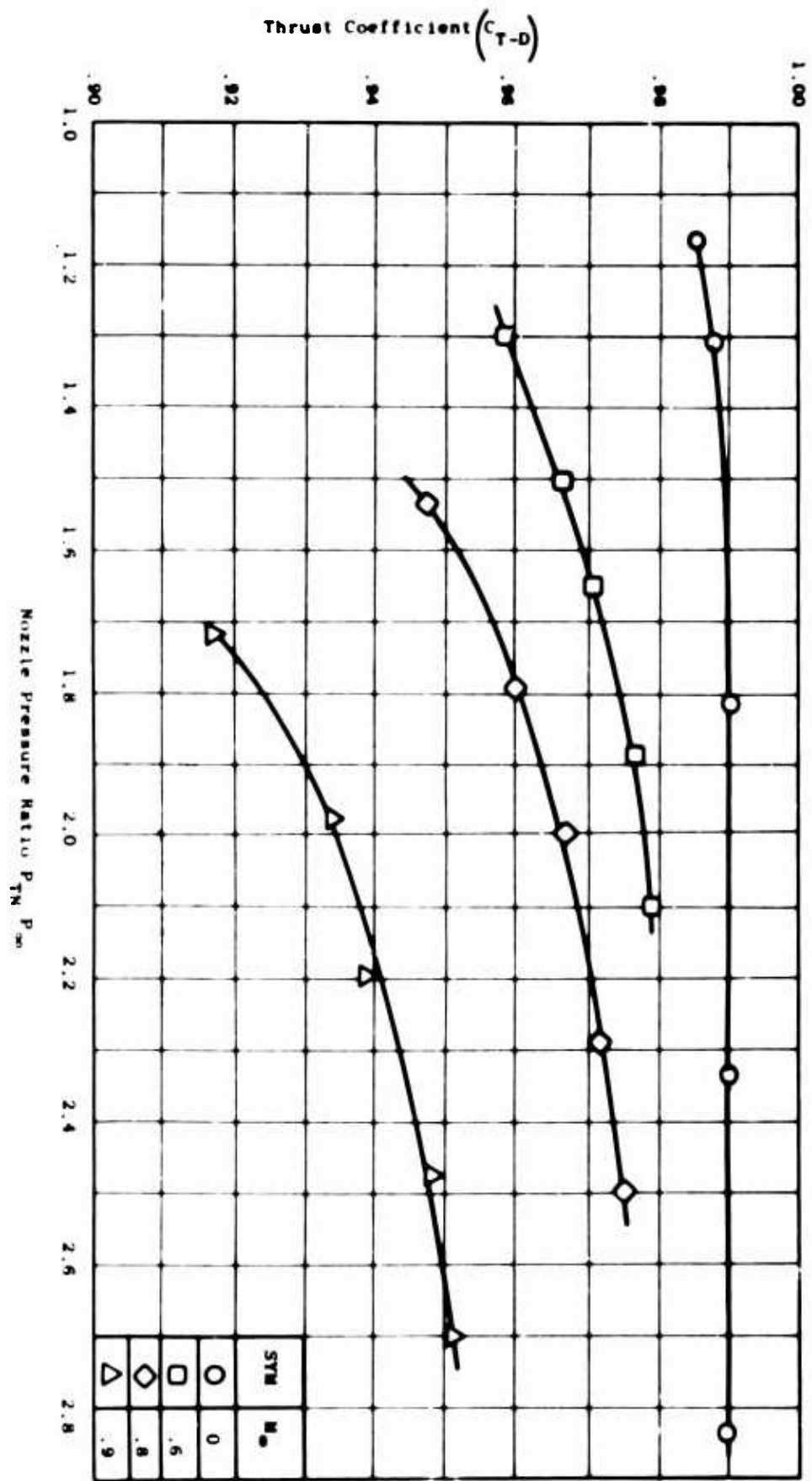


Figure 41. Exhaust System Performance as a Function of Mach No. and Pressure Ratio - Model 14.

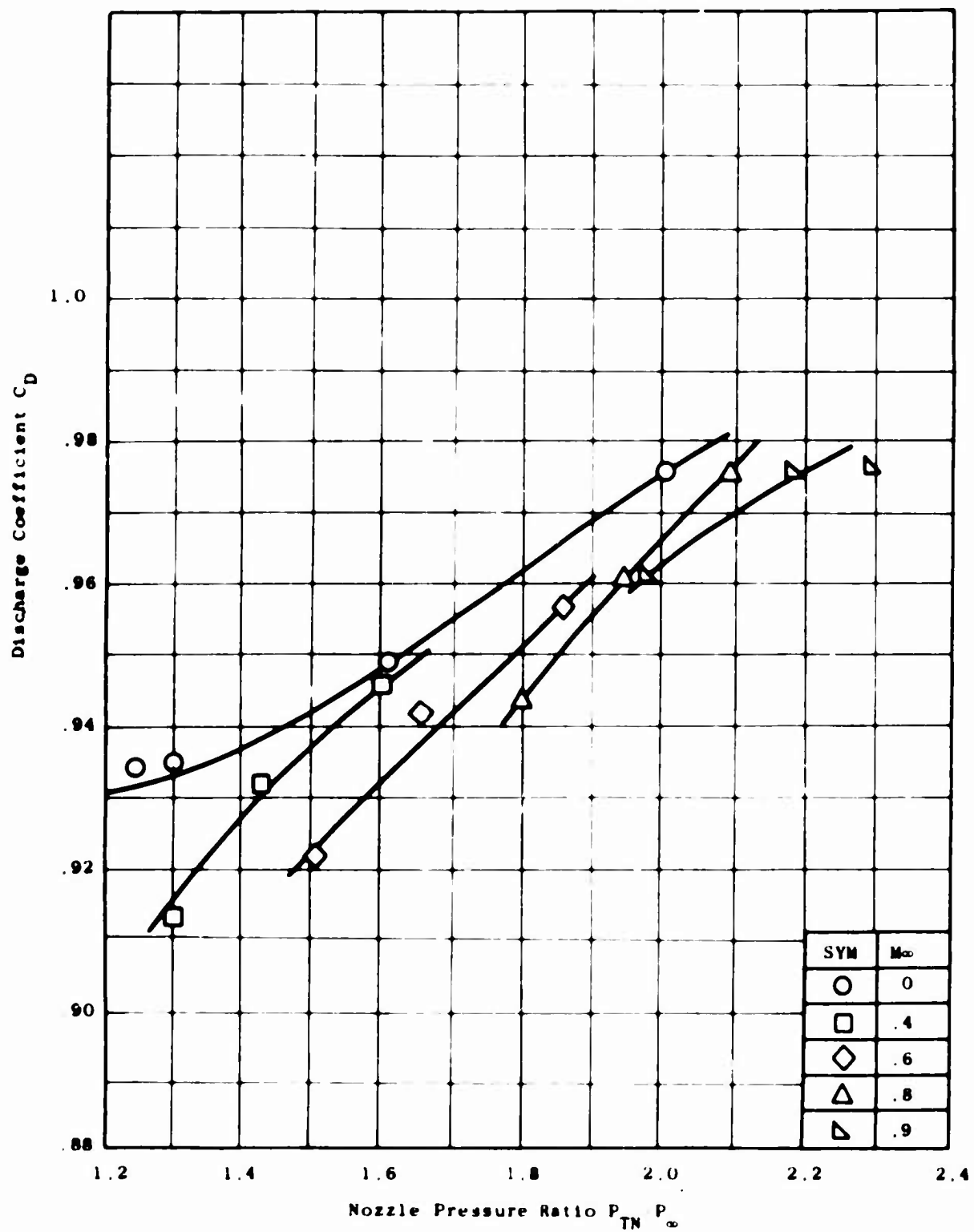


Figure 42. Discharge Coefficient Versus Mach Number and Pressure Ratio - Model 1.

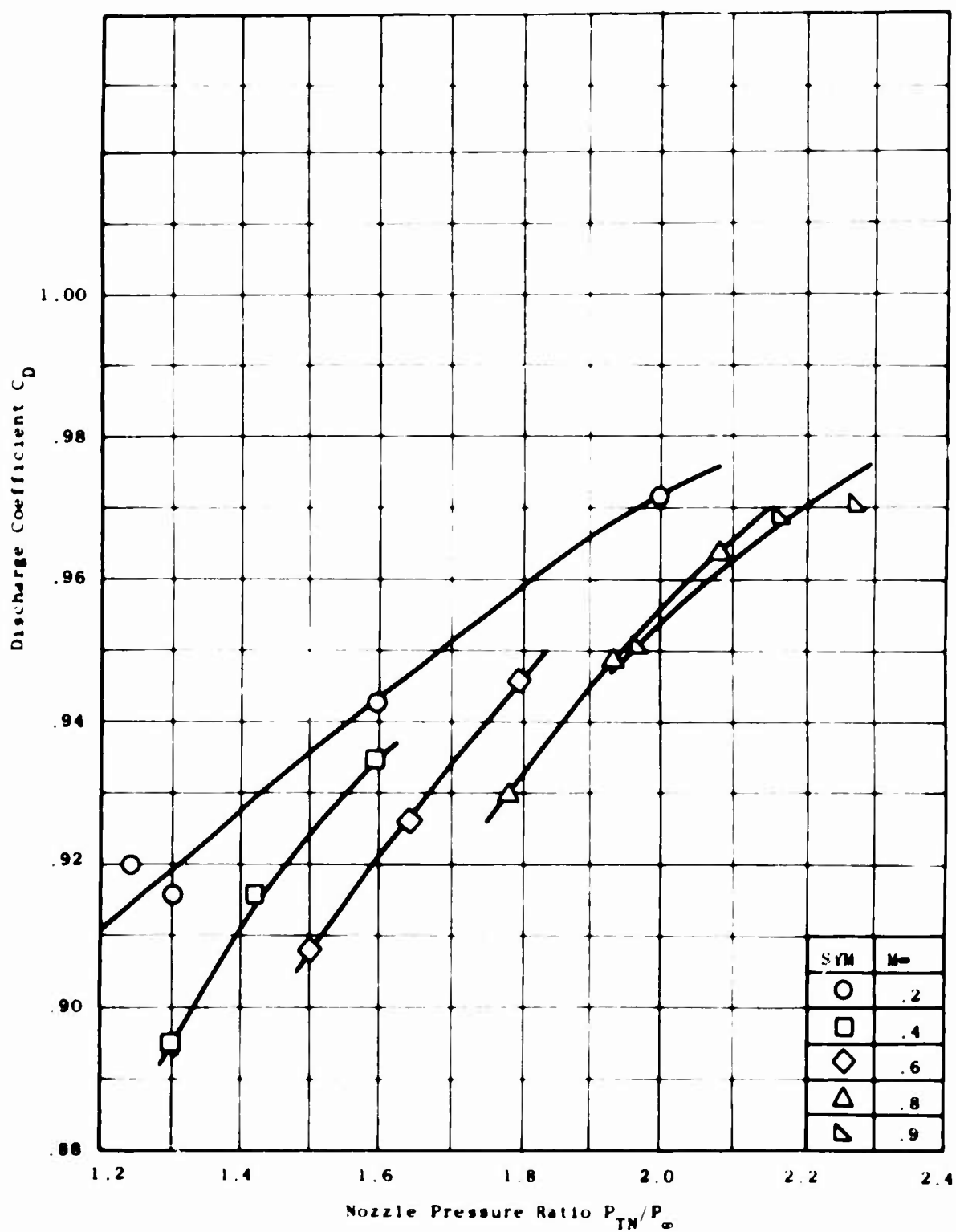


Figure 43. Discharge Coefficient Versus Mach Number and Pressure Ratio - Model 2.

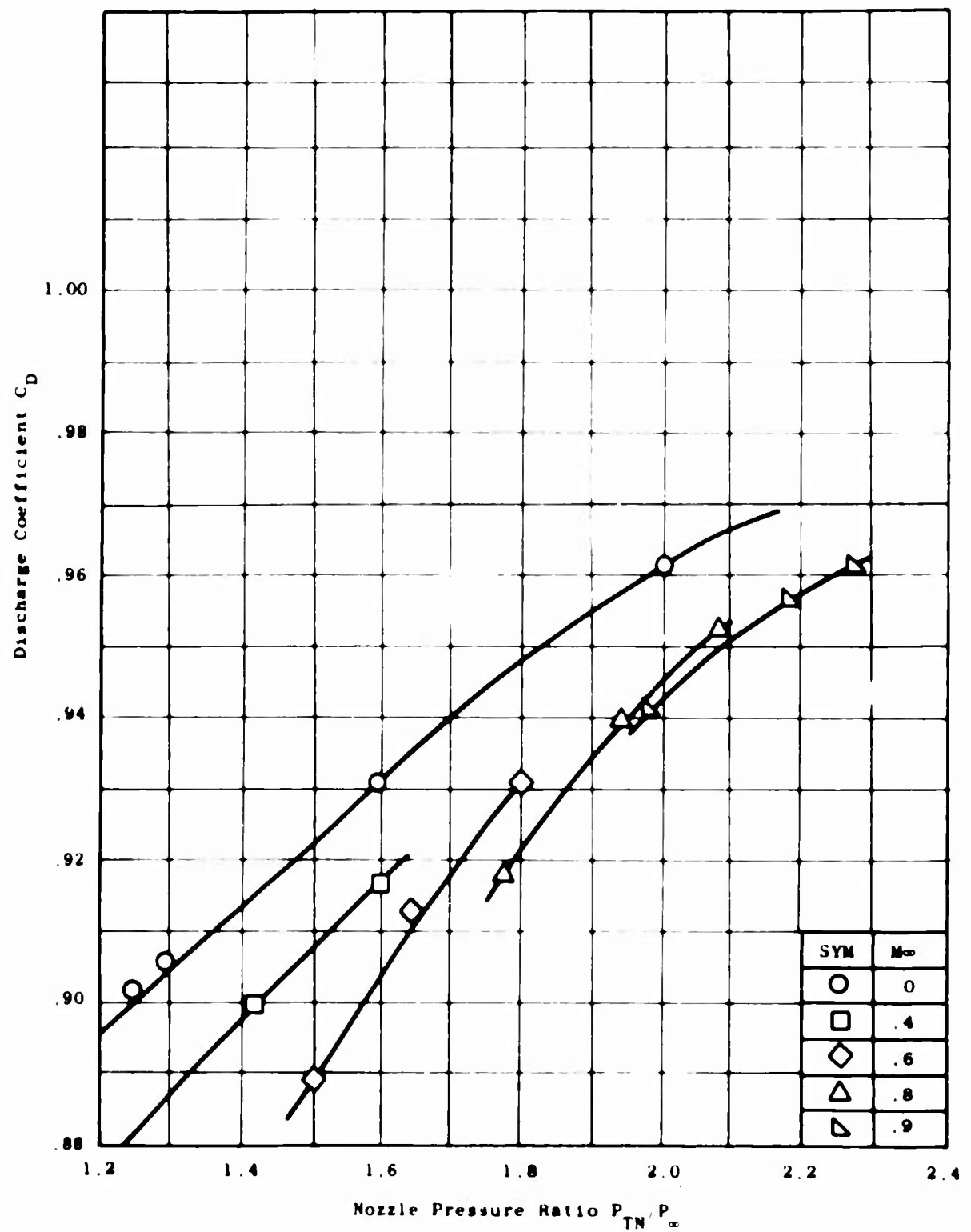


Figure 44. Discharge Coefficient Versus Mach Number and Pressure Ratio - Model 3.

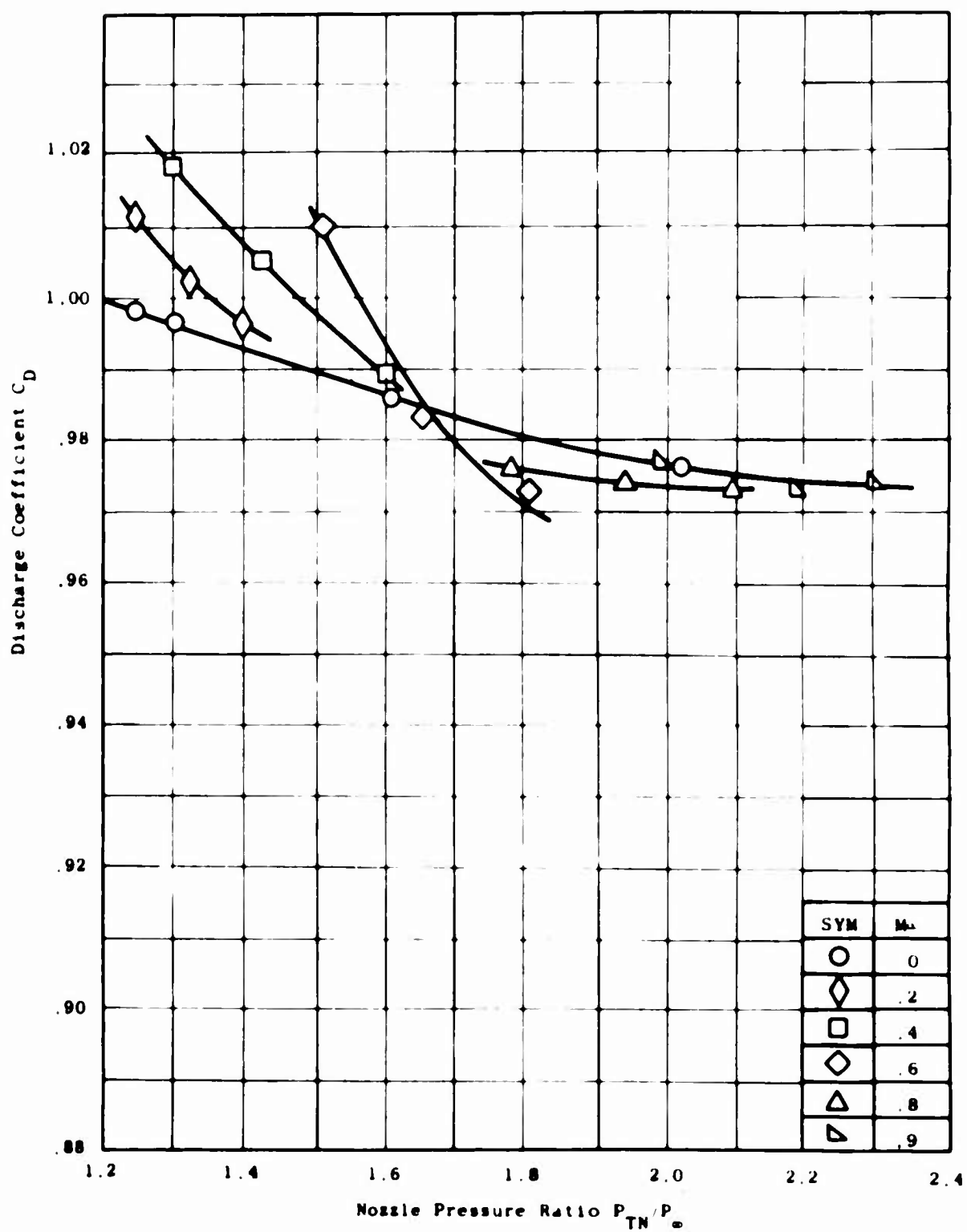


Figure 45. Discharge Coefficient Versus Mach Number and Pressure Ratio - Model 4.

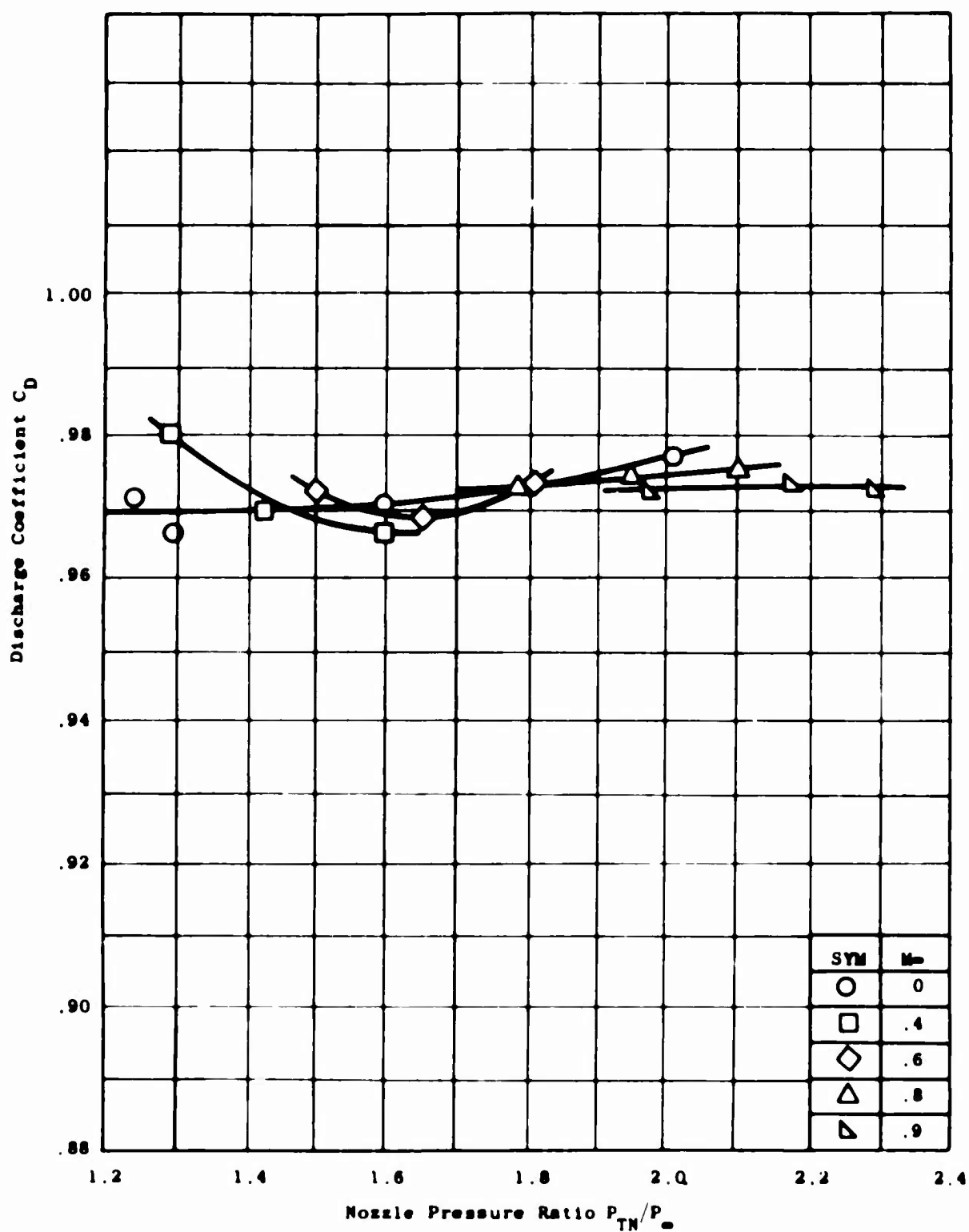


Figure 46. Discharge Coefficient Versus Mach Number and Pressure Ratio - Model 5.

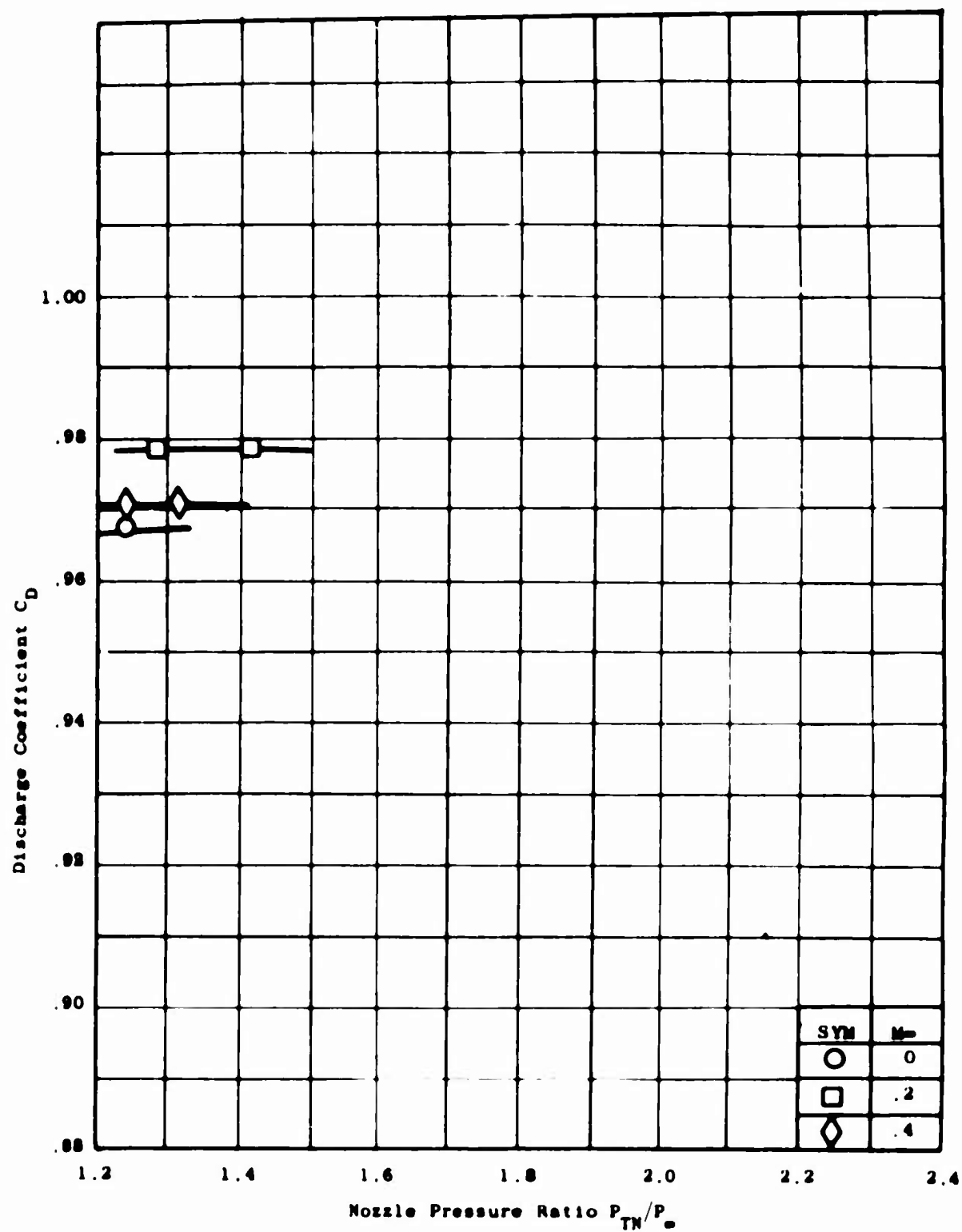


Figure 47. Discharge Coefficient Versus Mach Number and Pressure Ratio - Model 6.



Figure 48. Discharge Coefficient Versus Mach Number and Pressure Ratio - Model 7.

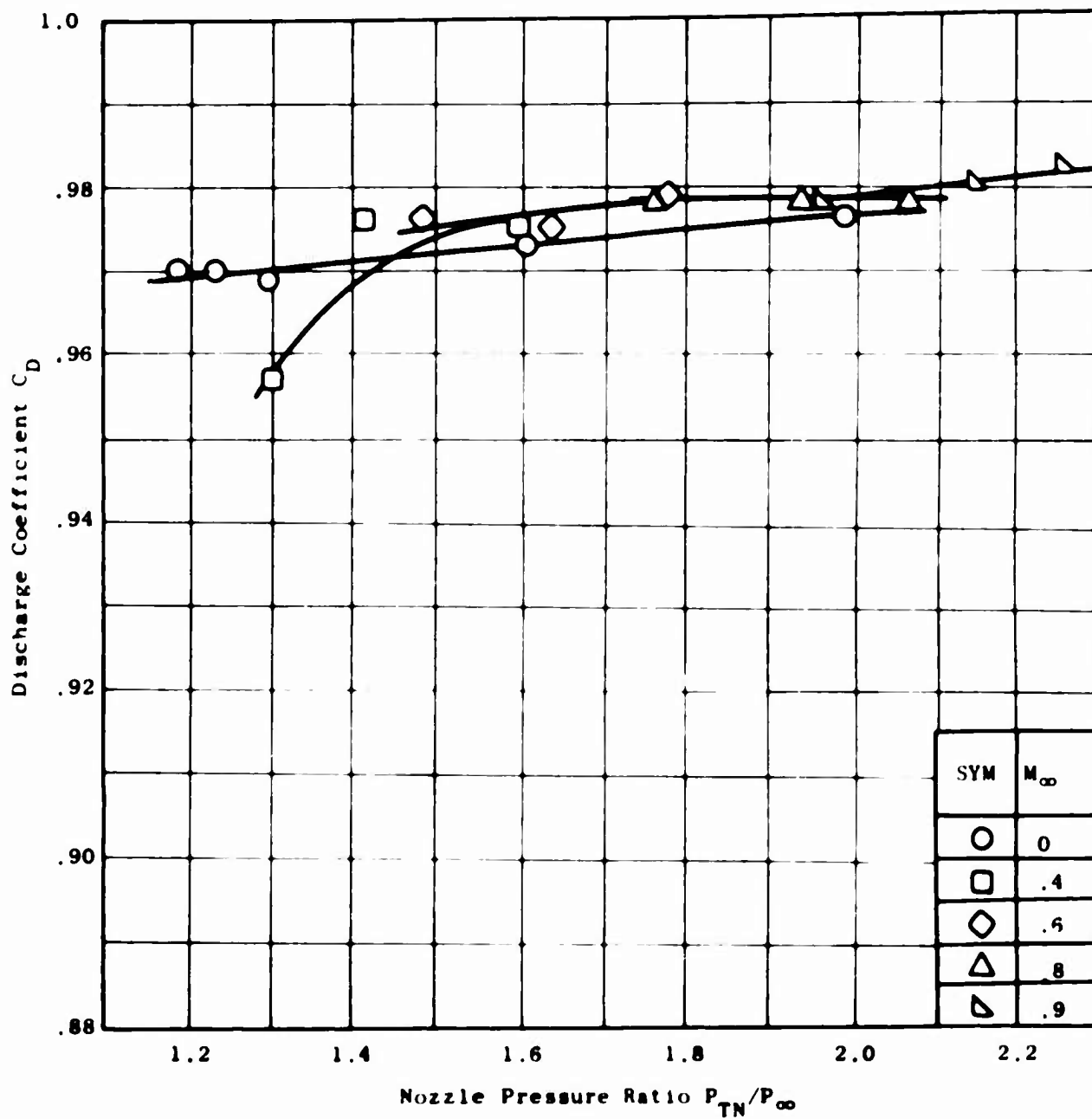


Figure 49. Discharge Coefficient Versus Mach Number and Pressure Ratio - Model 7A.

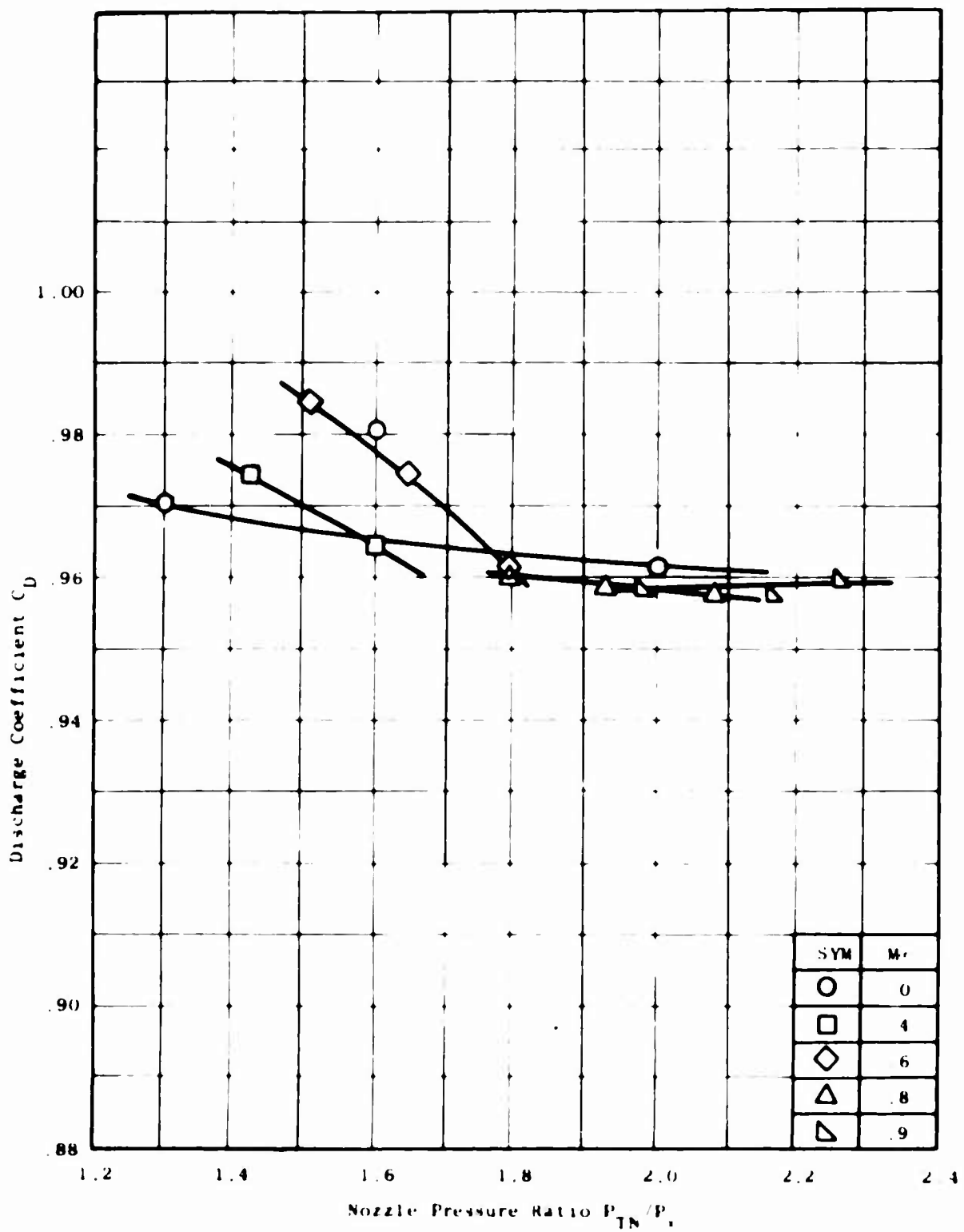


Figure 50. Discharge Coefficient Versus Mach Number and Pressure Ratio - Model 8.

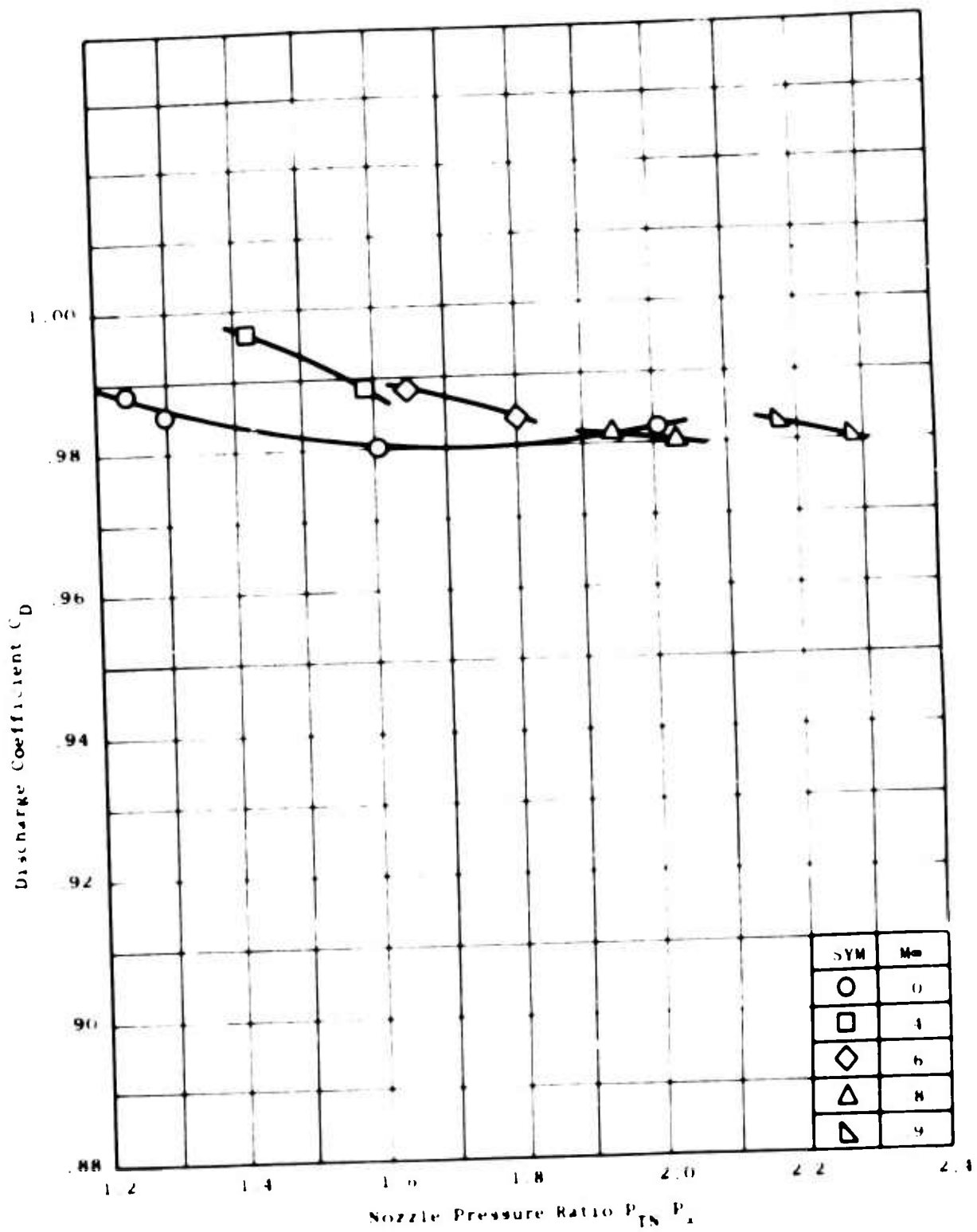


Figure 51. Discharge Coefficient Versus Mach Number and Pressure Ratio - Model 9.



Figure 52. Discharge Coefficient Versus Mach Number and Pressure Ratio- Model 10.

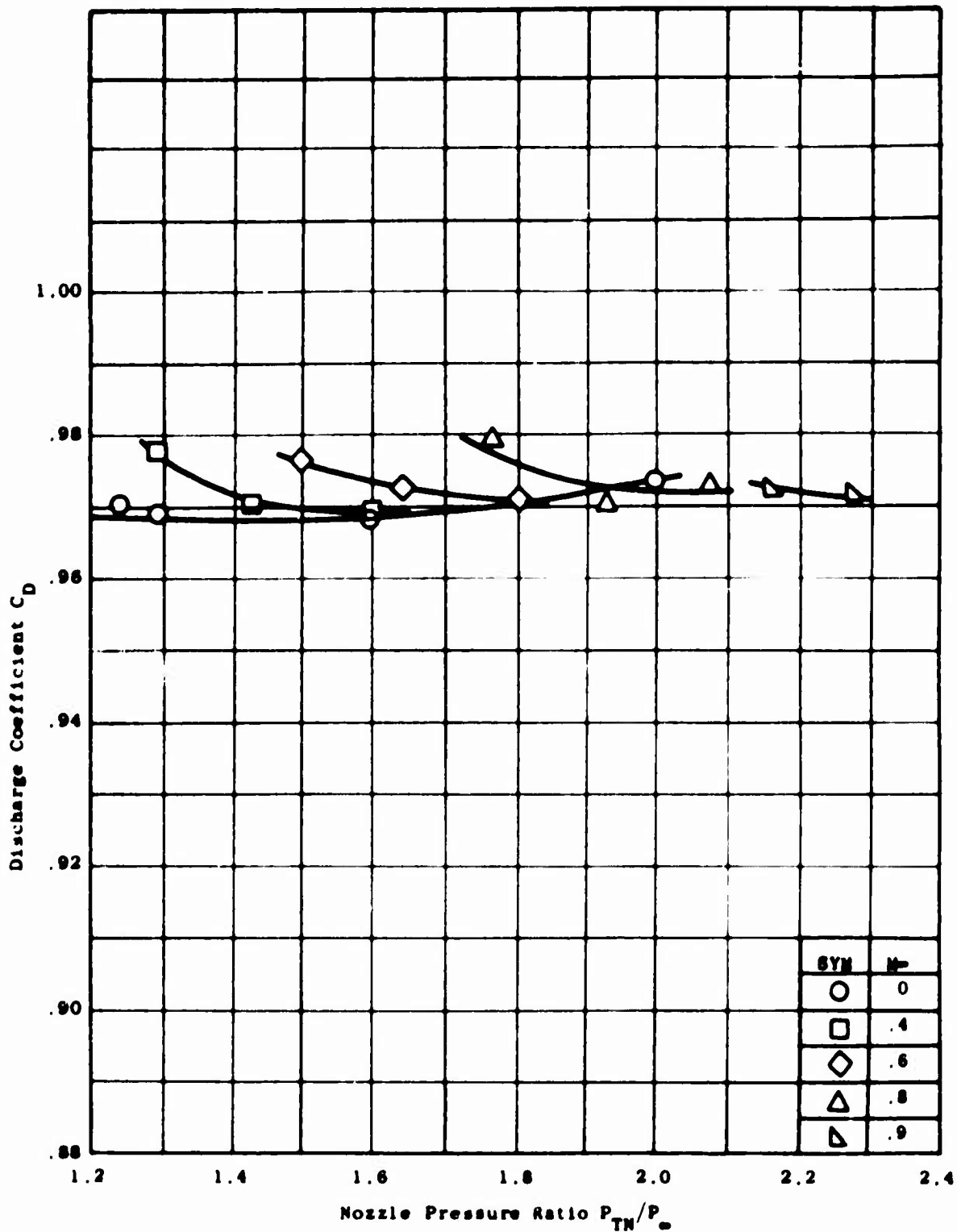


Figure 53. Discharge Coefficient Versus Mach Number and Pressure Ratio - Model 10A.

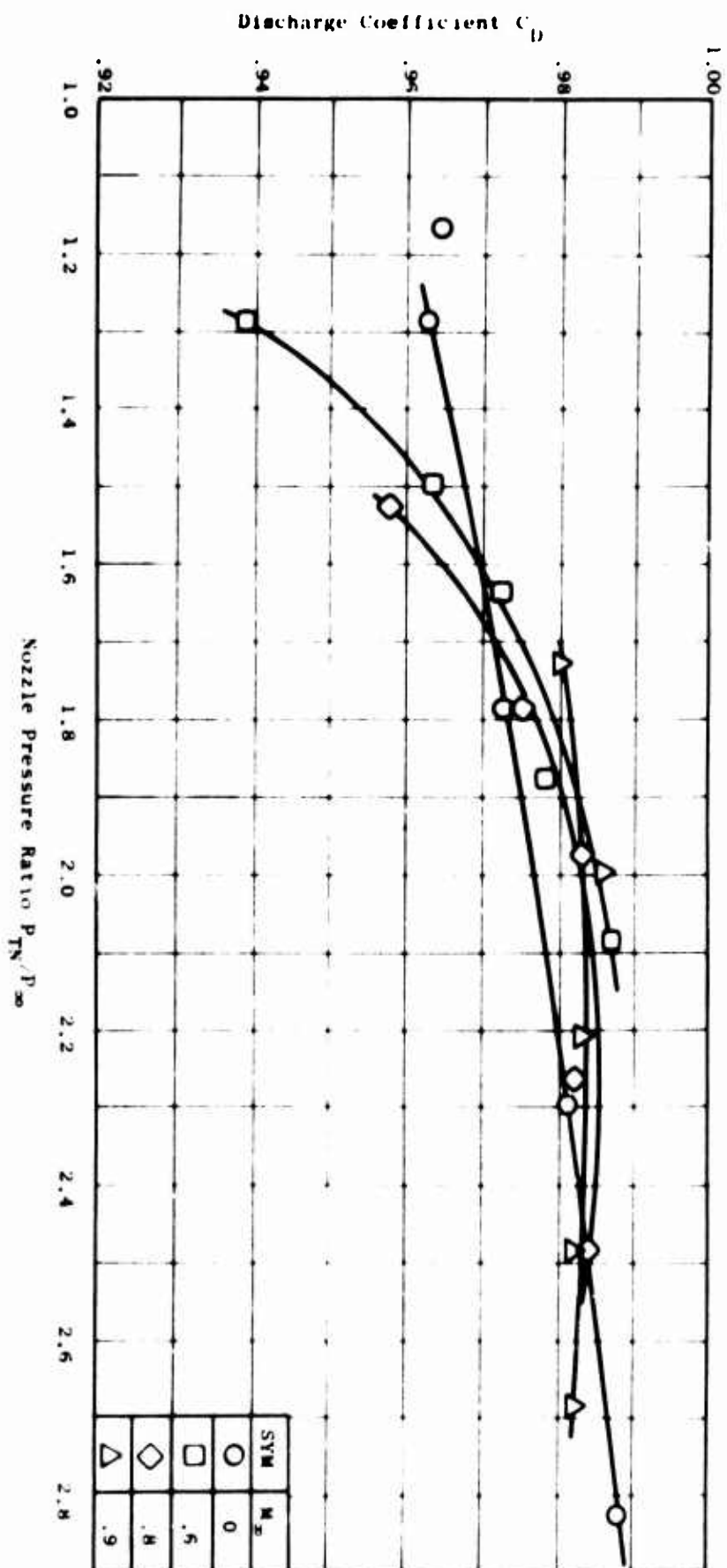


Figure 54. Discharge Coefficient Versus
Mach Number and Pressure
Ratio - Model 11.

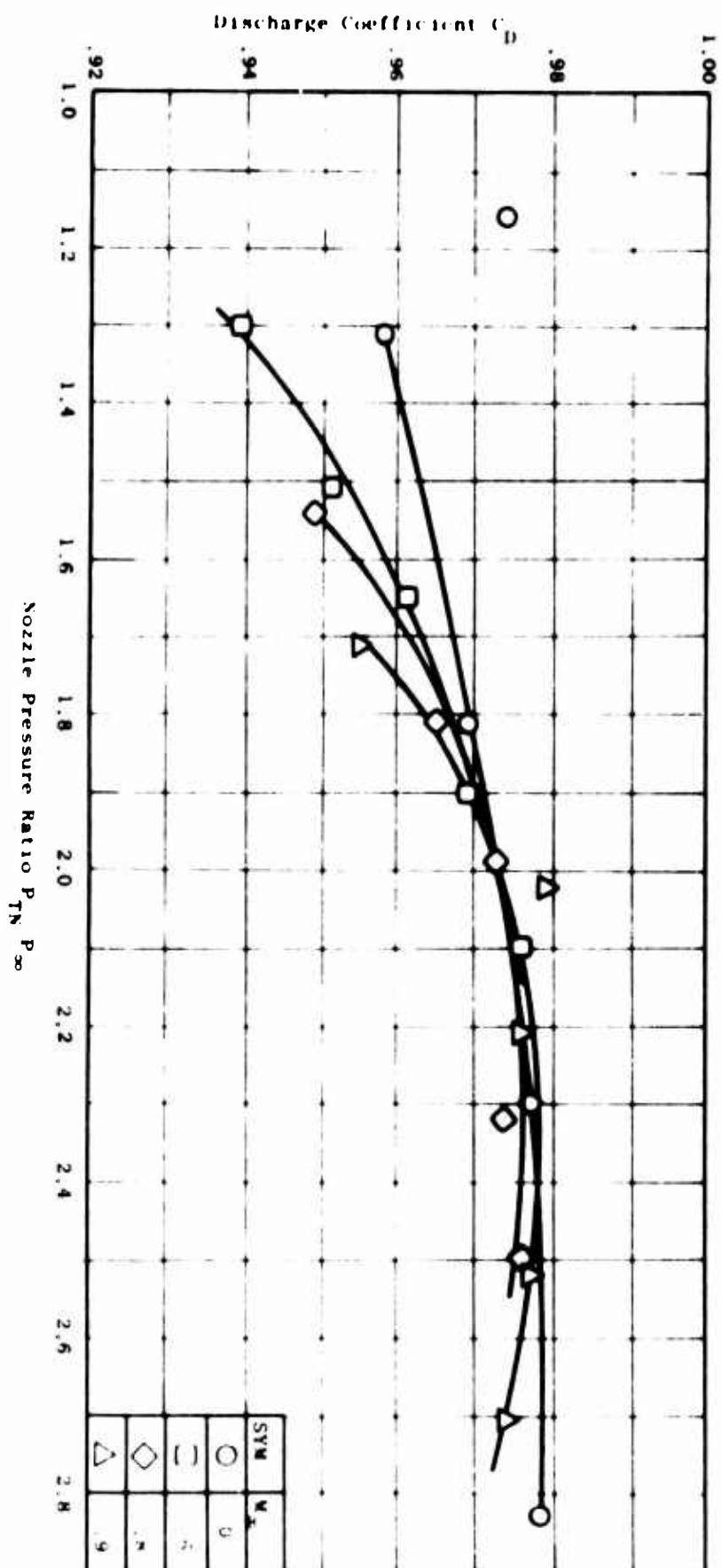


Figure 55. Discharge Coefficient Versus
Mach Number and Pressure
Ratio - Model 12.

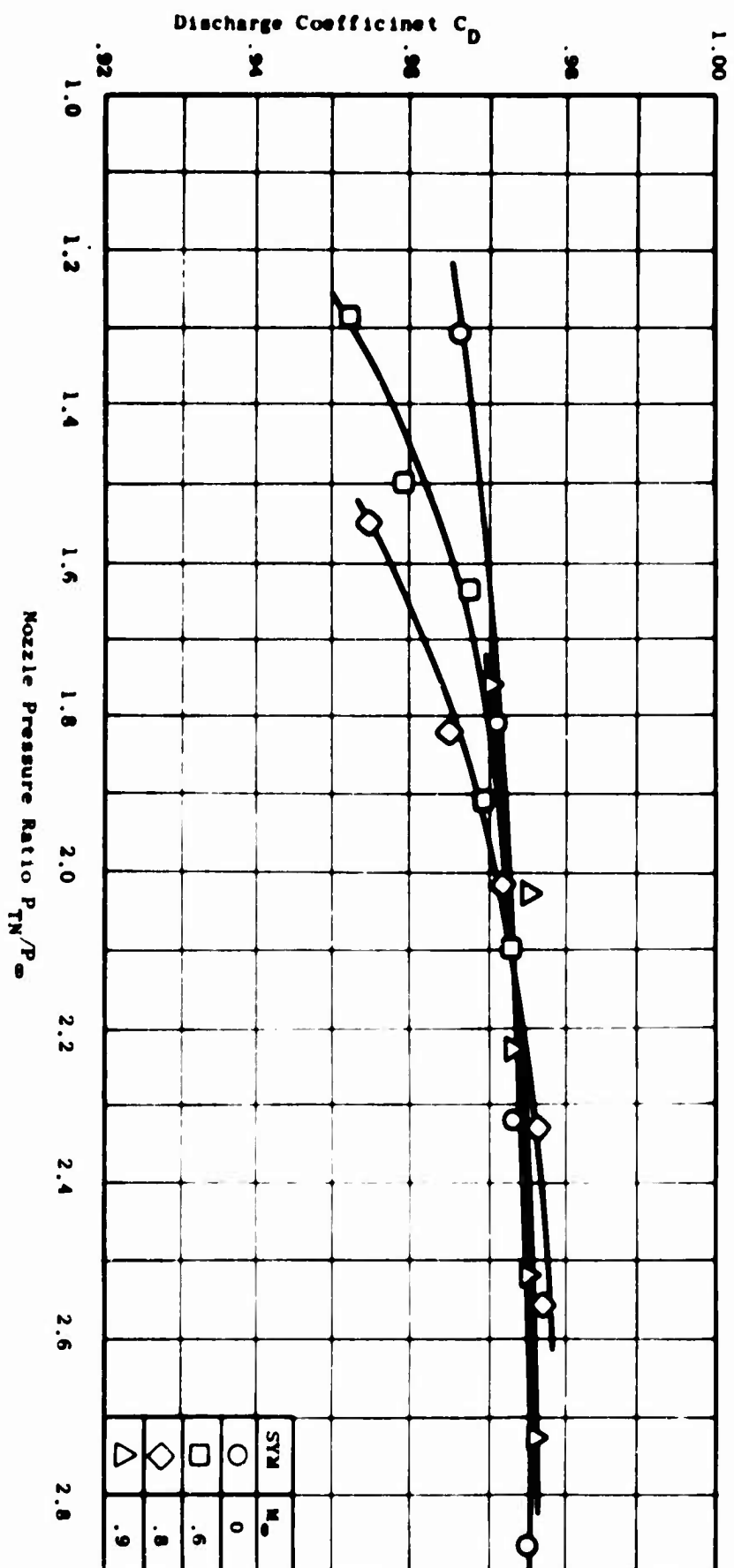


Figure 56. Discharge Coefficient Versus
Mach Number and Pressure
Ratio - Model 13.

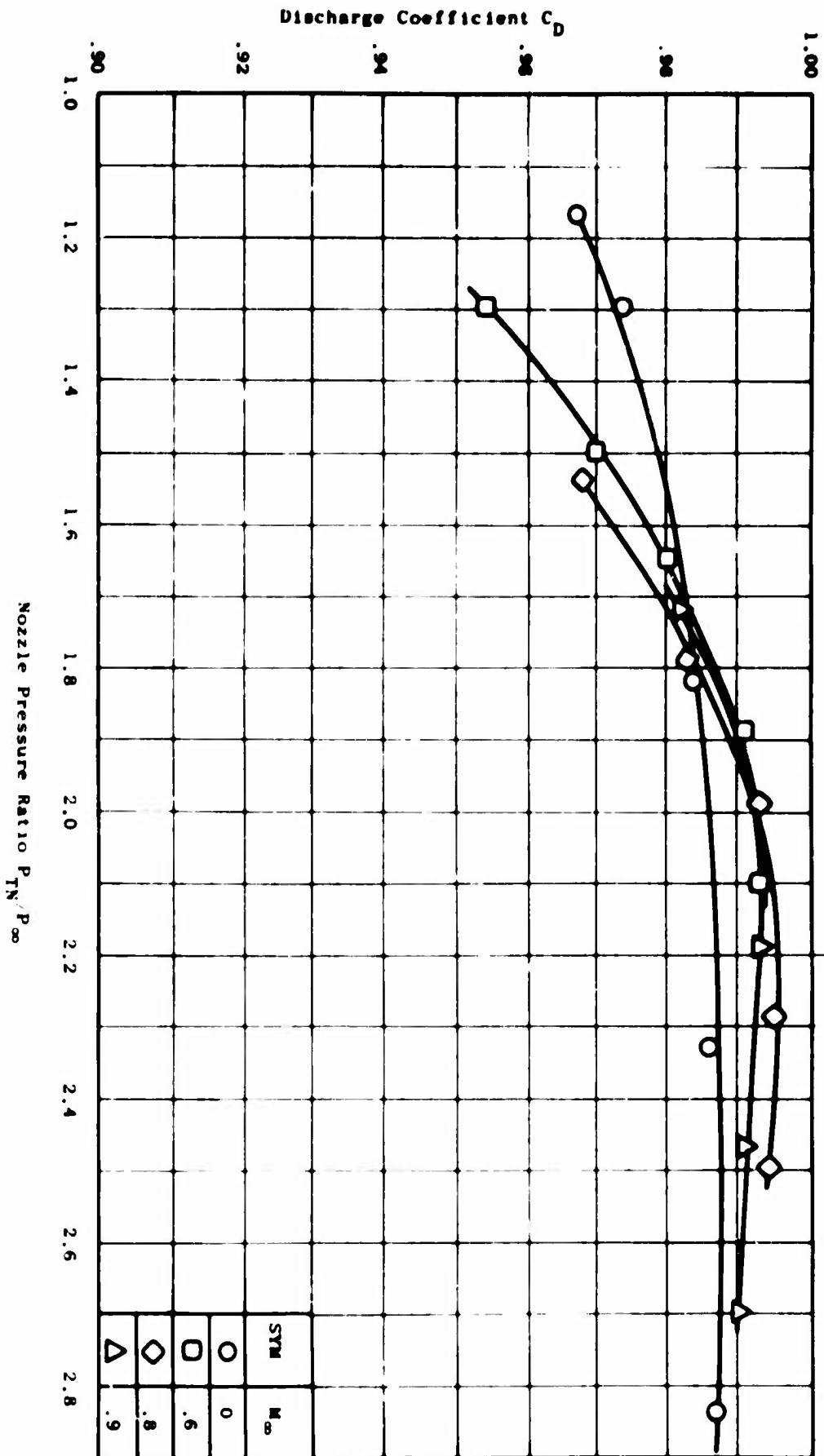


Figure 57. Discharge Coefficient Versus
Mach Number and Pressure
Ratio - Model 14.

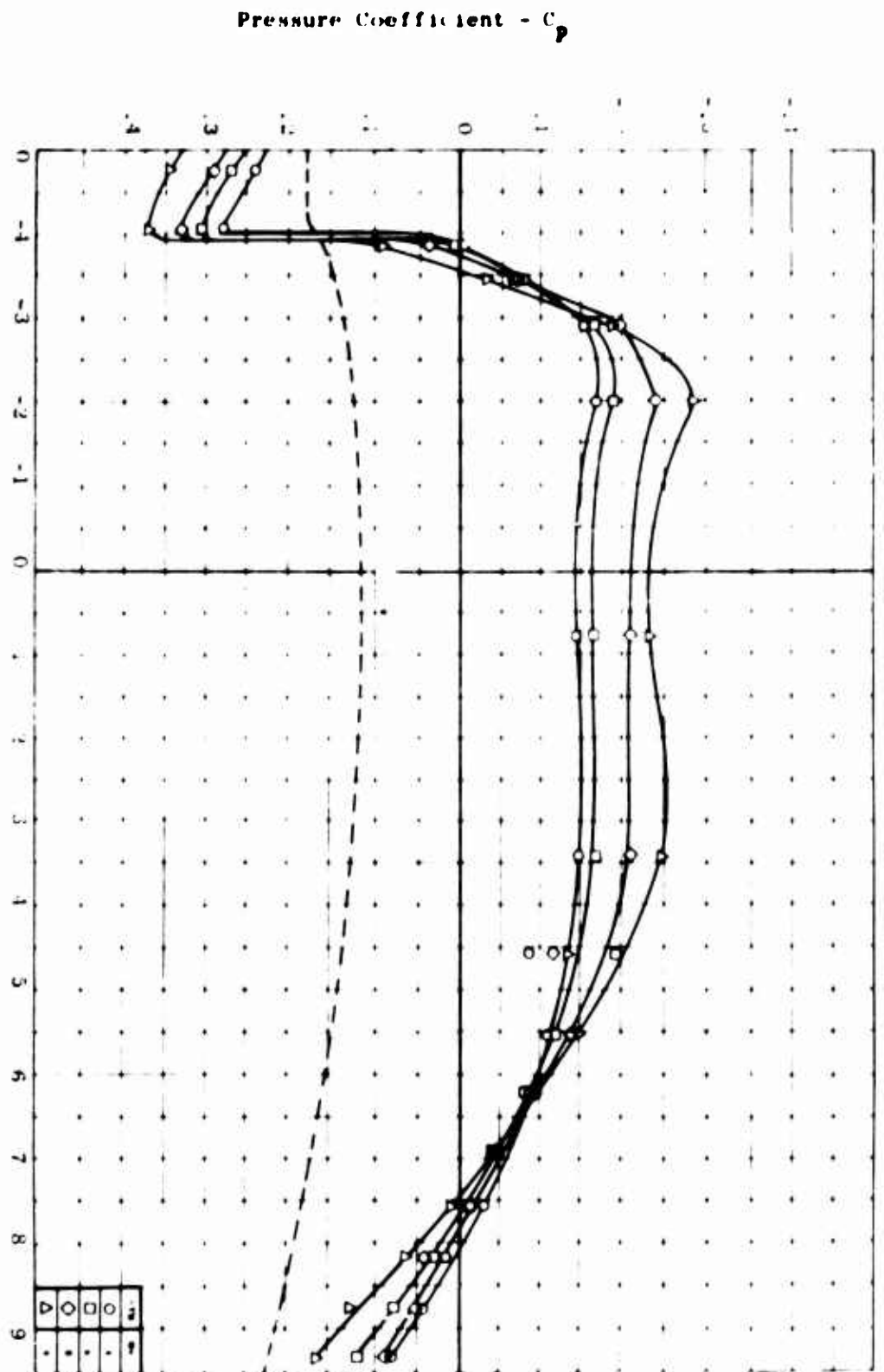


Figure 58. External Pressure Distribution
as a Function of Axial Distance
and Mach No. - Model 1.

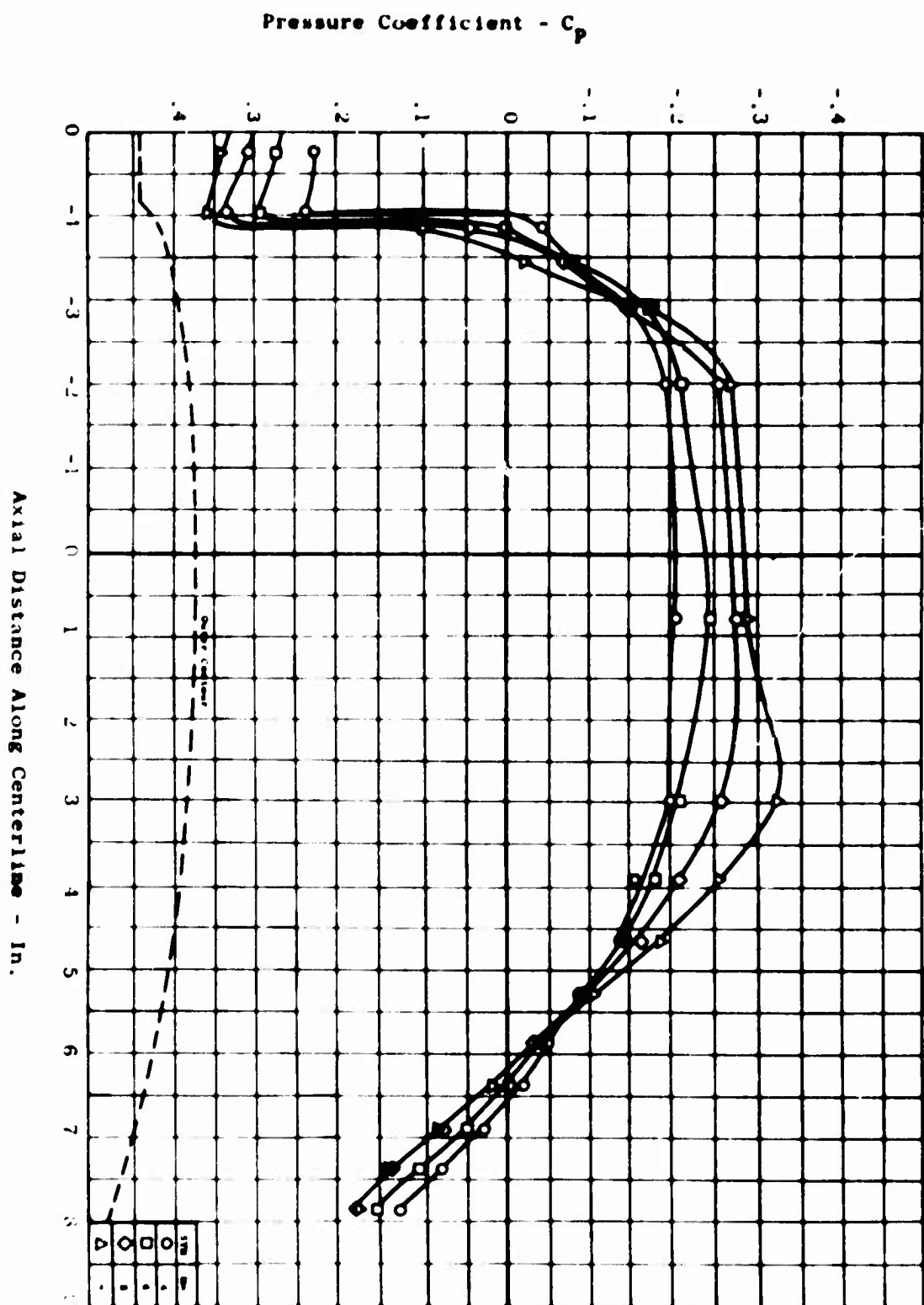


Figure 59. External Pressure Distribution
as a Function of Axial Distance
and Mach No. - Model 2.

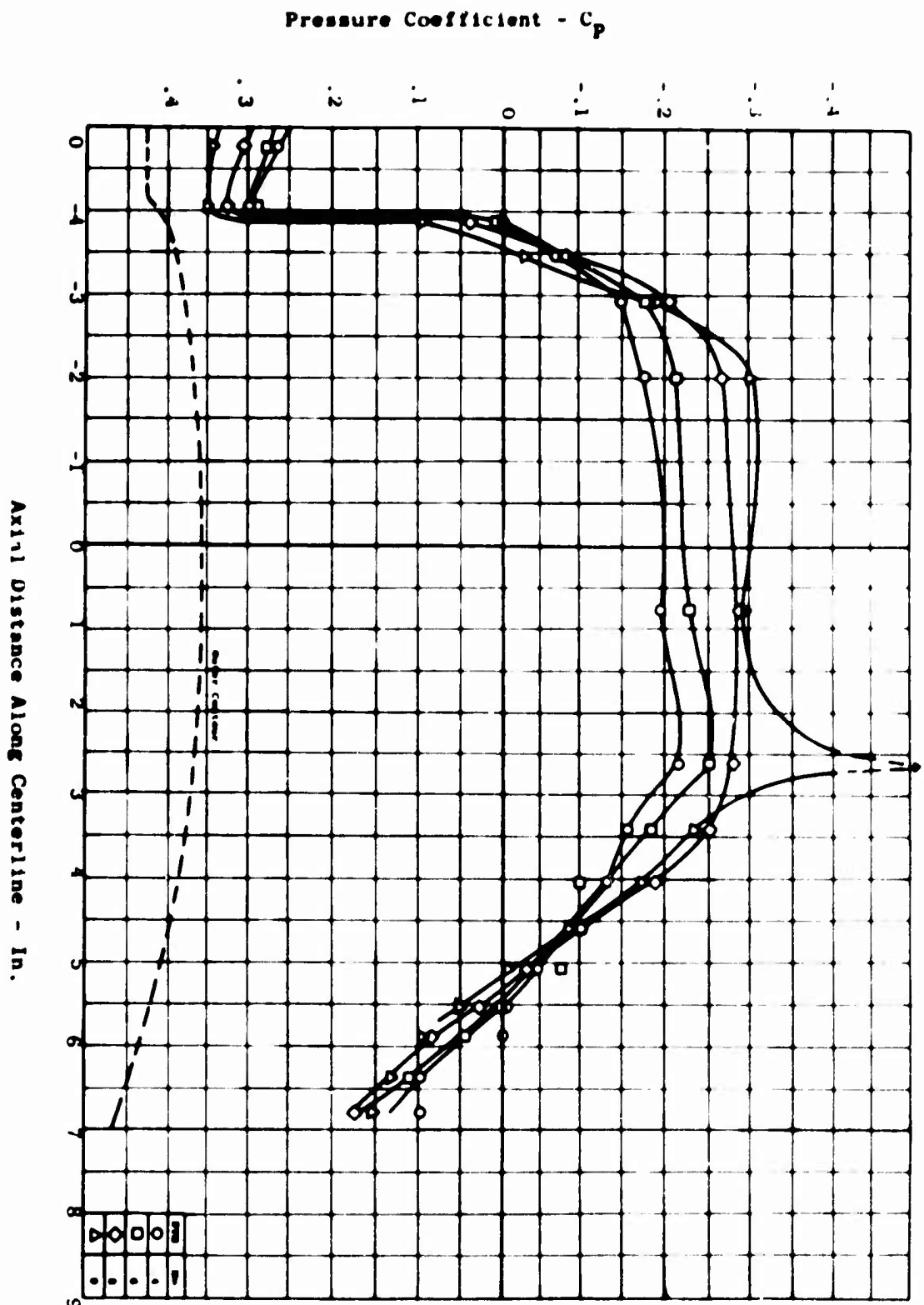
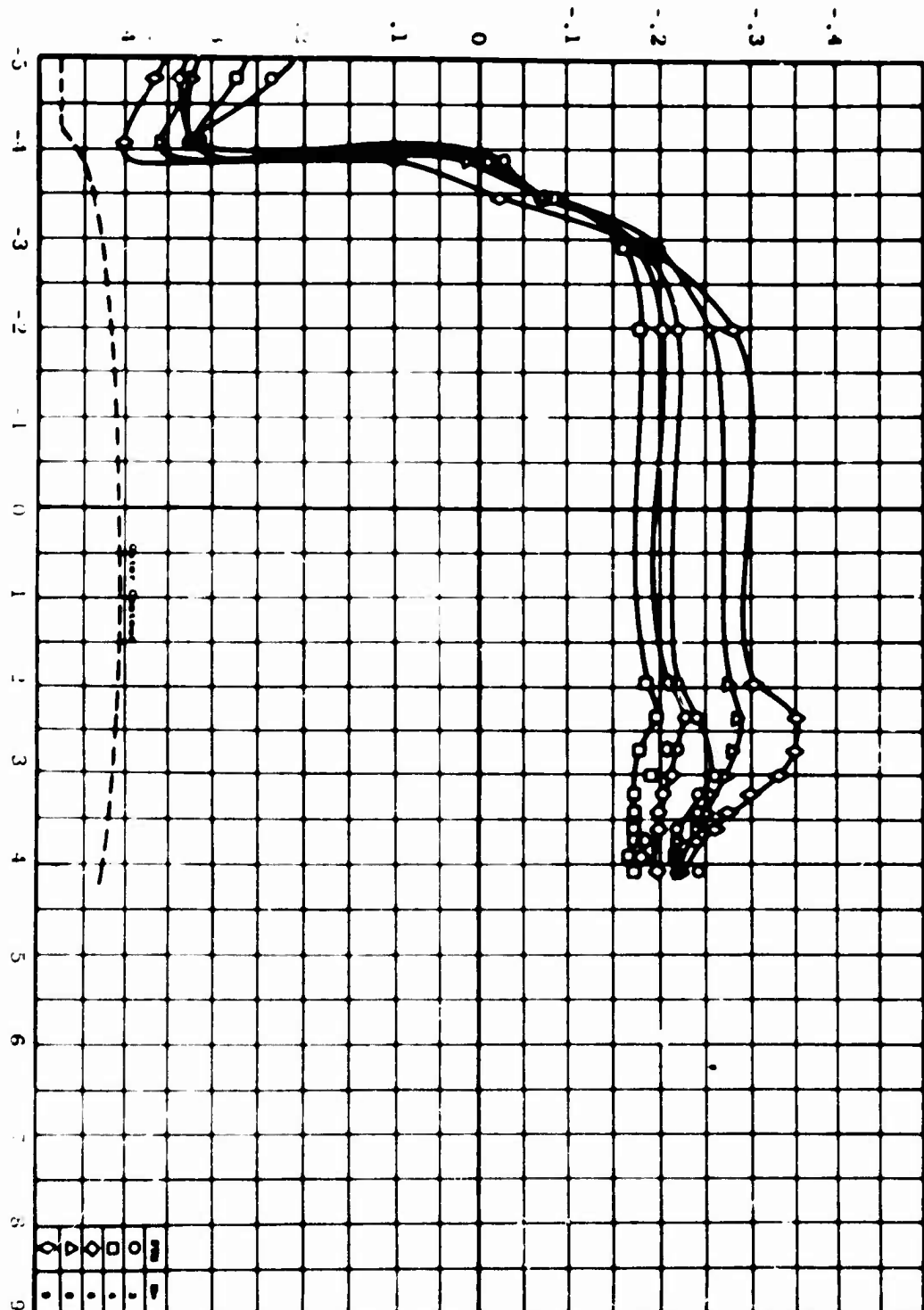


Figure 60. External Pressure Distribution
as a Function of Axial Distance
and Mach No. - Model 3.



Axial Distance Along Centerline - In.

Figure 61. External Pressure Distribution as a Function of Axial Distance and Mach No. - Model 4.

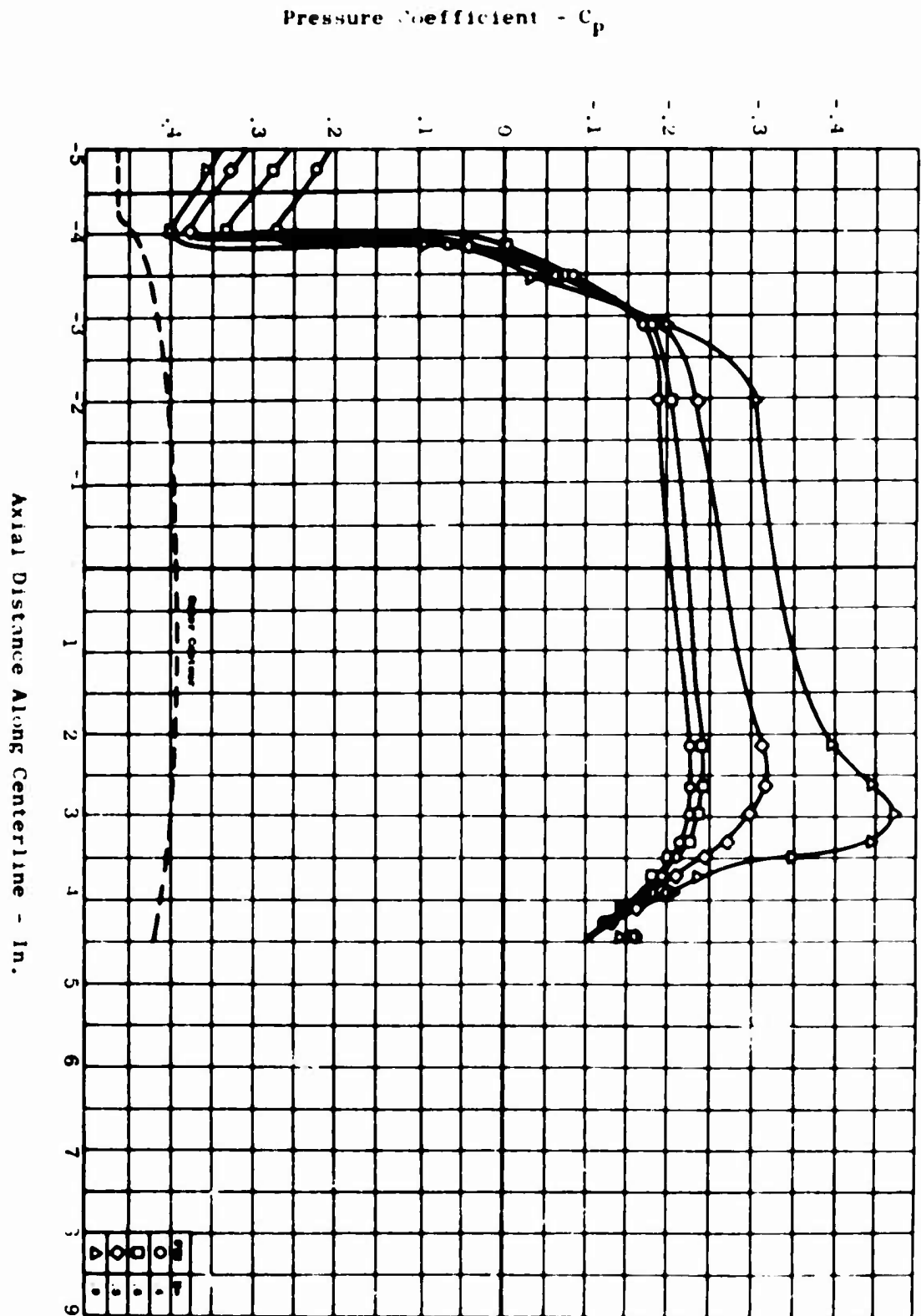


Figure 62. External Pressure Distribution
as a Function of Axial Distance
and Mach No. - Model 5.

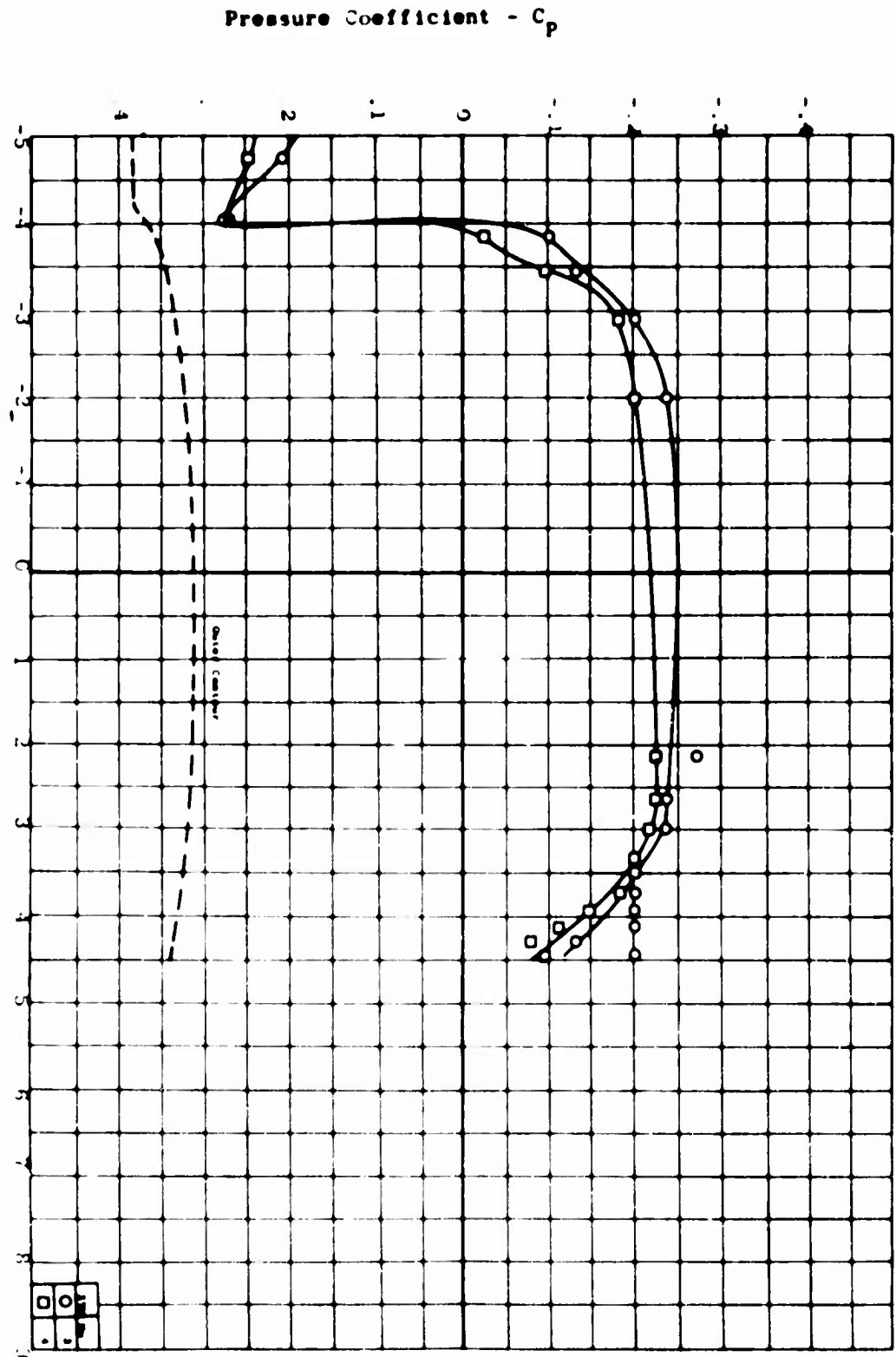


Figure 63. External Pressure Distribution
as a Function of Axial Distance
and Mach No. - Model 6.

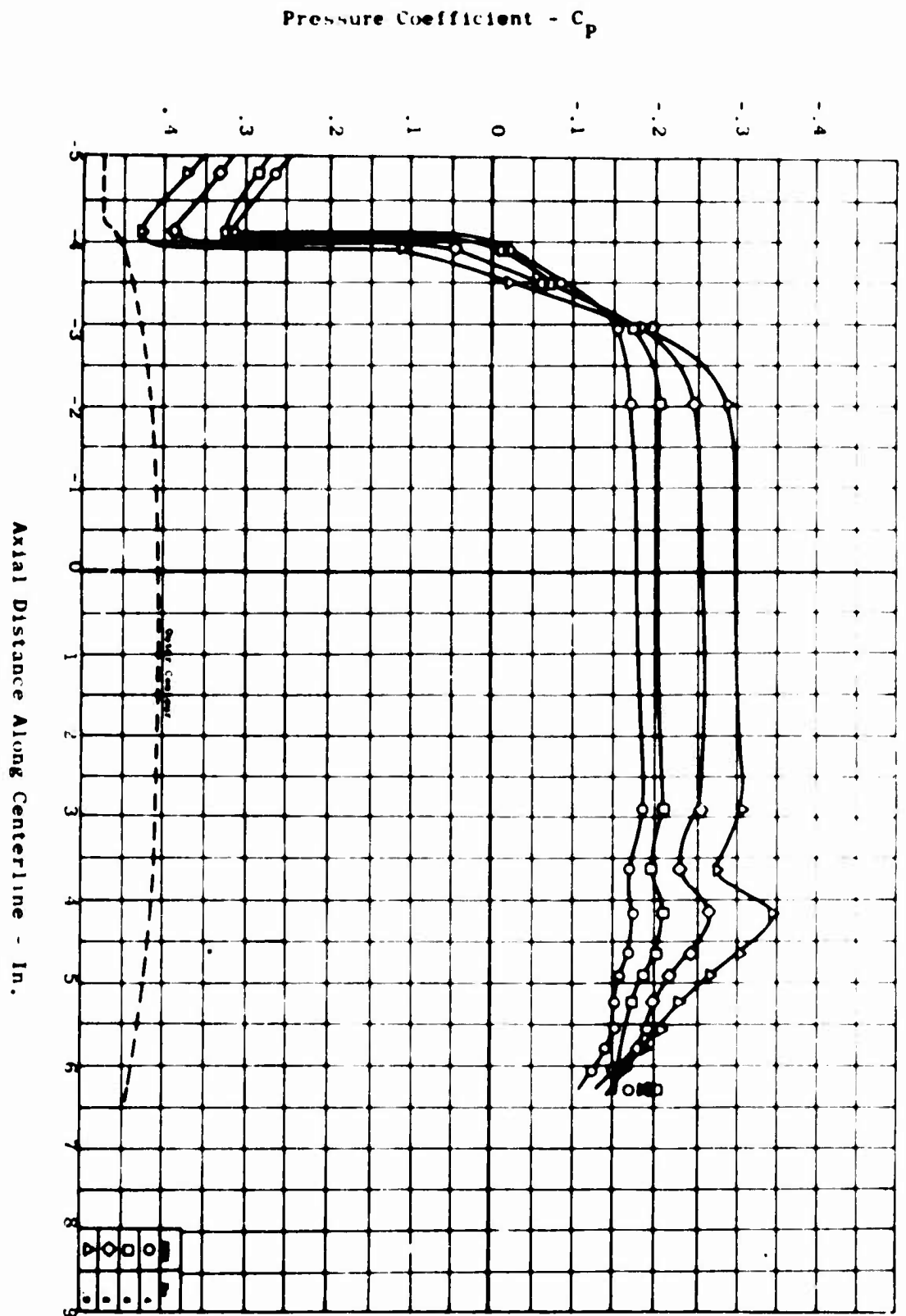


Figure 64. External Pressure Distribution
as a Function of Axial Distance
and Mach No. - Model 7.

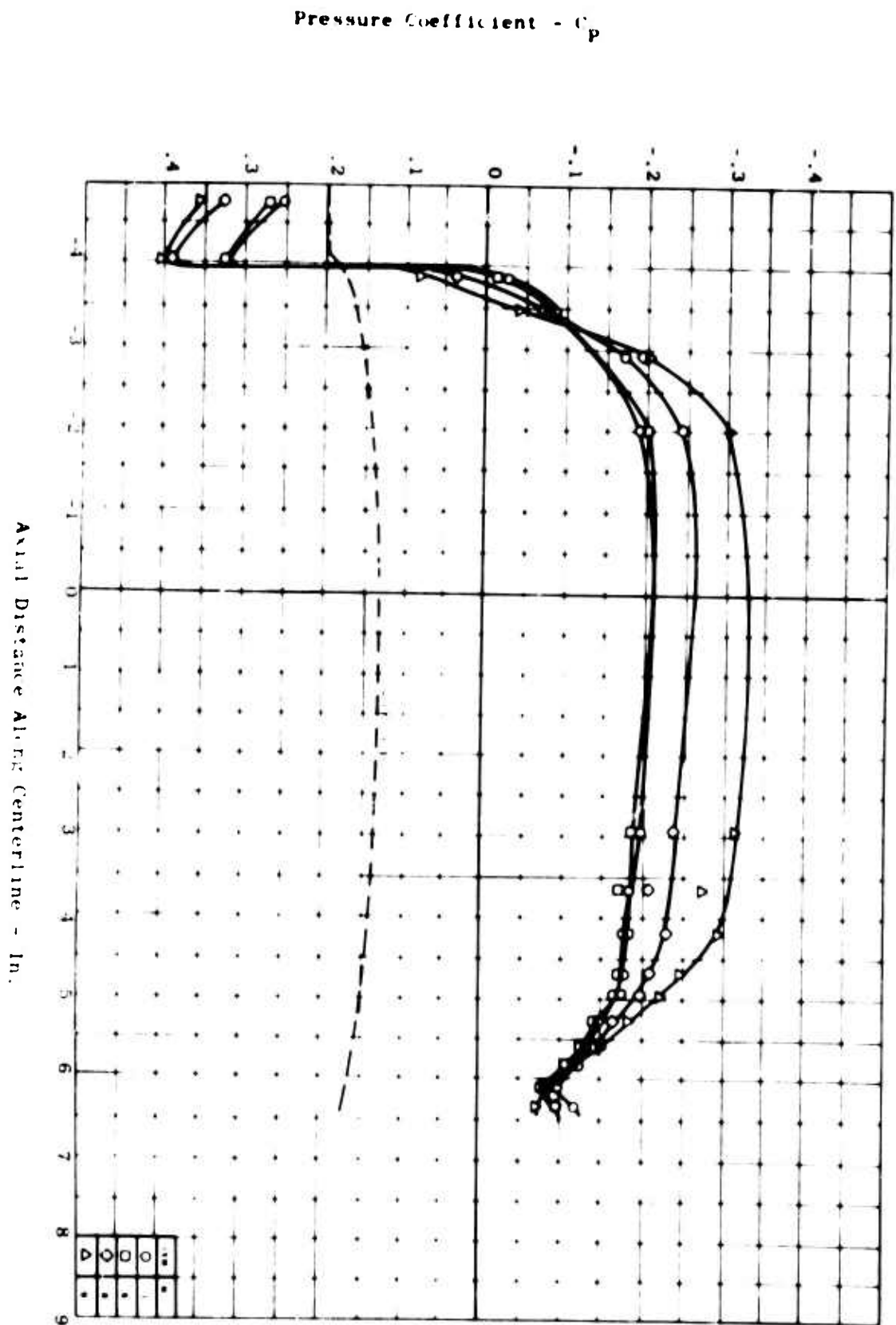
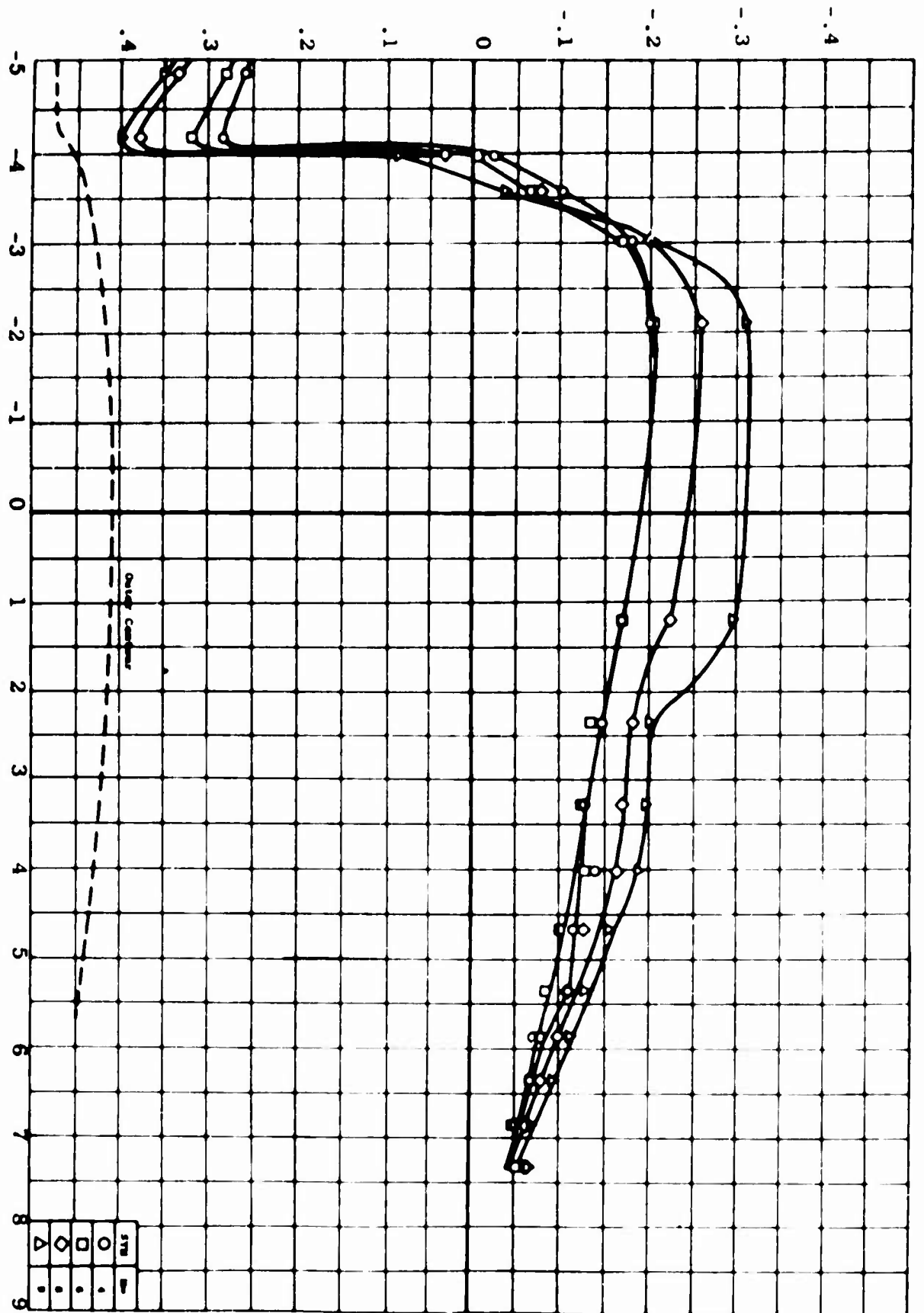


Figure 65. External Pressure Distribution
as a Function of Axial Distance
and Mach No. - Model 7A.

Pressure Coefficient - C_p 

Axial Distance Along Centerline - In.

Figure 66. External Pressure Distribution
as a Function of Axial Distance
and Mach No. - Model 8.

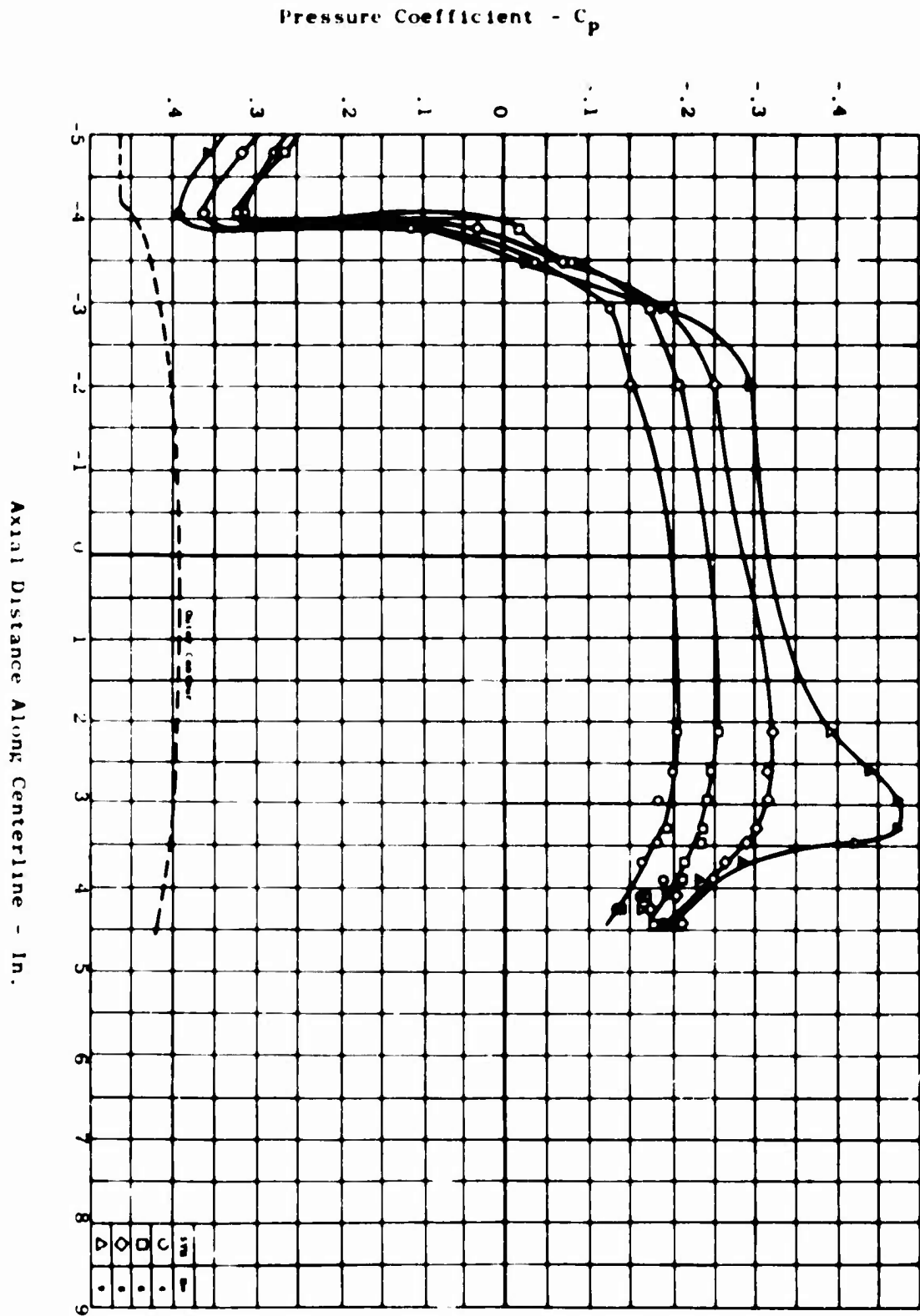
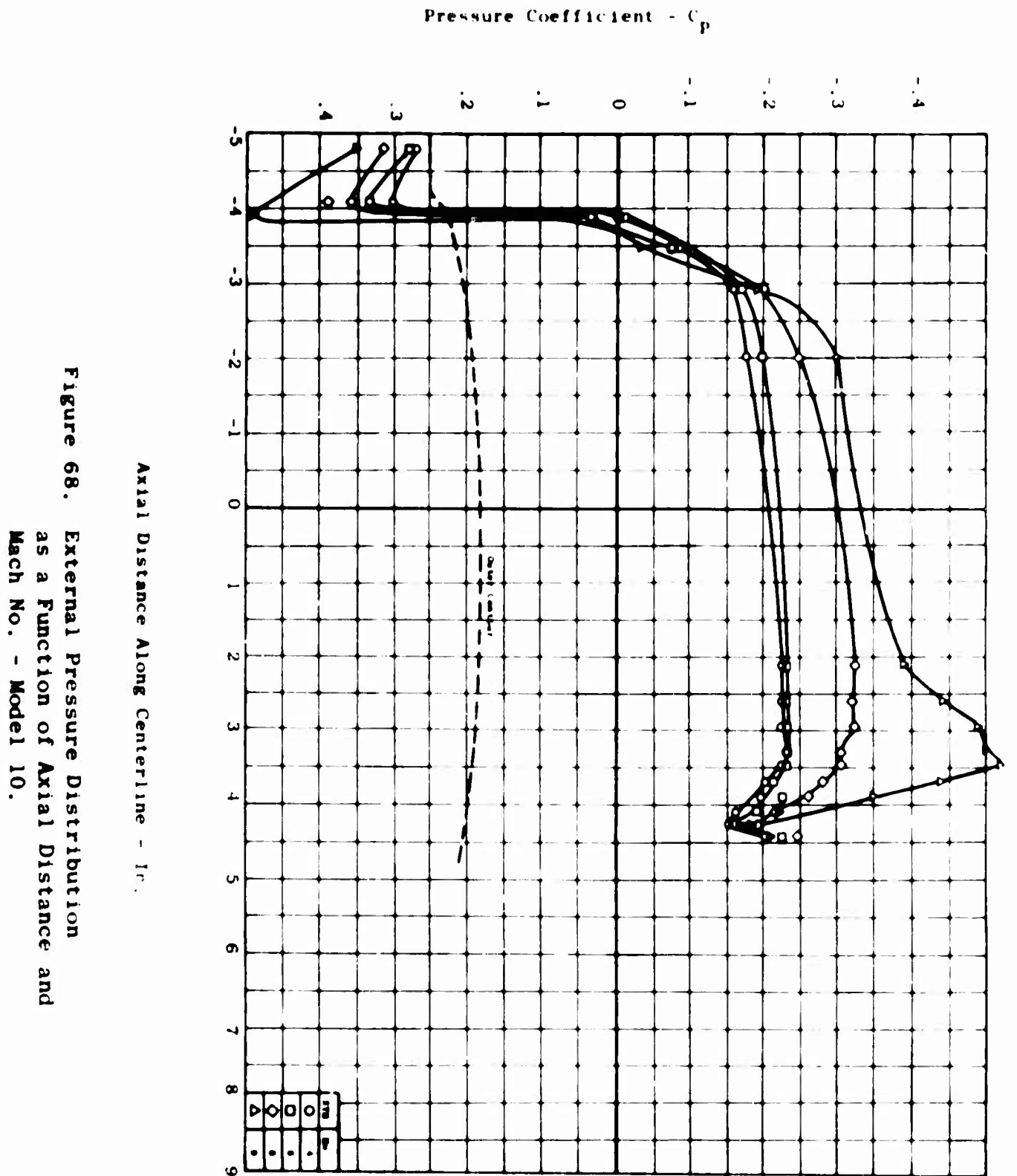


Figure 67. External Pressure Distribution
as a Function of Axial Distance
and Mach No. - Model 9.



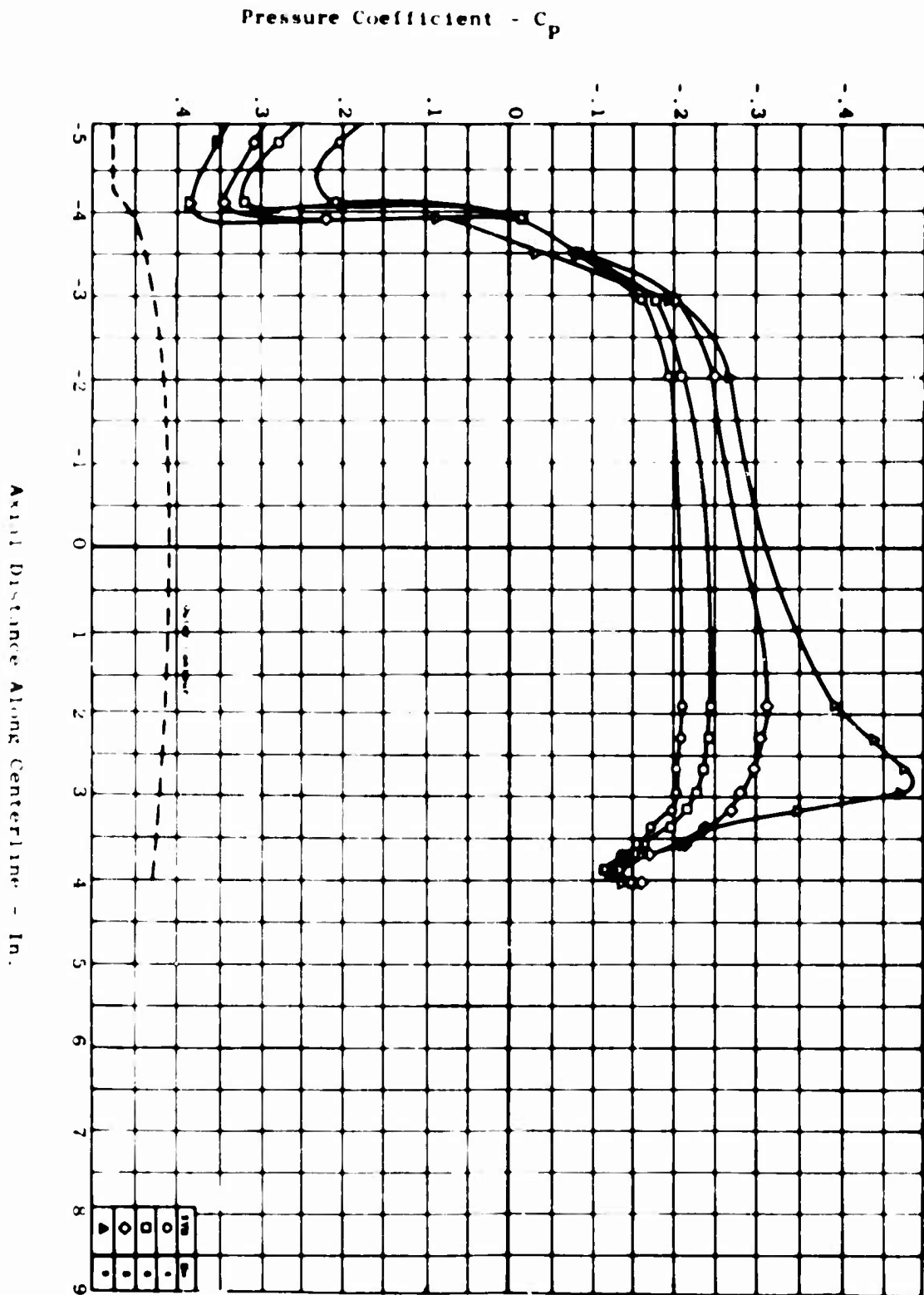


Figure 69. External Pressure Distribution as a Function of Axial Distance and Mach No. - Model 10A.

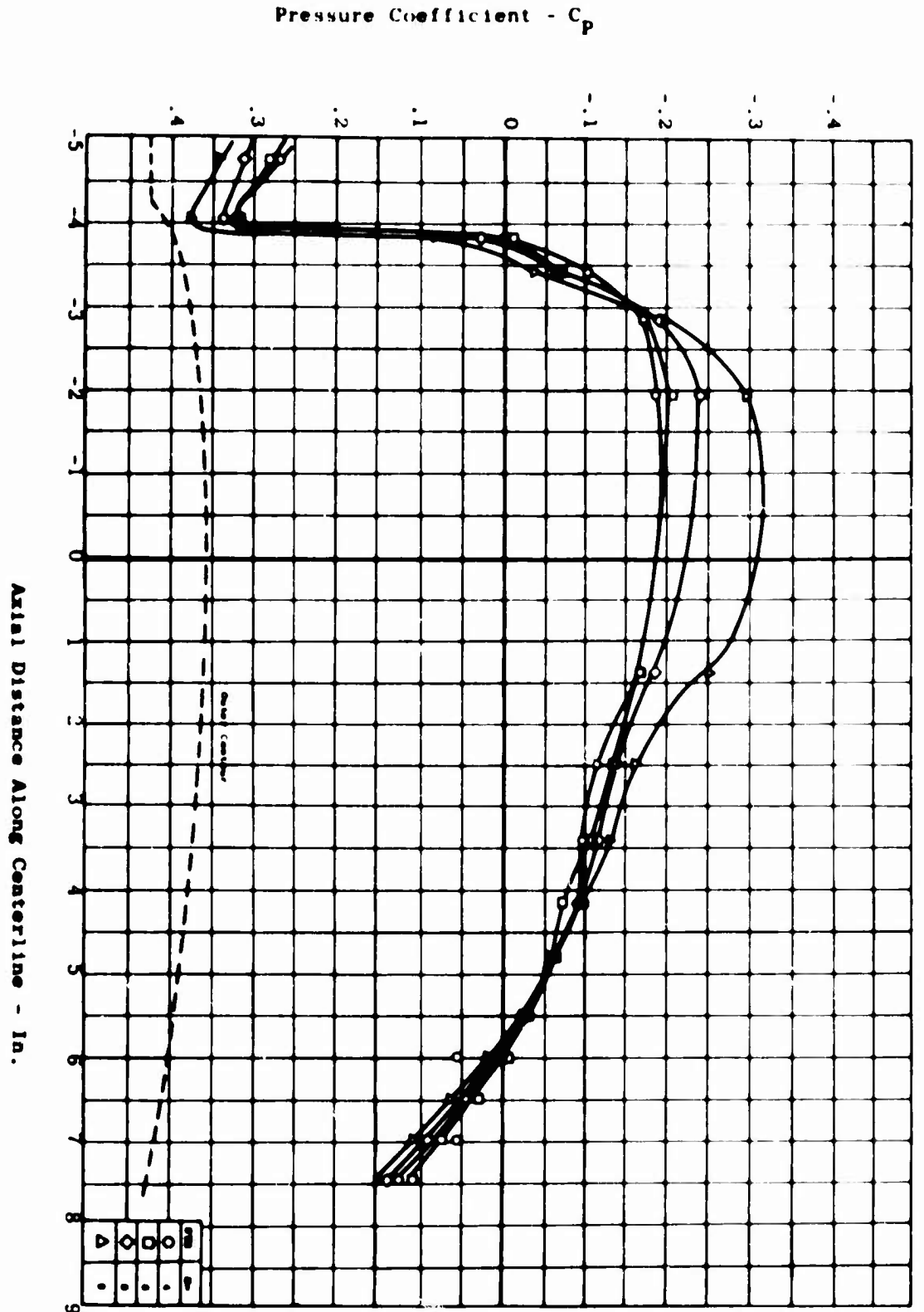


Figure 70. External Pressure Distribution
as a Function of Axial Distance
and Mach No. - Model 10B.

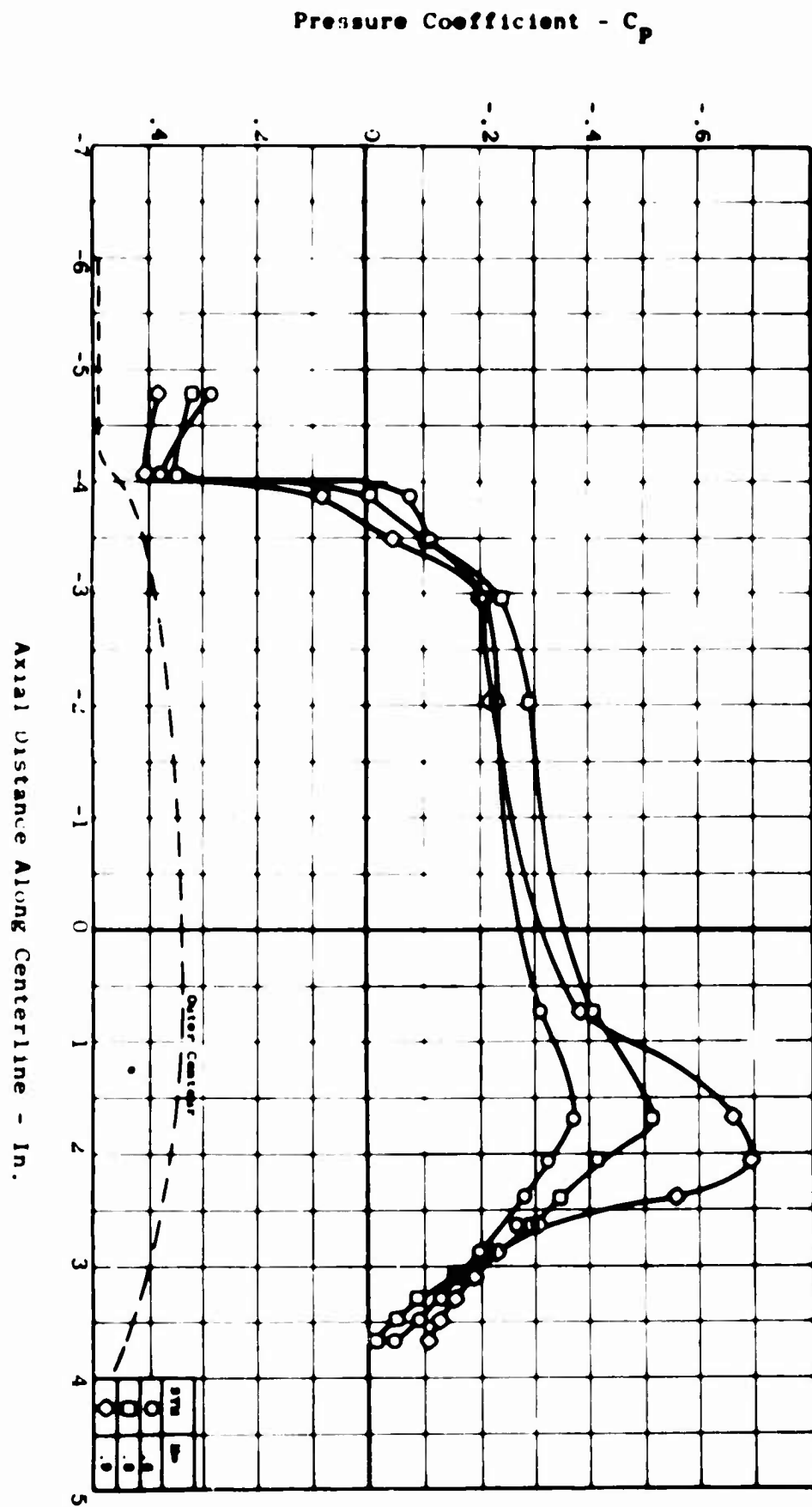


Figure 71. External Pressure Distribution
as a Function of Axial Distance
and Mach No. - Model 11.

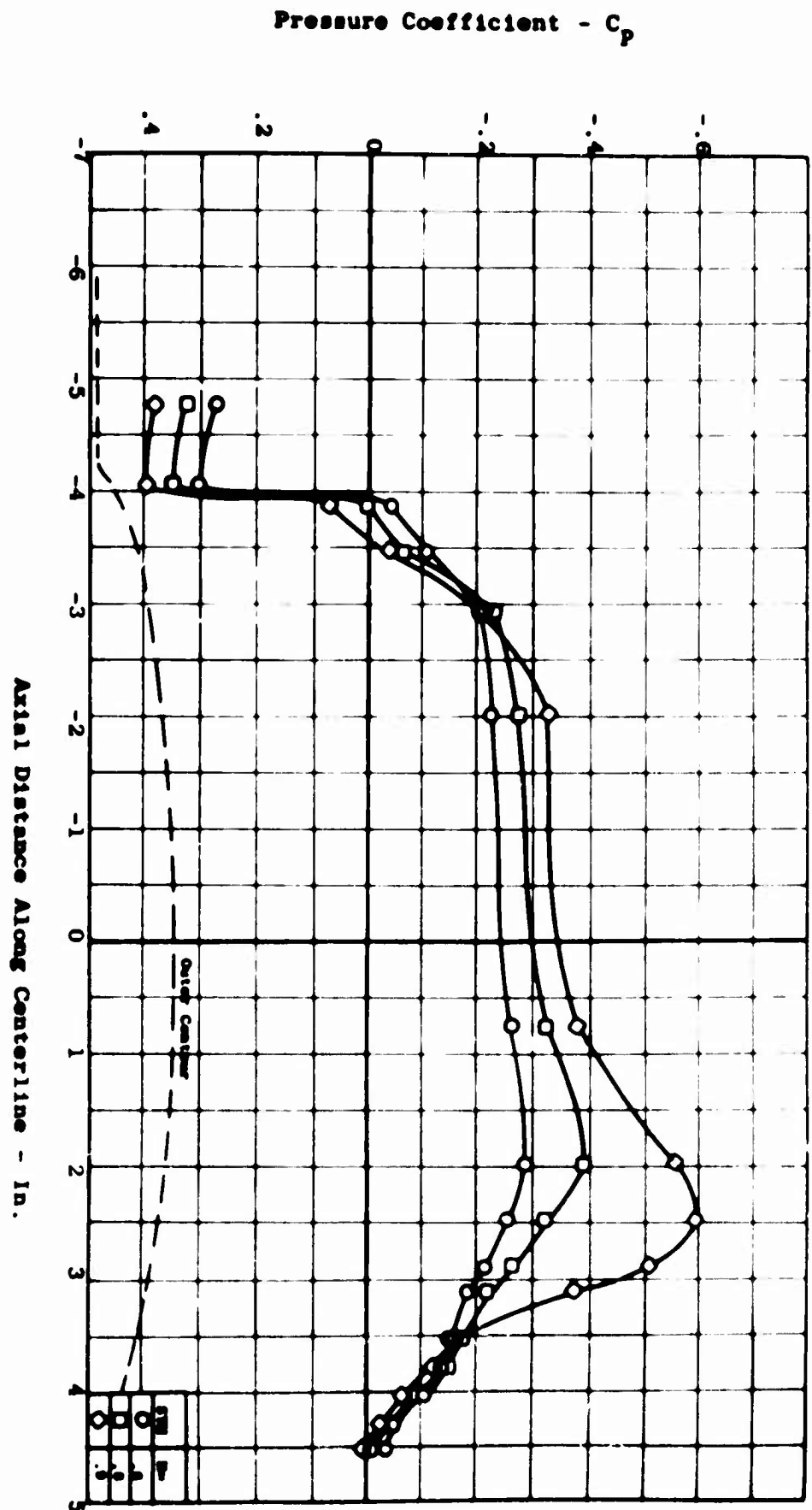


Figure 72. External Pressure Distribution
as a Function of Axial Distance and
Mach No. - Model 12.

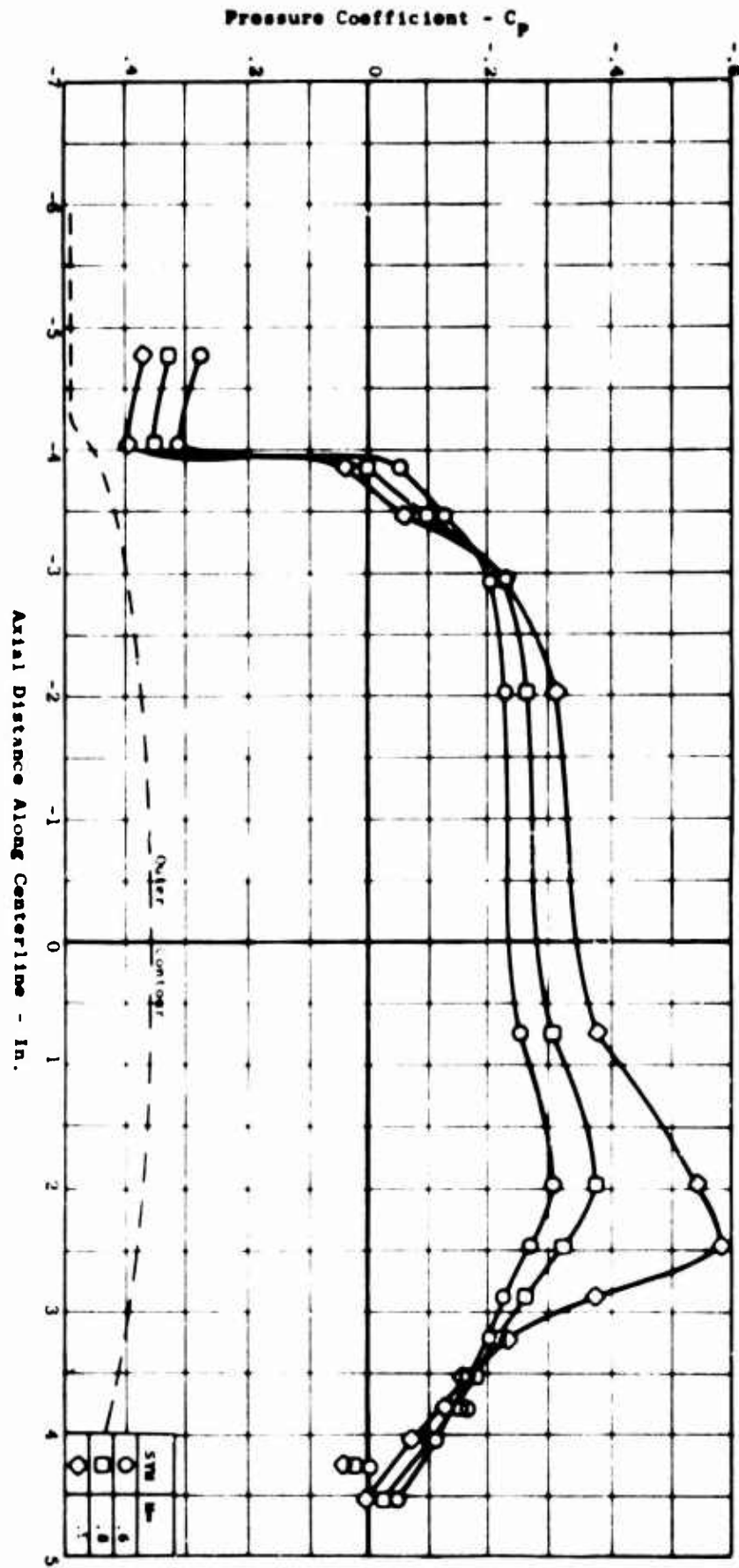


Figure 73. External Pressure Distribution as a Function of Axial Distance and Mach No. - Model 13.

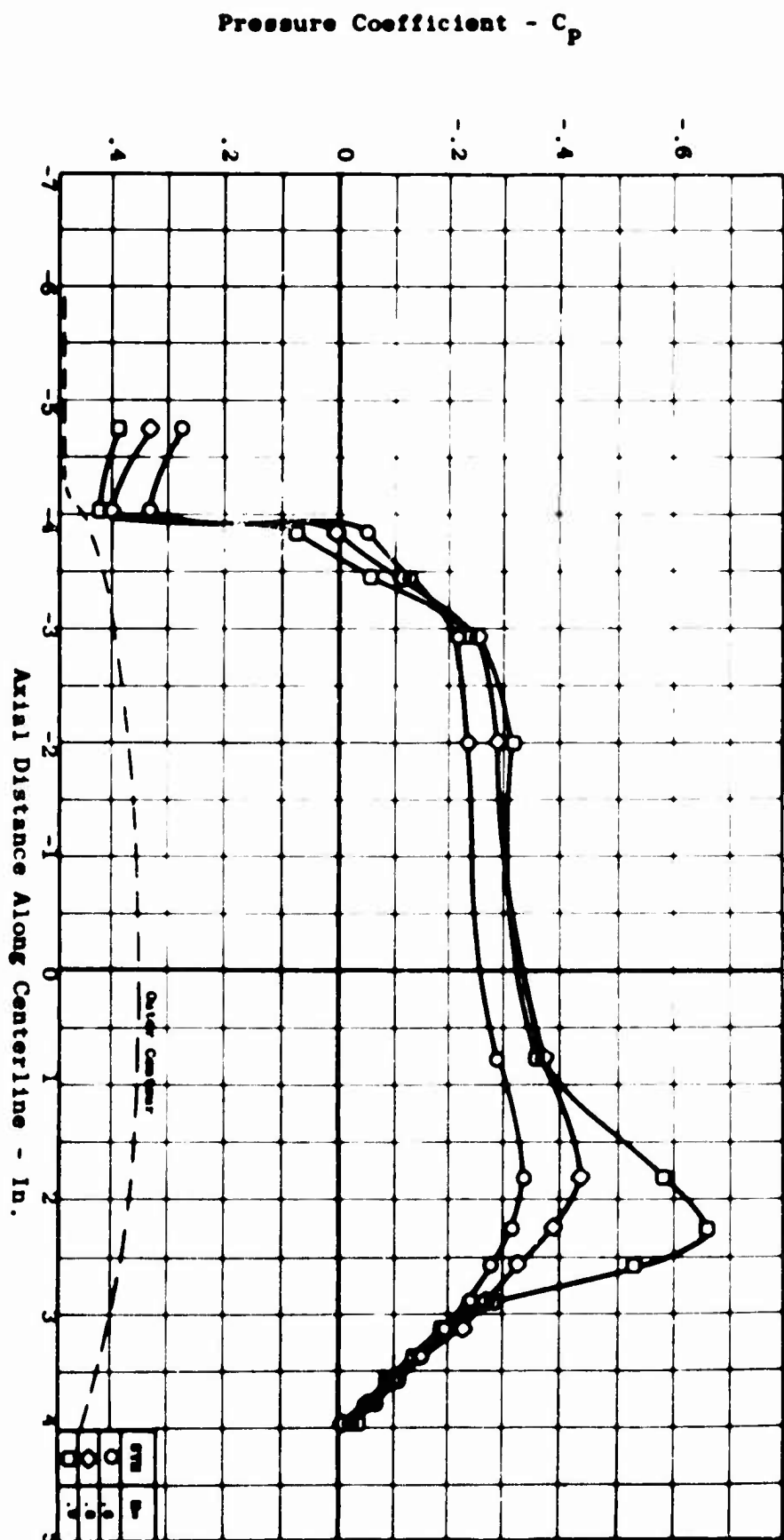


Figure 74. External Pressure Distribution
as a Function of Axial Distance
and Mach No. - Model 14.

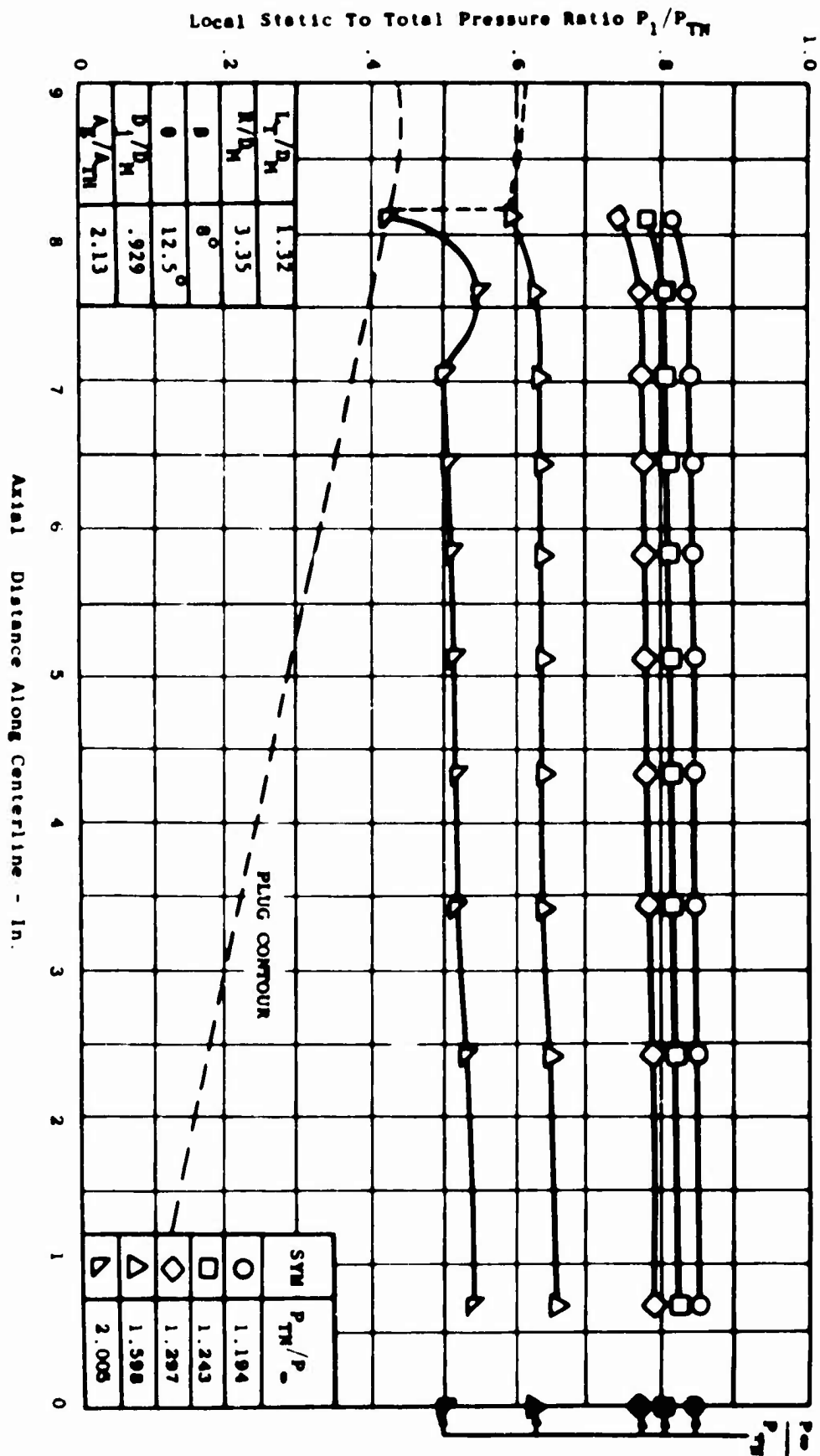


Figure 75. Plug Pressure Distribution
as a Function of Axial
Distance and Pressure Ratio-
Model 4, Mach No. = 0.

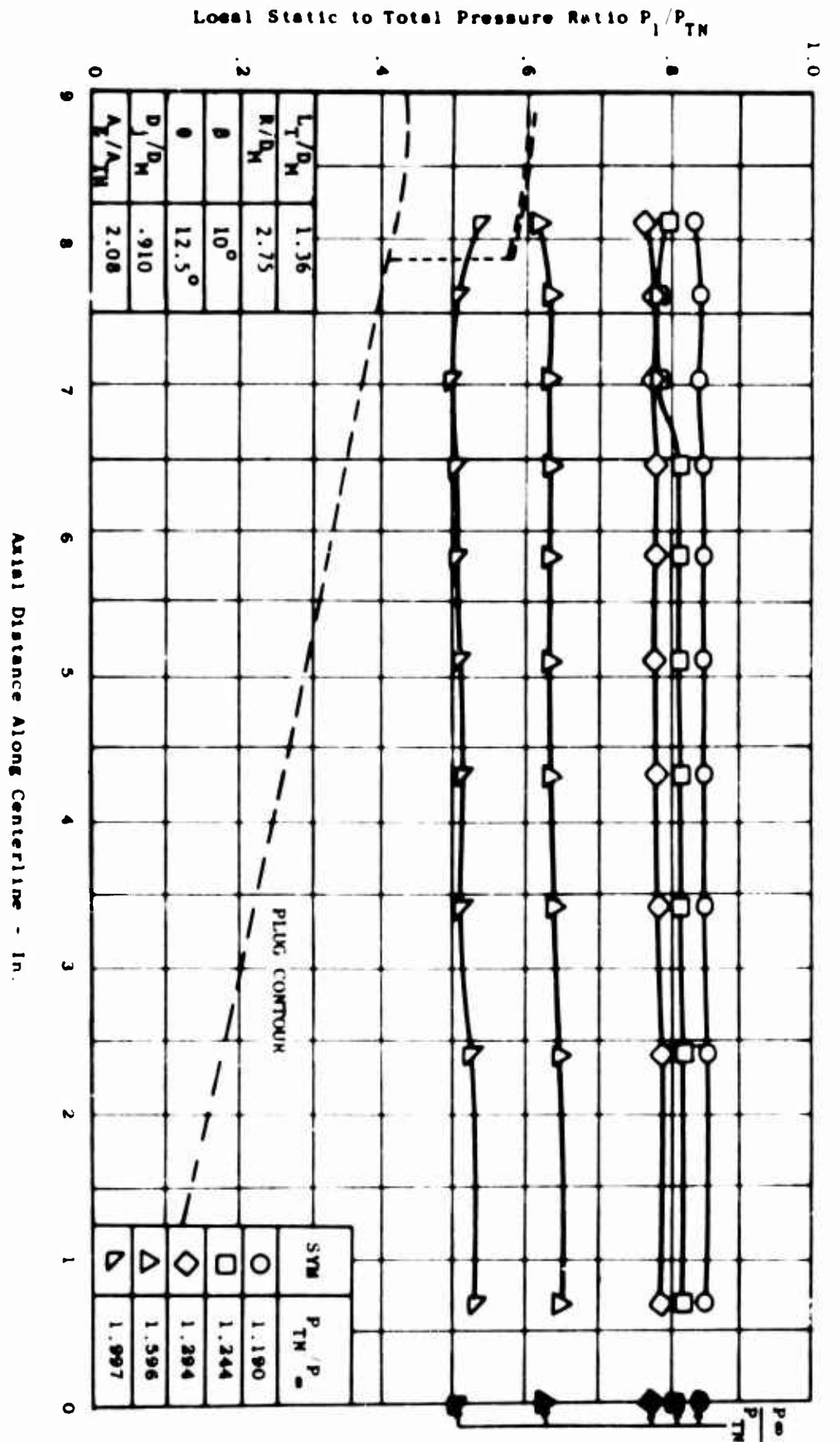


Figure 76. Nozzle Plug Static Pressure Distribution - Model 5, Mach No. = 0.

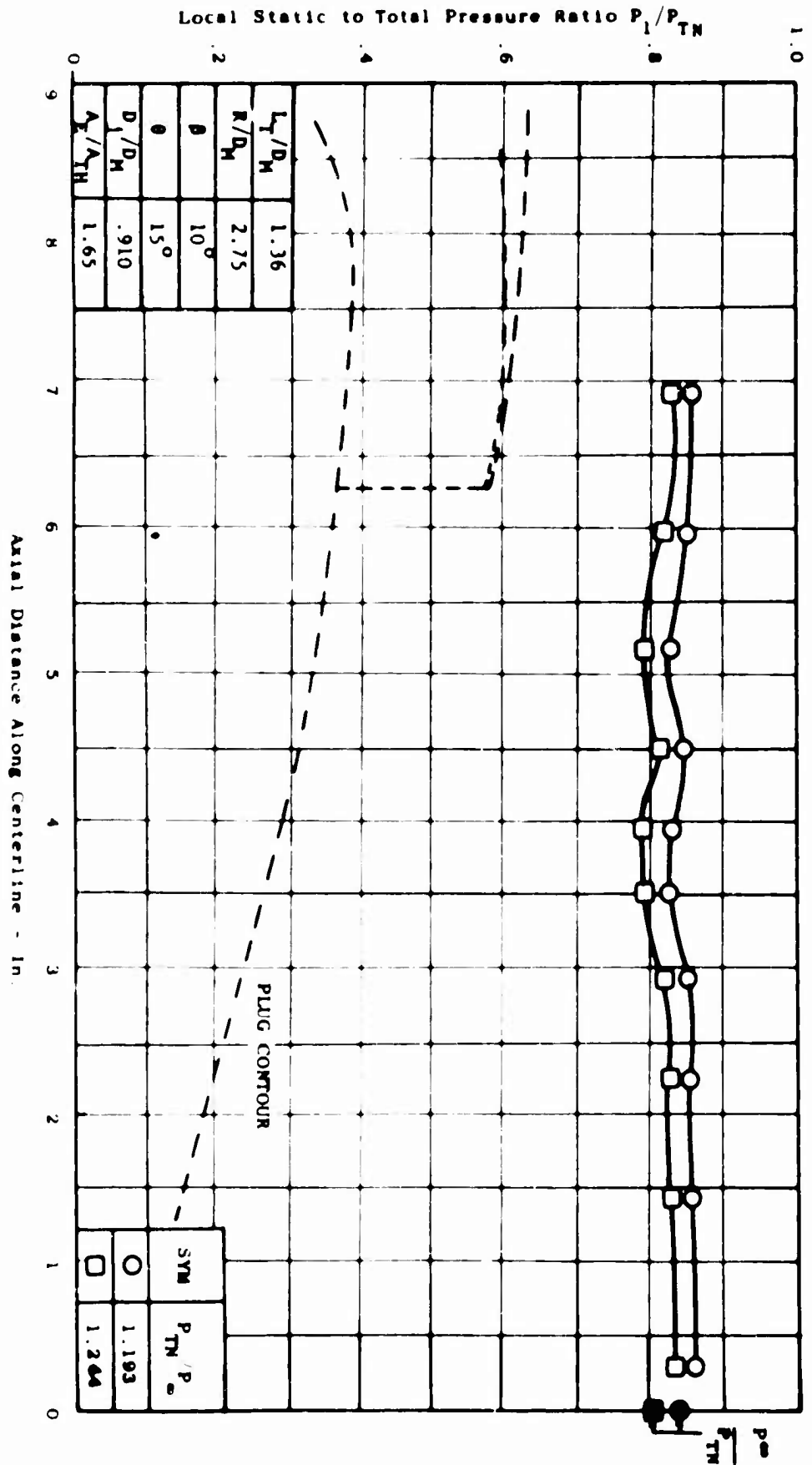


Figure 77. Nozzle Plug Static Pressure Distribution - Model 6, Mach No. = 0.

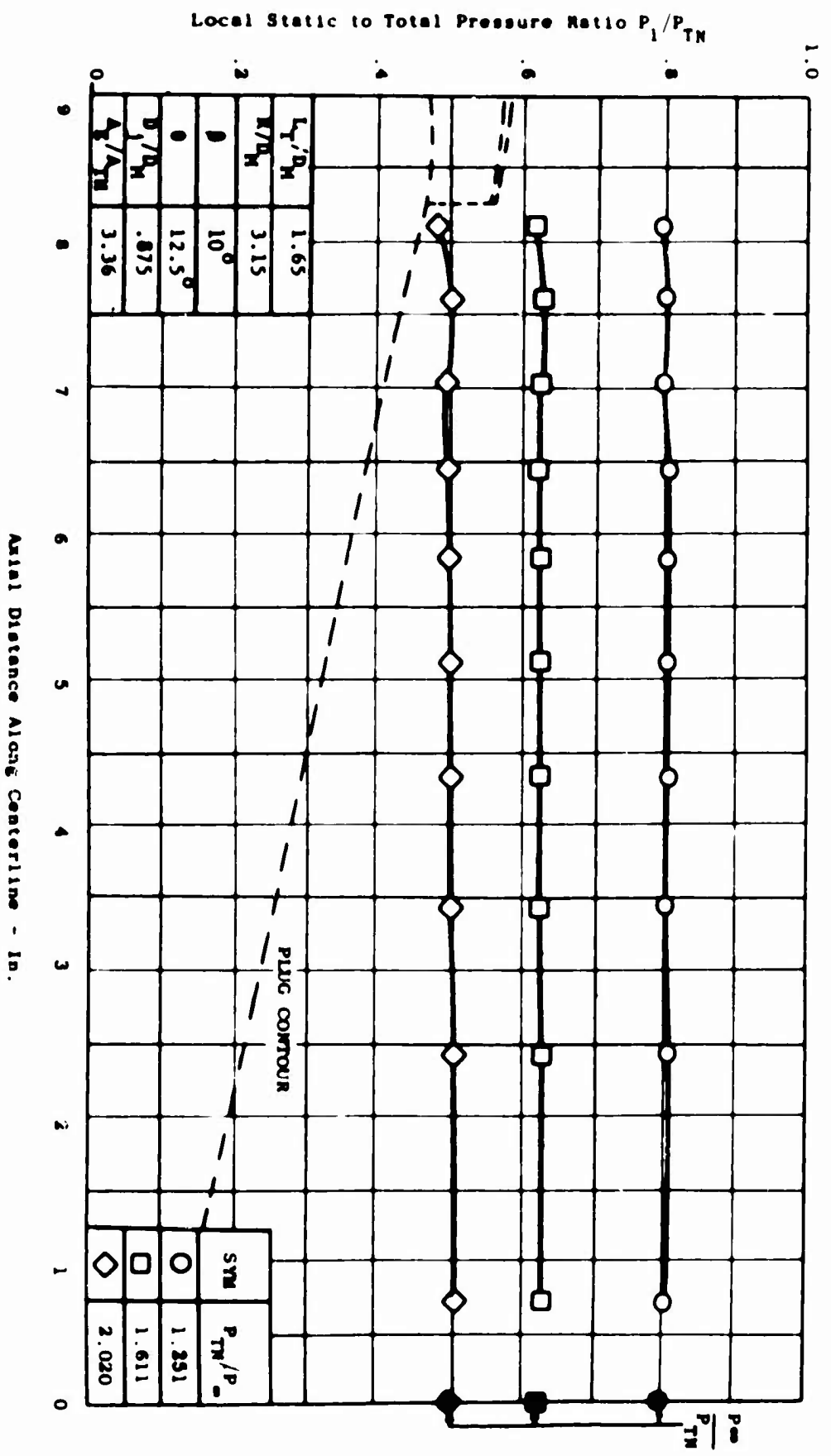


Figure 78. Nozzle Plug Static Pressure Distribution - Model 7, Mach No. = 0.

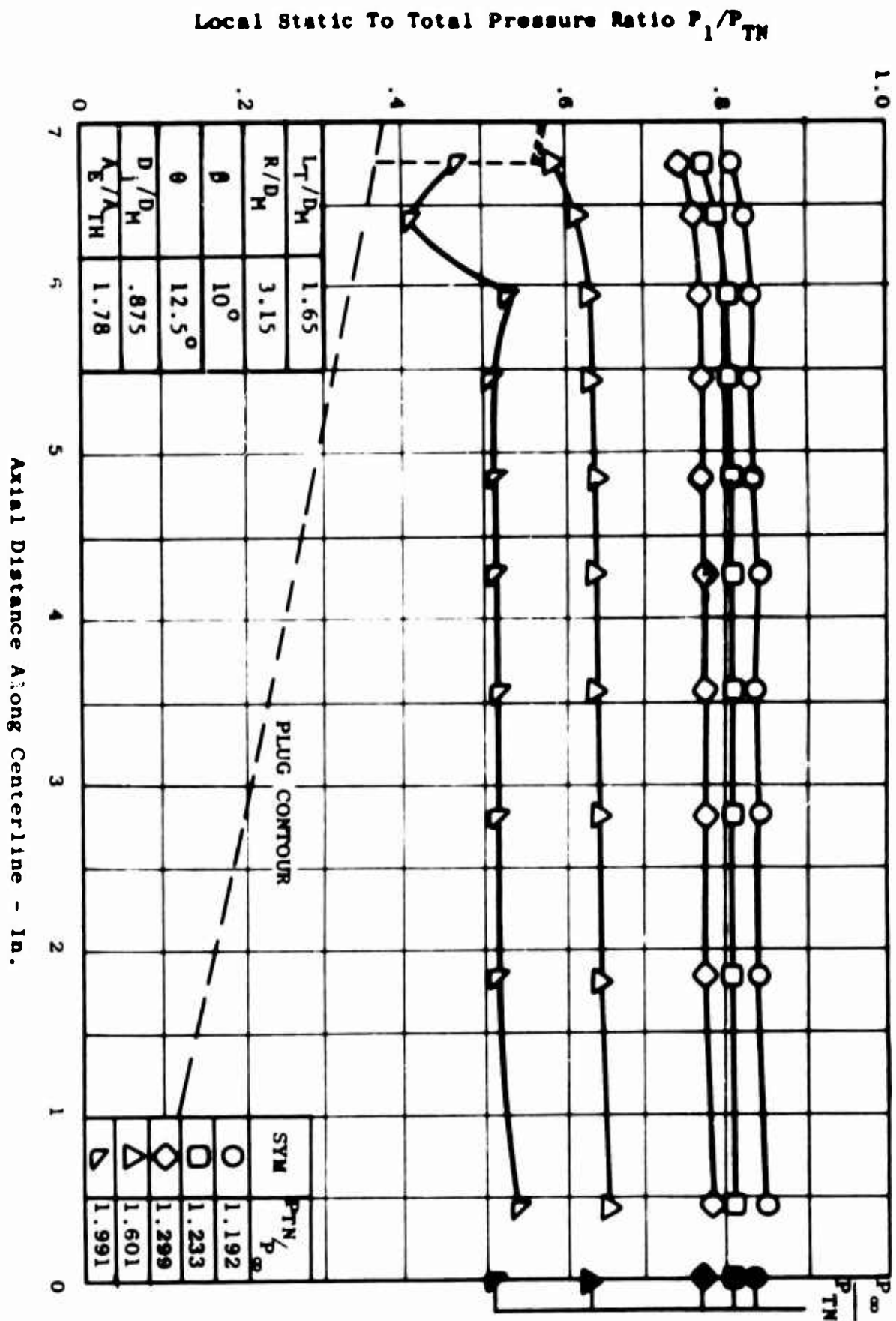


Figure 79. Plug Pressure Distribution
as a Function of Axial
Distance and Pressure Ratio-
Model 7A, Mach No. = 0.

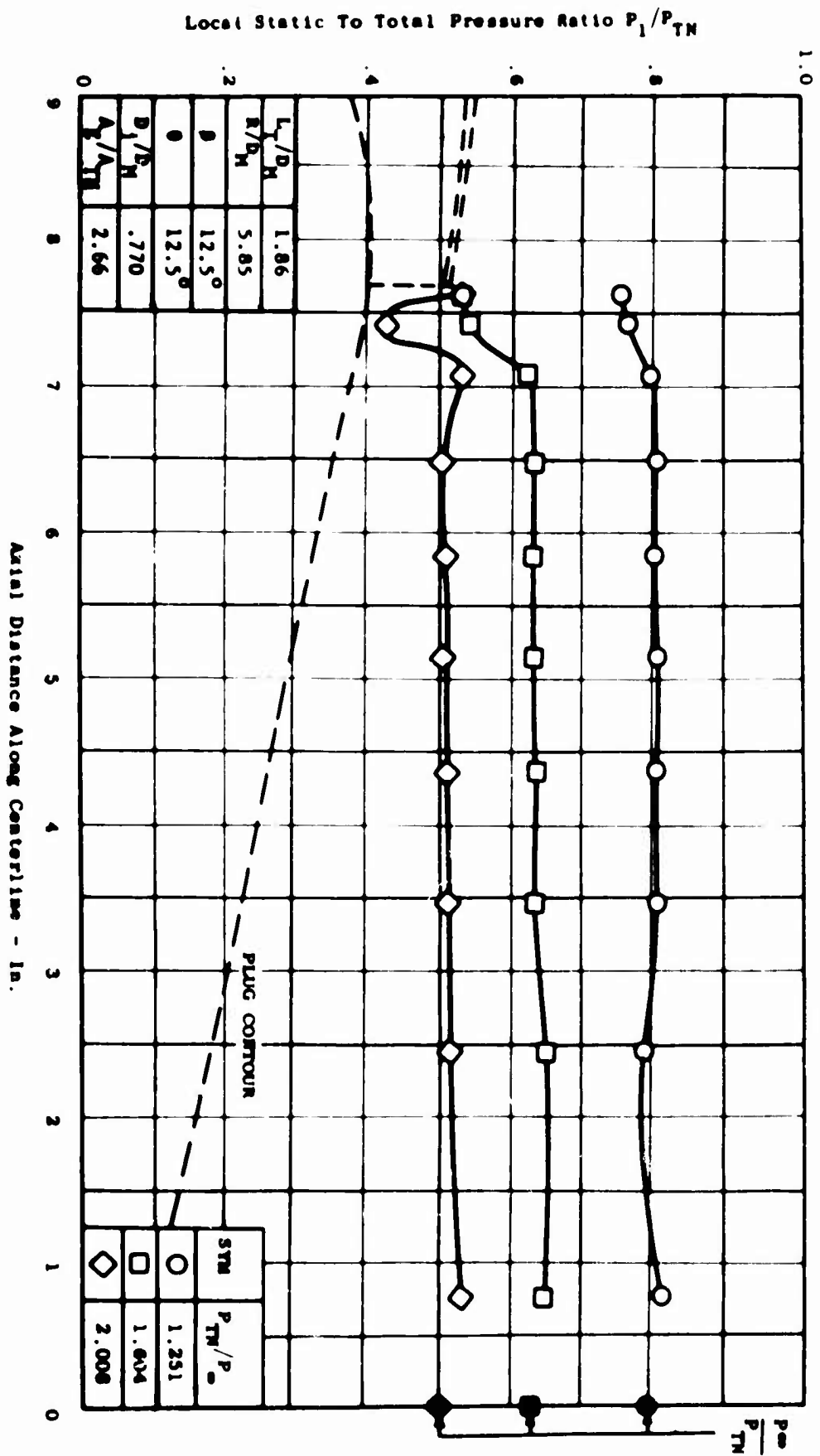


Figure 80. Plug Pressure Distribution as a Function of Axial Distance and Pressure Ratio-Model 8, Mach No. = 0.

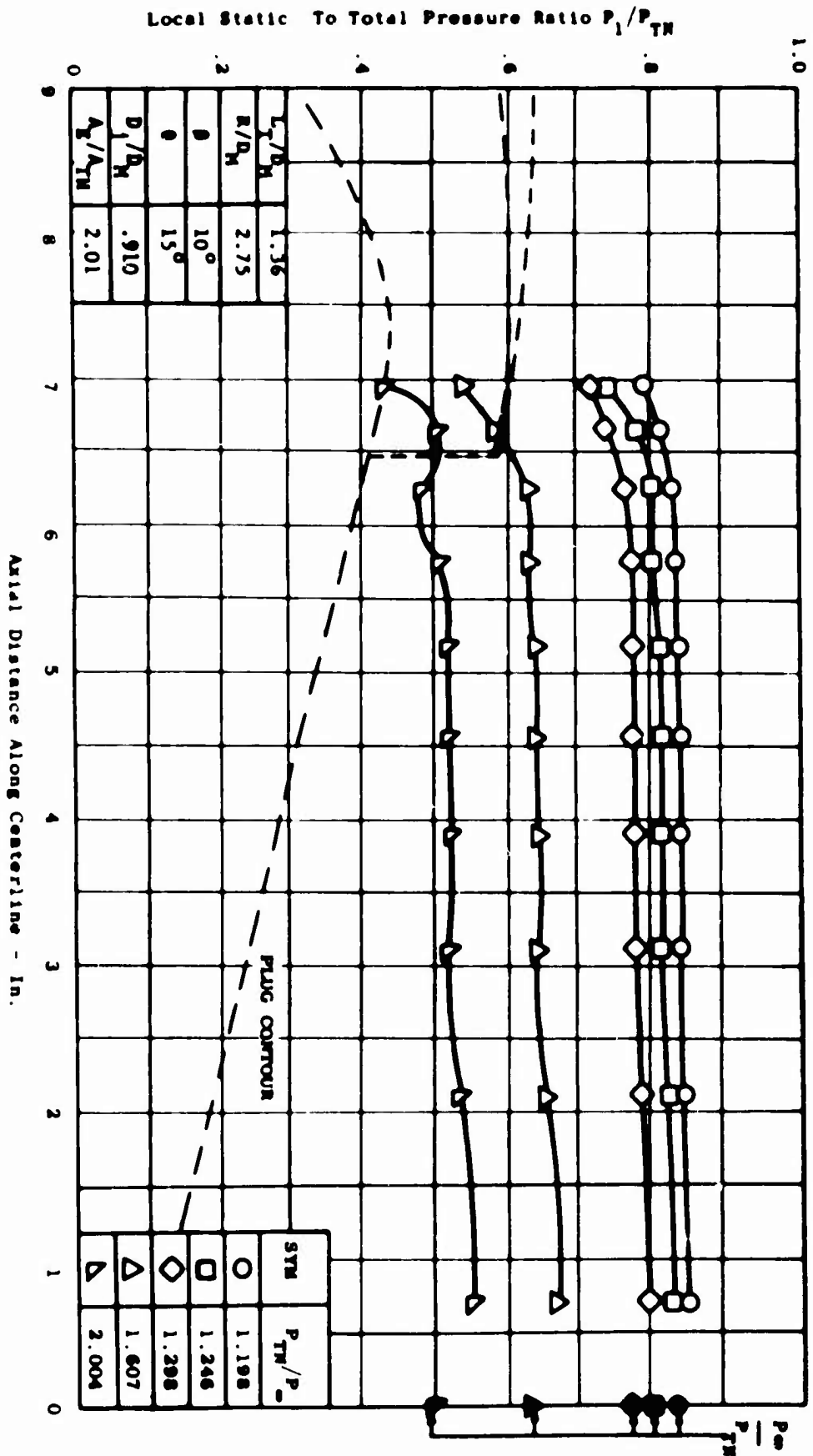


Figure 81. Plug Pressure Distribution
as a Function of Axial
Distance and Pressure Ratio-
Model 9, Mach No. = 0.

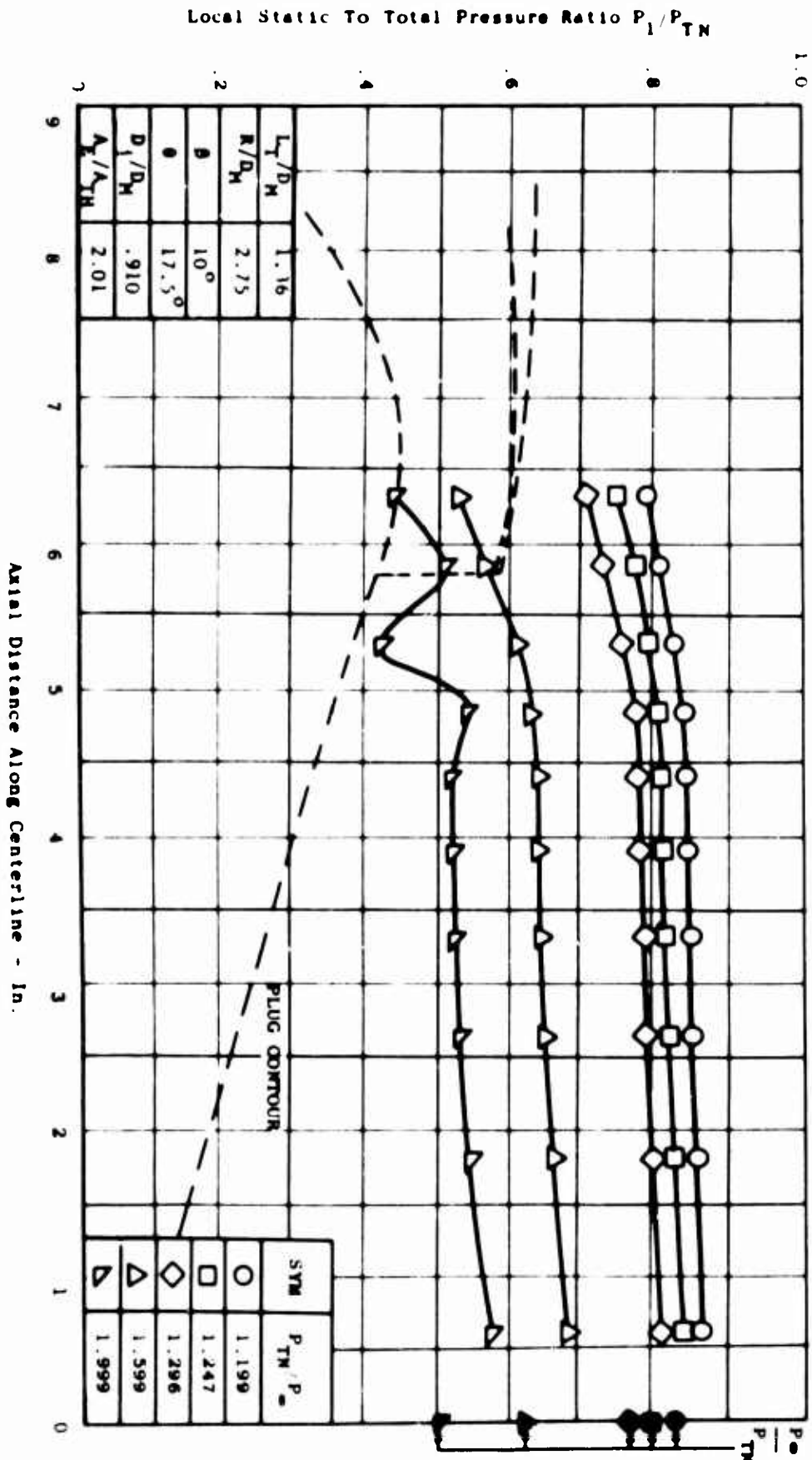


Figure 82. Plug Pressure Distribution as a Function of Axial Distance and Pressure Ratio- Model 10, Mach No. = 0.

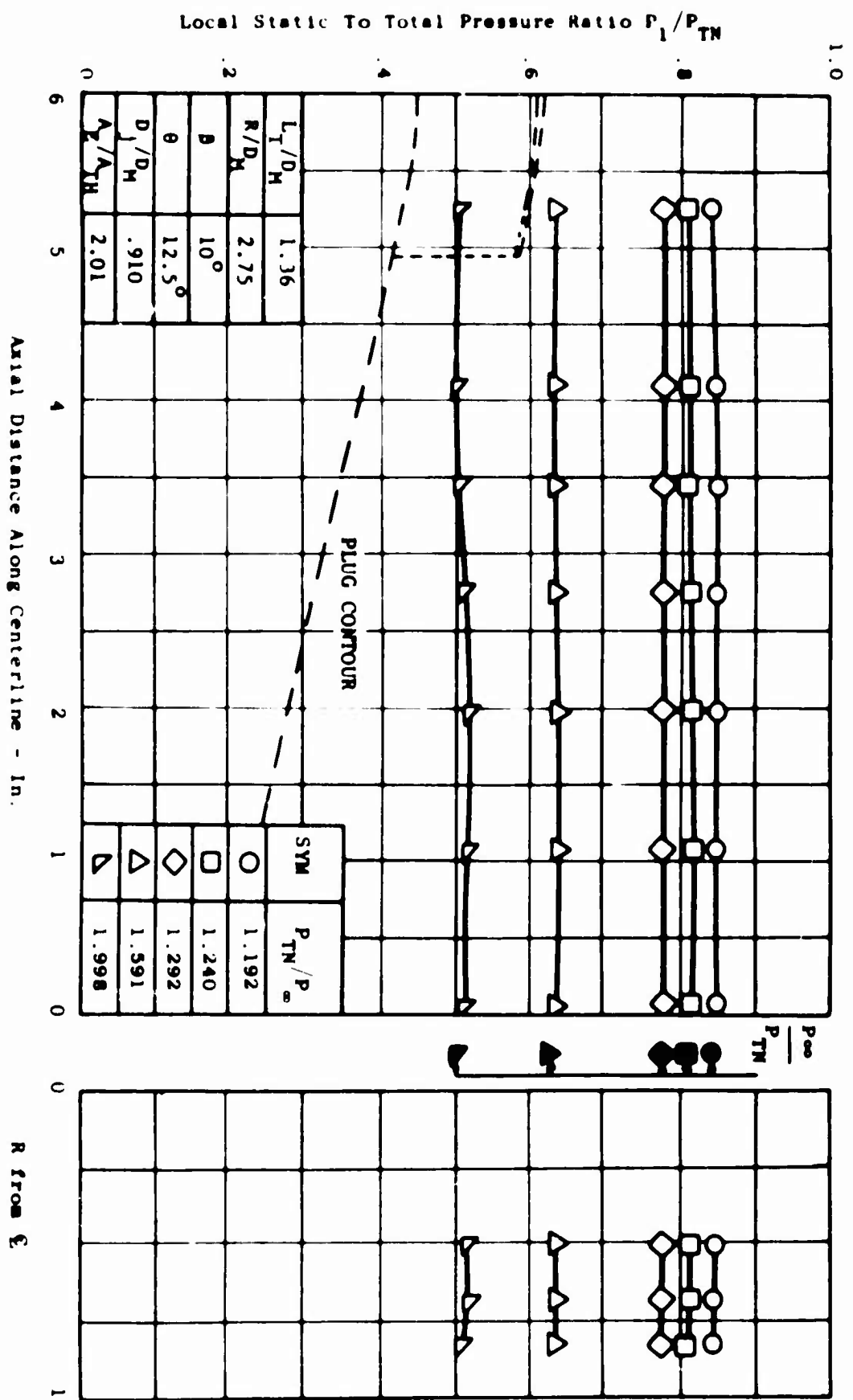


Figure 83. Plug Pressure Distribution as a Function of Axial Distance and Pressure Ratio- Model 10A, Mach No. = 0.

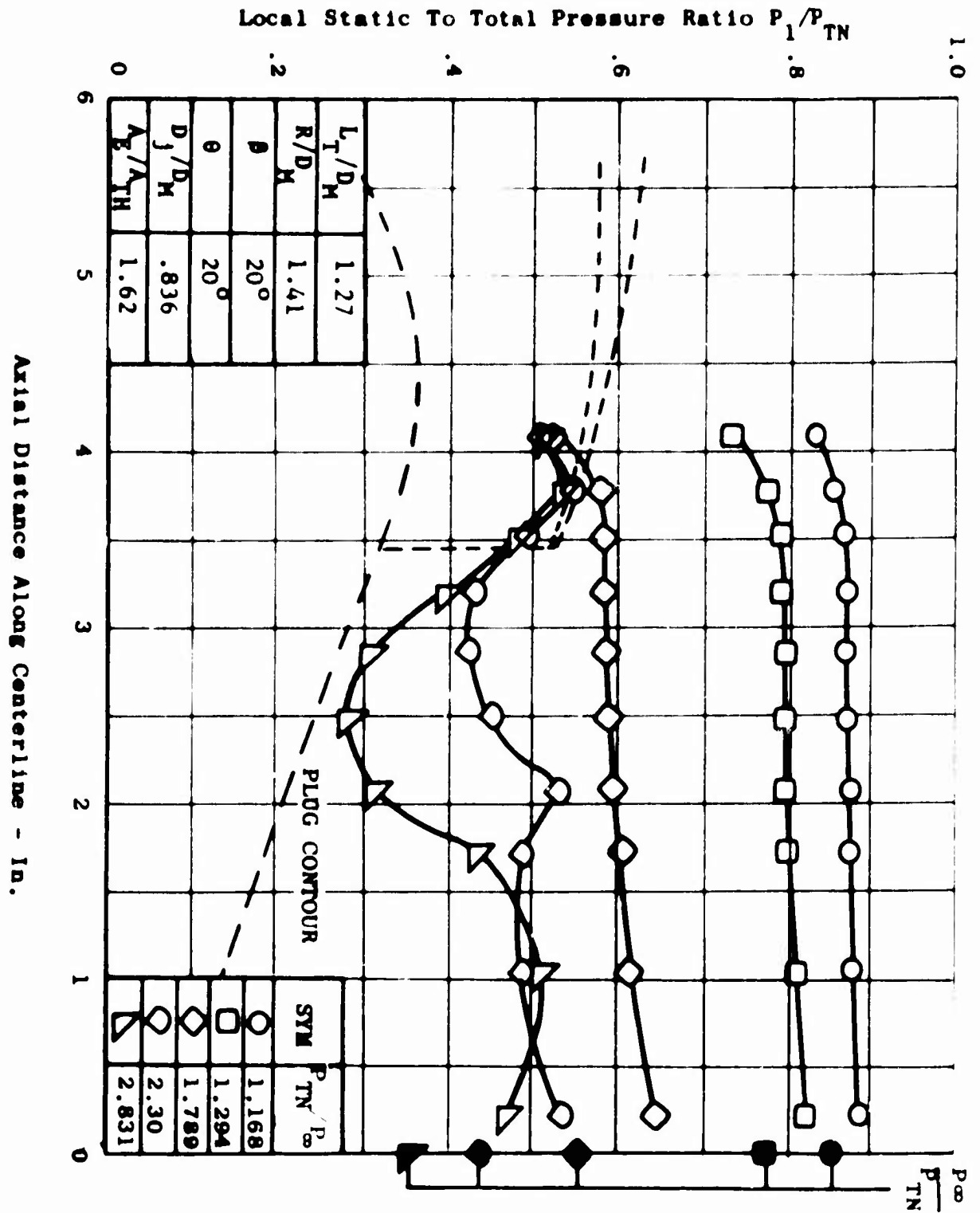


Figure 84. Plug Pressure Distribution as a function of Axial Distance and Pressure Ratio- Model 11, Mach No. = 0.

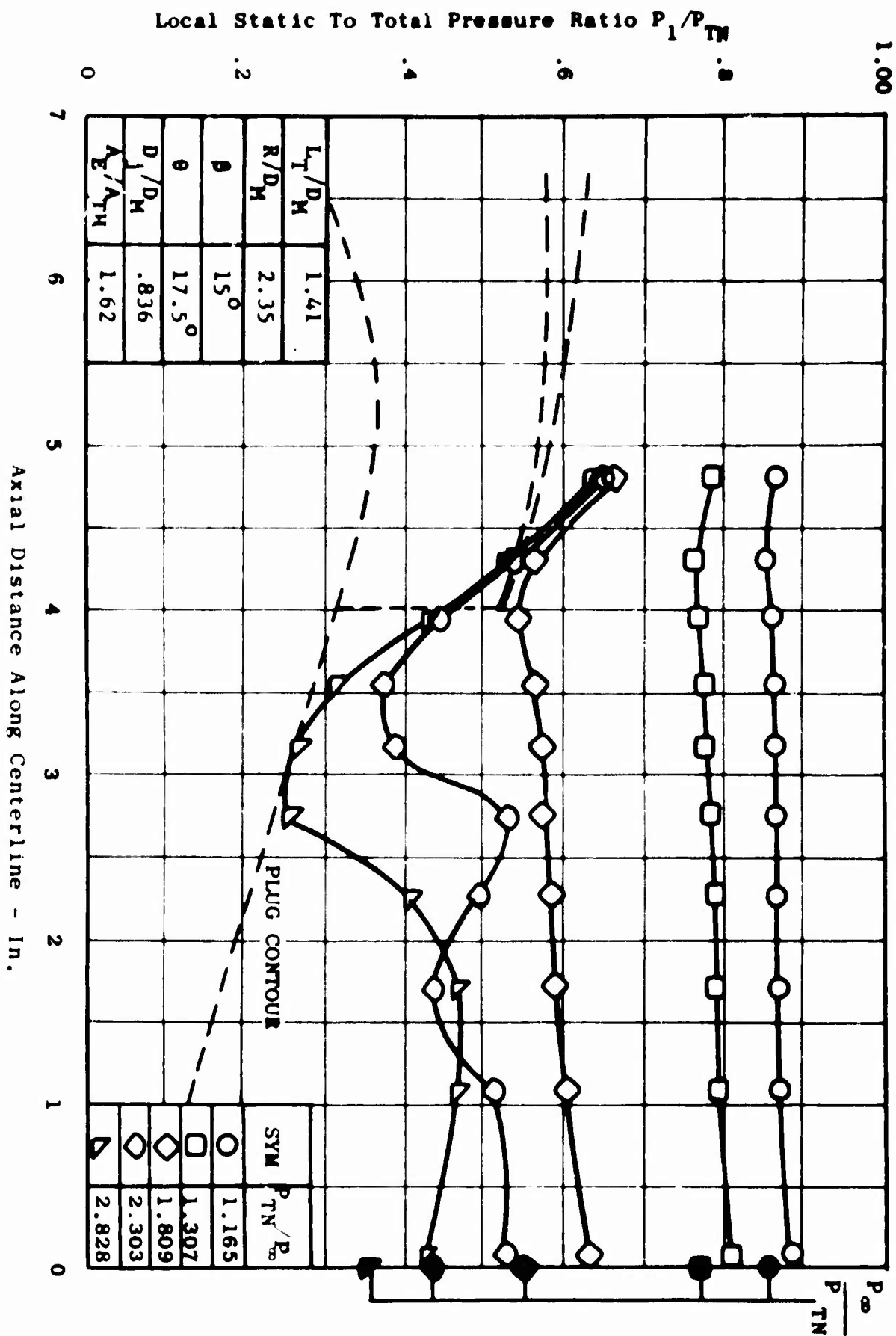
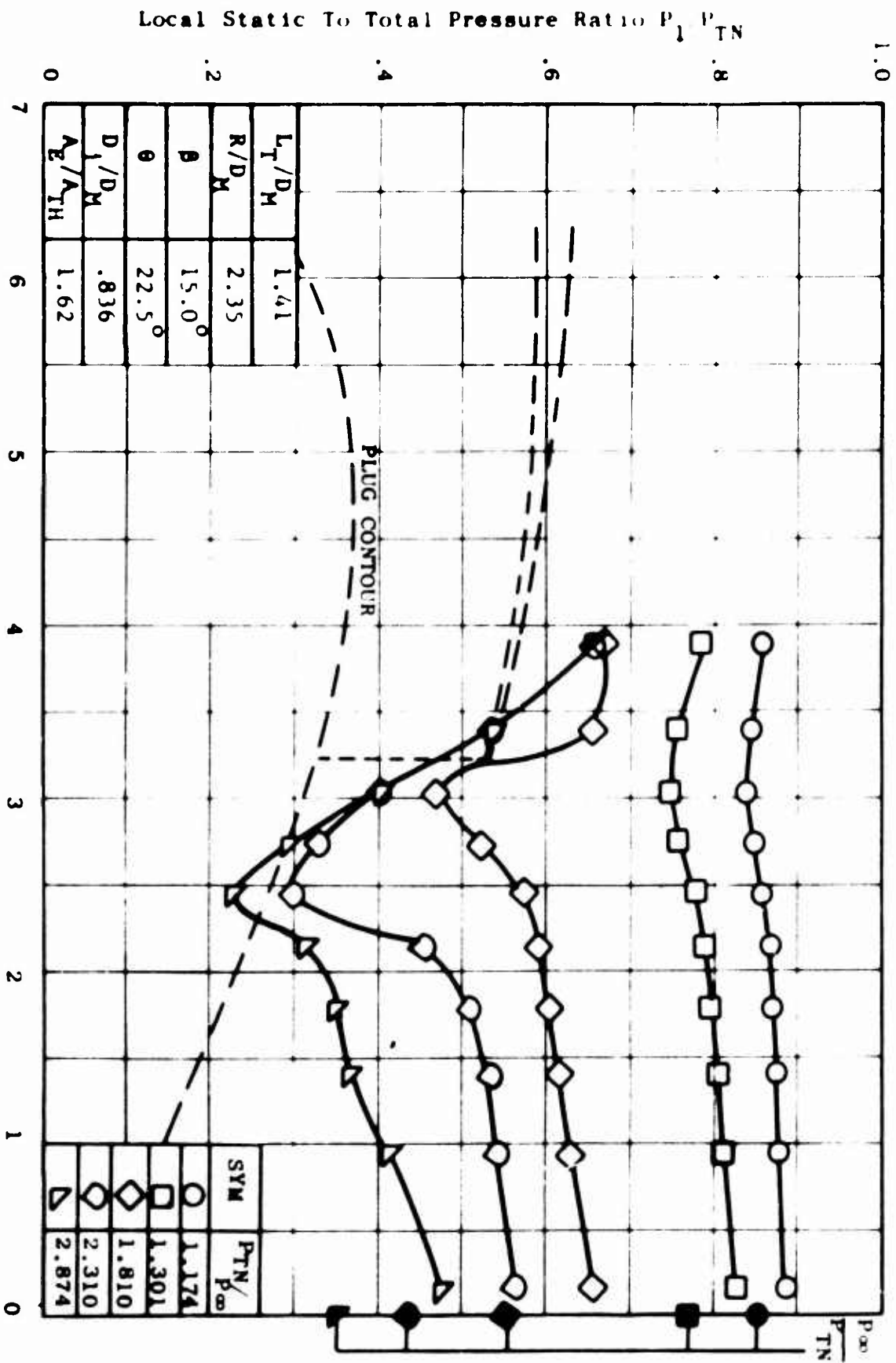


Figure 85. Plug Pressure Distribution as a Function of Axial Distance and Pressure Ratio-Model 12, Mach No. = 0.



Axial Distance Along Centerline - In.

Figure 86. Plug Pressure Distribution as a Function of Axial Distance and Pressure Ratio-Model 13, Mach No. = 0.

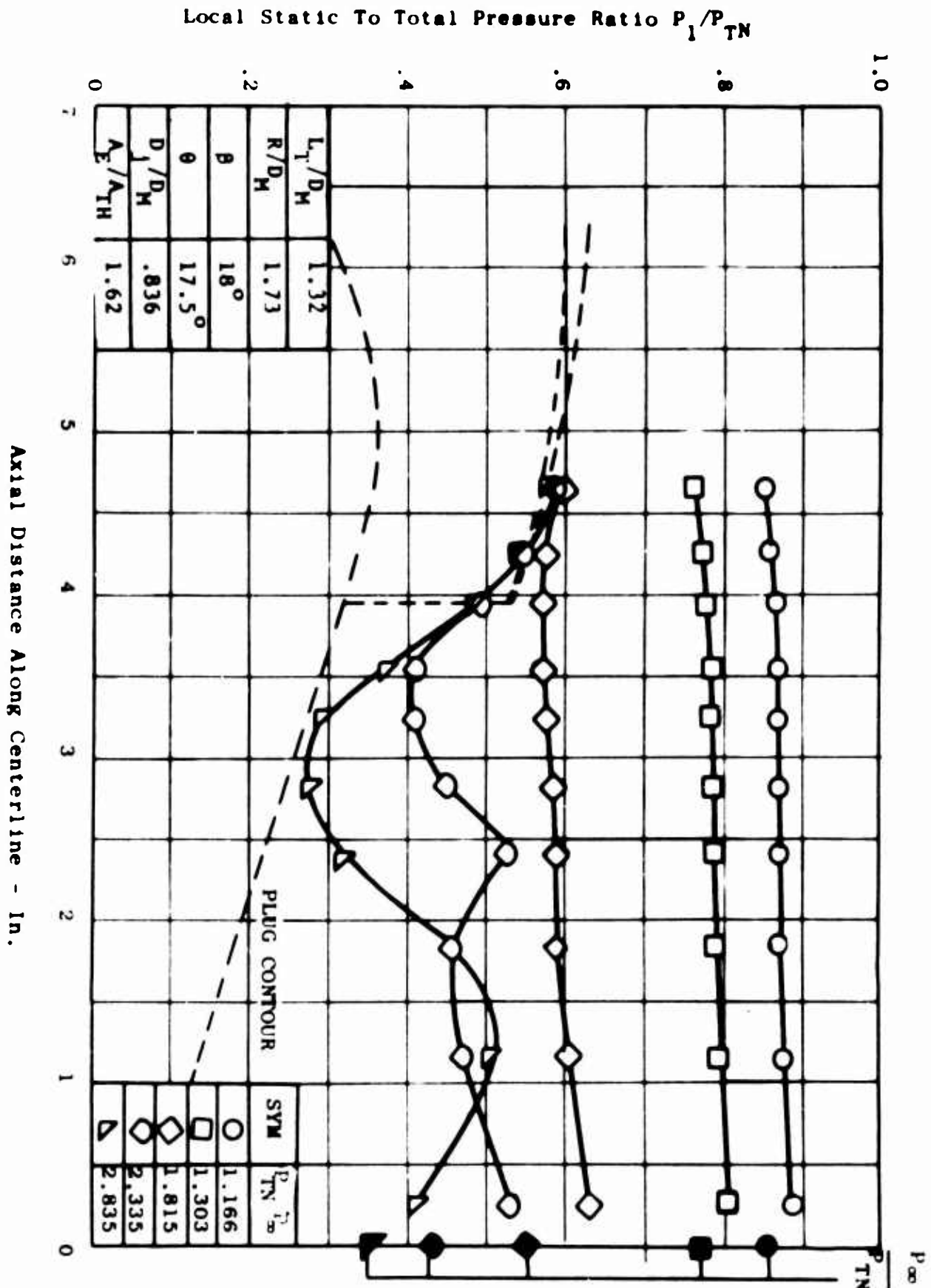


Figure 87. Plug Pressure Distribution as a Function of Axial Distance and Pressure Ratio-Model 14, Mach No. = 0.

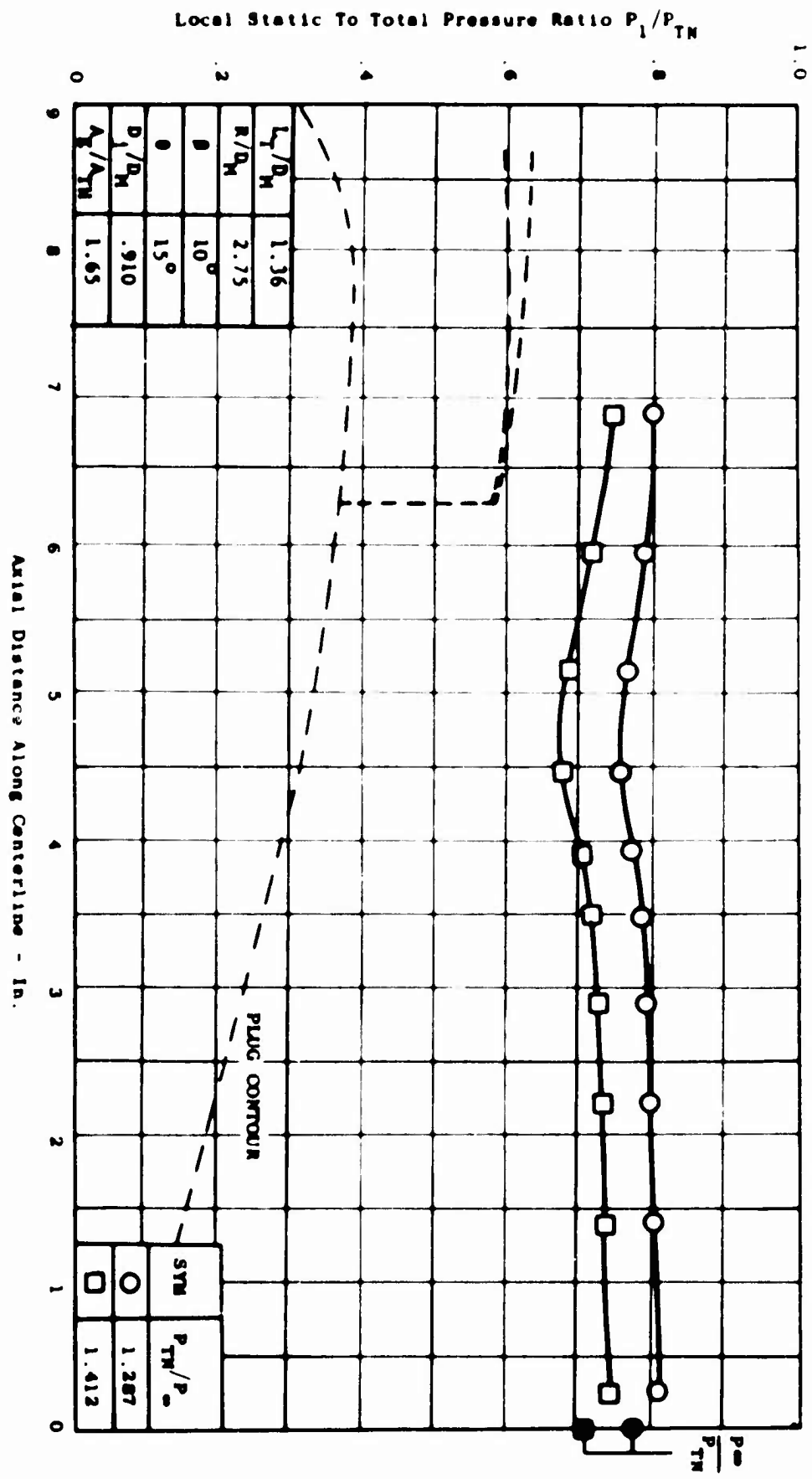


Figure 88. Plug Pressure Distribution
as a Function of Axial
Distance and Pressure Ratio-
Model 6, Mach No. = .4.

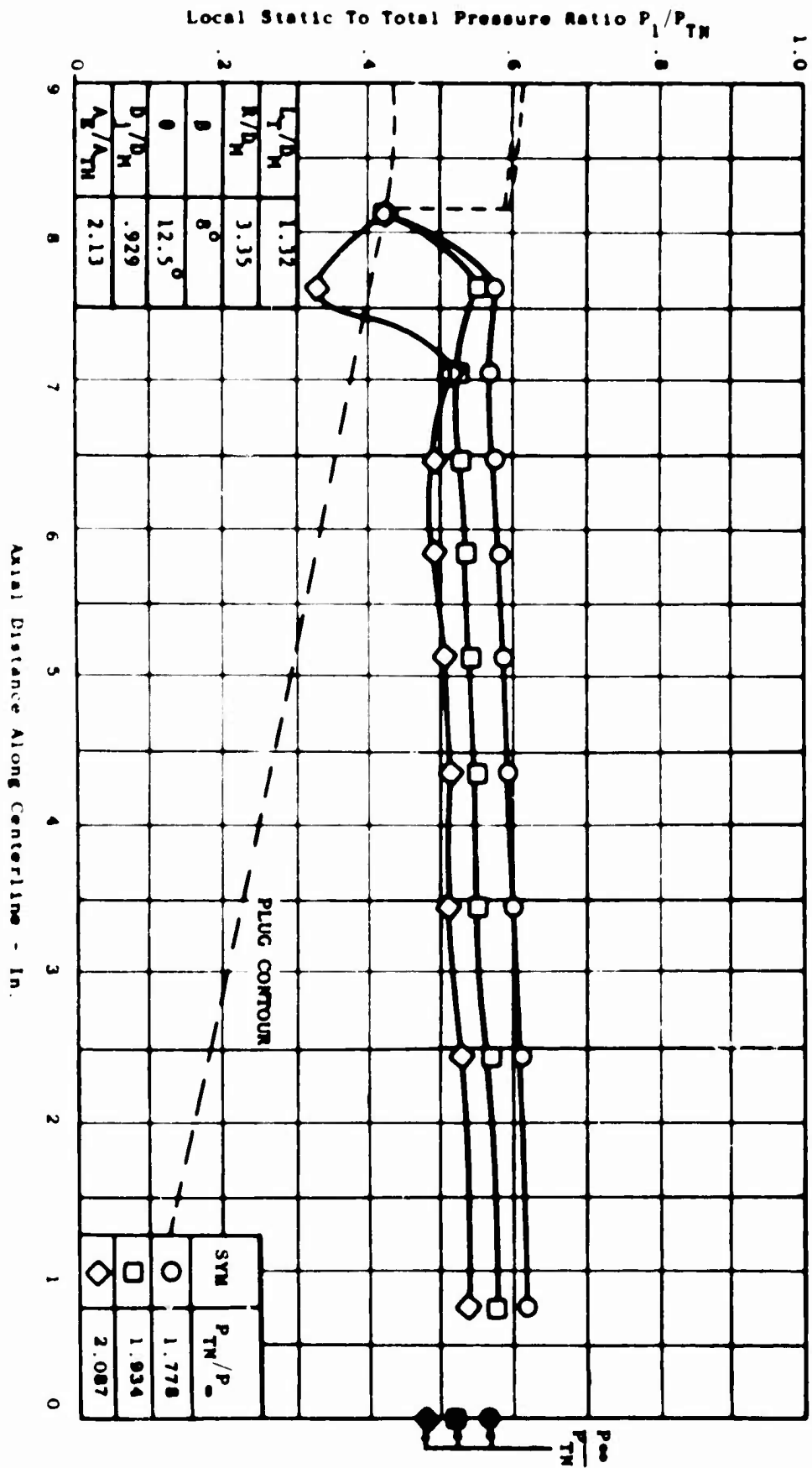


Figure 89. Plug Pressure Distribution
as a Function of Axial
Distance and Pressure Ratio-
Model 4, Mach No. = .8.

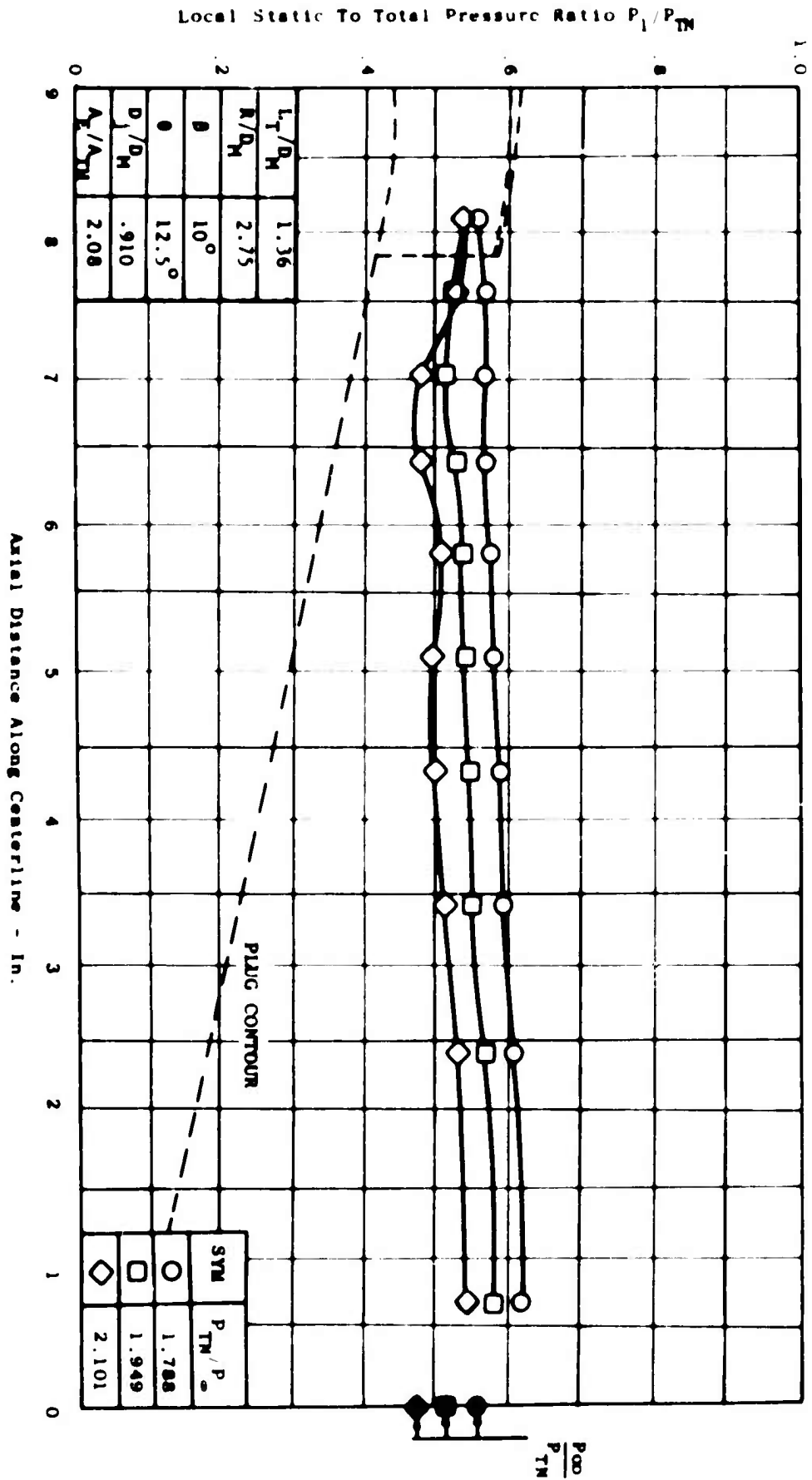


Figure 90. Plug Pressure Distribution
as a Function of Axial
Distance and Pressure Ratio-
Model 5, Mach No. = .8.

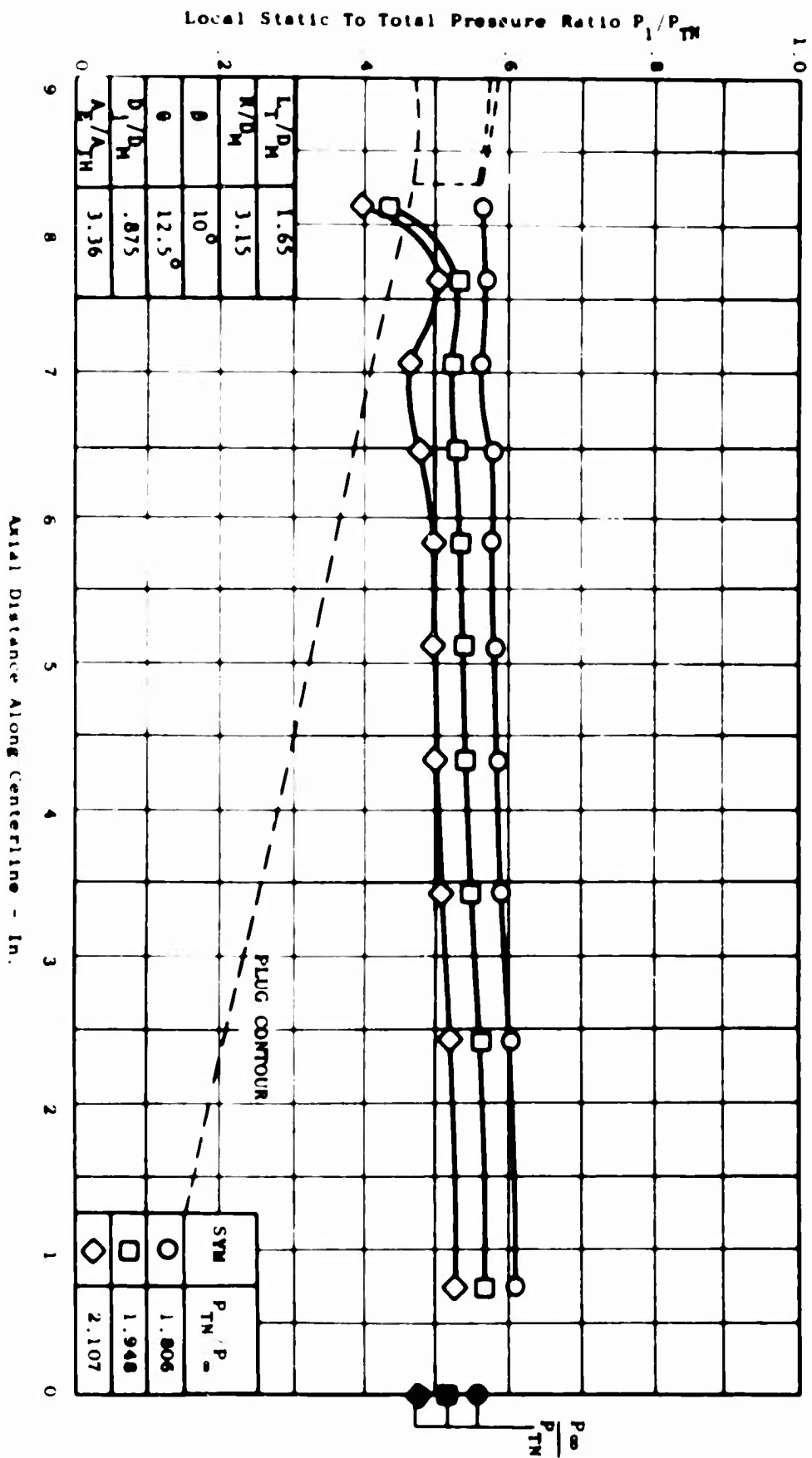


Figure 91. Plug Pressure Distribution
as a Function of Axial
Distance and Pressure Ratio-
Model 7, Mach No. = .8.

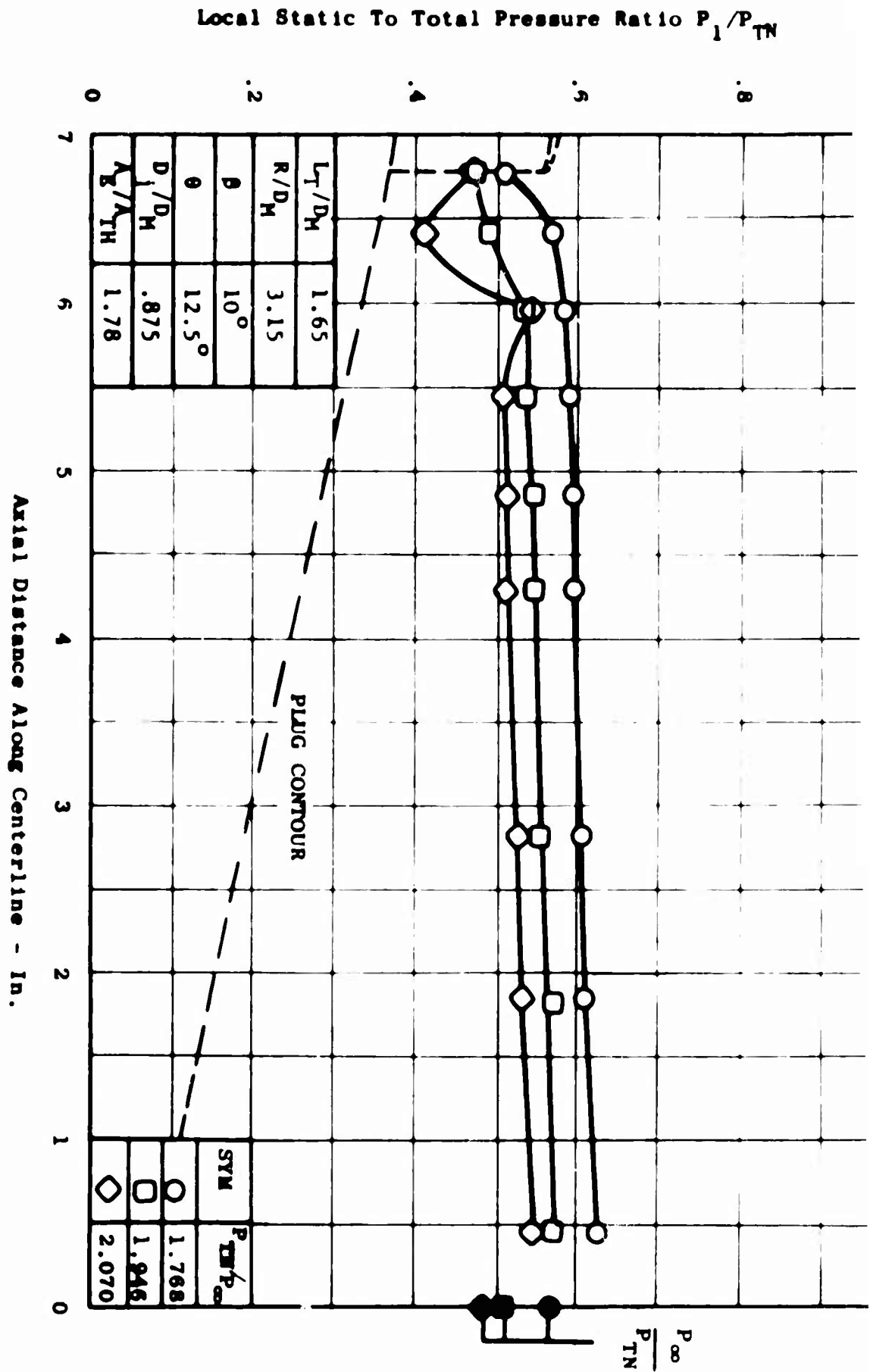


Figure 92. Plug Pressure Distribution as a Function of Axial Distance and Pressure Ratio-Model 7A, Mach No. = .8.

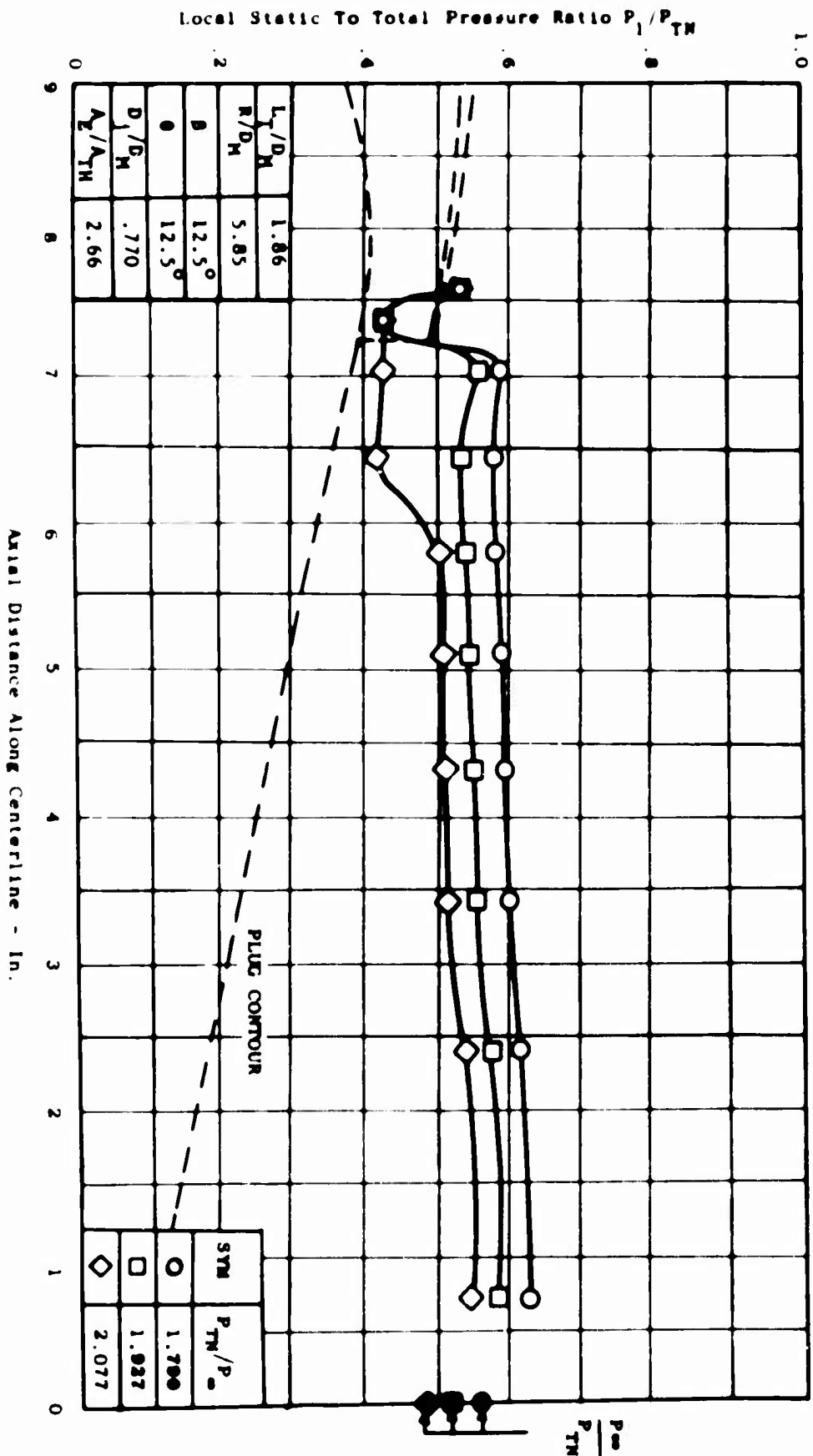


Figure 93. Plug Pressure Distribution as a Function of Axial Distance and Pressure Ratio-Model 8, Mach No. = .8.

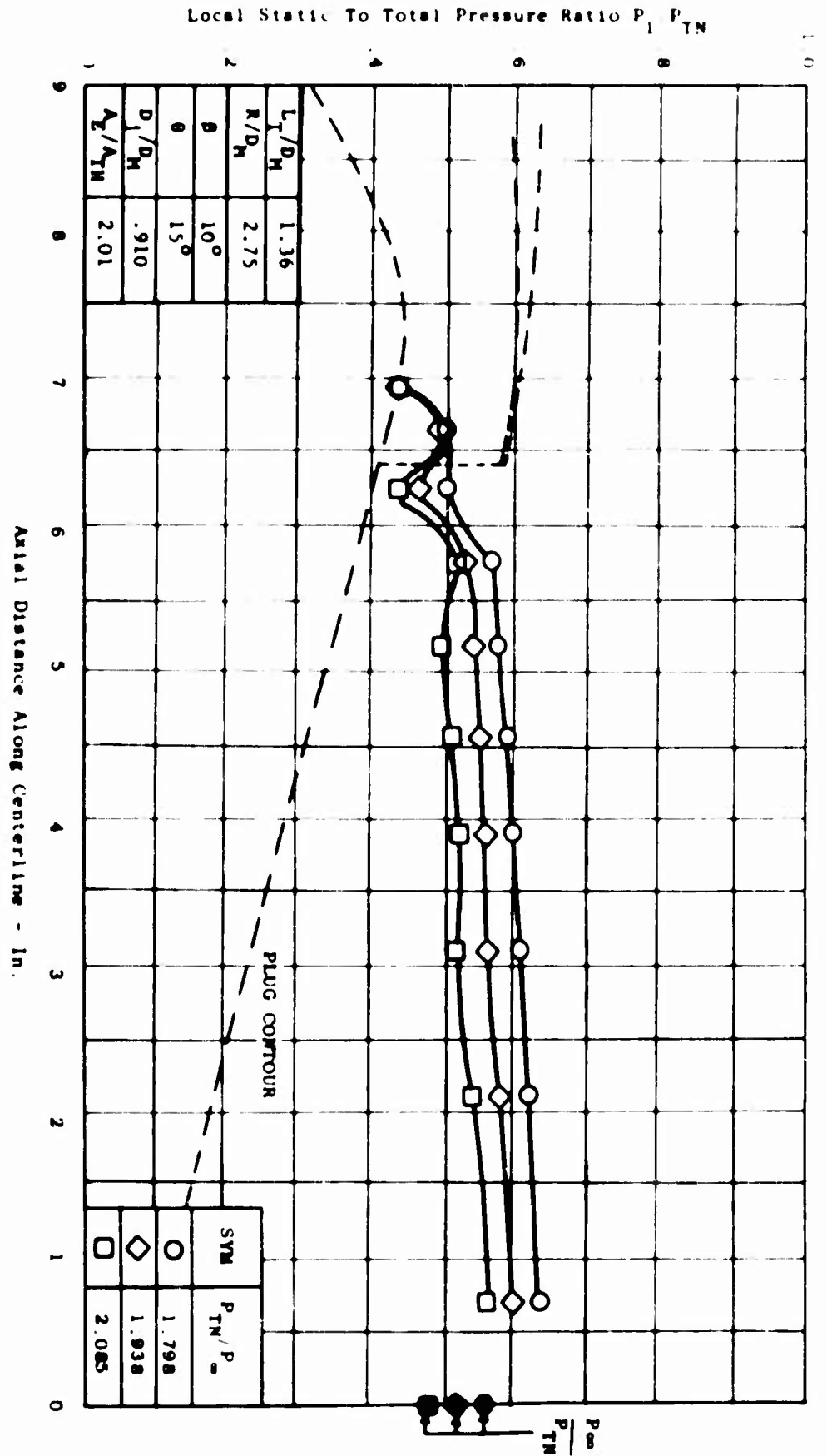


Figure 94. Plug Pressure Distribution
as a Function of Axial
Distance and Pressure Ratio-
Model 9, Mach No. =.8.

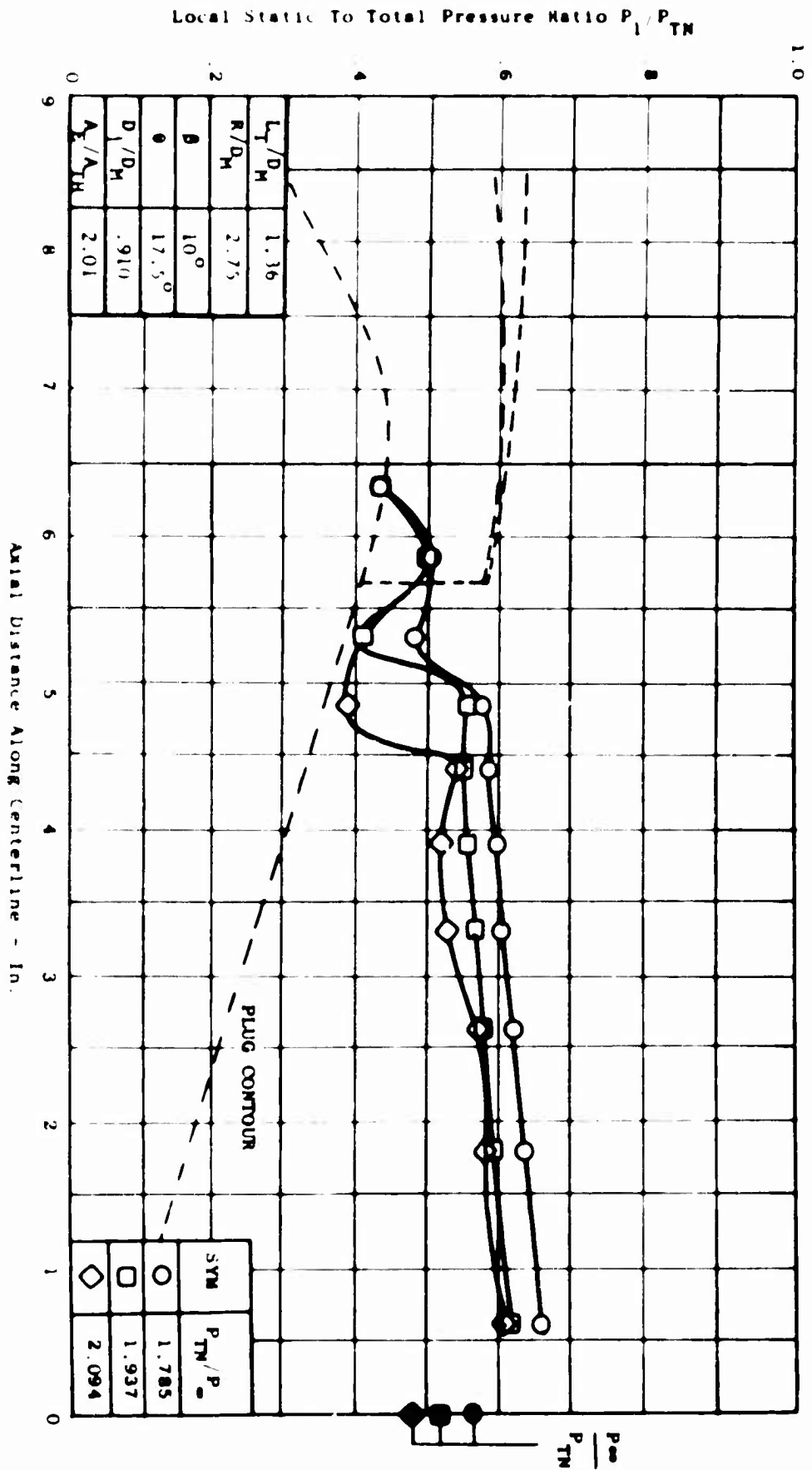


Figure 95. Plug Pressure Distribution
as a Function of Axial
Distance and Pressure Ratio-
Model 10, Mach No. = .8.

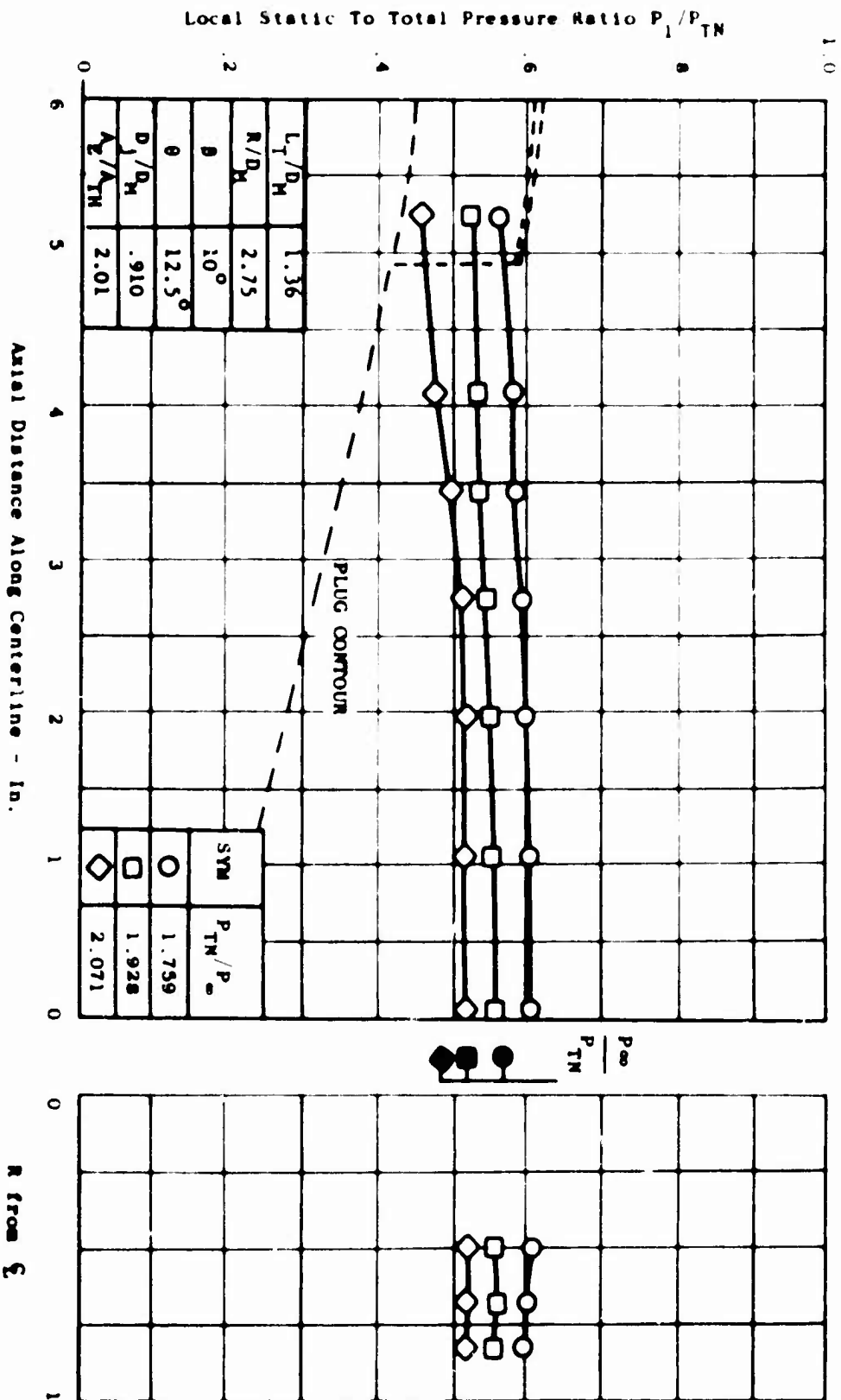


Figure 96. Plug Pressure Distribution as a Function of Axial Distance and Pressure Ratio-Model 10A, Mach = .8.

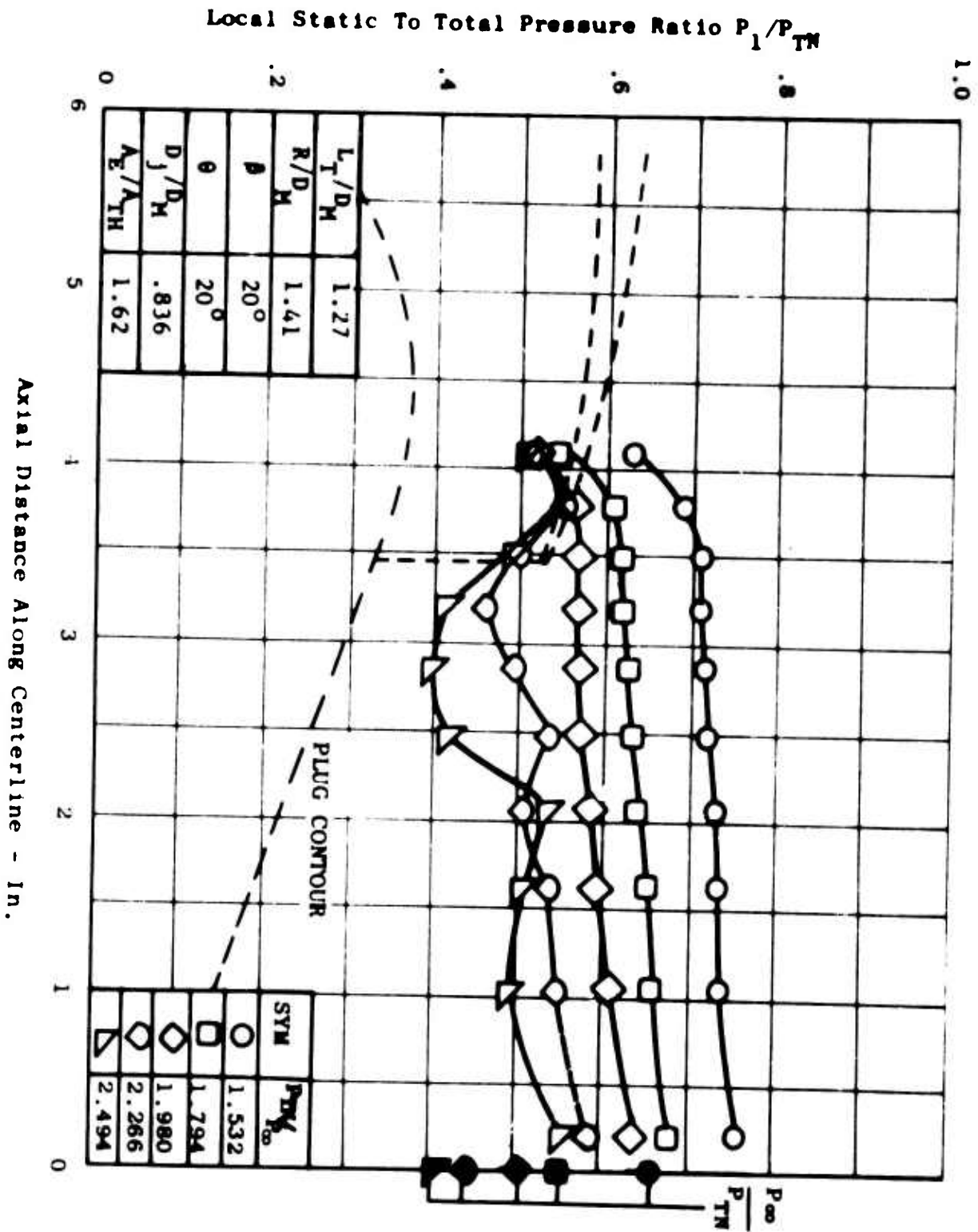


Figure 97. Plug Pressure Distribution as a Function of Axial Distance and Pressure Ratio-Model 11, Mach No. = .8.

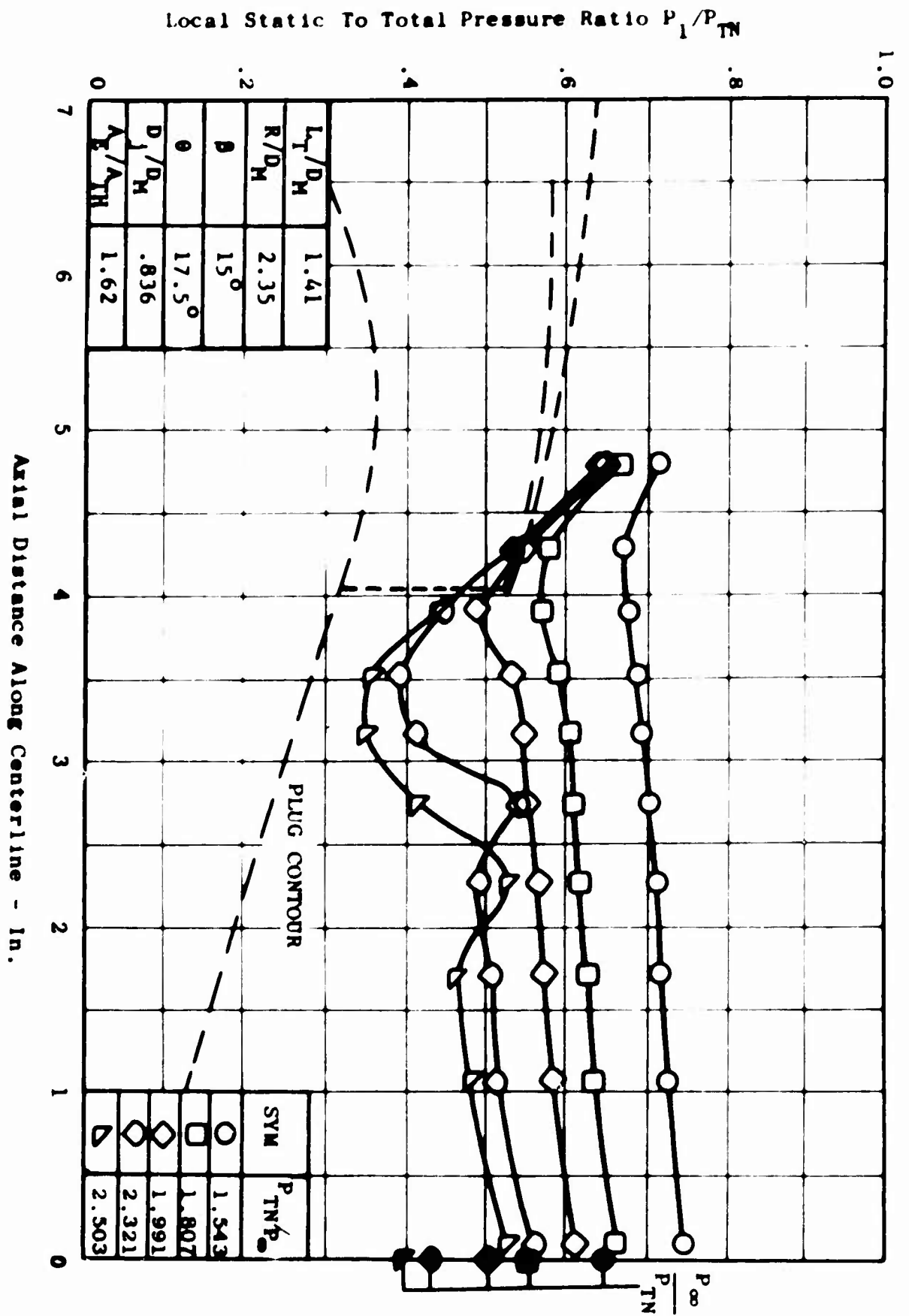


Figure 98. Plug Pressure Distribution
as a Function of Axial
Distance and Pressure Ratio-
Model 12, Mach No. = .8.

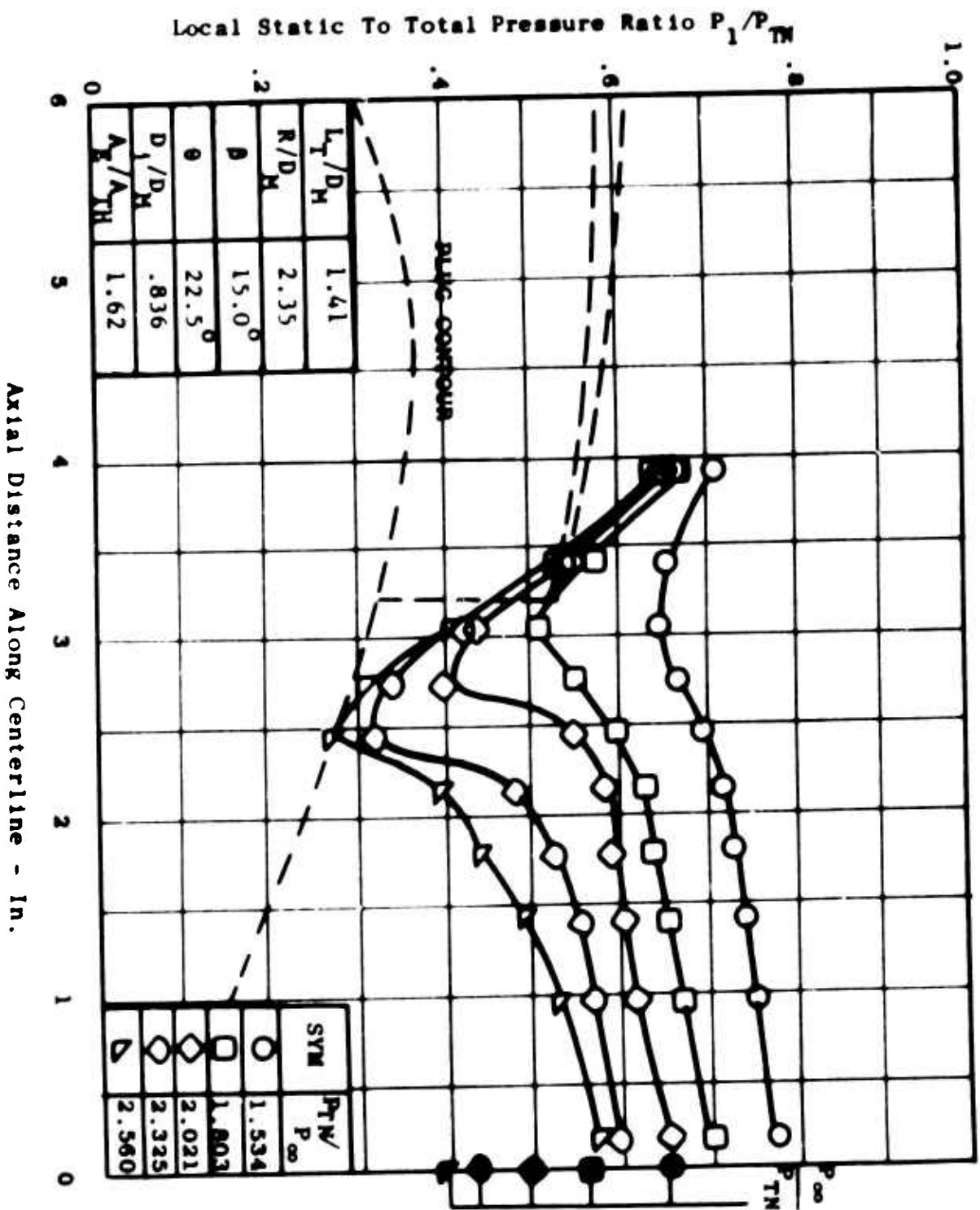


Figure 99. Plug Pressure Distributions as a Function of Axial Distance and Pressure Ratio, Model 13, Mach No. = .8.

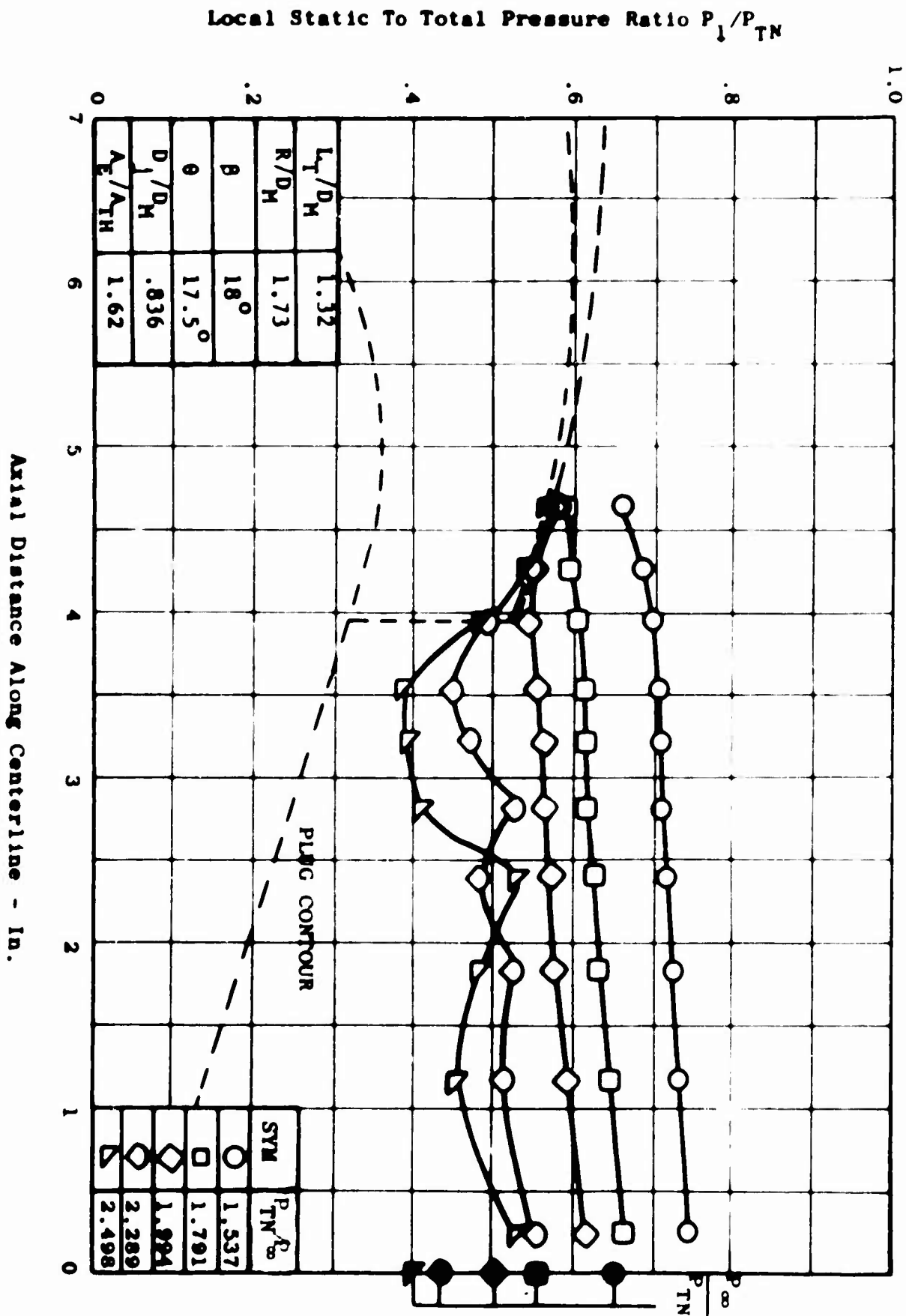


Figure 100. Plug Pressure Distribution
as a Function of Axial
Distance and Pressure Ratio-
Model 14, Mach No. = .8.

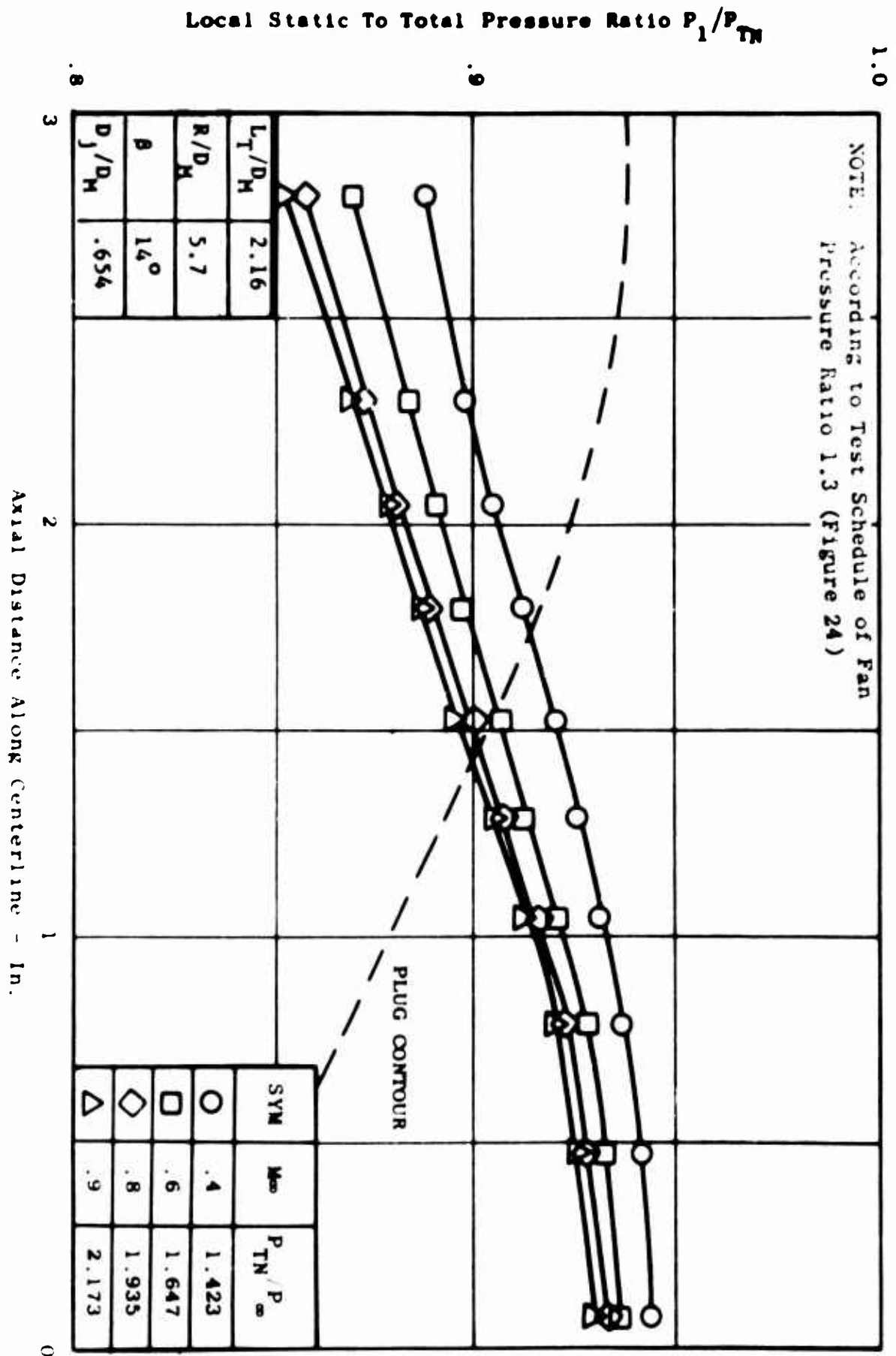


Figure 101. Plug Pressure Distribution as a Function of Axial Distance and Pressure Ratio-Model 1, Mach No. = All,

Local Static To Total Pressure Ratio P_1/P_{TN}

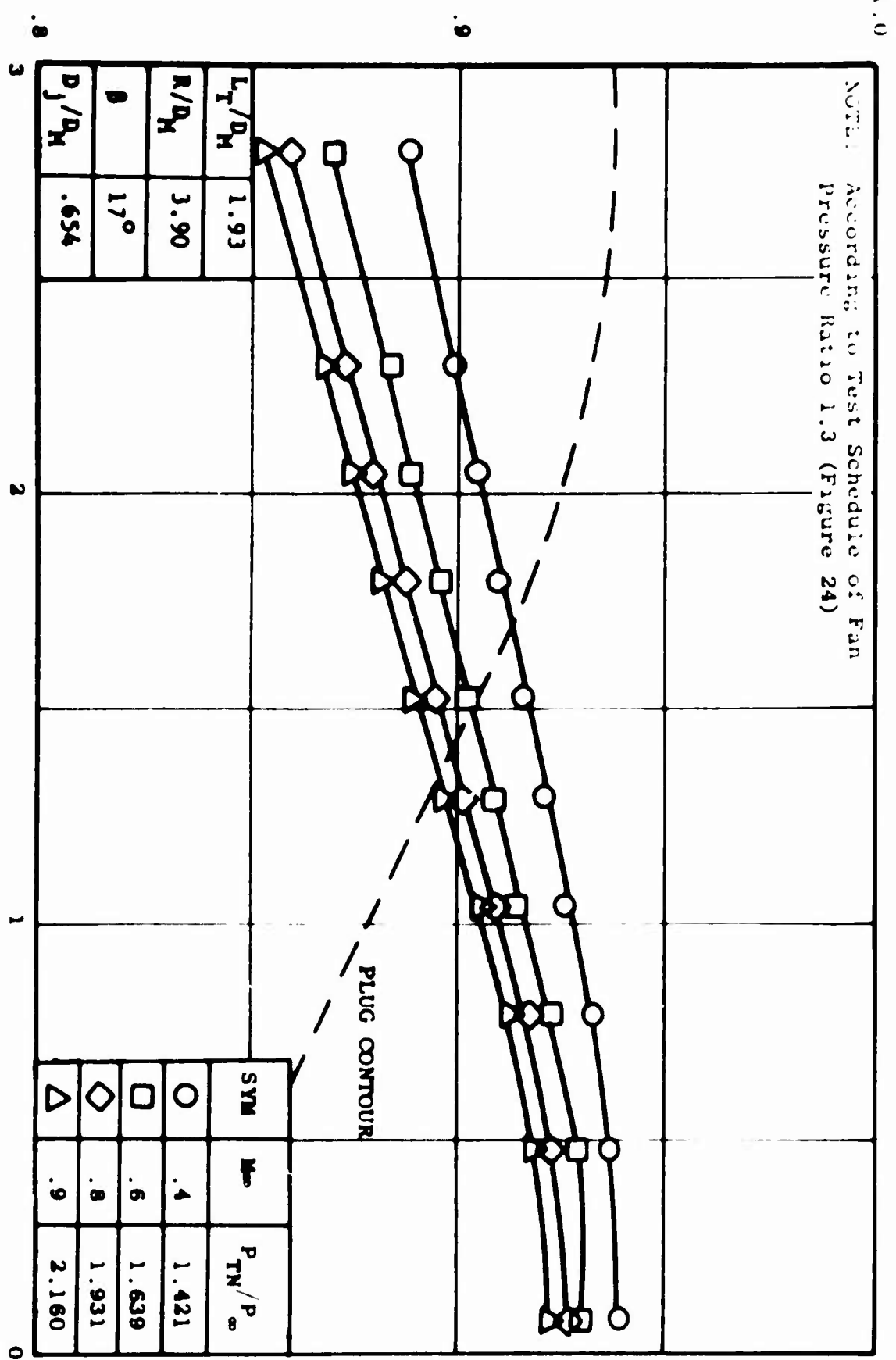


Figure 102. Nozzle Plug Static Pressure Distribution - Model 2, Mach No = All

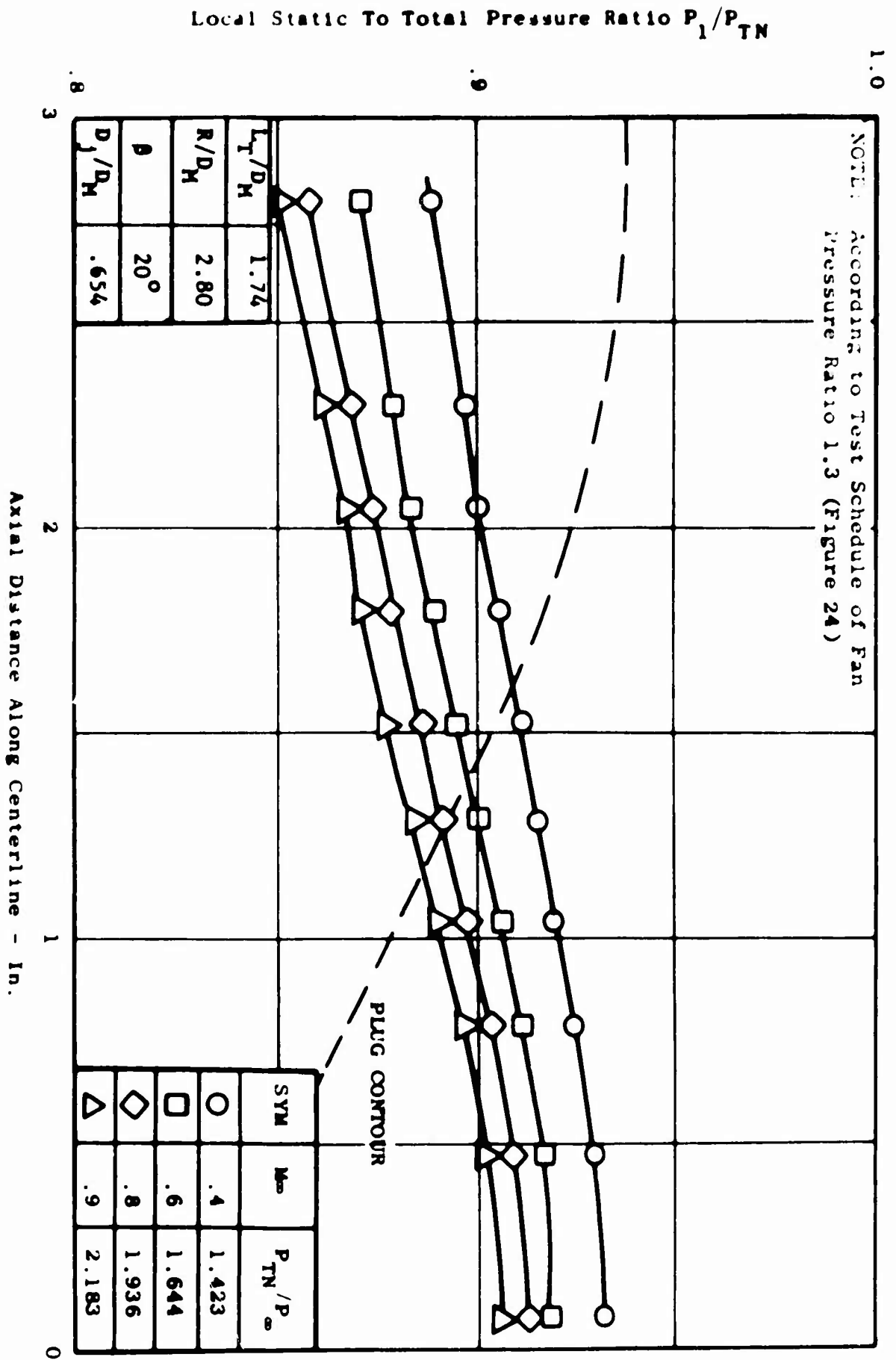


Figure 103. Nozzle Plug Static Pressure Distribution- Model 3, Mach No - All.

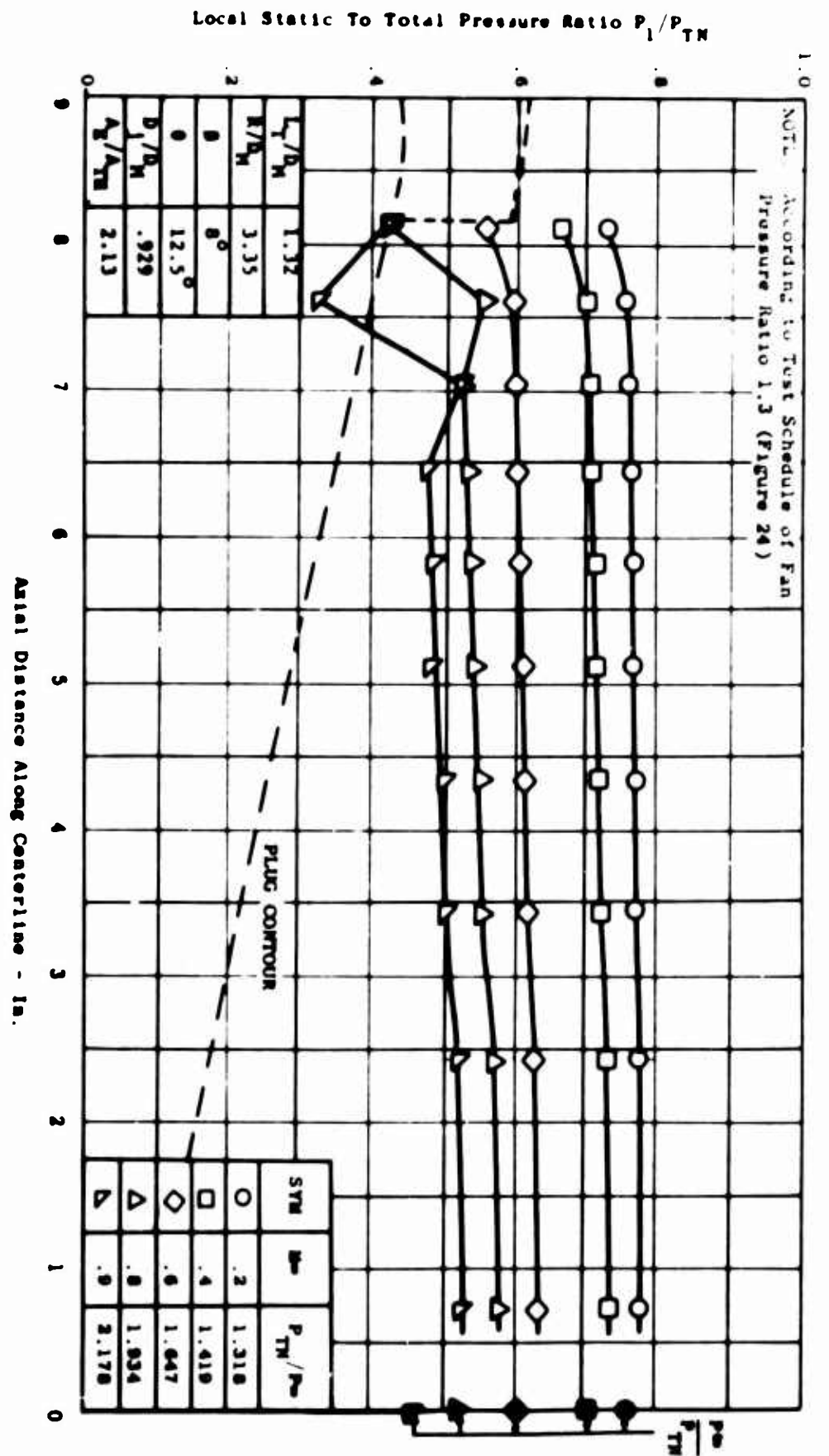


Figure 104. Nozzle Plug Static Pressure Distribution - Model 4, Mach No = All.

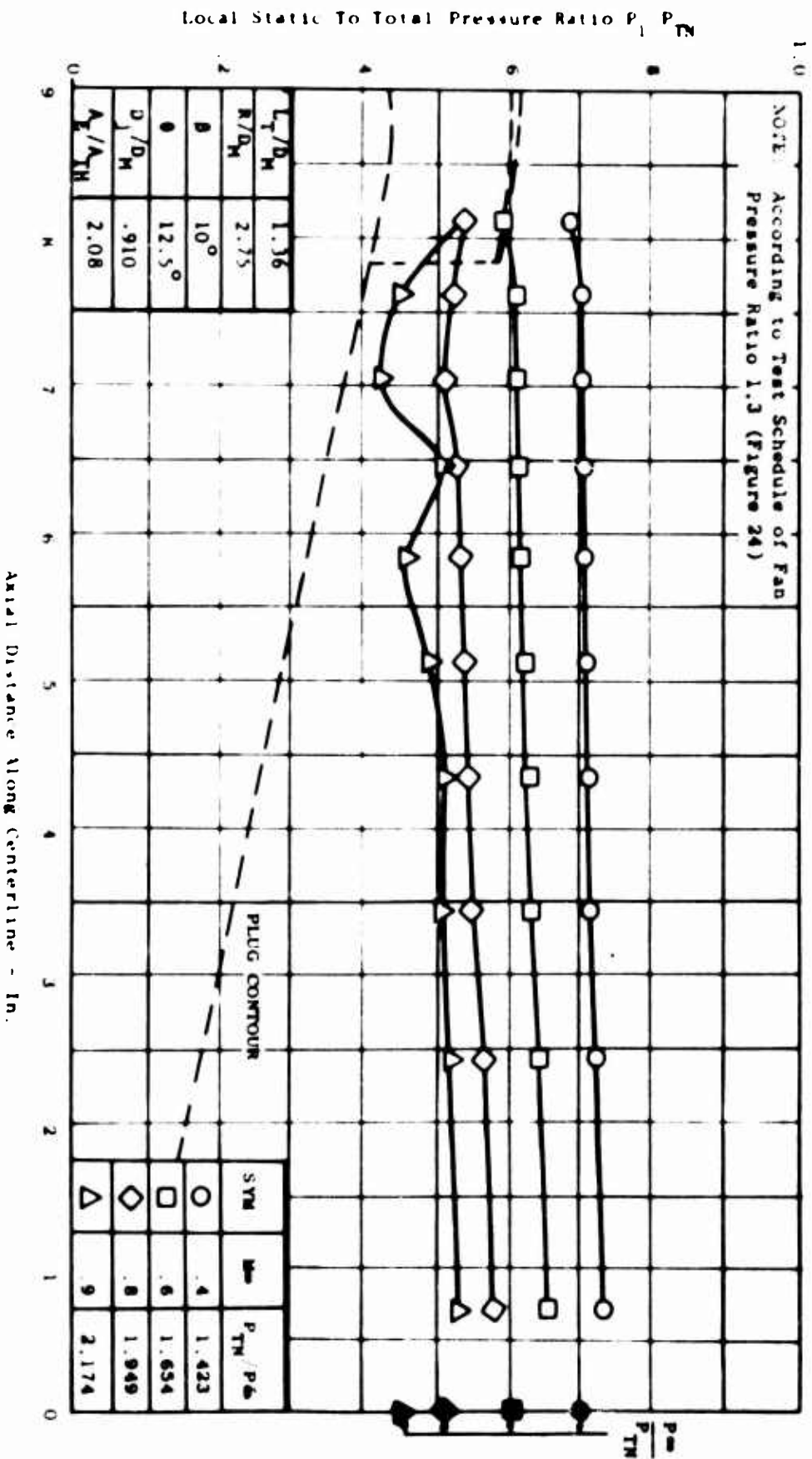


Figure 105. Nozzle Plug Static Pressure Distribution - Model 5, Mach No. = All

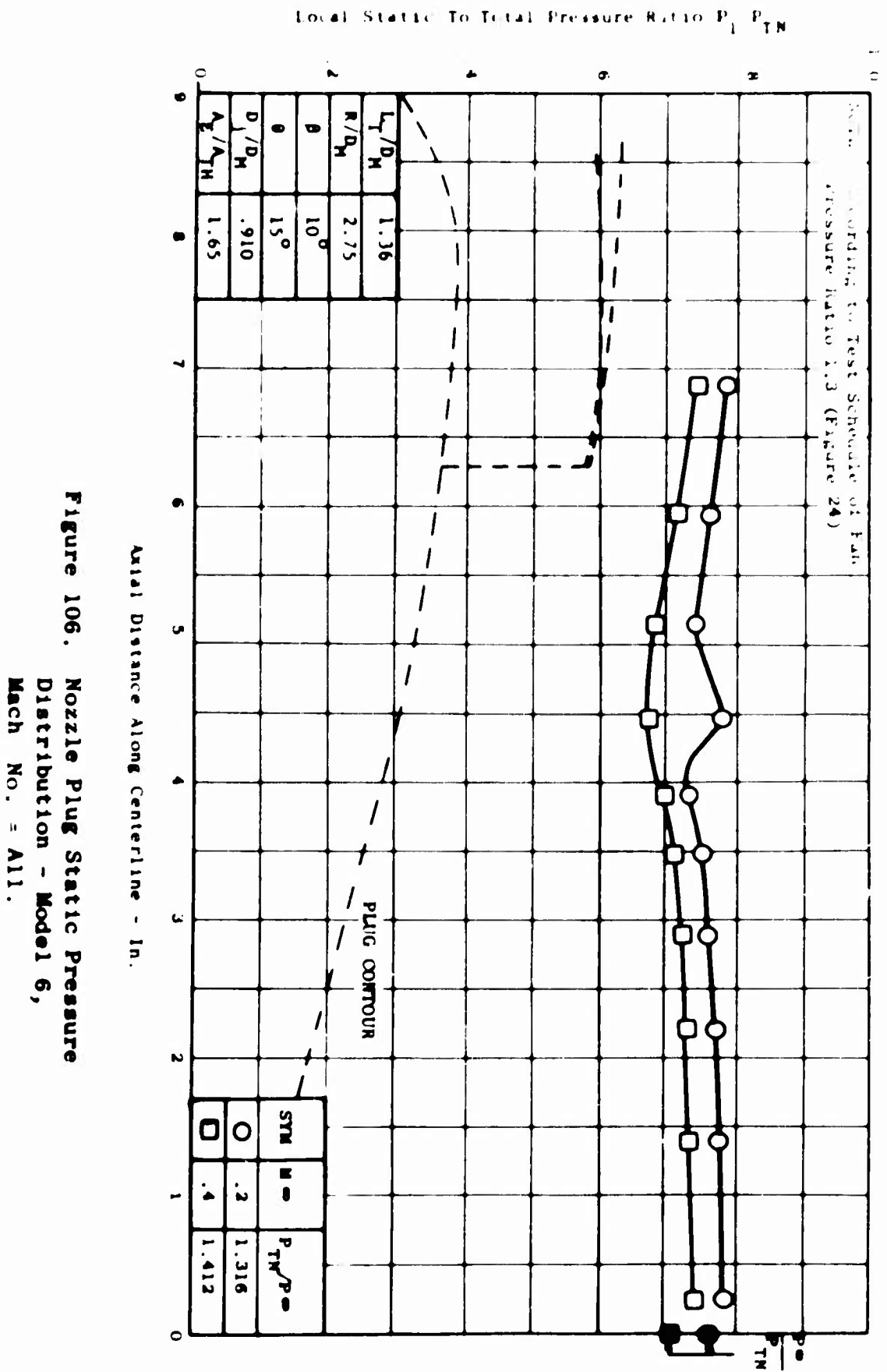


Figure 106. Nozzle Plug Static Pressure
Distribution - Model 6,
Mach No. = All.

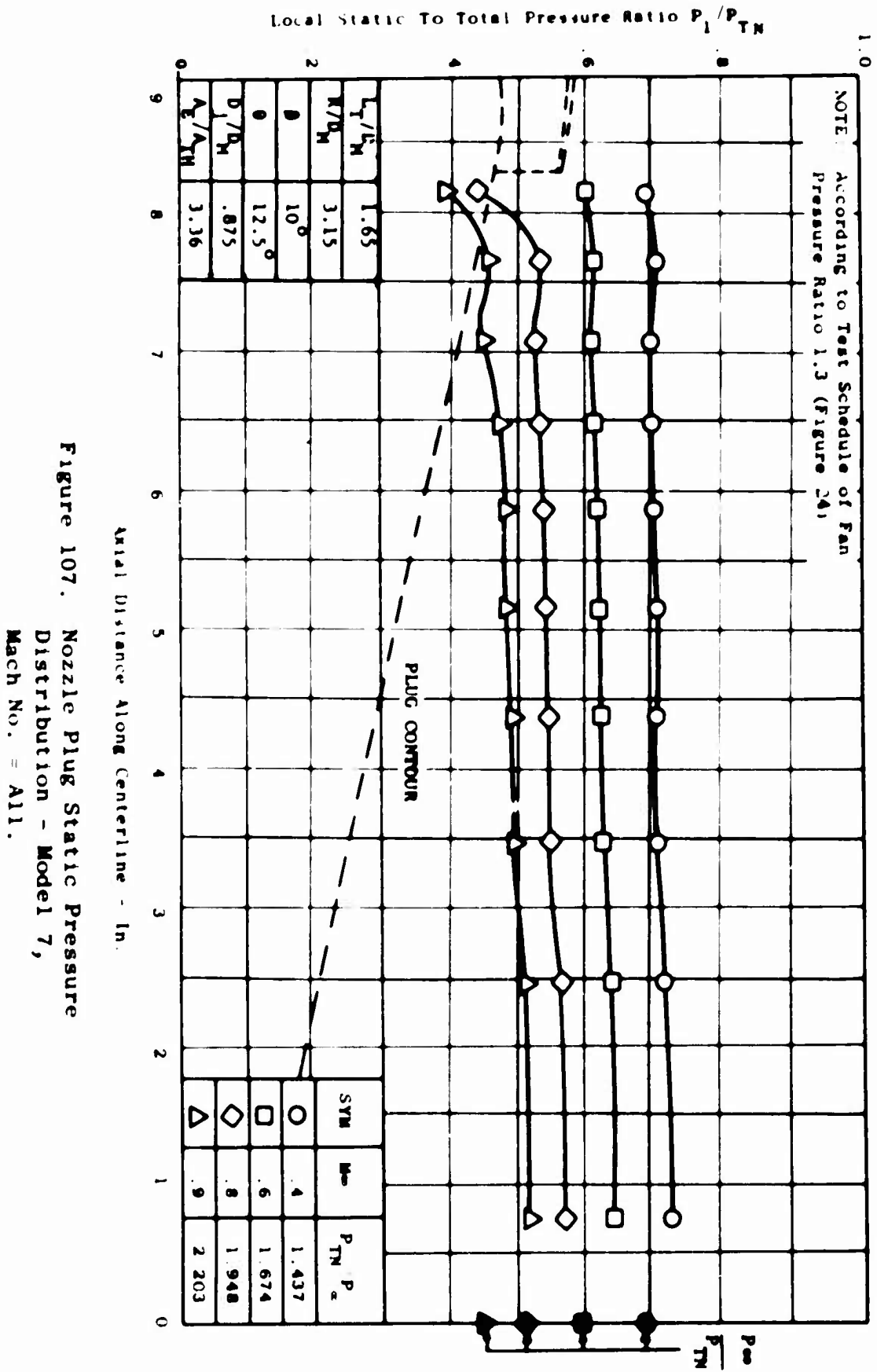


Figure 107. Nozzle Plug Static Pressure Distribution - Model 7, Mach No. = All.

Local Static To Total Pressure Ratio P_1/P_{TN}

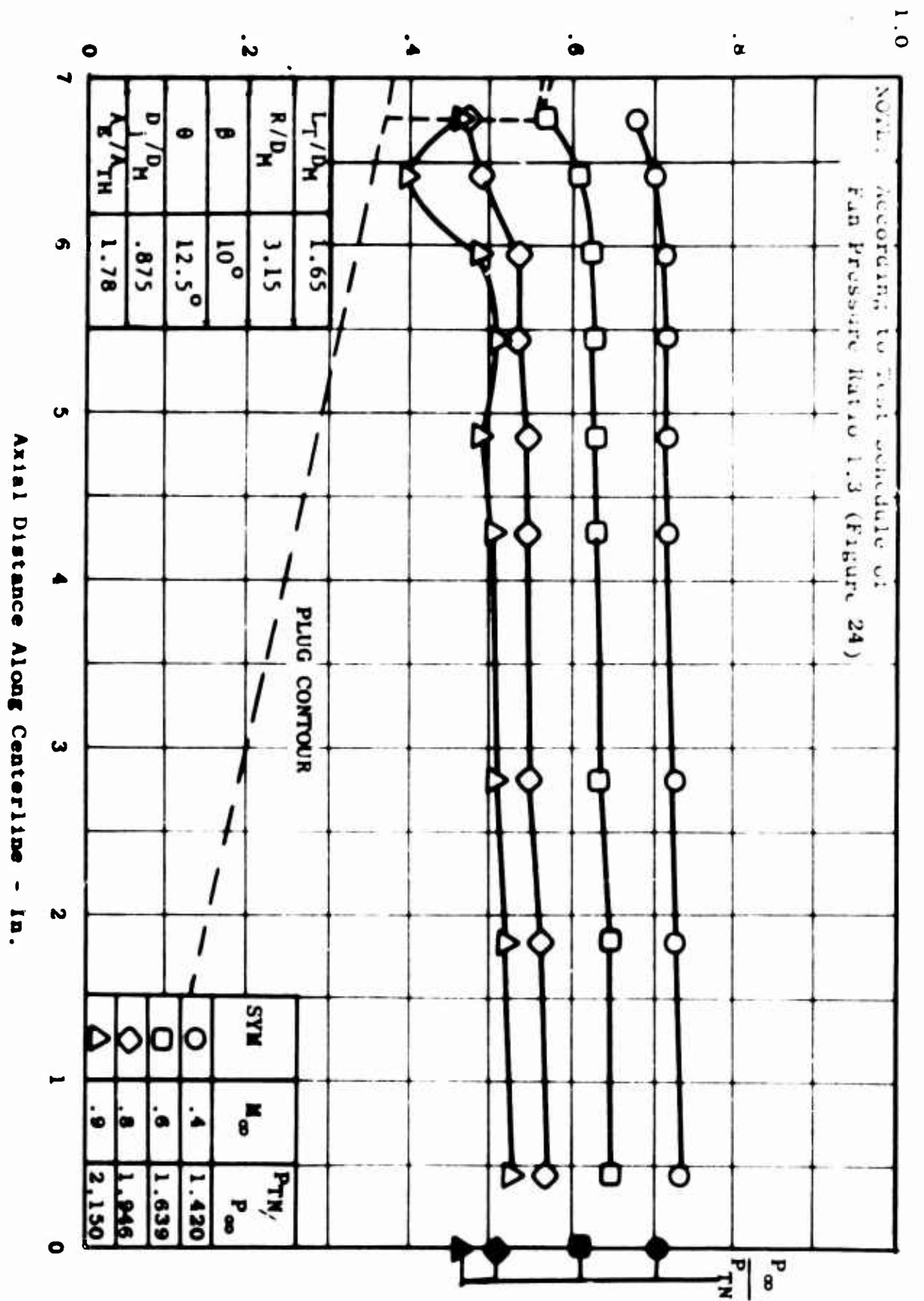


Figure 108. Plug Pressure Distribution as a Function of Axial Distance and Pressure Ratio-Model 7A, Mach No. = 11.1.

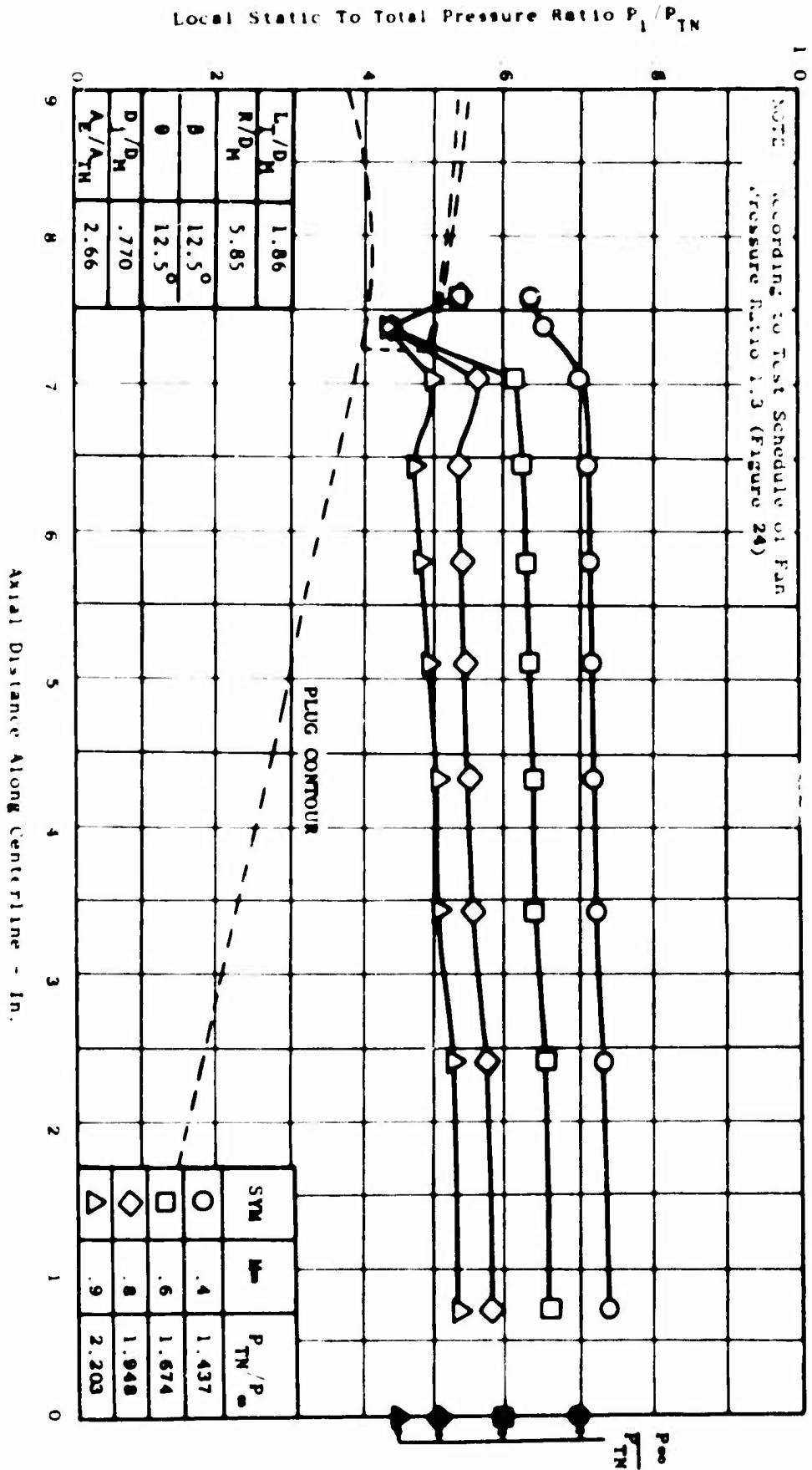


Figure 109. Nozzle Plug Static Pressure Distribution - Model 8, Mach No = All.

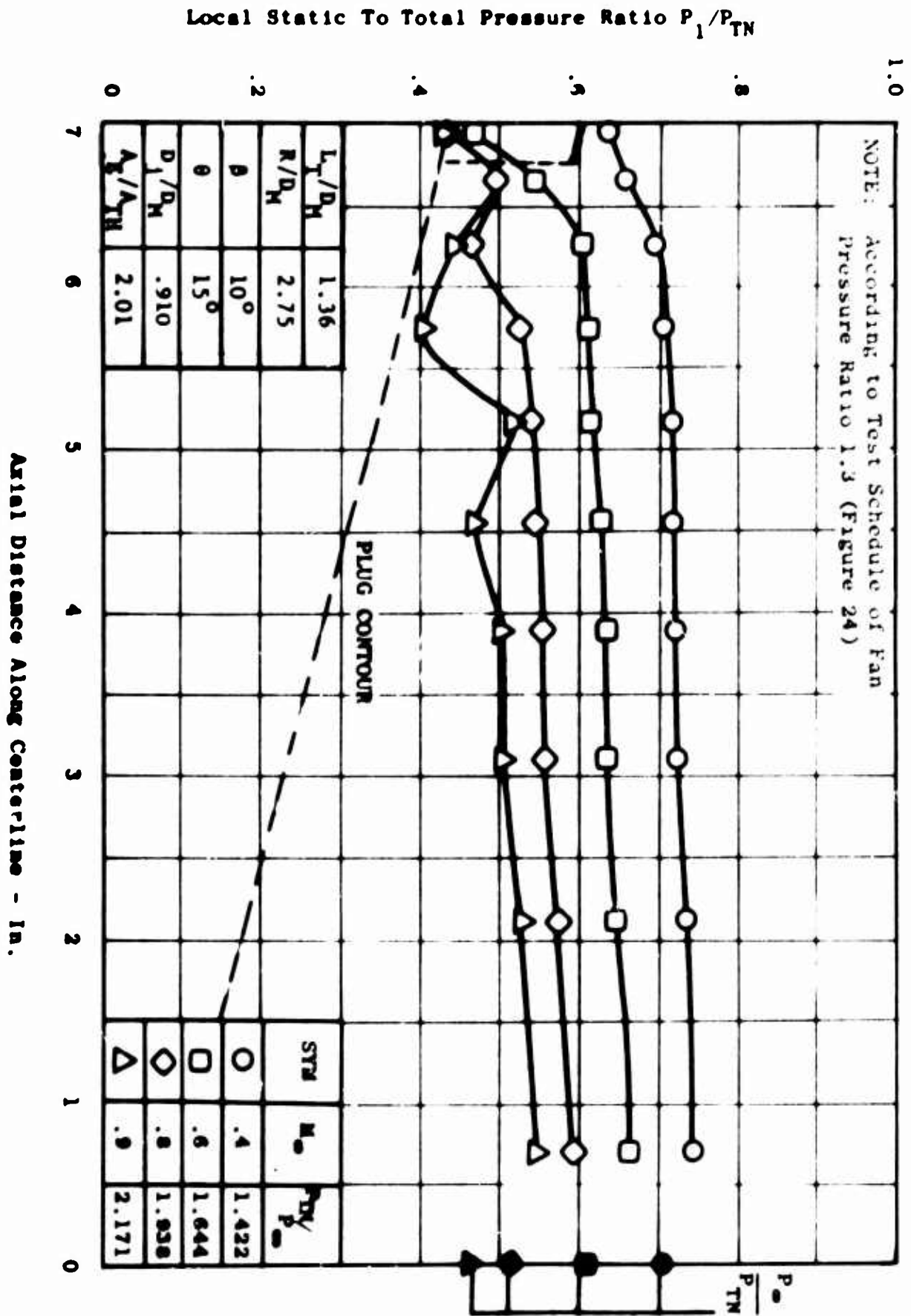


Figure 110. Plug Pressure Distribution as a Function of Axial Distance and Pressure Ratio-Model 9, Mach No. = All.

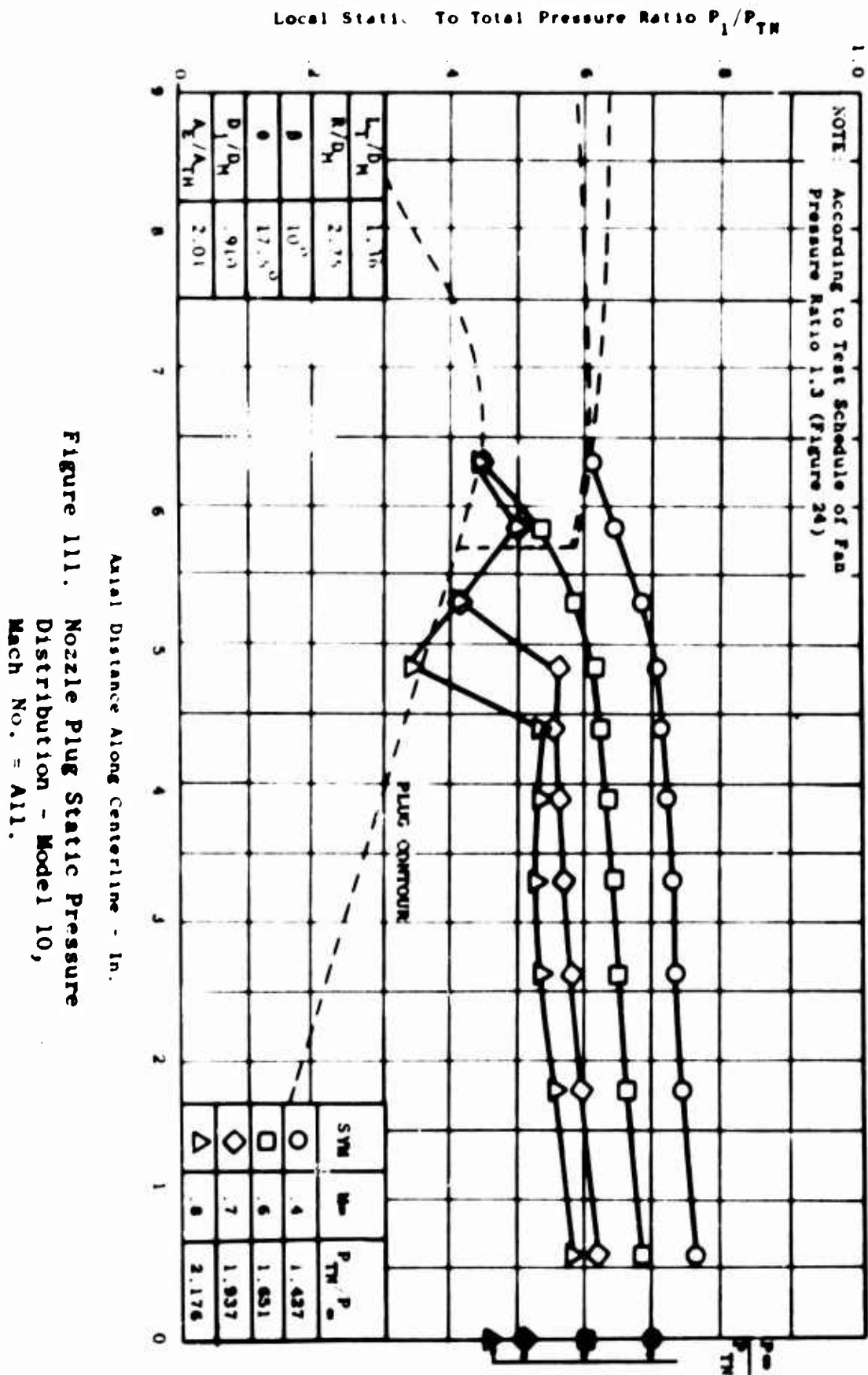


Figure 111. Nozzle Plug Static Pressure
Distribution - Model 10,
Mach No. = 1.1.

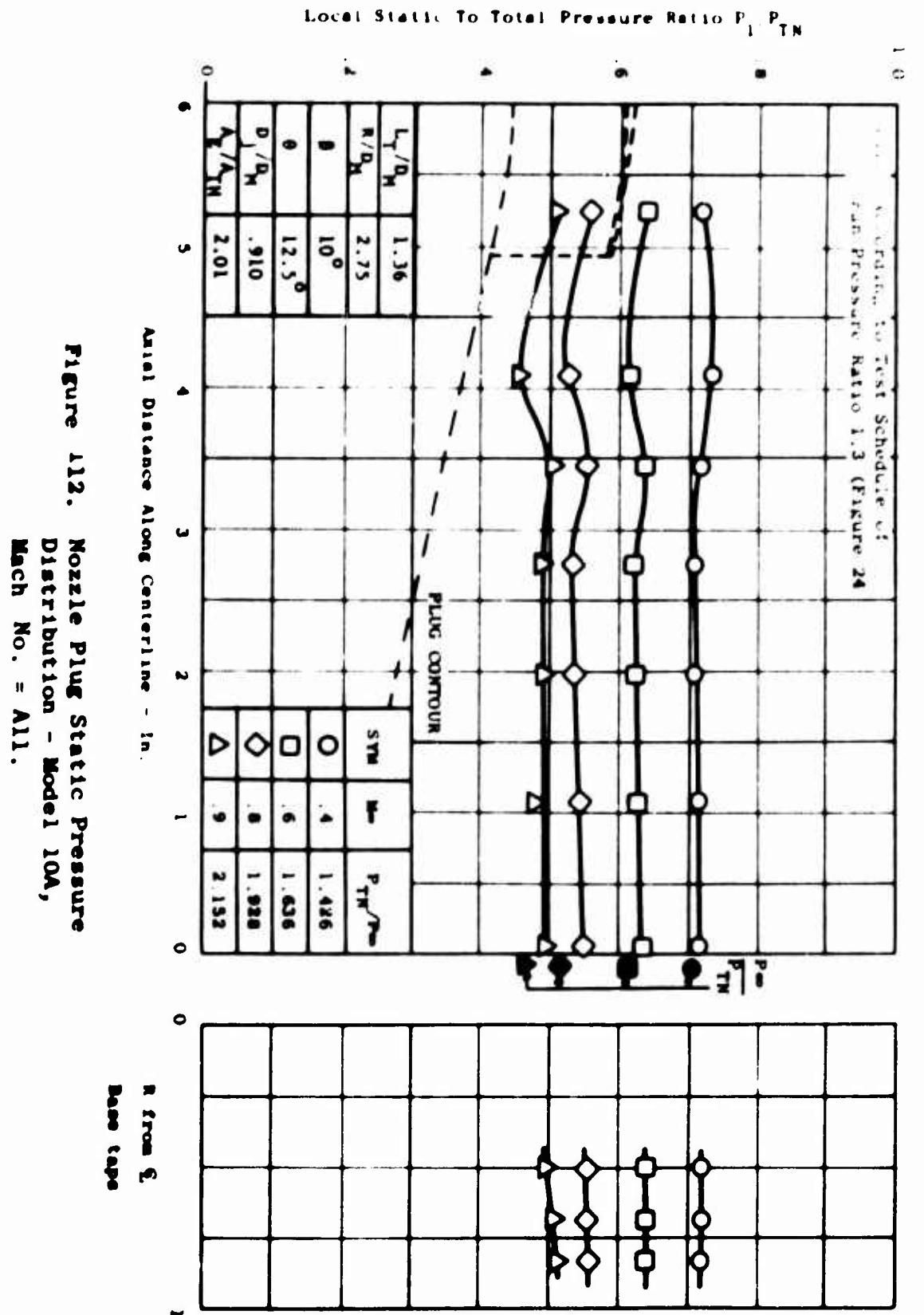


Figure 112. Nozzle Plug Static Pressure
Distribution - Model 10A,
Mach No. = 11.1.

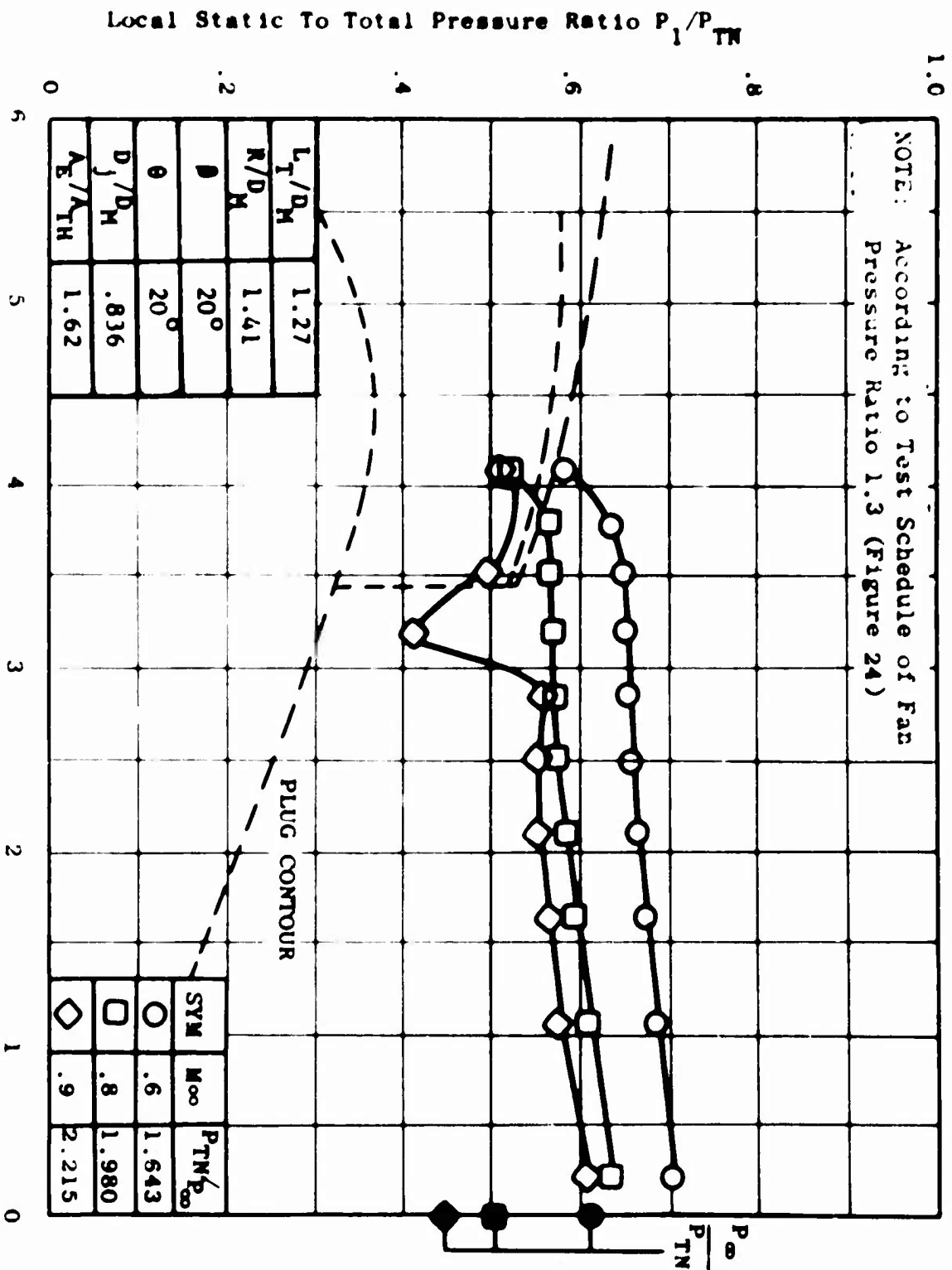


Figure 113. Plug Pressure Distribution as a Function of Axial Distance and Pressure Ratio-Model 11, Mach No. = A11

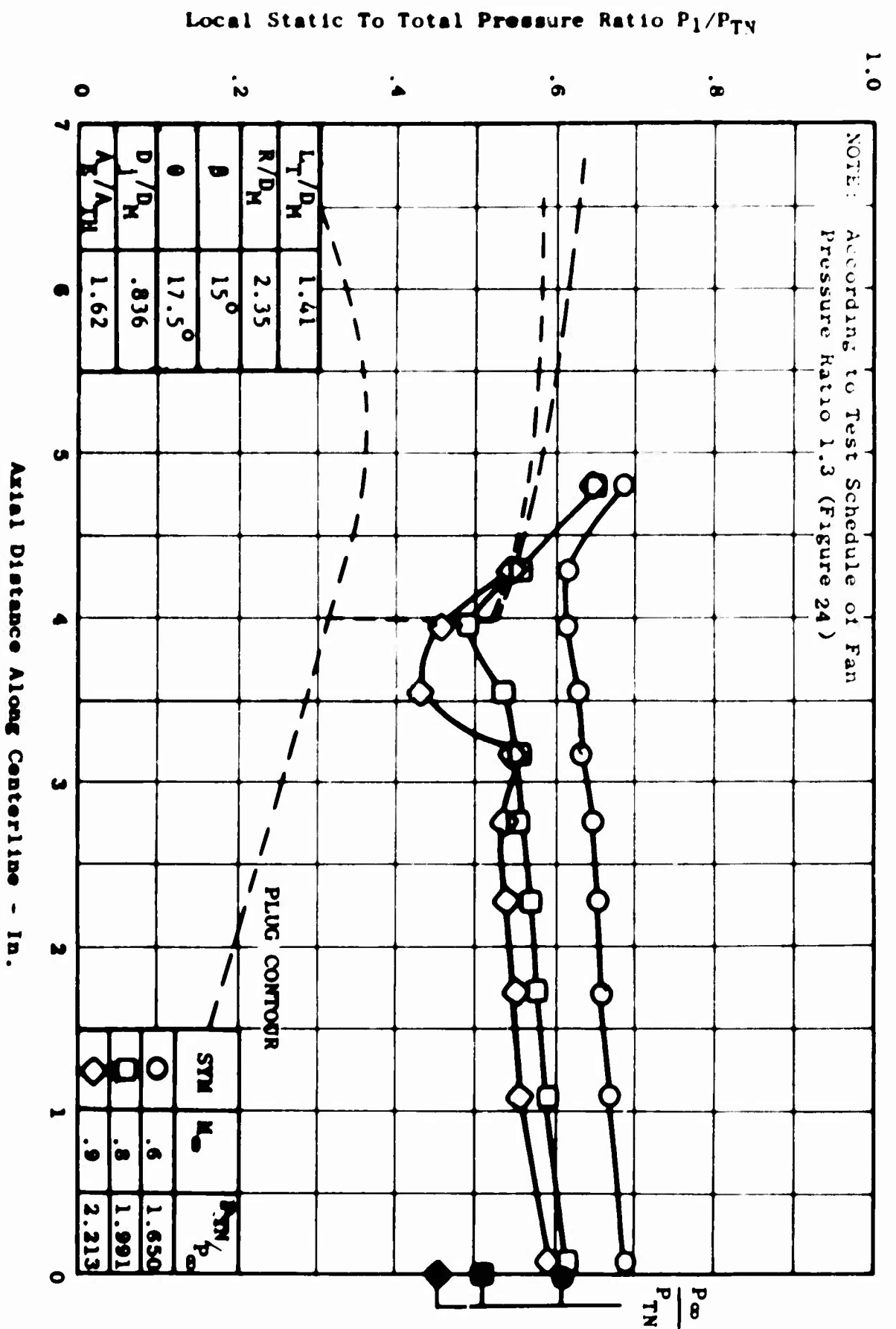


Figure 114. Plug Pressure Distribution
as a Function of Axial
Distance and Pressure Ratio-
Model 12, Mach No. = All.

Local Static To Total Pressure Ratio P_1/P_{TN}

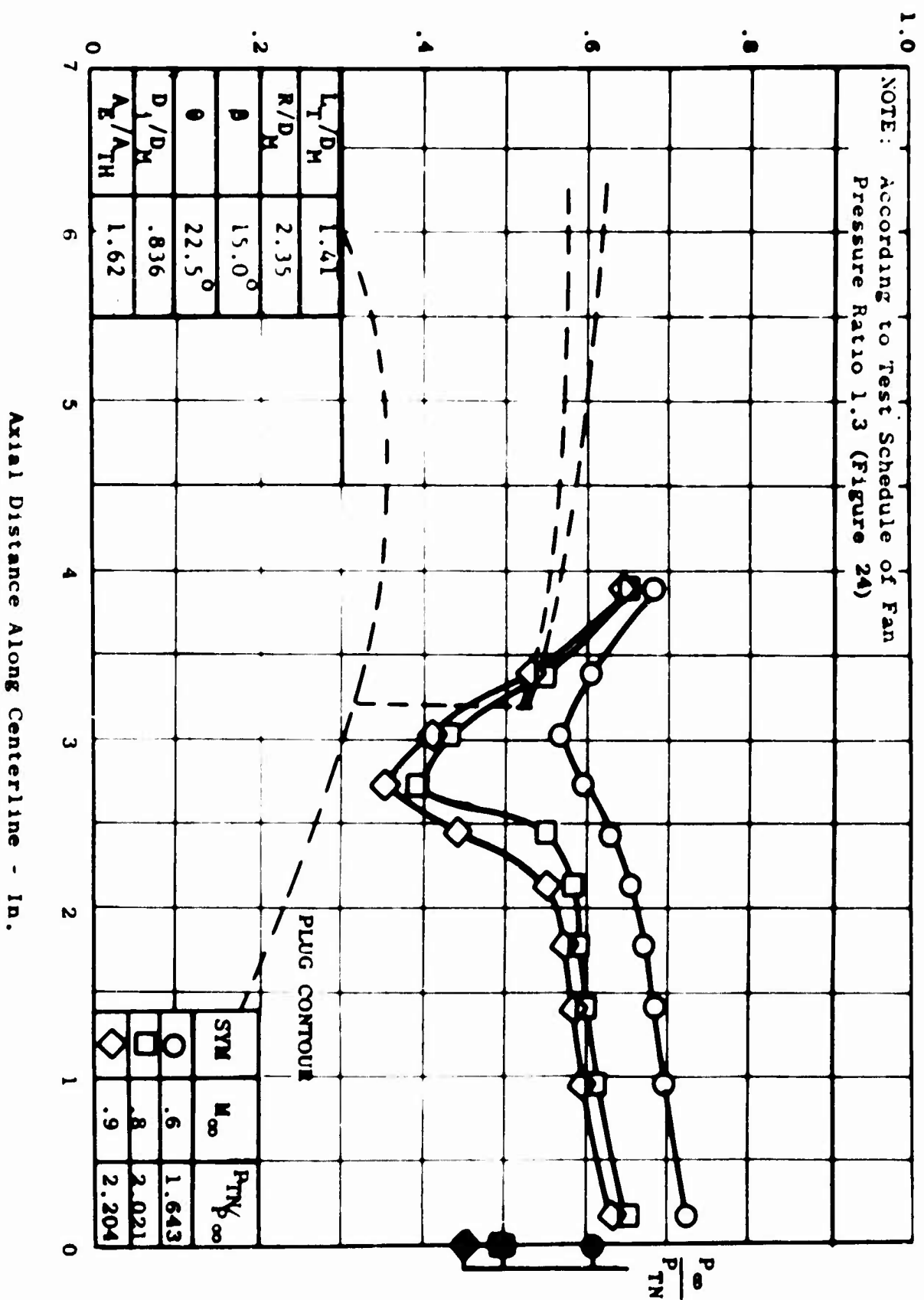


Figure 115. Plug Pressure Distribution as a Function of Axial Distance and Pressure Ratio-Model 13, Mach No. = All.

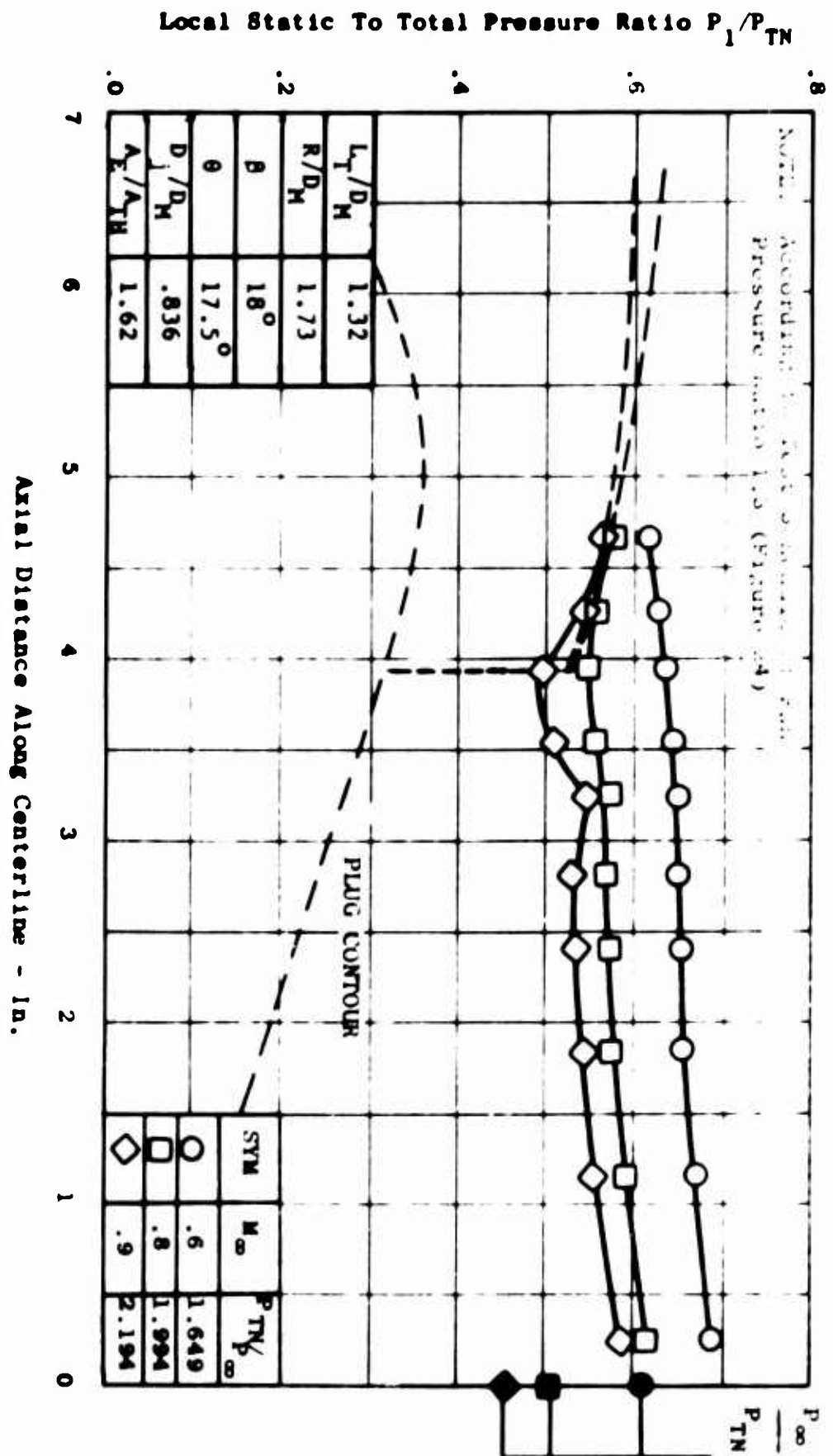


Figure 116. Plug Pressure Distribution as a Function of Axial Distance and Pressure Ratio-Model 14, Mach No. = 11.1.

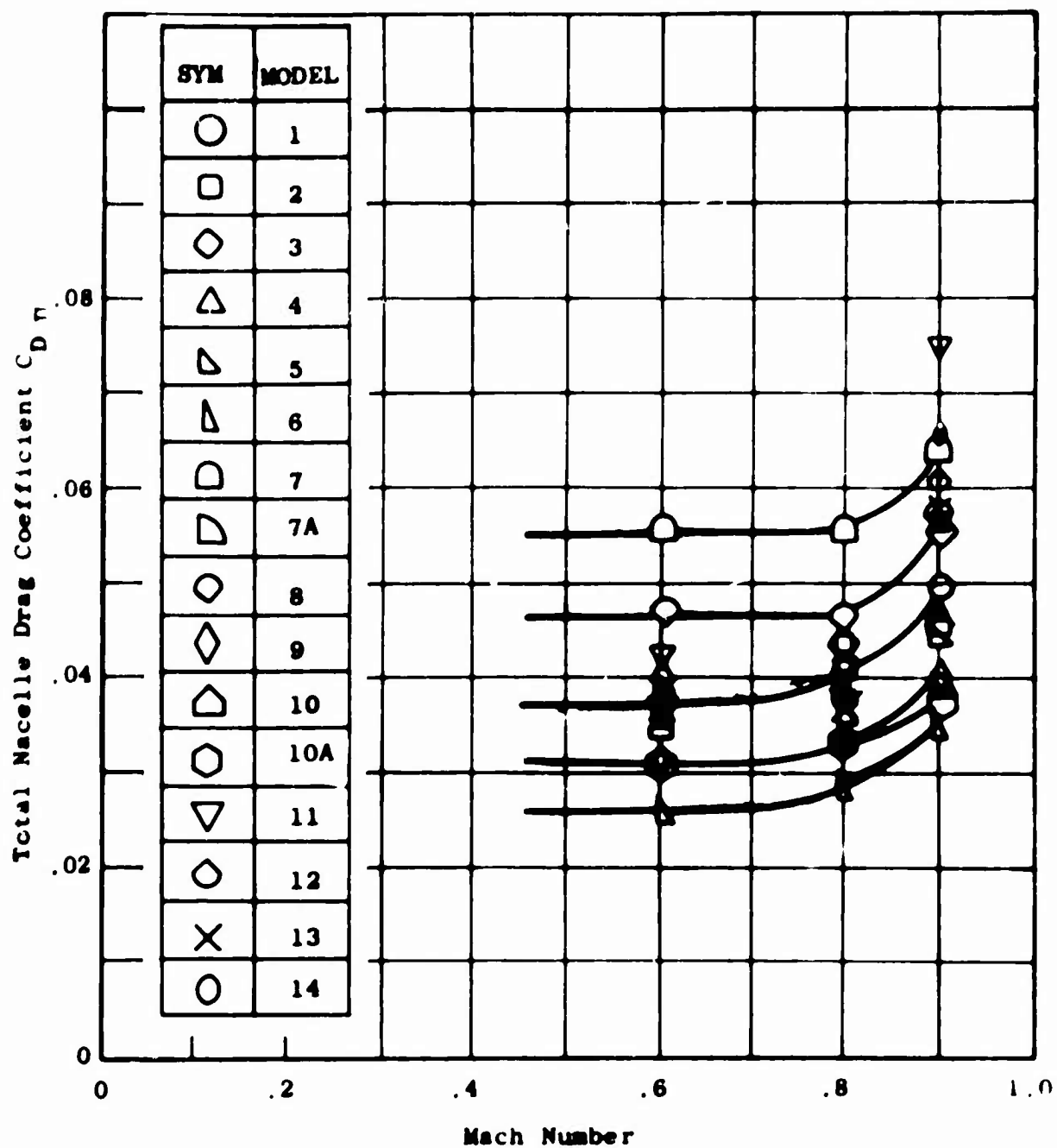


Figure 117. Total Nacelle Drag Coefficient (Including Friction) at Various Mach Numbers.

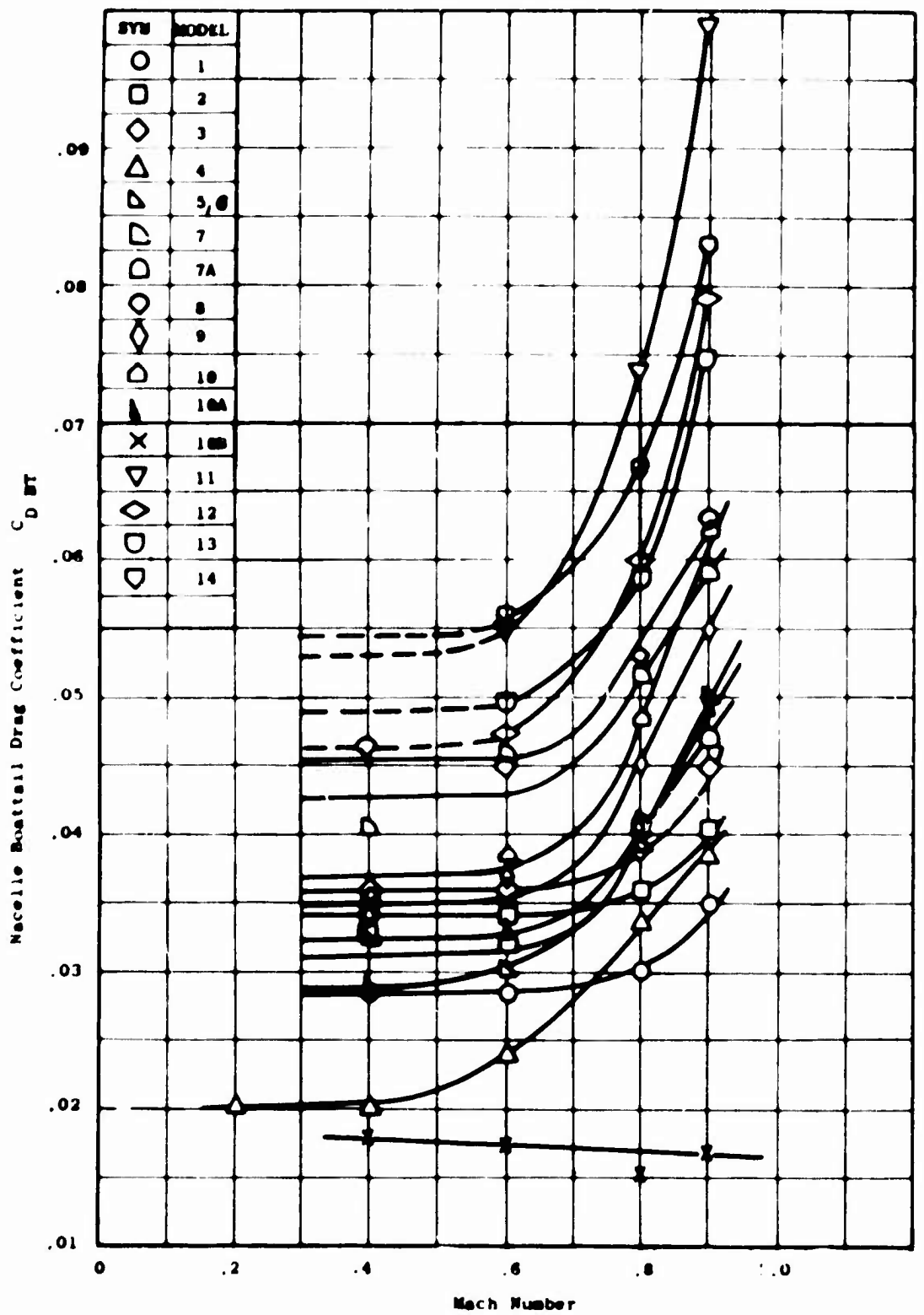


Figure 118. Nacelle Boattail Drag Coefficient (Not Including Friction) at Various Mach Numbers.

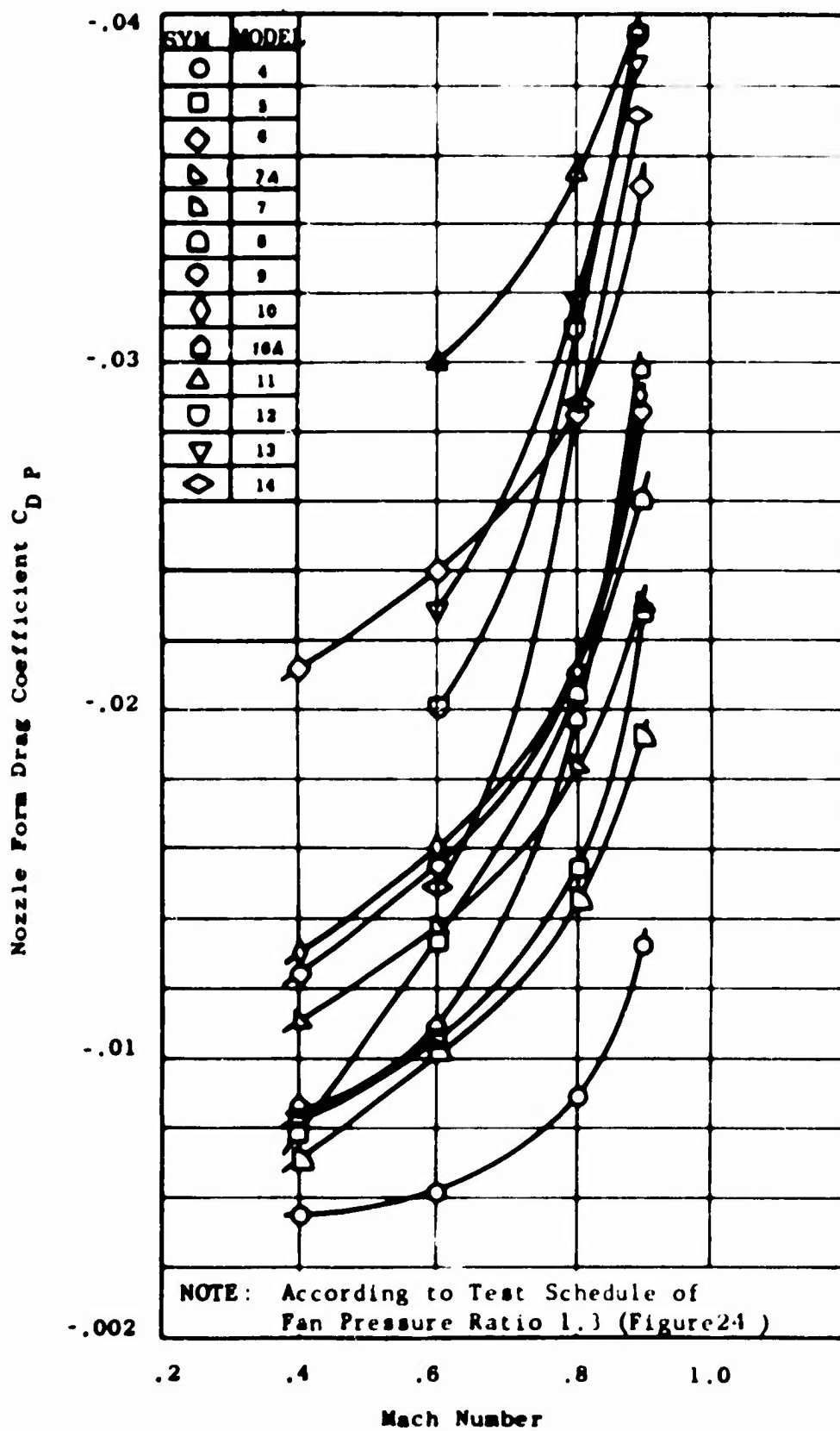


Figure 119. Nozzle Plug Form Drag Coefficient (Not Including Friction) at Various Mach Numbers.

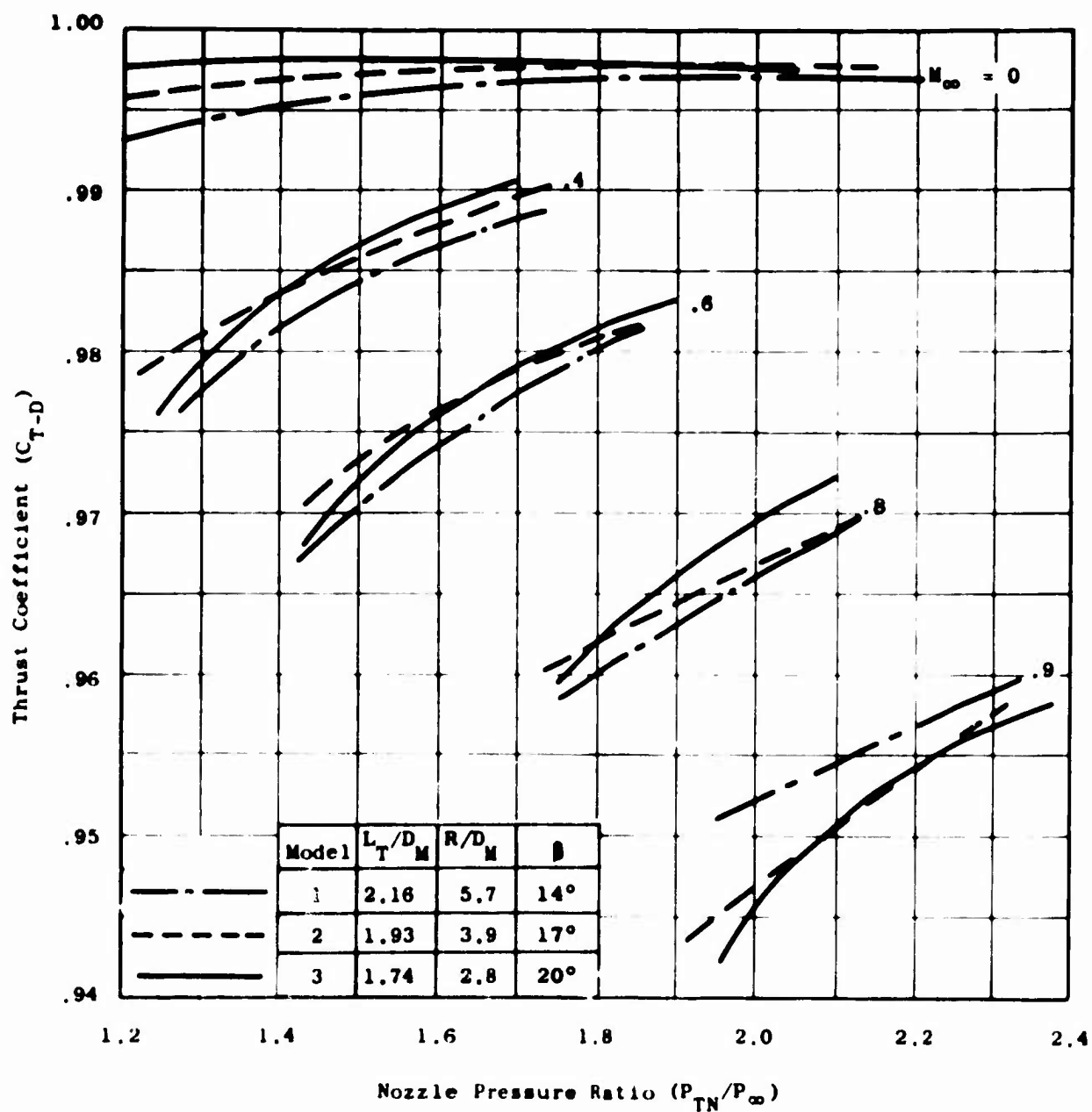


Figure 120. Performance Comparison of Conical Exhaust Systems.

SYM	MODEL	L_T/D_M	R/D_M	
◇	1	2.16	5.7	14°
□	2	1.93	3.9	17°
○	3	1.74	2.8	20°

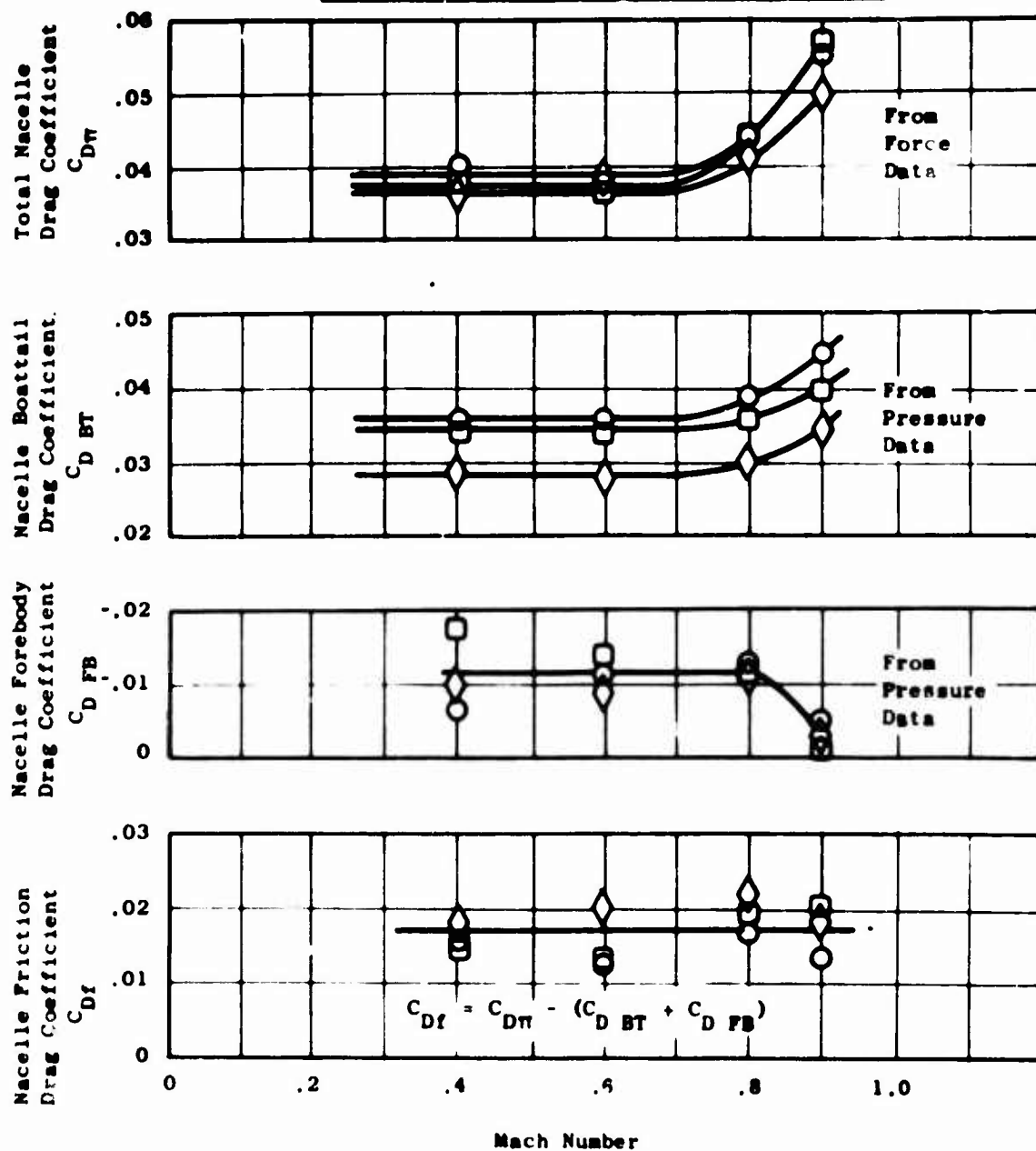


Figure 121. Comparison of Nacelle Drag Coefficients for Conical Exhaust Systems.

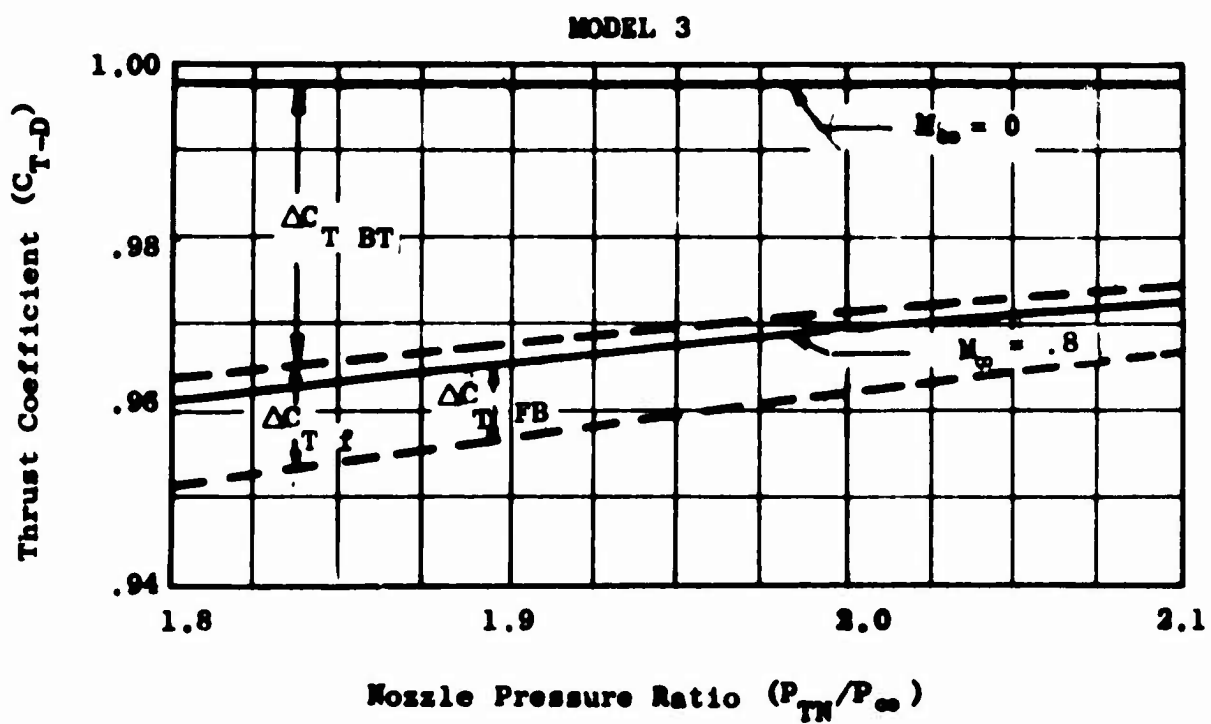
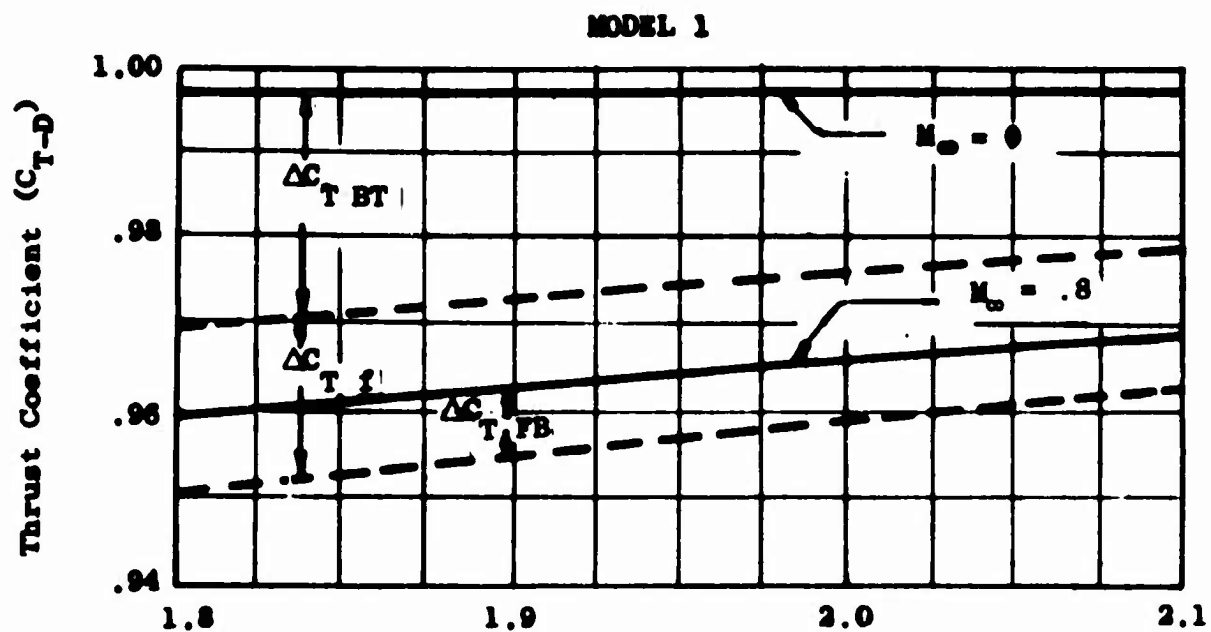


Figure 122. Loss Breakdown of Models 1 and 3 at Mach = .8.

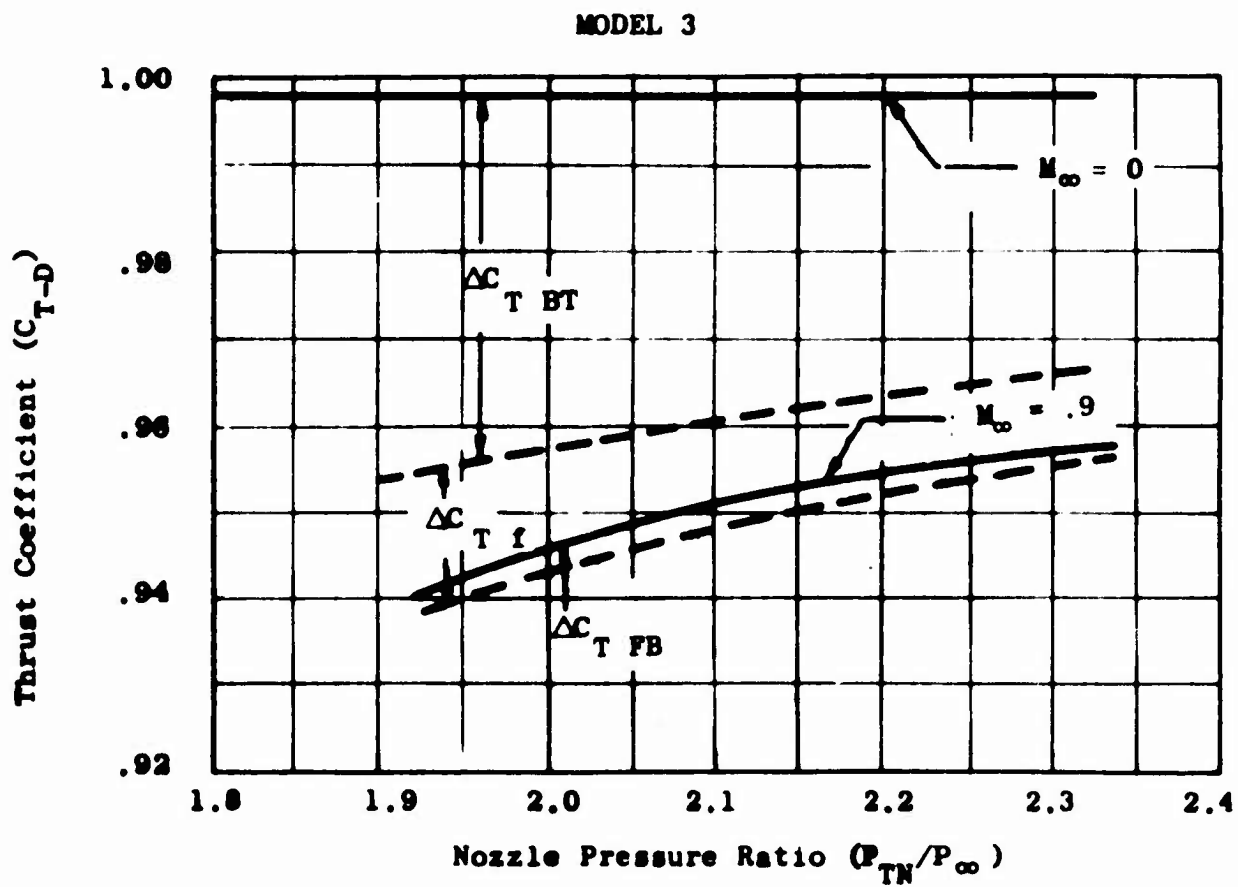
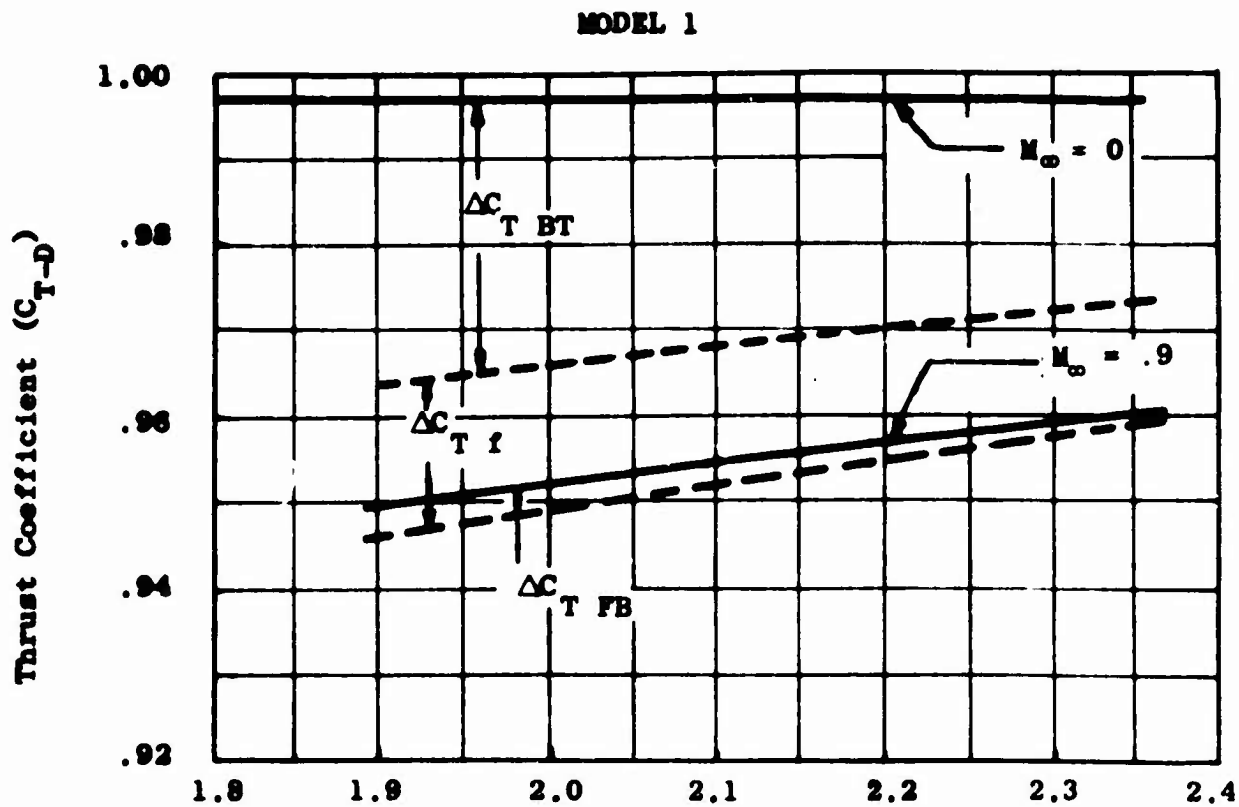
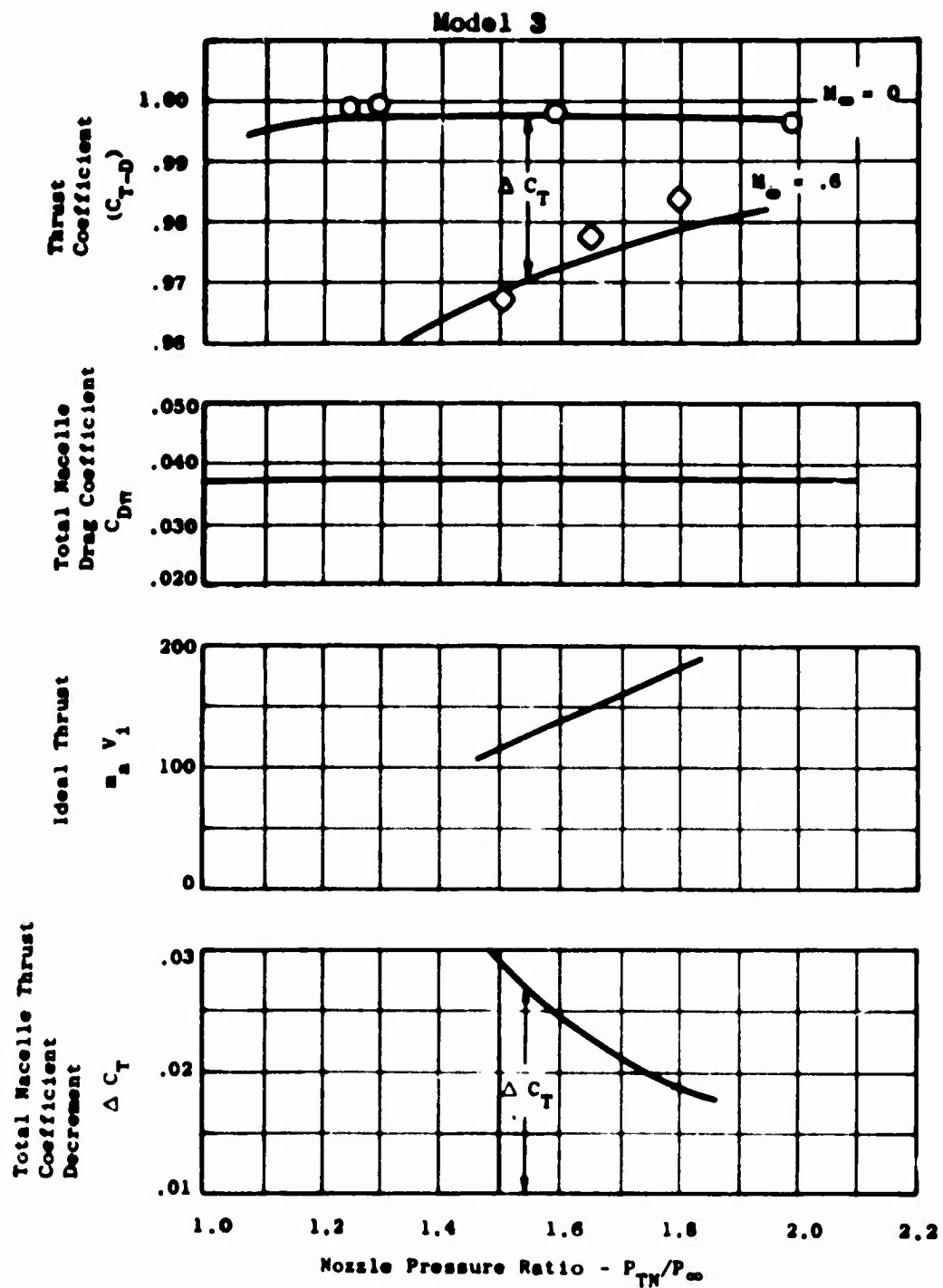


Figure 123. Loss Breakdown of Models 1 and 3 at Mach = .9



$$C_{T-D} = C_T(M_\infty = 0) - \frac{C_{Dm} q_\infty A_M}{(\dot{m}_a V_1)_i}$$

Figure 124. Analysis of Installed Performance.

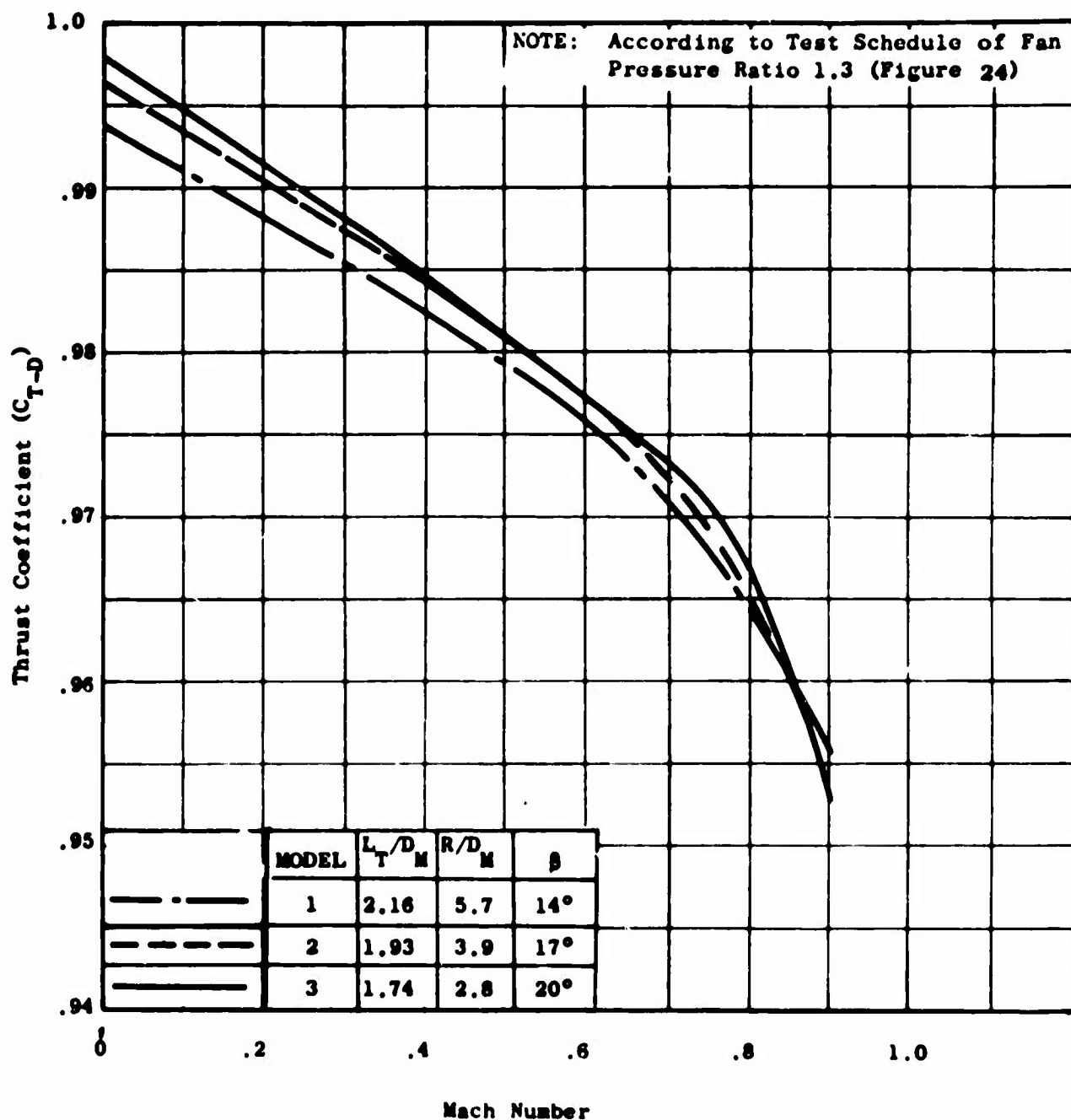


Figure 125. Performance Comparison of Conical Exhaust Systems for Test Schedule.

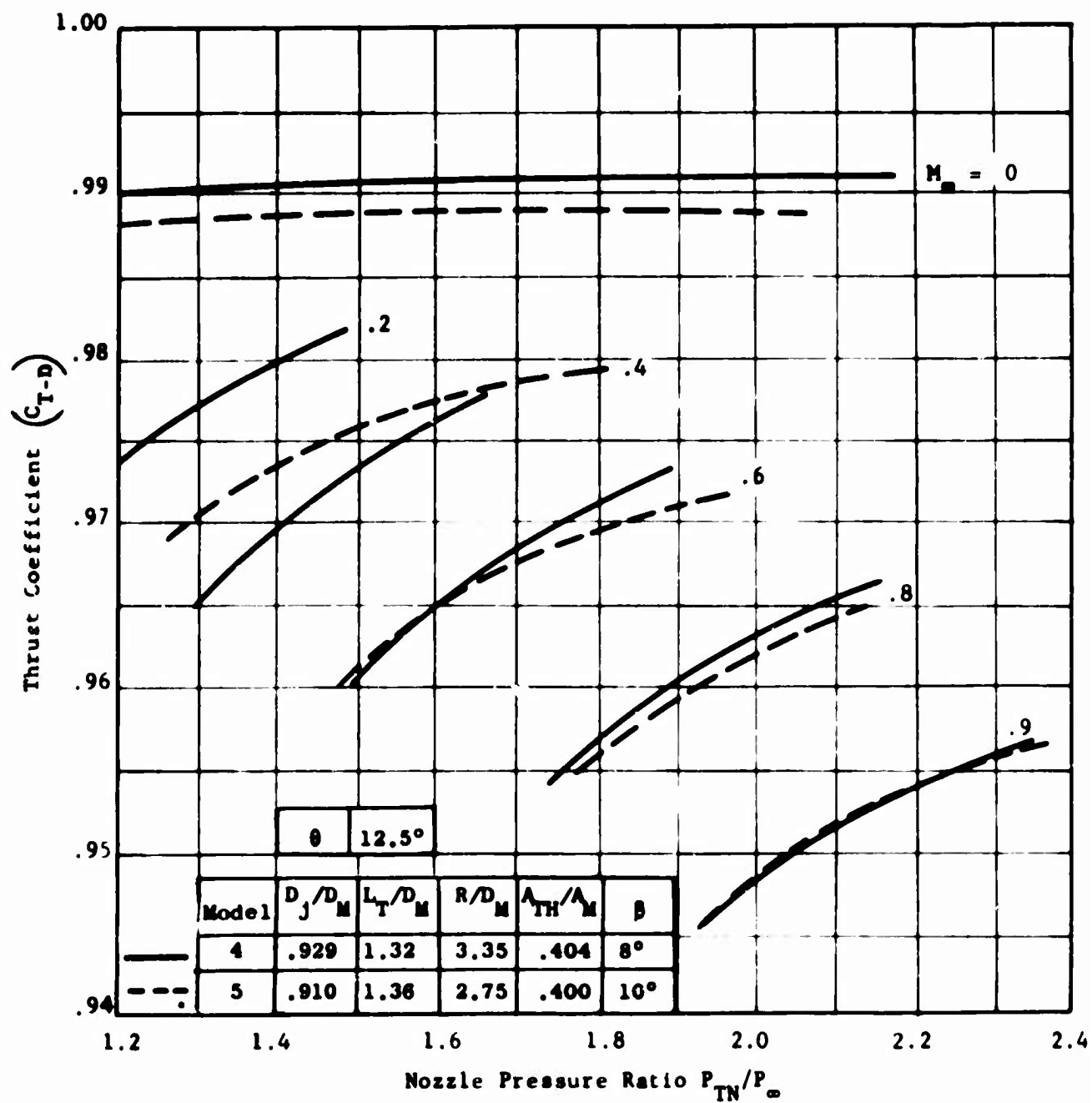


Figure 126. Effect of Boattail Geometry on Performance for Low Boattail Plug Nozzles - Models 4 and 5.

Nacelle Boattail Drag Coefficient - $C_{D_{BT}}$

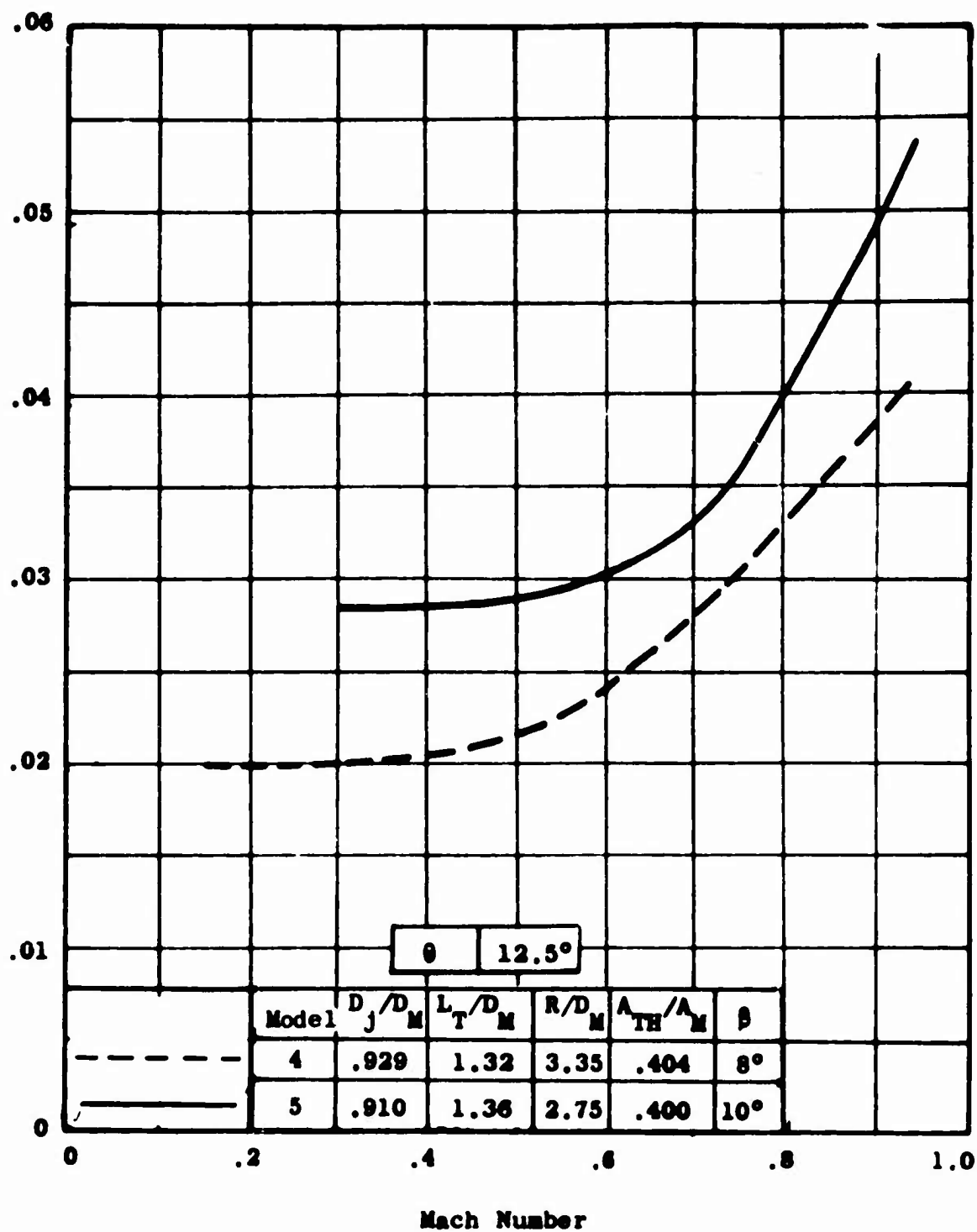


Figure 127. Comparison of Nacelle Boattail Drag Coefficient (Not Including Friction) Models 4 and 5.

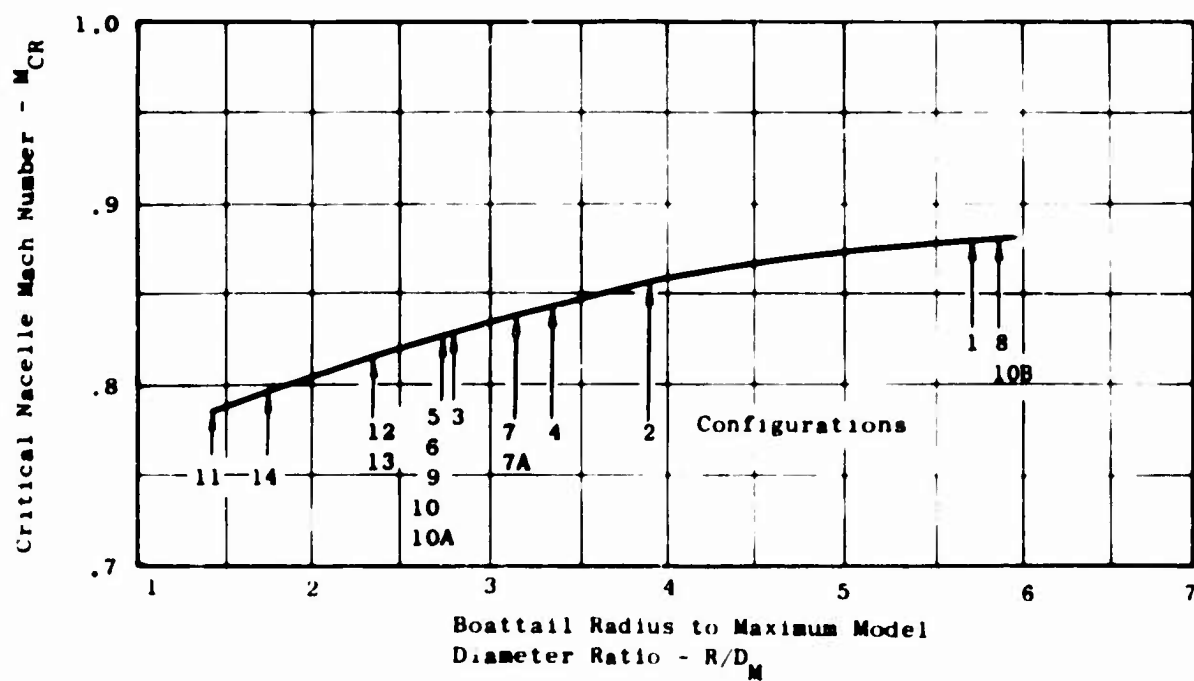
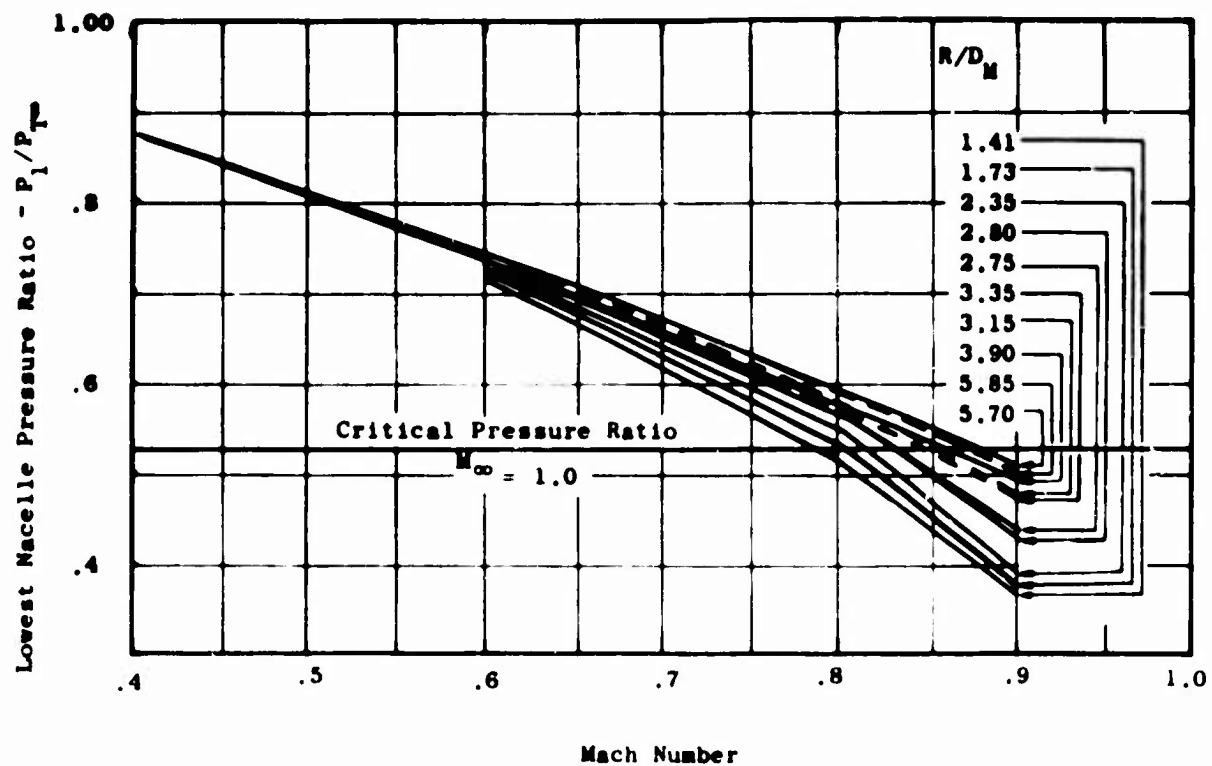


Figure 128 Model Critical Nacelle Mach Number.

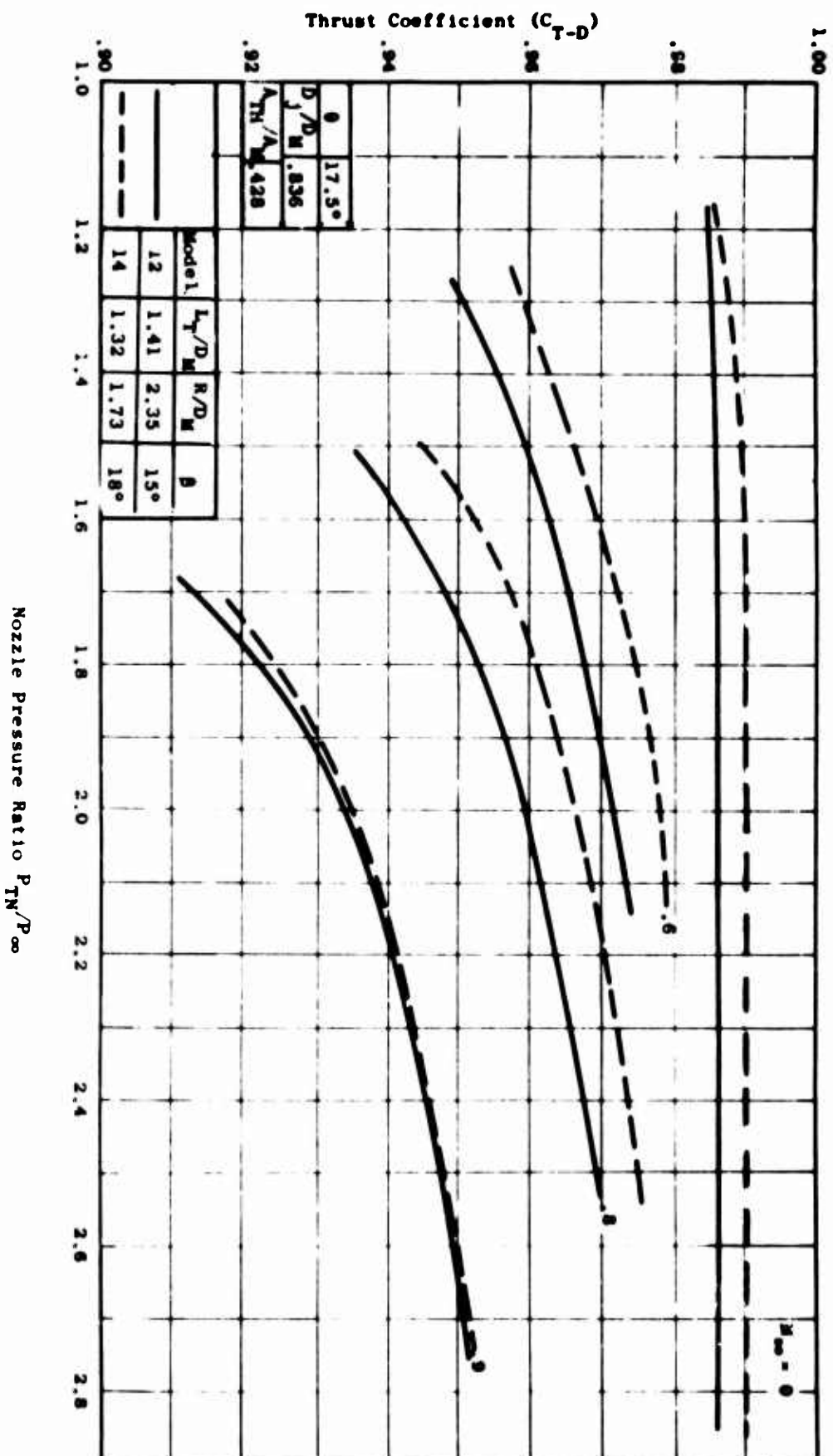


Figure 129. Effect of Boattail Geometry on Performance for High Boattail Plug Nozzles - Models 12 and 14.

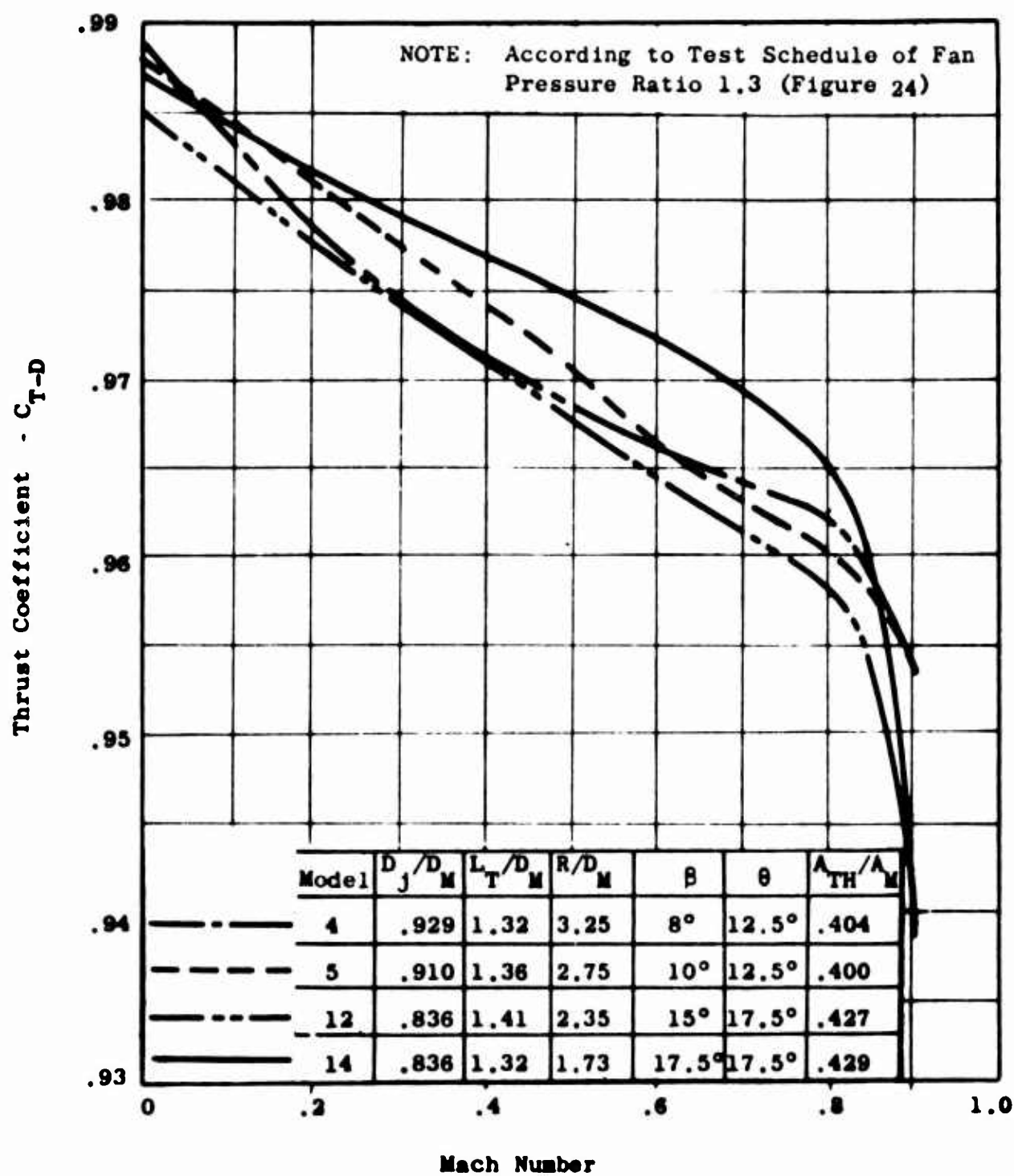


Figure 130. Performance Comparison of Low and High Boattail Plug Nozzles.

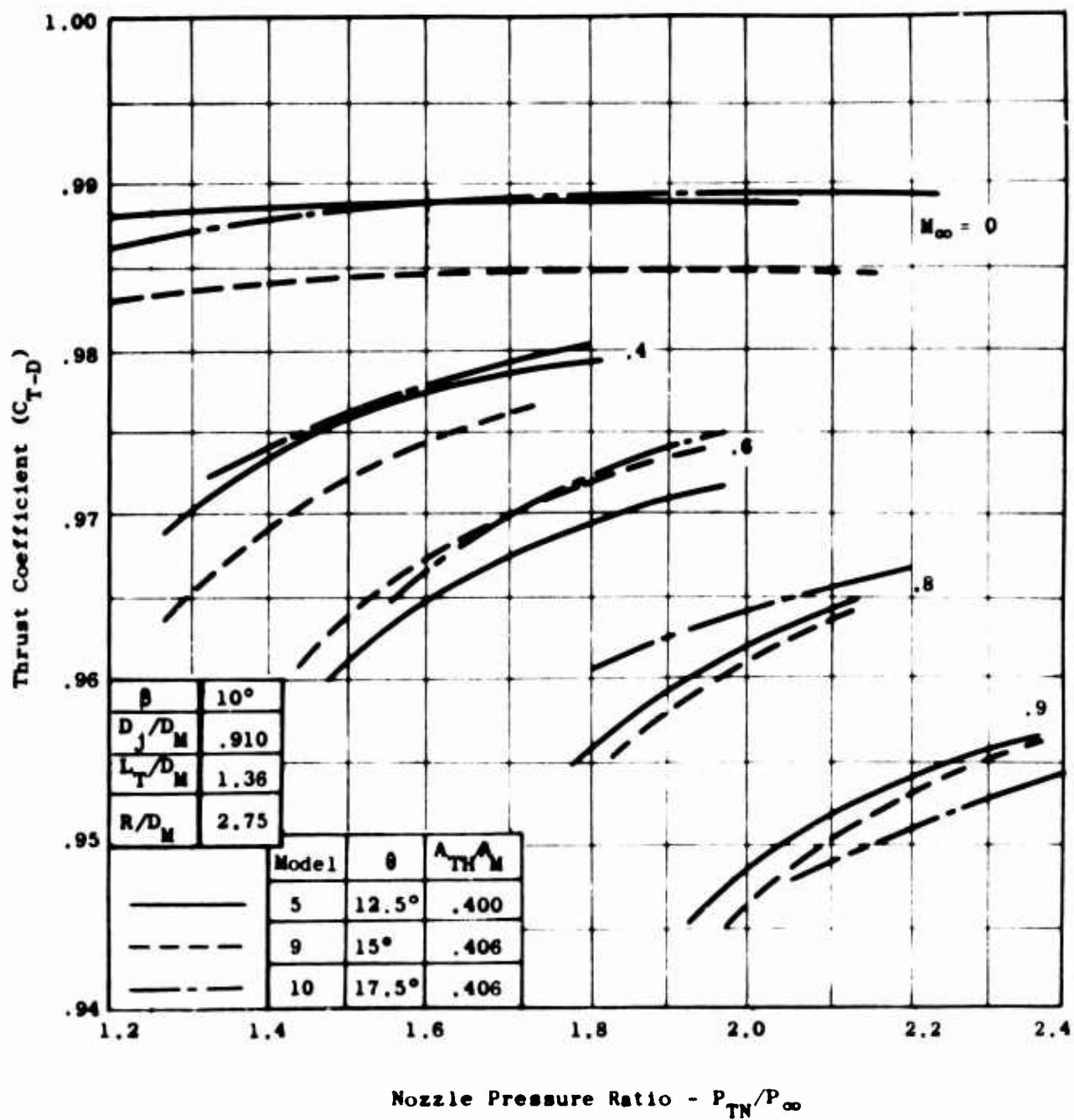


Figure 131. Effect of Plug Angle on Performance for Low Boattail Plug Nozzles - Model 5, 9 and 10.

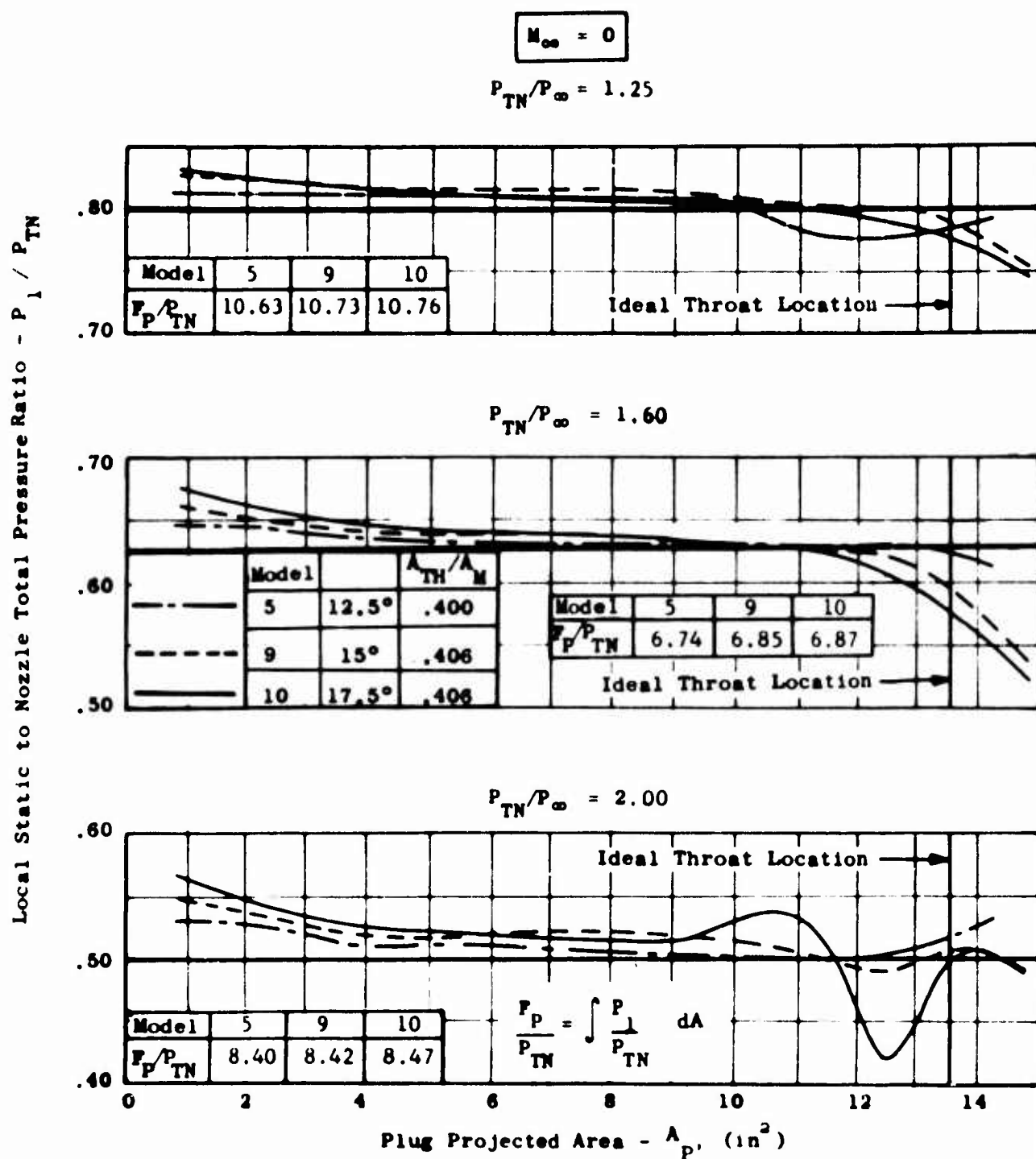


Figure 132. Comparison of Plug Forces for Models 5, 9, and 10 at Mach = 0.

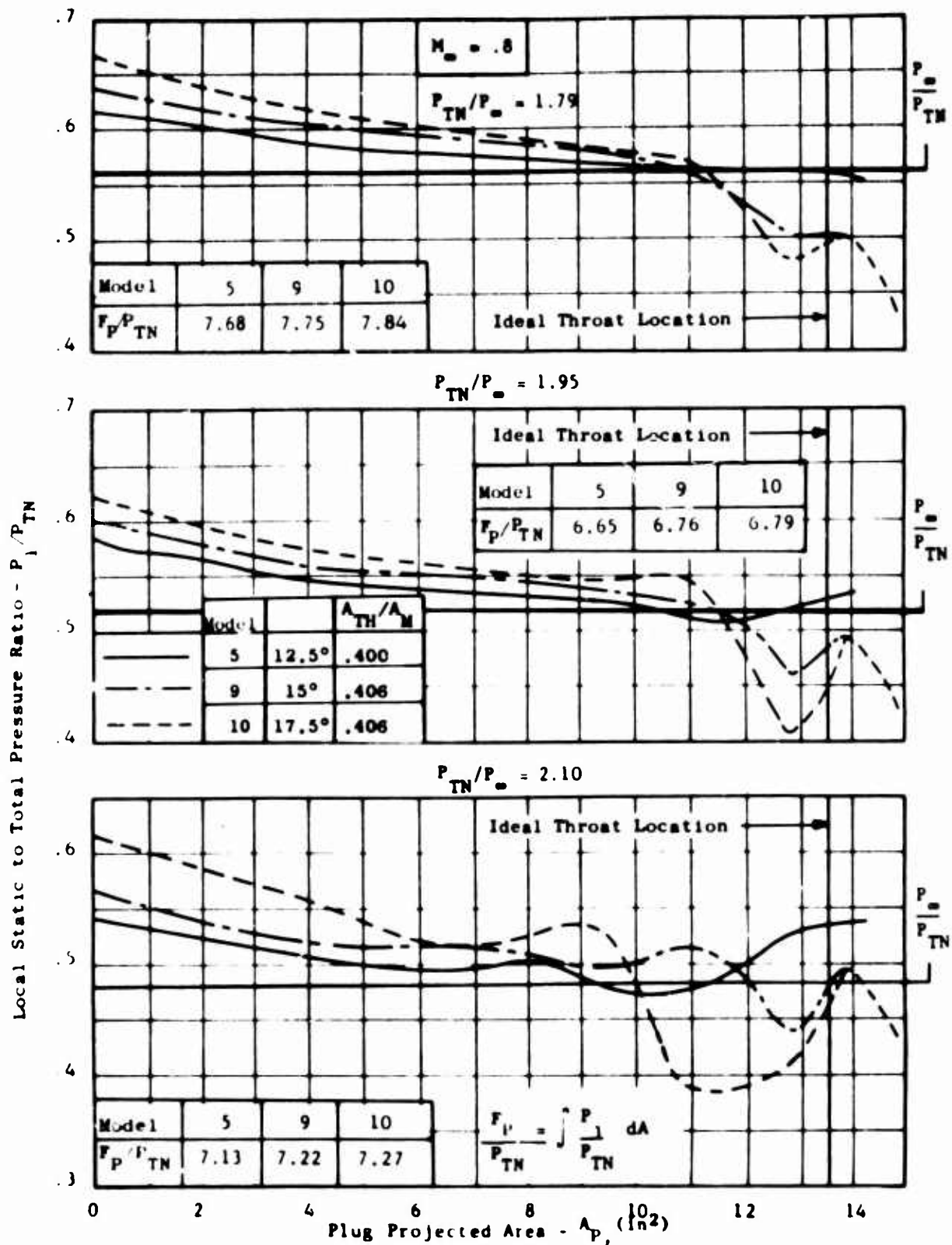


Figure 133. Comparison of Plug Forces for Models 5, 9, and 10 at Mach .8.

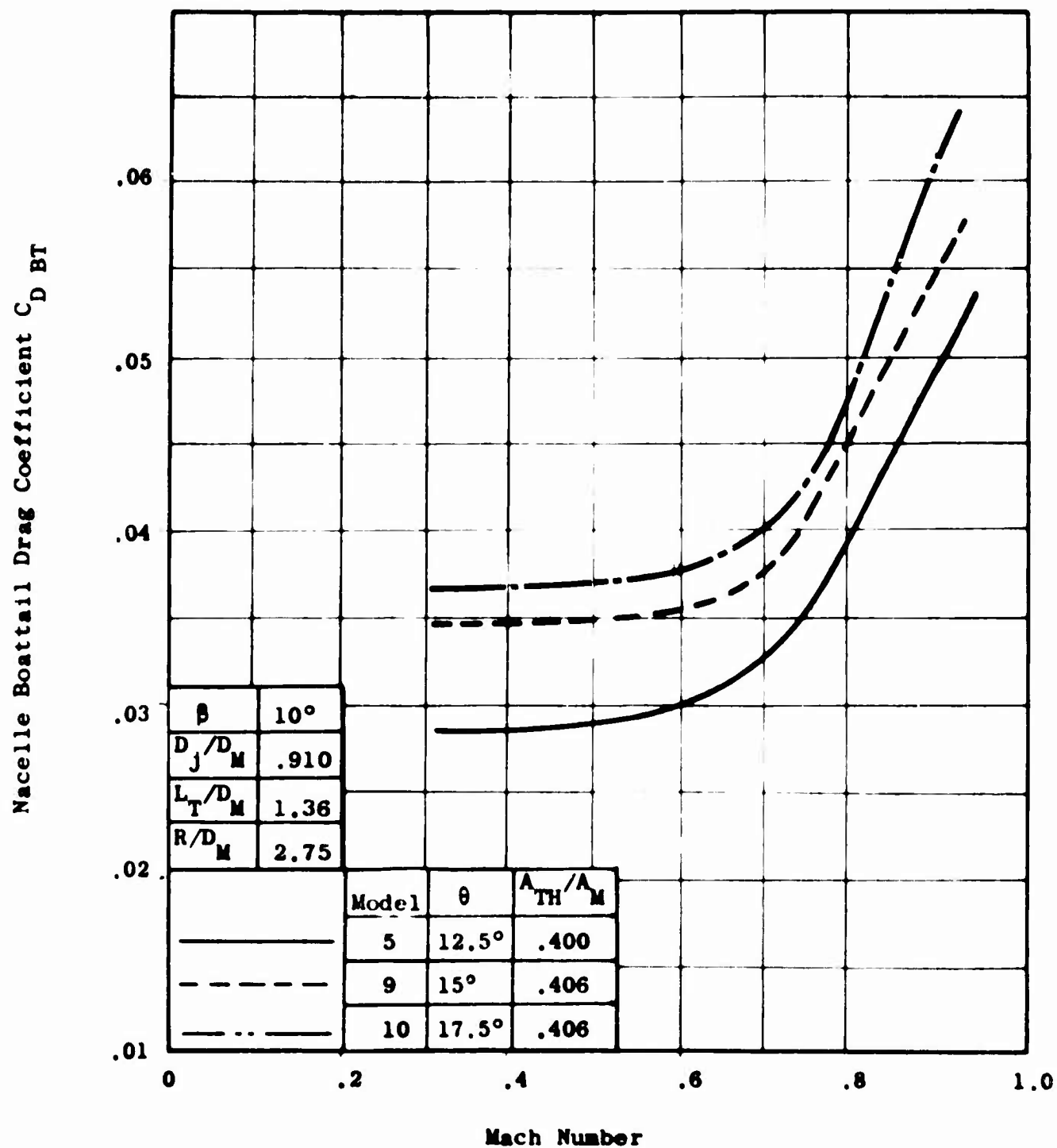


Figure 134. Comparison of Nacelle Boattail Drag Coefficient (Not Including Friction) Models 5, 9, and 10.

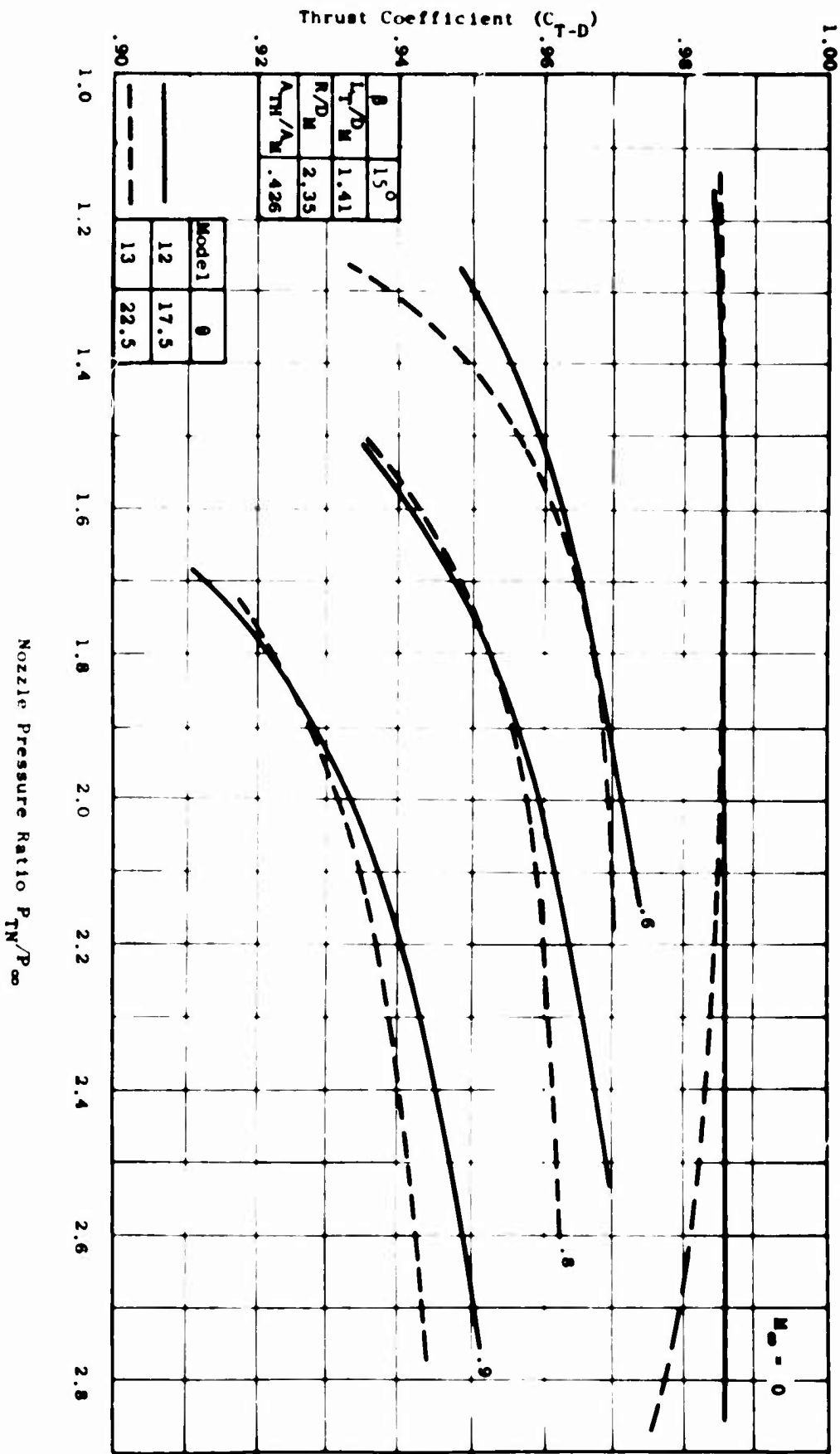


Figure 135. Effect of Plug Angle on Performance for High Boattail Plug Nozzle - Models 12 and 13.

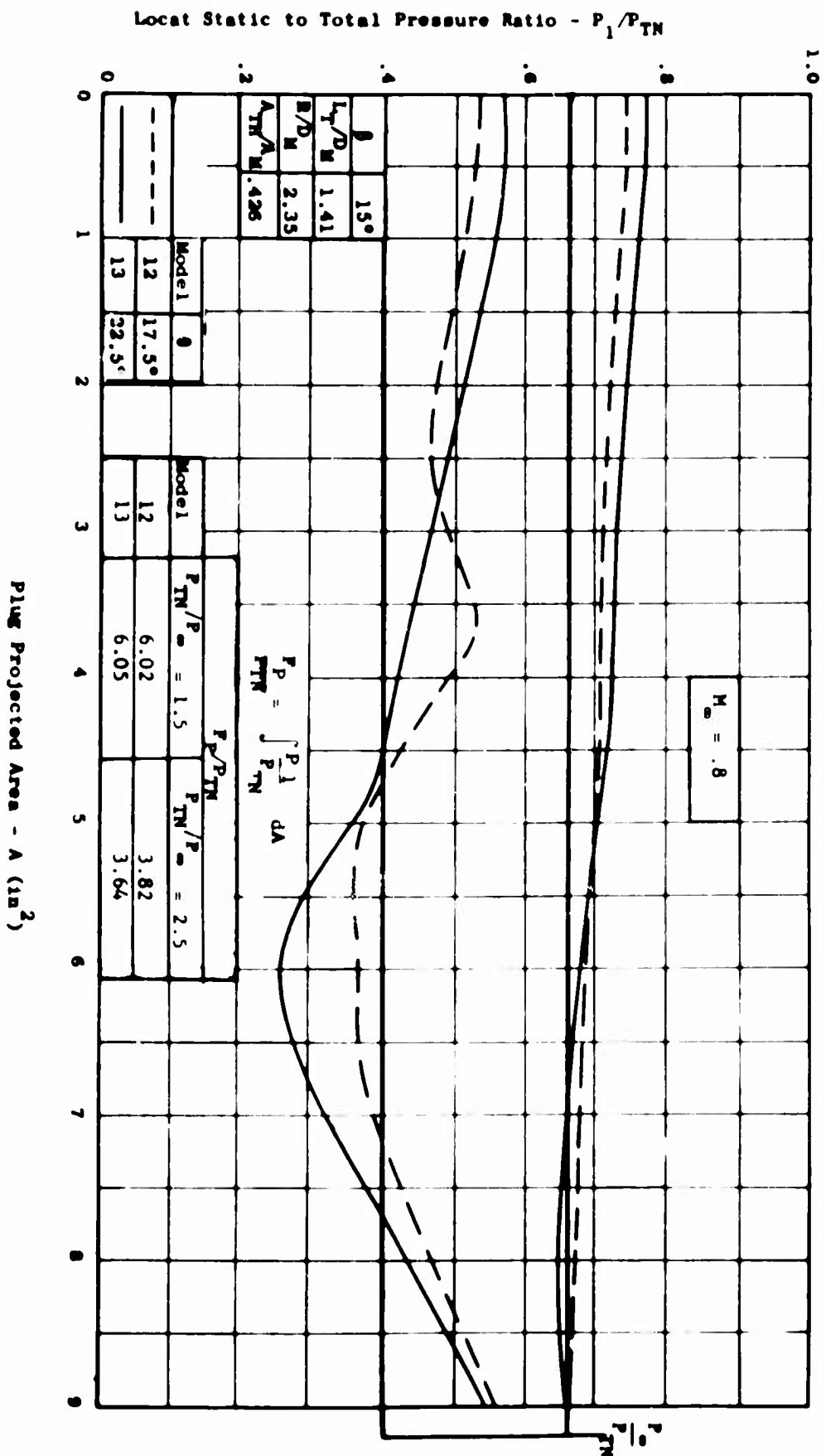


Figure 136. Comparison of Plug Forces Models 12 and 13 at Mach .8.

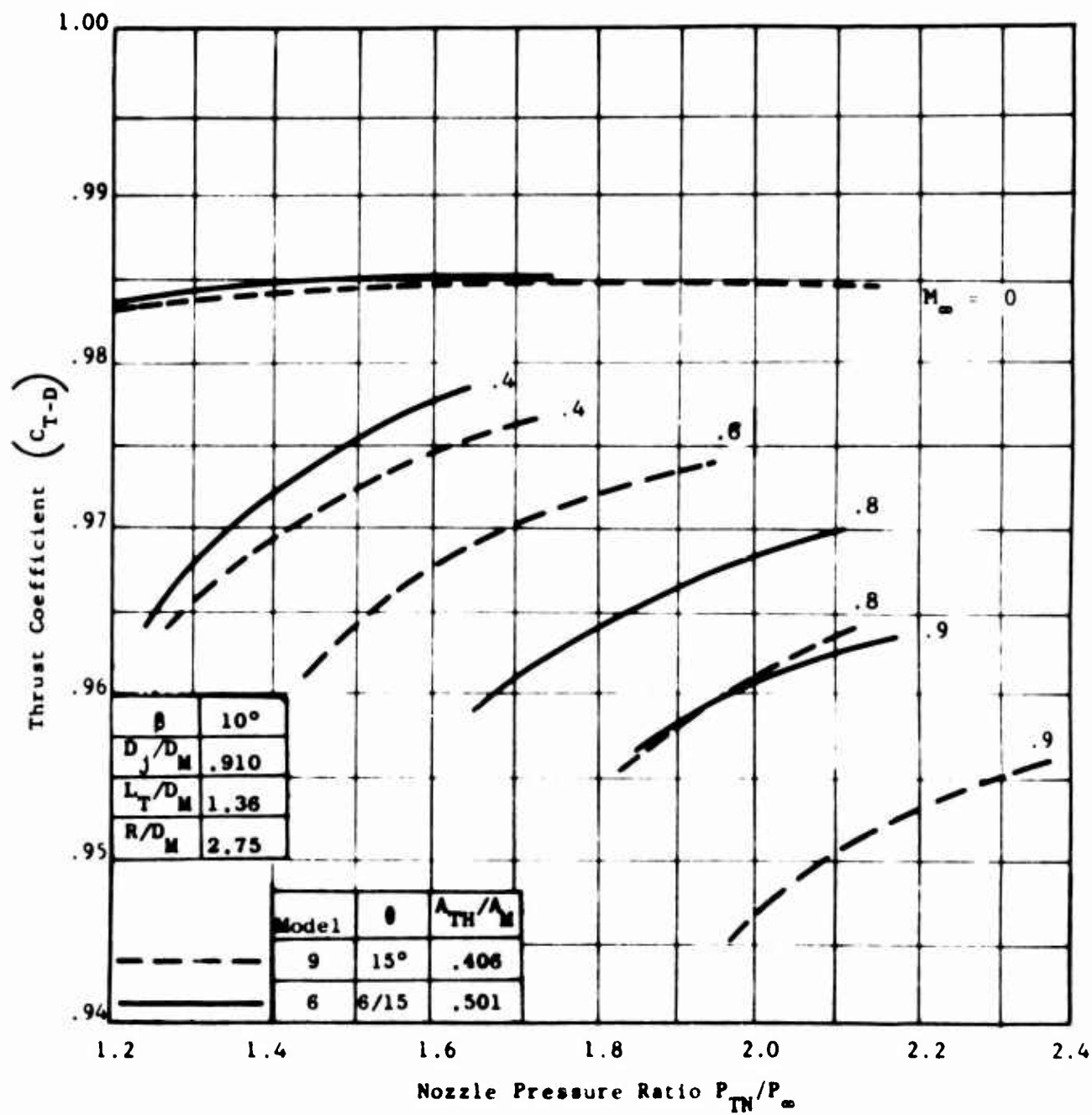


Figure 137. Effect of Throat Area on Performance for Expandable Plug Concept - Models 6 and 9.

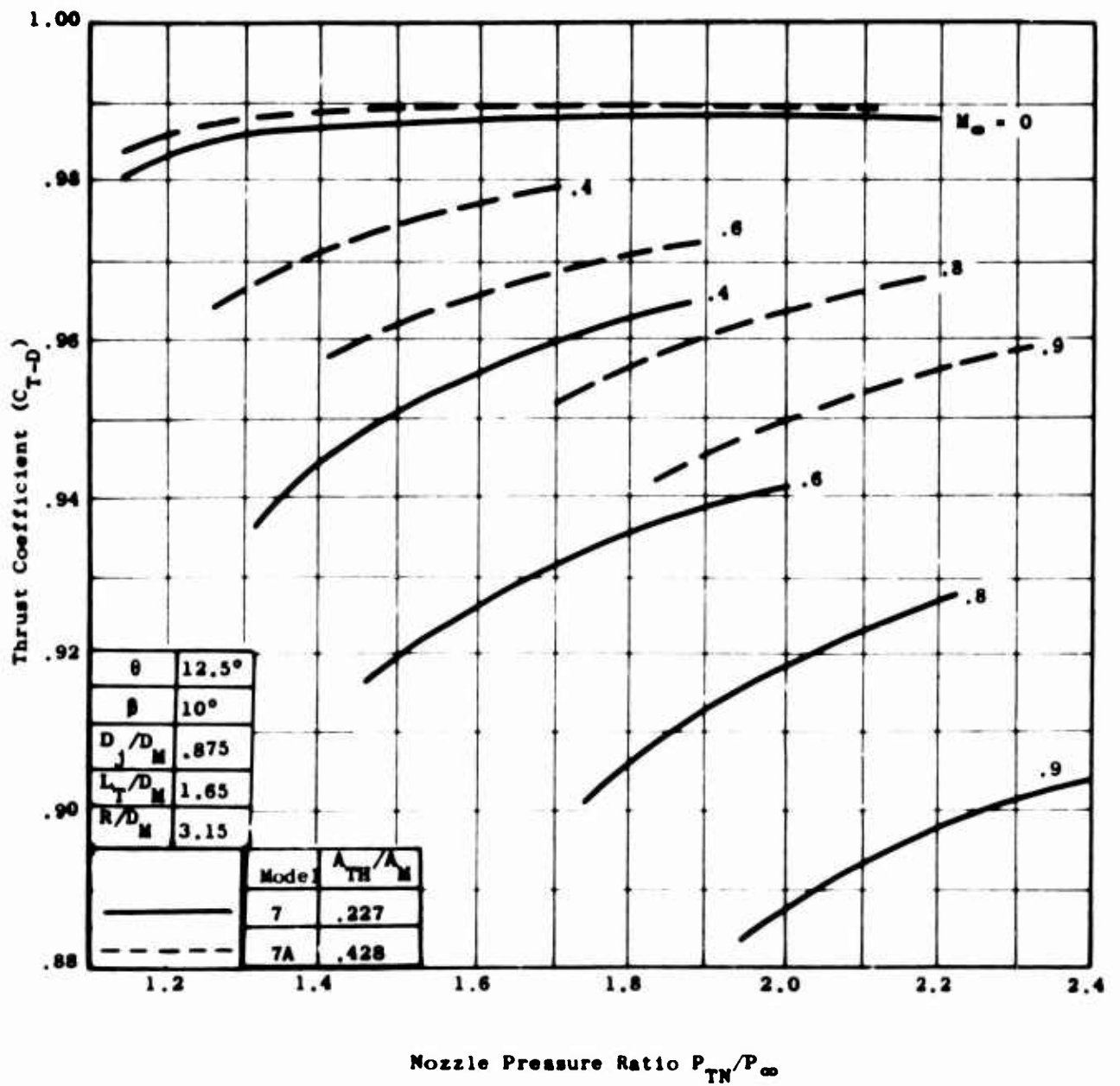


Figure 138. Effect of Area Ratio on Performance - Models 7 and 7A.

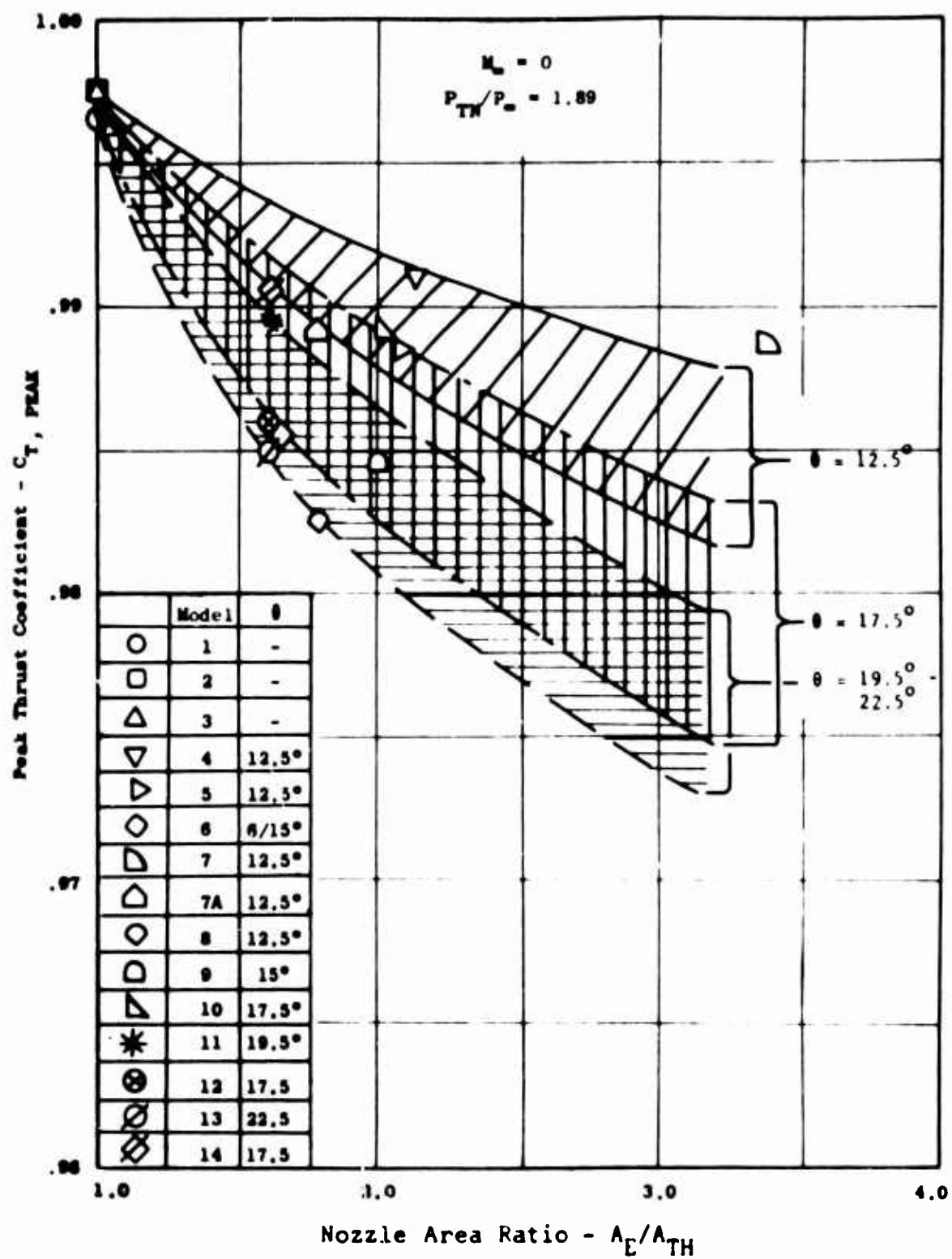


Figure 139. Effect of Area Ratio on Peak Performance at Mach Zero.

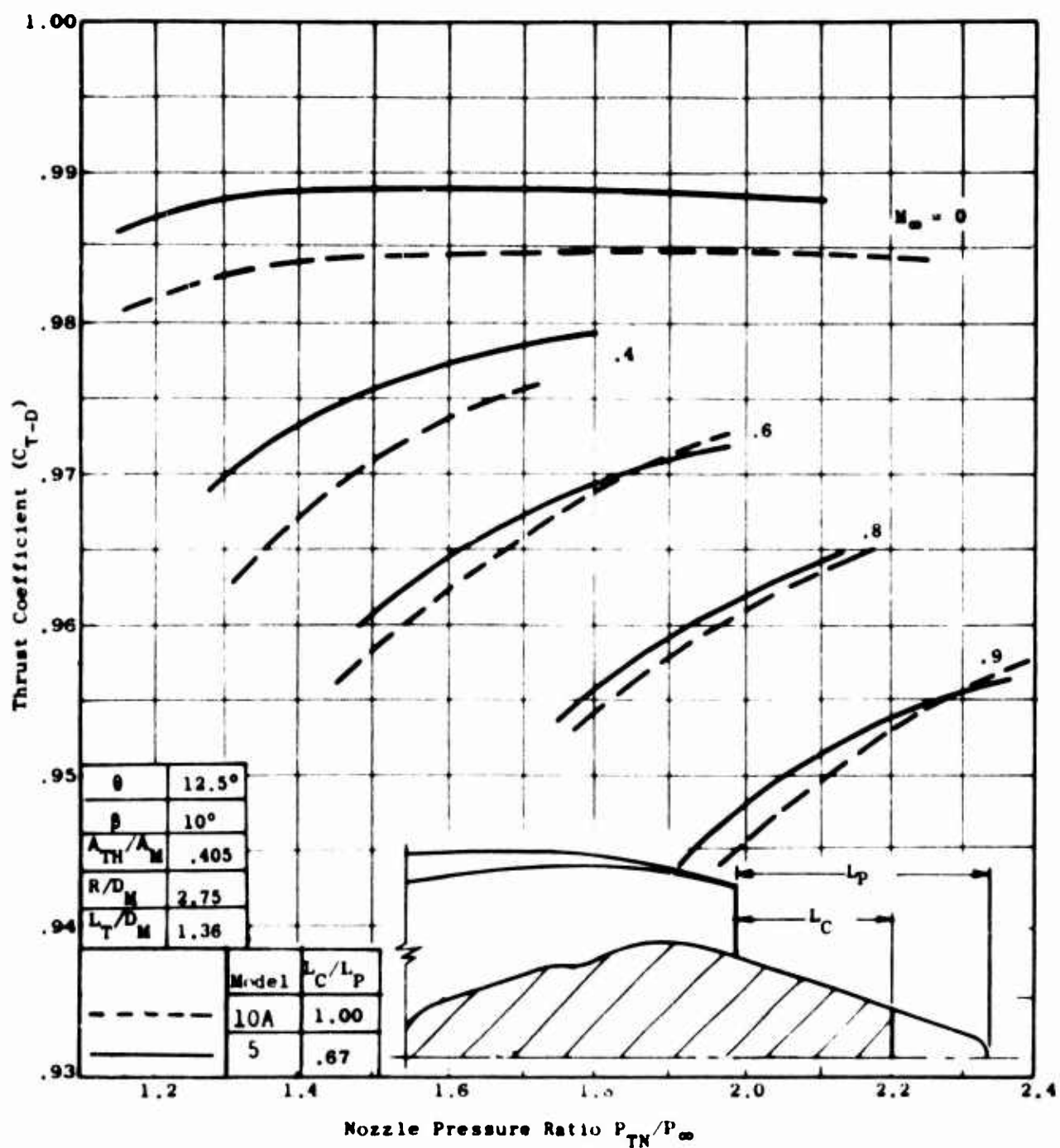
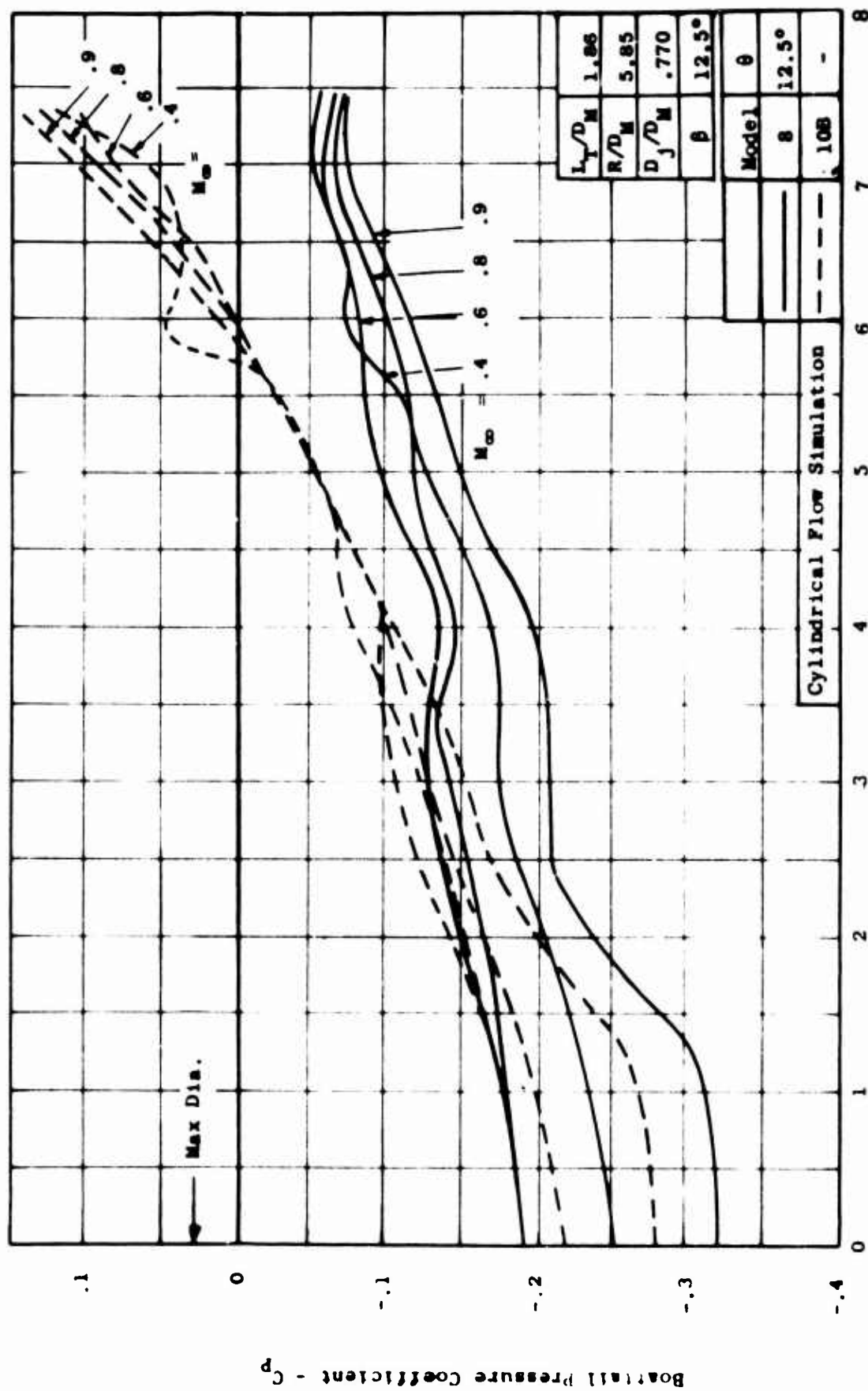


Figure 140. Effect of Plug Length on Performance for Plug Nozzle - Models 5 and 10A.



Axial Distance Along Shroud - In.

Figure 141. Effect of Simulated Cylindrical Flow on Boattail Pressure Coefficient - Models 8 and 10R

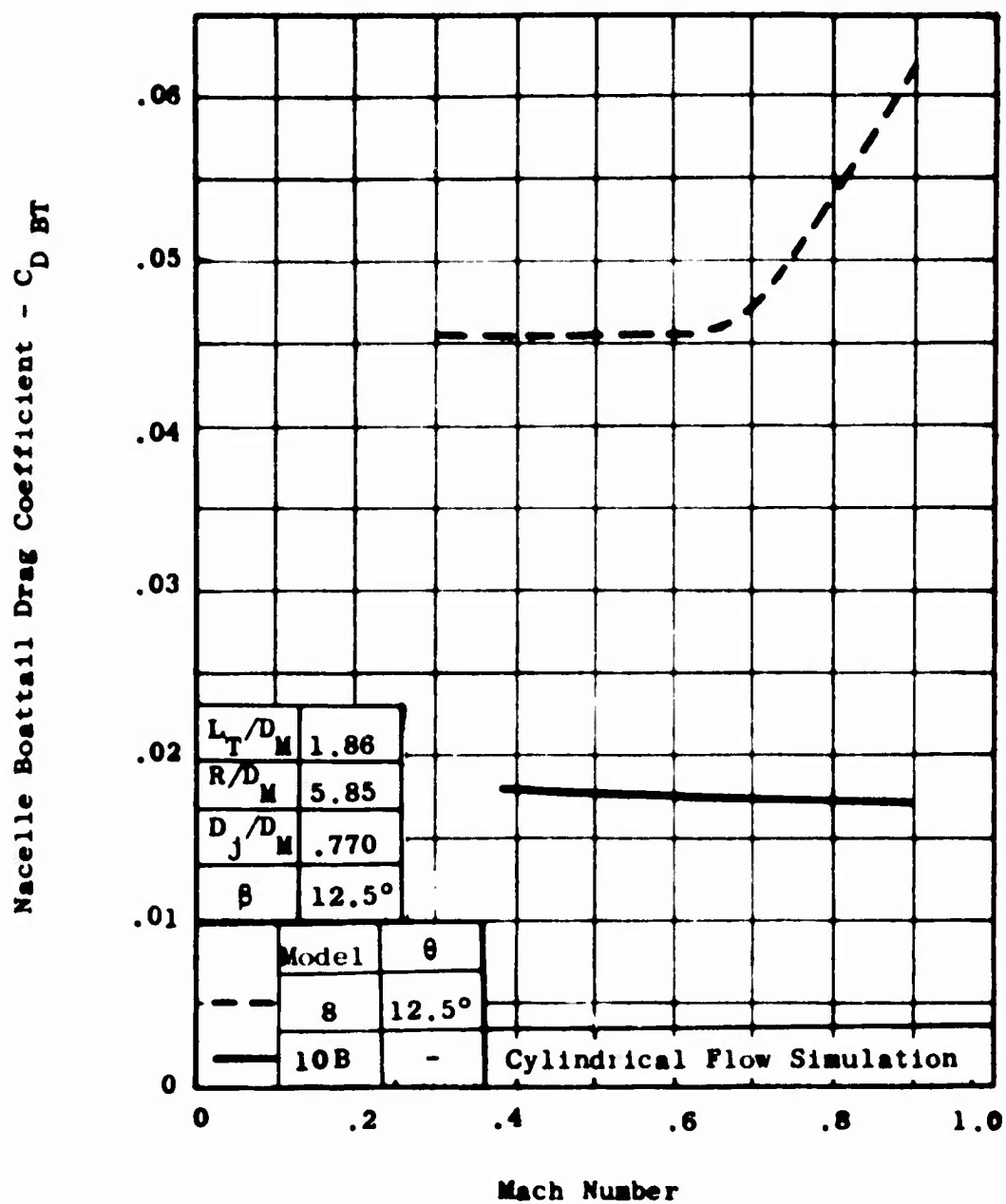


Figure 142. Comparison of Nacelle Boattail Drag Coefficient (Not Including Friction) Models 8 and 10B.

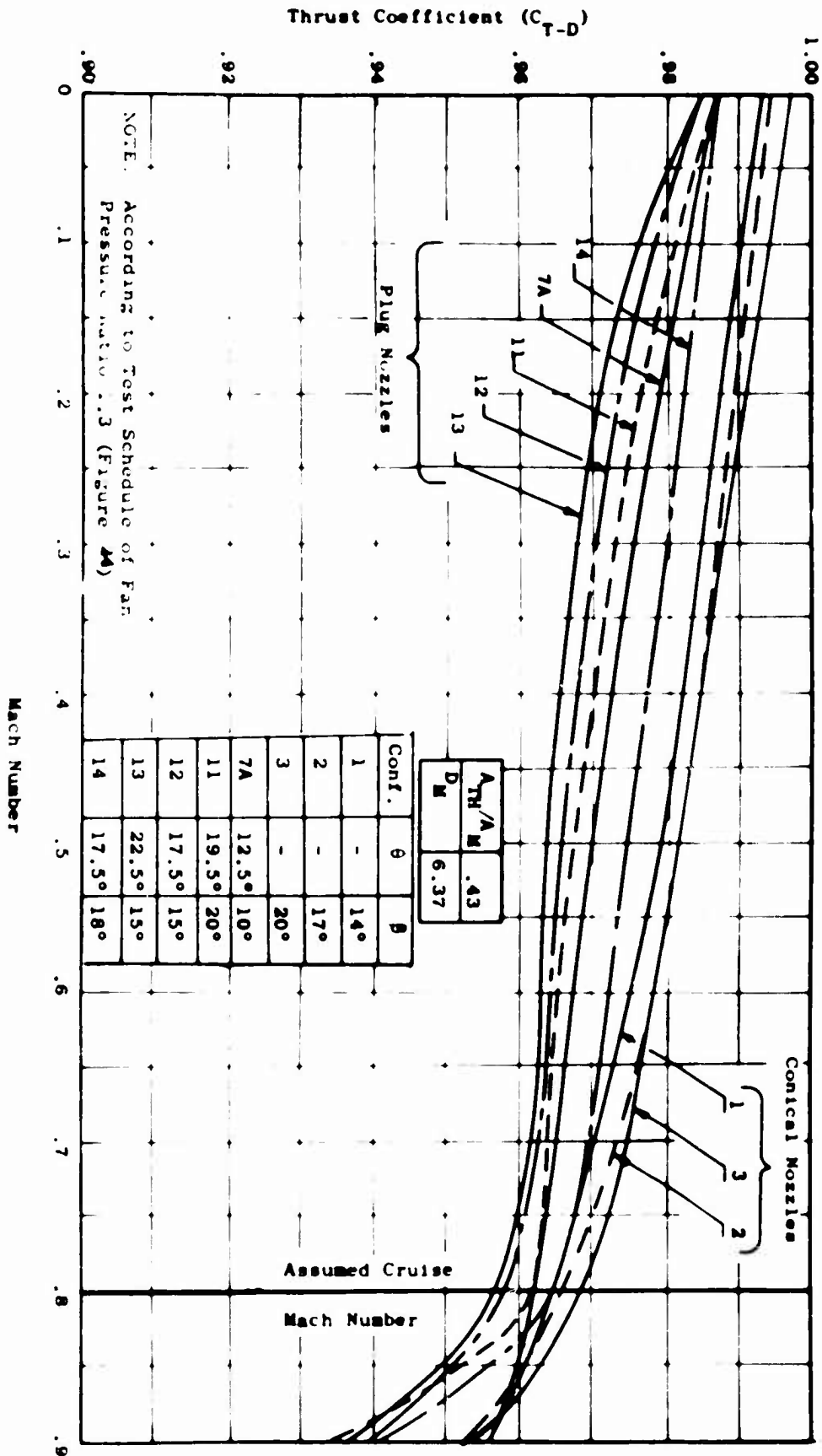


Figure 143. Comparison of Performance for All Models with Equal Throat Area.

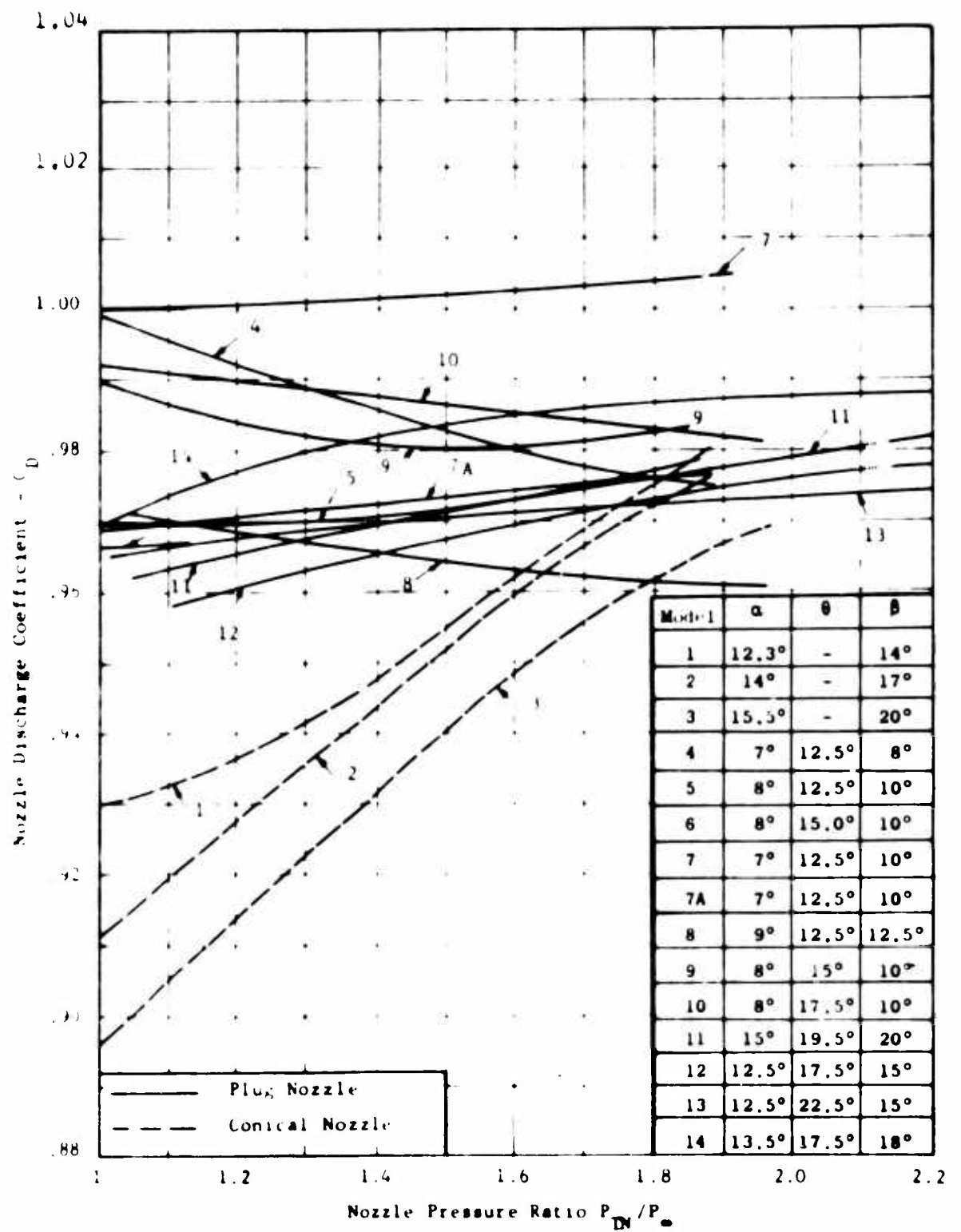


Figure 144. Comparison of Nozzle Discharge Coefficients at Unchoked Conditions.

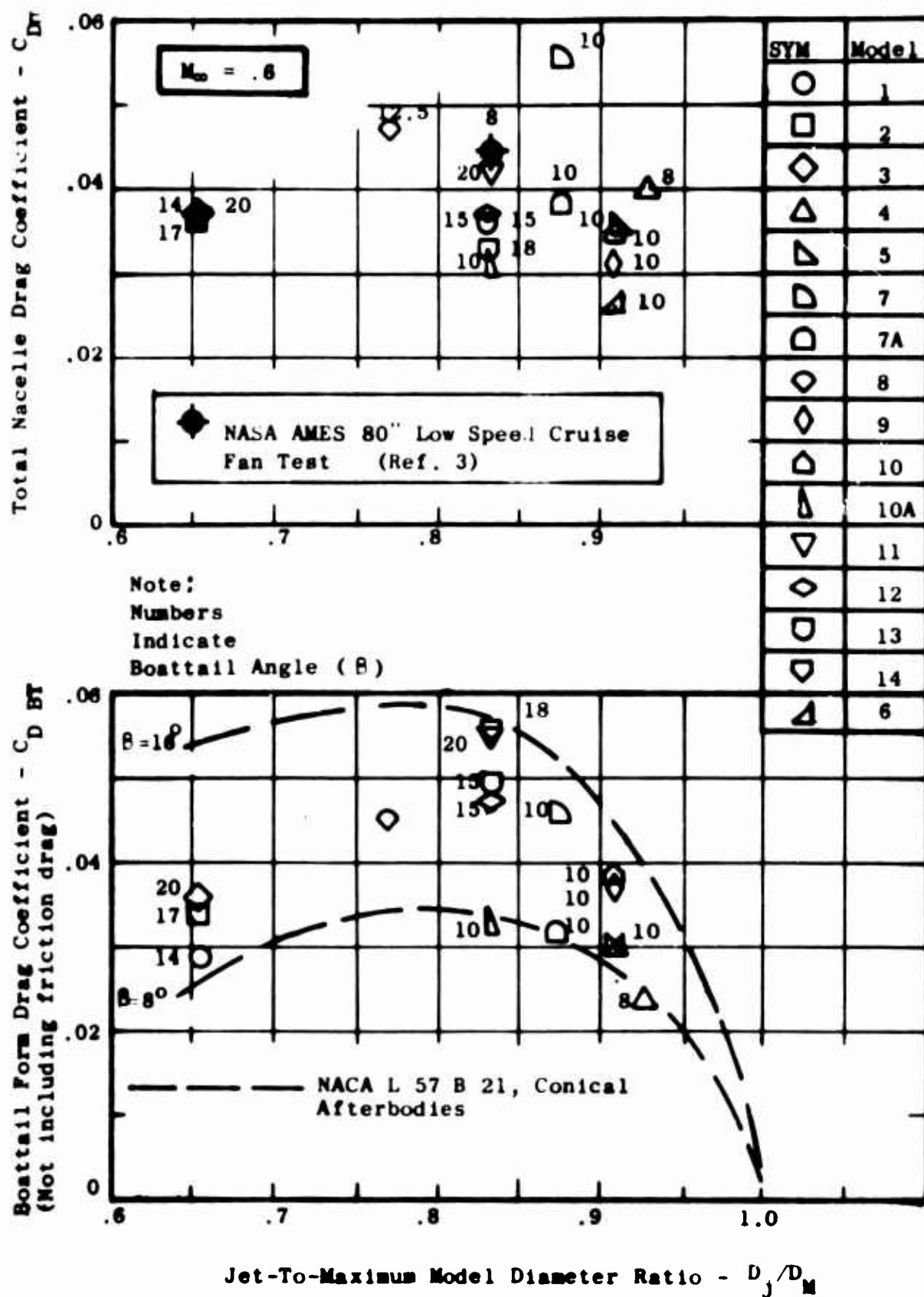
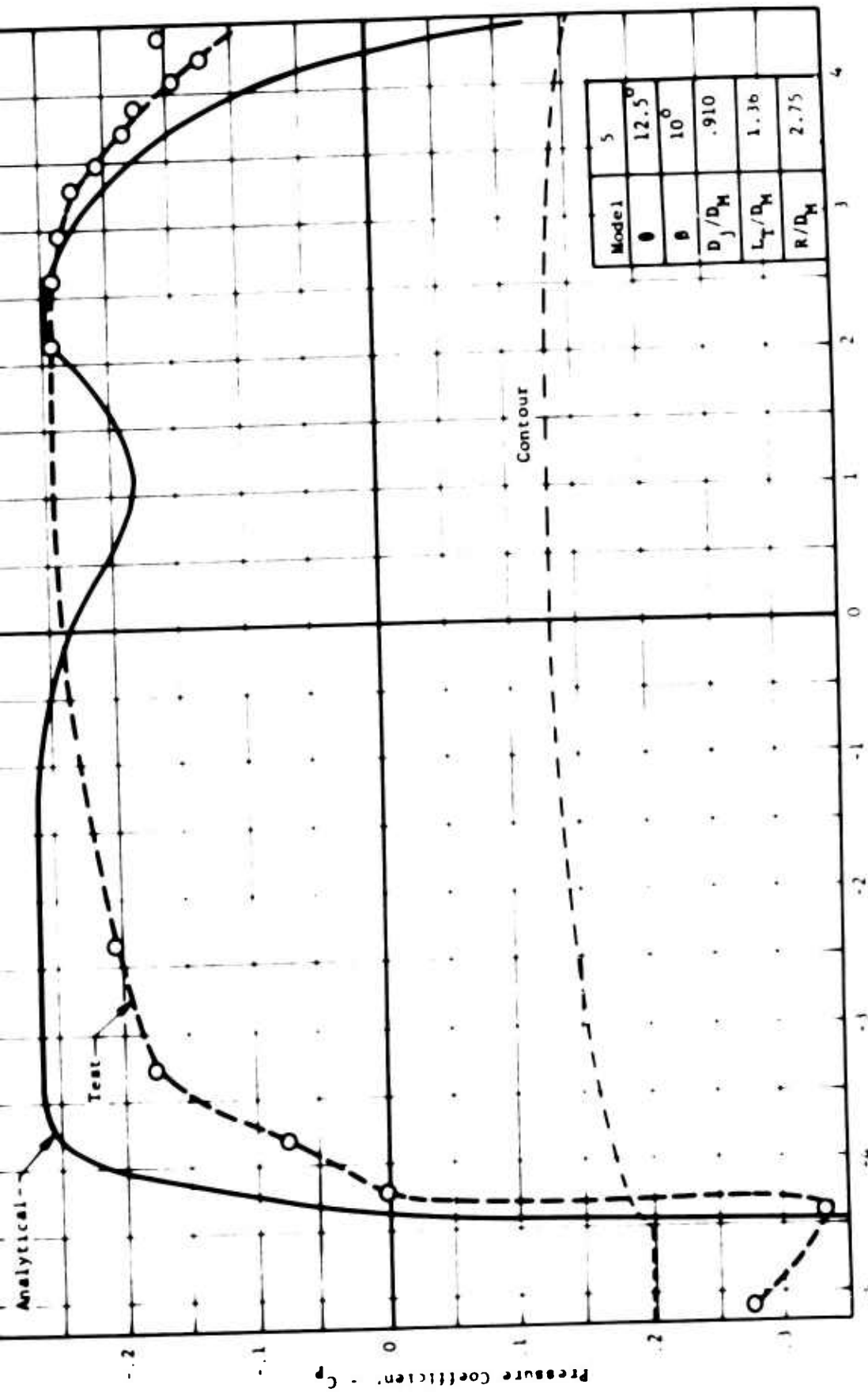


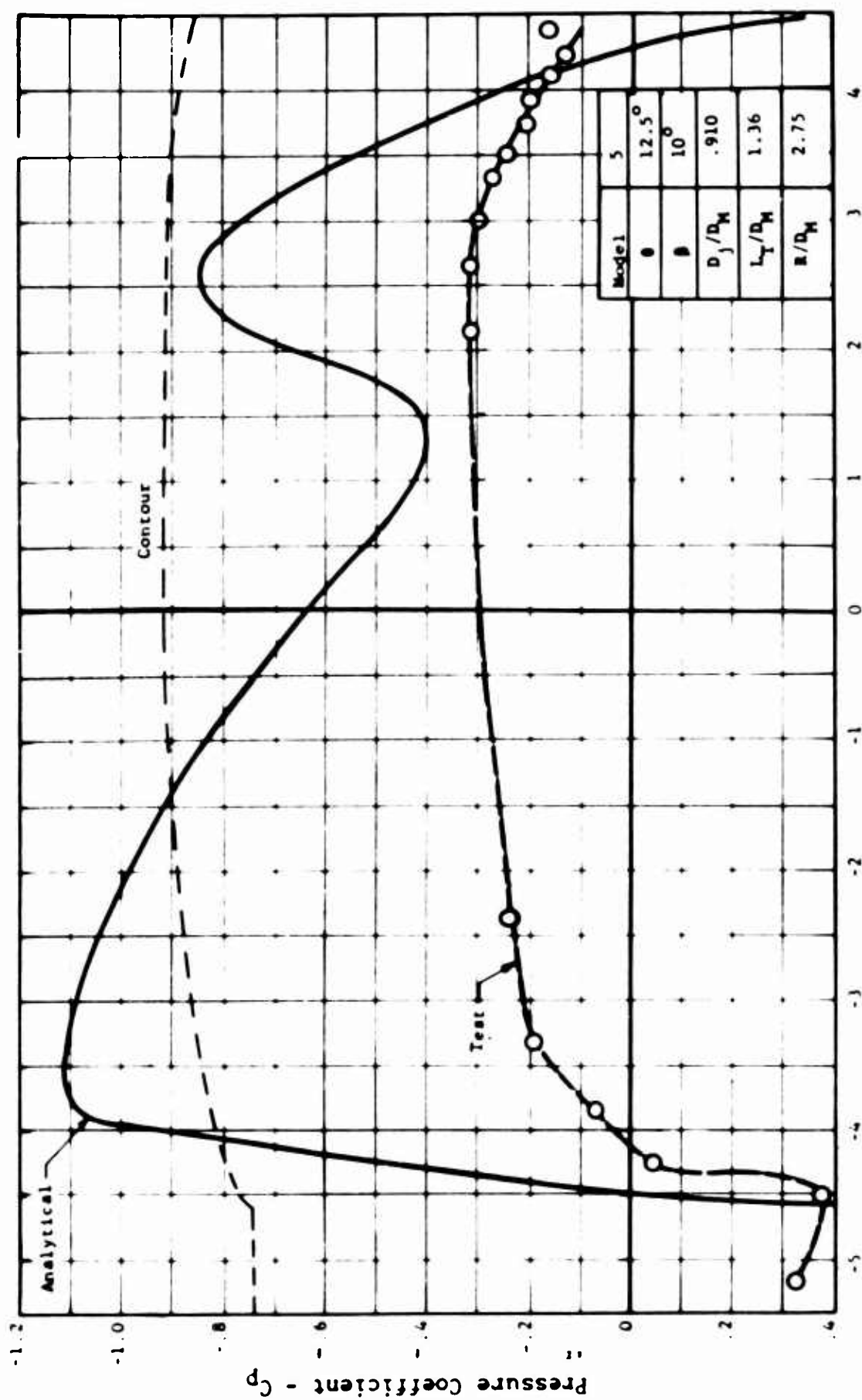
Figure 145. Comparison of Drag Coefficients to Other Test Data at Mach .6.





Axial Distance Along Centerline - In.

Figure 147. Comparison of Nacelle Pressure Distribution to Analytical Calculations at Mach .6.



Axial Distance Along Centerline - In.
 Figure 148. Comparison of Nacelle
 Pressure Distribution to
 Analytical Calculations
 at Mach .8.

DISTRIBUTION

U. S. Army Materiel Command	3
U. S. Army Mobility Command	2
U. S. Army Aviation Materiel Command	2
Chief of R&D, D/A	3
U. S. Army Transportation Research Command	42
U. S. Army Research and Development Group (Europe)	4
U. S. Army Natick Laboratories	1
U. S. Army Engineer Research and Development Laboratories	2
U. S. Army Signal Research and Development Laboratory Liaison Office	1
U. S. Army Limited War Laboratory	1
Army Research Office-Durham	1
U. S. Army Research Support Group	1
U. S. Army Engineer Waterways Experiment Station	1
U. S. Army Combat Developments Command	1
U. S. Army Combat Developments Command Aviation Agency	2
U. S. Army CDC, Transportation Agency	1
U. S. Army War College	1
U. S. Army Command and General Staff College	1
U. S. Army Transportation School	1
U. S. Army Aviation School	1
U. S. Army Transportation Center and Fort Eustis	1
U. S. Army Aviation Test Board	1
U. S. Army Aviation Test Activity	1
U. S. Army Representative, Air Force Systems Command, Andrews AFB	1
Air Force Systems Command, Wright-Patterson AFB	1
Air Force Flight Test Center, Edwards AFB	1
Air Proving Ground Center, Eglin AFB	1
Air University Library, Maxwell AFB	1
Bureau of Naval Weapons	6
U. S. Naval Postgraduate School	1
Naval Air Test Center	1
David Taylor Model Basin	2
Marine Corps Educational Center	1
Ames Research Center, NASA	2
NASA-LRC, Langley Station	2
Lewis Research Center, NASA	2
Manned Spacecraft Center, NASA	2

NASA Representative, Scientific and Technical Information Facility	2
National Aviation Facilities Experimental Center	1
Canadian Liaison Officer, U. S. Army Transportation School	1
Defense Documentation Center	20
U. S. Government Printing Office	1

General Electric Company, Evendale,
Ohio, LIFT/CRUISE FAN EXHAUST SYSTEM
RESEARCH PROGRAM - W. A. Fasching,
John Kutney

Technical Report 64-49, September
1964 (Contract DA 44-177-AMC-74T)
USATRECOM Task ID121401A14228.
Unclassified Report

Results of static and wind tunnel
cold-flow scale-model tests of
convergent-conical nozzles and
convergent-plug nozzles with a

(over)

1. Exhaust Nozzles
2. Lift/Cruise Fan Exhaust System
3. Task ID121401A14228

General Electric Company, Evendale,
Ohio, LIFT/CRUISE FAN EXHAUST SYSTEM
research program - W.A. Fasching,
John Kutney

Technical Report 64-59, September
1964 (Contract DA 44-177-AMC-74T)
USATRECOM Task ID121401A14228.
Unclassified Report

Results of static and wind tunnel
cold-flow scale-model tests of
convergent-conical nozzles and
convergent-plug nozzles with a

(over)

1. Exhaust Nozzles
2. Lift/Cruise Fan Exhaust System
3. Task ID121401A14228

General Electric Company, Evendale,
Ohio, LIFT/CRUISE FAN EXHAUST SYSTEM
RESEARCH PROGRAM - W.A. Fasching,
John Kutney

Technical Report 64-49, September
1964 (Contract DA 44-177-AMC-74T)
USATRECOM Task ID121401A14228.
Unclassified Report

Results of static and wind tunnel
cold-flow scale-model tests of
convergent-conical nozzles and
convergent-plug nozzles with a

(over)

1. Exhaust Nozzles
2. Lift/Cruise Fan Exhaust System
3. Task ID121401A14228

Technical Report 64-49, September
1964 (contract DA 44-177-AMC-74T)
USATRECOM Task ID121401A14228.
Unclassified Report

Results of static and wind tunnel
cold-flow scale-model tests of
convergent-conical nozzles and
convergent-plug nozzles with a

(over)

1. Exhaust Nozzles
2. Lift/Cruise Fan Exhaust System
3. Task ID121401A14228

forebody and various afterbodies, simulating lift/cruise fan nacelle installations, are reported. Thrust-, drag-, and discharge-coefficients as well as model surface pressure distributions are presented for the representative lift/cruise fan nozzle pressure ratio range of 1.2 to 2.4 and flight Mach numbers of .0, .4, .6, .8, and .9. The test results are analyzed and compared to other test data and analytical calculations.

fore body and various afterbodies, simulating lift/cruise fan nacelle installations, are reported. Thrust-, drag-, and discharge-coefficients as well as model surface pressure distributions are presented for the representative lift/cruise fan nozzle pressure ratio range of 1.2 to 2.4 and flight Mach numbers of .0, .4, .6, .8, and .9. The test results are analyzed and compared to other test data and analytical calculations.

forebody and various afterbodies, simulating lift/cruise fan nacelle installations, are reported. Thrust-, drag-, and discharge-coefficients as well as model surface pressure distributions are presented for the representative lift/cruise fan nozzle pressure ratio range of 1.2 to 2.4 and flight Mach numbers of .0, .4, .6, .8, and .9. The test results are analyzed and compared to other test data and analytical calculations.

forebody and various afterbodies, simulating lift/cruise fan nacelle installations, are reported. Thrust-, drag-, and discharge-coefficients as well as model surface pressure distributions are presented for the representative lift/cruise fan nozzle pressure ratio range of 1.2 to 2.4 and flight Mach numbers of .0, .4, .6, .8, and .9. The test results are analyzed and compared to other test data and analytical calculations.

General Electric Company, Evendale,
Ohio, LIFT/CRUISE FAN EXHAUST SYSTEM
RESEARCH PROGRAM - W. A. Pasching,
John Kutney

Technical Report 64-49, September
1964 (Contract DA 44-177-AMC-74T)
USATRECOM Task ID121401A14228.
Unclassified Report

Results of static and wind tunnel
cold-flow scale-model tests of
convergent-conical nozzles and
convergent-plug nozzles with a

(over)

General Electric Company, Evendale,
Ohio, LIFT/CRUISE FAN EXHAUST SYSTEM
RESEARCH PROGRAM - W. A. Pasching,
John Kutney

Technical Report 64-49, September
1964 (Contract DA 44-177-AMC-74T)
USATRECOM Task ID121401A14228.
Unclassified Report

Results of static and wind tunnel
cold-flow scale-model tests of
convergent-conical nozzles and
convergent-plug nozzles with a

(over)

1. Exhaust Nozzles
2. Lift/Cruise Fan Exhaust System
3. Task ID121401A14228

General Electric Company, Evendale,
Ohio, LIFT/CRUISE FAN EXHAUST SYSTEM
research program - W. A. Pasching,
John Kutney

Technical Report 64-59, September
1964 (Contract DA 44-177-AMC-74T)
USATRECOM Task ID121401A14228.
Unclassified Report

Results of static and wind tunnel
cold-flow scale-model tests of
convergent-conical nozzles and
convergent-plug nozzles with a

(over)

1. Exhaust Nozzles
2. Lift/Cruise Fan Exhaust System
3. Task ID121401A14228

General Electric Company, Evendale,
Ohio, LIFT/CRUISE FAN EXHAUST SYSTEM
RESEARCH PROGRAM - W. A. Pasching,
John Kutney

Technical Report 64-49, September
1964 (Contract DA 44-177-AMC-74T)
USATRECOM Task ID121401A14228.
Unclassified Report

Results of static and wind tunnel
cold-flow scale-model tests of
convergent-conical nozzles and
convergent-plug nozzles with a

(over)

1. Exhaust Nozzles
2. Lift/Cruise Fan Exhaust System
3. Task ID121401A14228

Technical Report 64-59, September
1964 (Contract DA 44-177-AMC-74T)
USATRECOM Task ID121401A14228.
Unclassified Report

Results of static and wind tunnel
cold-flow scale-model tests of
convergent-conical nozzles and
convergent-plug nozzles with a

(over)

1. Exhaust Nozzles
2. Lift/Cruise Fan Exhaust System
3. Task ID121401A14228

Technical Report 64-49, September
1964 (Contract DA 44-177-AMC-74T)
USATRECOM Task ID121401A14228.
Unclassified Report

Results of static and wind tunnel
cold-flow scale-model tests of
convergent-conical nozzles and
convergent-plug nozzles with a

(over)

forebody and various afterbodies, simulating lift/cruise fan nacelle installations, are reported. Thrust-, drag-, and discharge-coefficients as well as model surface pressure distributions are presented for the representative lift/cruise fan nozzle pressure ratio range of 1.2 to 2.4 and flight Mach numbers of .0, .4, .6, .8, and .9. The test results are analyzed and compared to other test data and analytical calculations.

fore body and various afterbodies, simulating lift/cruise fan nacelle installations, are reported. Thrust-, drag-, and discharge-coefficients as well as model surface pressure distributions are presented for the representative lift/cruise fan nozzle pressure ratio range of 1.2 to 2.4 and flight Mach numbers of .0, .4, .6, .8, and .9. The test results are analyzed and compared to other test data and analytical calculations.

forebody and various afterbodies, simulating lift/cruise fan nacelle installations, are reported. Thrust-, drag-, and discharge-coefficients as well as model surface pressure distributions are presented for the representative lift/cruise fan nozzle pressure ratio range of 1.2 to 2.4 and flight Mach numbers of .0, .4, .6, .8, and .9. The test results are analyzed and compared to other test data and analytical calculations.

forebody and various afterbodies, simulating lift/cruise fan nacelle installations, are reported. Thrust-, drag-, and discharge-coefficients as well as model surface pressure distributions are presented for the representative lift/cruise fan nozzle pressure ratio range of 1.2 to 2.4 and flight Mach numbers of .0, .4, .6, .8, and .9. The test results are analyzed and compared to other test data and analytical calculations.

BLANK PAGE